LABORATORY TESTS AND NUMERICAL MODEL OF GEOTHERMALLY HEATED BRIDGE DECK WITH ATTACHED HYDRONIC LOOP

by

Teng Li

Presented to the Faculty of the Graduate School of

The University of Texas at Arlington

in Partial Fulfillment of the Requirements

for the Degree of

DOCTOR OF PHILOSOPHY

THE UNIVERSITY OF TEXAS AT ARLINGTON

December 2020

This dissertation work is dedicated to my parents and my wife for their constant support and sincere love for me.

ACKNOWLEDGEMENT

First, I would like to express my deepest gratitude to my research advisor, Dr. Xinbao Yu, for his sincere guidance, support, and encouragement during my doctoral research. I sincerely appreciate the friendly research environment and fantastic research facilities he provided me during my Ph. D. studies. I truly learned a lot from his excellent guidance and motivation, which significantly helped my dissertation research come to fruition.

I am also grateful to Dr. Anand J. Puppala, Dr. Suyun Ham, and Dr. Kent L. Lawrence for their willingness to serve on my committee. Their valuable comments, considerations, and time are very appreciated.

Furthermore, I would like to thank the Texas Department of Transportation (TxDOT) for their financial support. The staff members of the Department of Civil Engineering. Guatam Eapi, Ms. Irma Rose Dodd, Ms. Sara K. Ridenour, and Ms. Jamie L Thompson, gave me a lot of academic and administrative assistance, for which I am grateful.

I would also like to thank my colleagues, Dr. Aritra Banerjee, Dr. Sarat Congress, Dr. Mohammad Rakib Hasan, Dr. Shi He, Omid, Gang, Mark, Sunil, Xuelin, Nice, Subhas, Sandesh, Samrat, Hiramani, Mandakini, Tom, Taryn, and Esmat for their assistance and sincere encouragement during my dissertation research.

Finally, I would like to thank my beloved parents, parents-in-law, and wife, for their endless love and encouragement. None of this would have happened without them.

November 15th, 2020

ABSTRACT

LABORATORY TESTS AND NUMERICAL MODEL OF GEOTHERMALLY HEATED BRIDGE DECK WITH ATTACHED HYDRONIC LOOP

Teng Li

The University of Texas at Arlington, 2020

Supervising Professor: Xinbao Yu

An accumulation of ice and snow on pavement slabs and bridge decks always adversely impacts driving conditions and results in motorist accidents. The use of the more popular deicing methods, including plowing, salting, and sanding, is limited by their relatively high cost for materials, fuel, maintenance, and labor. Geothermal energy, which is considered a renewable, sustainable, clean (i.e., zero carbon emission), and directly used energy source, has been successfully applied to bridges and pavements for deicing. However, existing geothermal bridge and pavement deicing designs are primarily employed for new bridges where hydronic loops, which are considered internal heating, are embedded in the concrete deck during the bridges' construction. An alternative external geothermal heating system has been developed, in which hydronic loops are attached to the bottom of the bridge deck and encapsulated in a layer of spray foam to heat existing pavement slabs and bridge decks under severe winter events.

This research study is based on an accurate understanding of the heat transfer mechanism of an externally heated hydronic slab and on a comprehensive numerical analysis of the heating requirements and expected performances of the external system. A heated concrete slab was

fabricated and installed in an environmental chamber in the structural lab at the University of Texas at Arlington (UTA), and with the help of COMSOL software, the slabs were replicated to analyze the heating performance of the external design. The slab-scale finite element model was fully calibrated by 16 laboratory heating response tests under time-dependent and stationary approaches that were used to simulate the complex heat transfer mechanisms of an externally heated deck and predict its steady-state surface temperatures under various ambient below-freezing temperatures. The results of the transient heating processes indicated temperature deviations, however, and the temperature drop at the interface zone (interface heat transfer) needs to be validated.

One internally and one externally heated concrete blocks were utilized to investigate two critical interface heat transfers, convective heat loss from the environment and thermal contact between PEX pipes and the concrete, by employing a series of heating tests that were performed in a freezer box. This study aims to utilize theoretical contributions to develop an updated thermal contact model and the convective coefficient to develop more finite element models that comprehensively understand the heat transfer process that occurs in an externally heated bridge deck. The improved results will, for the first time, be utilized in COMSOL to simulate the heating tests conducted in the freezer box and to obtain better agreements of the temperature profiles along the vertical direction and transient heating processes between the measured and simulated results.

In this study, the external geothermal bridge deicing system was deployed on a mock-up bridge deck in the field and was tested during several winter events with non-heating, heating, and deicing tests. A 3-dimensional Multiphysics finite element model of the heated deck was developed in COMSOL and fully calibrated with the results of the field tests in the transient analyses. The predicted temperatures of the FEM models were compared with the thermocouple readings at the inlet and outlet of the bridge loops, at different depths of the bridge decks in the

simulated winter tests. In the calibrated FEM model, a record snowfall that occurred in the spring of 2015 was simulated by applying the equivalent heat flux loss needed for melting the snow on the deck. The heated bridge deck maintained a minimum temperature of 0.3 °C (32.6 °F) during the snow event, with a supplied inlet temperature of 43.3 °C (110 °F); the flux loss on the deck surface was around 220 W/m^2. The FEM model was capable of providing satisfactory simulations of bridge heating during winter events. The external geothermal bridge deicing system maintained a snow-free deck during the record snow event and is ready for implementation.

Finally, a series of design charts were developed by utilizing the reformative model to perform the design process of an externally heated bridge deck under parametric studies. This is the first numerical design guideline to be performed in this research area.

Keywords: Deicing, Hydronic Loops, External Heated Bridge Deck, Geothermal Energy, Numerical Analysis, Heating Performance, Parametric Studies, Design Charts

TABLE OF CONTENTS

LIST OF ILLUSTRATIONS

LIST OF TABLES

F

CHAPTER 1 INTRODUCTION AND BACKGROUND

1.1 General

Bridges are an essential part of transportation systems and play a vital role in the development of a nation's economy and security. Snow and ice have negative impacts on drivers' behavior, bridge friction, roadway capacity, and vehicle maneuverability, and cause dangerous driving conditions that lead to an increased risk of crashes. In the US, over 70 percent of roads are in regions that have more than five inches (13 cm) of snow annually (Perkins et al. 2012). From 2000 to 2010, 642 winter events occurred in Texas, and in the US, 7000 lives are lost every year due to winter storms. Therefore, deicing pavements and bridge decks is an essential part of transportation maintenance during the winter. The most commonly used method of melting ice is the application of salts and other chemicals that are placed directly on the surfaces of the pavements and bridges. However, as many researchers have shown in previous studies, these snow/ice-melting agents are costly and result in accelerated corrosion and degradation of pavements and bridge structures (Bowers and Olgun 2014; Koch et al. 2002; Naito et al. 2010; Virmani et al. 1983). Even more serious is the potential for them to invade rivers and soils that are near these infrastructures, contaminating them through infiltration and surface runoff. Therefore, a series of technological advances, including hydronic systems (Alonso-Estébanez et al. 2017; Asfour et al. 2016; Mirzanamadi et al. 2018; Wu et al. 2011), electrical systems (Liu et al. 2017), and heat pipes (Wang et al. 2017), have been developed as alternatives to chemical applications for deicing bridge decks/pavements.

In hydronic heating systems, the fluid carrying the heat extracted from the underground soils is circulated by a pump through hydronic loop systems that are embedded within the bridge deck to transfer heat energy to the bridge deck surface by conduction. Instead of using external

circulating power to circulate the fluid, the available working fluid, including Freon, ammonia, and CO2 (Wang et al. 2017) is first evaporated at the evaporator portion the heat pipe. Then, the produced vapor flows upward, is condensed in the condenser portion of the pipe, and finally travels to the deck surface for the heating operation. To use gravity to complete the fluid circulation between the evaporator and condenser portions, the inclination of the heat pipe system's relative to the horizontal plane needs to be considered during the system's installation. The electricity utilized as a heat source in electrical heating systems is supplied by electric cables embedded within the bridge deck, and the resistance of the electrical wires and the applied voltage have a major effect on the performance of the electric heating system (Liu 2005).

Hydronic heating is currently the most commonly used and promising method of the three available advanced heating technologies. Unlike for heat pipe systems, the pipe's inclination does not have to be considered in hydronic systems since it depends on external power to circulate the fluid flow, but the interior cleanliness of each heat pipe plays a remarkable role in the system's performance. The disadvantages are higher construction and installation costs. Hydronic systems are capable of providing higher heating efficiency than electrical systems since energy loss occurs during the power transmission in the form of heat. What is more important is that it is possible to detect potential dangers caused by aging or damaged insulation materials.

The ground is viewed as an ideal heat source for deicing bridge decks, as it can provide a relatively constant temperature and heat storage capacity at a certain depth (Bowers 2016; Brandl 2006; Ozudogru et al. 2014). Because of its sustainability, renewability, and non-pollution, geothermal energy has been utilized in several recently developed pavement and bridge deicing techniques, just as it has in ground-source heat pumps (GSHPs), geothermal energy piles (GEPs), and borehole thermal energy storage (BTES) (Amayta et al. 2012; Nam and Chae 2014; Sterpi et

al. 2018; Zhang et al. 2017). For example, GEPs are considered economical and innovative approaches to accessing geothermal energy for heating and cooling buildings and bridges. The primary design parameters for GEPs, including the thermal conductivity of the in-situ soils and turbulent flow conditions, play a remarkable role on the GEP performance (Abdelaziz et al., 2011). Recent research findings, through an efficient, mixed 1D-3D numerical model validated by experimental and numerical data, indicate that coupling energy piles with heat pumps can obtain significant benefits in the application of ground energy sources and systems (Carotenuto et al. 2017). In a geothermal energy heating system, the bridge deck/pavement operates as a solar energy collector during the summer, and the energy can be transferred into the ground and stored for heating in the winter. Because the injection/extraction efficiency is subjected to temperature and moisture changes in the thermal interfaces between the pile/boreholes and surrounding soil, laboratory tests were conducted under controlled boundary conditions, such as 1-D thermal gradients or temperature cycles, and analyzed (Fadejev et al. 2017; Lei et al. 2019; Shang et al. 2011; Xiao and Suleiman 2015). The application of ground-source heating technology is economical and has the added advantage of minimizing cracking during initial concrete curing by decreasing the bridge deck's temperature (Bowers and Olgun 2014). Without even taking the environmental benefits into account, a case study in North Texas showed that the overall benefits of GHDS (geothermal heat pump deicing systems) are 2.6 times greater than their overall costs (Habibzadeh-Bigdarvish et al. 2019). The application of new materials in combination with heating technologies has also been gradually developed. In a recent analysis of thermal and hygrometric characteristics of building structures, it was found that when recycled plastic is utilized as a concrete aggregate, it can significantly increase energy efficiency, which is beneficial for studying how thermal and hygrometric behavior affects a building structure (Colangelo et al.

2013). Similar combinations of new materials and technologies are expected to be developed for geothermal heating applications.

It is unfortunate that this technology is still encountering a series of challenges due to the lack of reliable design guidelines. Many design parameters, including material properties, geometric configurations, operational factors, control scenarios, and environmental circumstances, can affect the system's heating performance and lifecycle cost. Therefore, it is important to evaluate combinations of design parameters when implementing a geothermally heated bridge deck. Due to the limitations of laboratory, field test conditions, and the number of tests required, numerical modeling is often used to perform parametric studies under various conditions to optimize the system design.

Many numerical modeling analyses have been performed on the heat transfer behaviors within a bridge deck and between the slab and the surrounding environment. The heat transfer processes, from the circulating fluid to the deck surface, are essential for analyzing the bridge deck's heating performance and thermal behaviors, which is critical to the accuracy of numerical modeling. The development of the hydronic snow-melting models can be grouped in terms of steady-state and transient approaches. Steady-state models are developed based on the assumption that the heating system is in a steady state; hence the discontinuous operation and various environmental circumstances are not considered in this analysis. Transient models focus on analyzing multiple surface conditions of a heated bridge deck/pavement surface, including ice/snow phase changes under snowy scenarios. The descriptions of hydronic snow-melting models will be presented in detail in Chapter 2.

Previous studies relied on an internal heat source that was installed inside the concrete deck during the construction of the bridge, but its design cannot be applied to existing bridges, which

have the most critical need for deicing. In this research, a series of experimental and numerical studies were conducted to determine the feasibility of developing an external heating design for heating existing bridges to melt the ice and snow on them.

This research aims to provide a comprehensive understanding of the heating and heat transfer mechanisms of externally heated bridge decks under various heating scenarios, using numerical and experimental approaches. Validated FEM models and series of design charts were developed as numerical design tools for the externally heated bridge decks.

1.2 Problem Statement

Most geothermal heating studies concentrate on the internal heating design embedded in new bridge decks during the construction phase; few studies have been performed on the use of geothermal energy to externally heat bridges. Due to a limited number of studies, progress was slow on researching the use of interface heat transfer for hydronically heated bridge decks, e.g., pipe and concrete interface, and concrete and air interface. Comprehensive information pertaining to the heat transfer process, starting with the supplied heat-carrier fluids and ending at the bridge deck surface, is lacking. Various parameters, including bridge deck properties, weather conditions, control systems, the layout of the heating elements, and geometric configurations, can affect the heating efficiency and heat transfer behavior within the bridge deck. However, it is practically impossible for laboratory and field tests to provide a comprehensive evaluation of the effects of the various combinations of design parameters on the system's performance. Non-sufficient conductions of laboratory and field tests also limited the analysis of the externally heated bridge deck's feasibility. Finally, there were no snow melting simulations for externally heated bridge decks, and no standard design charts were available for this new design.

1.3 Research Objectives

Severe winter conditions result in serious vehicular accidents. Thus, the goal of this geothermal heated bridge/pavement project is to provide TxDOT with a more renewable, sustainable, and cleaner approach to deicing bridges and pavements than the current method of using snow-melting agents that may result in chemical corrosion. Most of the geothermal heating systems applied to de-ice bridges in the winter previously were installed in the concrete deck during the bridge's construction. As an alternative that could be applied to existing bridges, bridge deck models were developed with external heating hydronic loops systems encapsulated in geofoam spray to provide insulation. A series of design charts, performed by the evaluated FEM model developed in COMSOL Multiphysics, were used to analyze the heating performance of the external design. (COMSOL is a finite element method (FEM) tool that can be used to facilitate geothermal external heating design for future implementation and instrumentation, thus remarkably alleviating treacherous road conditions and ensuring transportation safety during extreme winter conditions. The specific research tasks are listed below, and Fig. 1-1 shows the flowchart for the research tasks.

(1) Numerical analyses of a laboratory test of a geothermal slab-scale bridge deck externally heated under controlled temperature

(2) Element-scale heating test to study interface heat transfer mechanisms

(3) Numerical investigations of field tests of a mock-up bridge deck externally heated under variable operation scenarios

(4) Development of design charts based on a series of numerical parametric analyses of externally heated bridge decks:

a) Thickness of the heated concrete slab

b) Pipe spacing

c) Environmental factors (ambient temperature, wind speed, rate of snowfall, and flow rate)

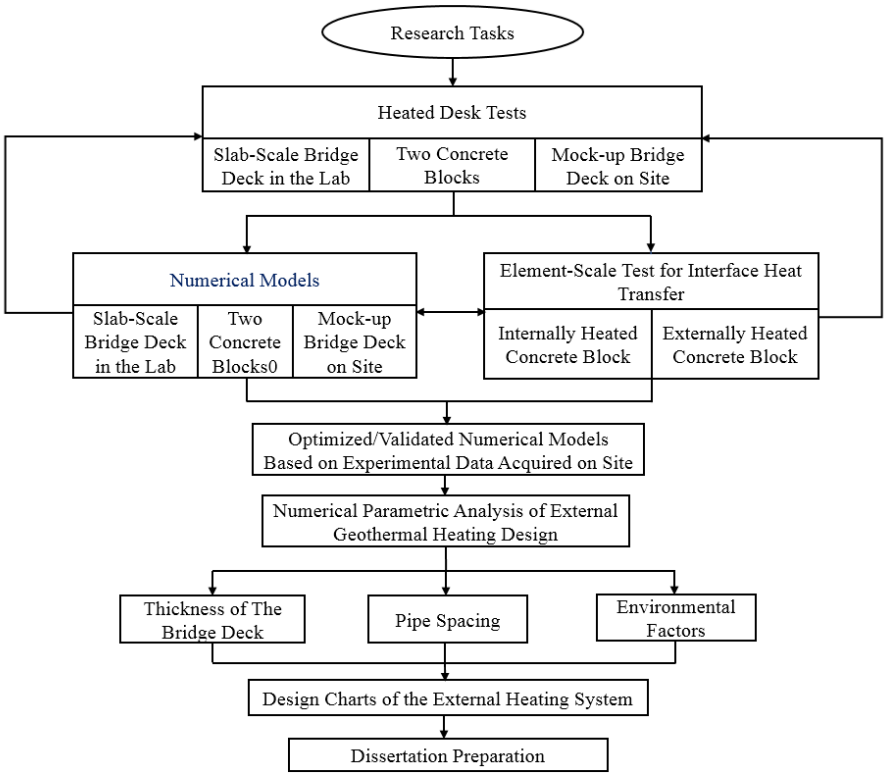

Figure 1-1 Flowchart of the research tasks

1.4 Organization of Dissertation

This dissertation is divided into seven chapters.

Chapter 1: Introduction and background

- Overview: The first chapter introduces a heating system that uses geothermal energy for melting snow on bridge decks/pavements. The research objectives are discussed and emphasize the intellectual merit and broader impacts of this dissertation. This research presents the limitations of current published research findings, which this dissertation aims to enhance.

Chapter 2: Literature review

- Overview: The application of geothermal energy for bridge deck/pavement deicing is presented in this chapter. The development of the numerical hydronic snow-melting models is summarized in terms of steady-state and transient approaches, and a series of experimental investigations and case studies that were conducted on bridge deck/pavement deicing are discussed. Comparisons are made of internally and externally heated bridge decks, and the research findings on externally geothermal heated bridge decks provide an overall understanding of this newly developed heating design that can be applied to existing bridges/pavements.

Chapter 3: Numerical analyses of a laboratory test of a geothermal bridge deck externally heated under controlled temperature.

- Overview: This chapter discusses a 3D FEM model of the externally heated deck created in COMSOL Multiphysics (COMSOL 2016). Its transient simulation was calibrated using the experimental results acquired in the environmental chamber. The calibrated finite element model was further verified by the steady-state results of 15 environmental chamber tests. A comprehensive analysis of the heat transfer mechanism and energy balance was performed with the aid of the FEM model. The calibrated model can be a useful tool for heat transfer analyses and the design of externally heated hydronic bridges.
- Journal: Applied Thermal Engineering (published)

Chapter 4: Element-scale heating test to study interface heat transfer mechanisms

- Overview: This chapter introduces experimental and numerical investigations of element-scale heating tests to study interface heat transfer mechanisms. To decrease the difficulty of experimental construction and computational time in numerical analysis, two concrete

blocks, one with an internal heating system and one with an external heating system, were constructed and installed in the structural lab at the University of Texas at Arlington (UTA) and were utilized to conduct the heating tests covered in this chapter. A series of experimental measurements calibrated the replicated FEM models that were developed in COMSOL Multiphysics. The interface heat transfer mechanisms, including block surface-air convection and pipe-concrete thermal contact, were further analyzed, and better agreement between numerical and experimental results was obtained.

- Journal: International Journal of heat and mass transfer (ready for submission)

Chapter 5: Heating performance of a novel externally-heated geothermal bridge deicing system: field tests and numerical simulations

- Overview: A 3D FEM model of an externally heated mock-up bridge deck was developed in COMSOL Multiphysics and was validated by the experimental data collected from three practical operations: non-heating, heating, and heating and deicing. A numerical investigation was conducted to estimate the practical feasibility of melting snow with the external heating system by using the validated FEM model under the conditions of one of the most severe snow events that has occurred in the Dallas/Fort Worth (DFW) area. The simulated results illustrated that the calibrated FEM model could be viewed as an accurate numerical framework for estimating externally heated bridge decks' heating performance during snow events.
- Journal: Renewable Energy (ready for submission)

Chapter 6: Externally heated bridge deck design by utilizing a series of design charts developed under various conditions

- Overview: A series of parametric studies performed by the validated finite element models were utilized to provide a comprehensive design process of an externally heated bridge deck. Stationary models were employed to analyze the interactions between thermal supplies and the average steady-state temperatures on the deck surface, and the application of transient models to estimate the heating times required to raise the average temperatures at the deck surface above freezing (0 °C/32 °F) under various weather conditions and geometric configurations.
- Journal: To be selected.

Chapter 7: Conclusions and recommendations.

- Overview: This chapter summarizes the significant and novel research findings derived from this dissertation. The limitations of the research and recommendations for future studies on externally heated geothermal bridge decks are also discussed.

CHAPTER 2 LITERATURE REVIEW

2.1 Introduction

Bridges have always been a critical element of the transportation infrastructure system, as they significantly impact society and the economy. Icy bridge decks result in hazardous driving conditions and traffic accidents during severe winter events every year. From 2000 to 2010, 642 winter events occurred in Texas and 7,000 lives are lost every year in the U.S. because of severe weather conditions. Therefore, the deicing of bridges and deck/pavements is considered one of the top maintenance assignments during the winter for transportation departments. Currently, the application of chemical deicers, including calcium chlorides or sands, is the most commonly used method employed. Fig.2-1 shows a deicing truck distributing deicers on a bridge deck surface. Unfortunately, these snow/ice-melting deicers contain chlorides that result in the corrosion of steel reinforcements and the degradation of pavements/bridge structures (Koch et al. 2002; Naito et al. 2010; Ozudogru et al. 2014; Virmani et al. 1983; Yunovich et al. 2003). Even more serious is the potential for contamination of the rivers and soils near these infrastructures through infiltration and surface runoff. The high cost of the repairs, fuel, and labor also limits the use of these methods and makes the development of alternative deicing approaches necessary.

Figure 2-1. North Texas hit with record snowfall; Fort Worth a ghost town (http://www.star-telegram.com/)

The U.S. Department of Transportation classifies snow melting technological advances for enhancing the performance of a heating system and reducing energy consumption during deicing and snow melting operations into three categories: hydronic (Alonso-Estébanez et al. 2017; Asfour et al. 2016; Mirzanamadi et al. 2018; Wu et al. 2011), heat pipes (Liu et al. 2017), and electrical (Wang et al. 2017). This literature review showed that the hydronic heating system is currently the most commonly used method. The significant components of a geothermal heating system for bridge decks/pavements are a ground-loop heat exchanger (GLHE) system and hydronically heated pavement slabs and bridge decks (Chiasson and Spitler 2001b). The fluid extracted from under the ground flows into a heat pump where it is heated to the desired temperature and pumped into the bridge deck/pavement. In the summer, solar energy can be collected by the bridge deck/pavement and transferred into the ground to be stored as energy that can be used in the winter.

Most previous studies focused on an internal heat source that is embedded within the concrete deck during the pouring operation. This internal heating design cannot be applied to

existing bridges, however, where the demands for deicing are highest. Therefore, a hydronic heating design with an external heat source was developed that can be applied to existing bridges.

Section 2.2 of this chapter presents an overview of a geothermal energy application for bridge deck/pavement deicing that includes a geothermal energy foundation, geothermal heat pump, and design of hydronically geothermal heating systems. The geothermally hydronic snow-melting models are classified into either steady-state or transient models. Results of experimental investigations of the geothermally heated bridge deck are shown in Section 2.3. A series of experimental experiments and case studies performed in Europe, Asia, and the U.S. that used geothermal energy for deicing bridge decks/pavements are also discussed in this chapter (Sections 2.4 and 2.5). Finally, the research focuses on the externally geothermal heated bridge decks dealt with in Section 2.6 and provide a comprehensive understanding of the heating design.

2.2 Application of Geothermal Energy for Bridge/Pavement Deicing

The advanced deicing technology was developed based on sustainability, renewability, and safety of the ground-source heat pumps (GSHPs), geothermal energy piles (GEPs), and borehole thermal energy storage (BTES) (Amayta et al. 2012; Nam and Chae 2014; Sterpi et al. 2018; Zhang et al. 2017). This section provides an overview of a hydronically heated bridge deck that was developed by extracting geothermal energy from the underground to provide the heat sources for the bridge deck/pavement.

2.2.1 Ground Source Heat Pump Systems

The underground is considered an ideal source of heat that can be applied to bridge deck/pavements in the winter because of its ability to maintain a relatively constant temperature at a certain depth. The heat is extracted by circulating fluid by utilizing a heat pump that was invented by Lord Kelvin in 1852. Over the last 10 to 20 years, the number of geothermal energy applications

for heating and cooling operations for buildings or other infrastructures has remarkably increased because of the ground-source heat pumps (GSHPs).

Shallow geothermal energy systems (SGES) have evolved into an increasingly popular method by which to provide efficient heating and cooling for buildings or other infrastructures, as they are able to utilize the relatively constant temperature of the ground that is below a depth of more than 10 m to perform practical operations (Bowers and Olgun 2014). Additional borehole installation work is not required since the heat exchanger systems and building foundations can integrate with thermal activation (Brandl 2006). Shallow geothermal energy also can be employed in other areas such as grain drying and greenhouse temperature regulation (Lund and Boyd 2016; Minsk 1999). With the application of shallow geothermal energy, ground-source heat pump (GSHP) systems are capable of providing more efficient heating and cooling for buildings and other infrastructures than traditional heat pump systems (Lund and Boyd 2016). Thus, they have been developed rapidly globally, particularly in parts of Europe, North America, and China.

GSHP systems can be operated as either an energy source (heating) or an energy sink (cooling), and Fig. 2-2 depicts a schematic of both. In the heating mode, the fluid carrying the heat extracted from the underground soils is circulated through the vertical energy piles/boreholes or building/infrastructure foundations and the loops embedded in horizontal trenches. Before being pumped into the hydronic loop systems installed in buildings or infrastructures, the fluid first flows into the heat pump system to be heated at the desired temperature. Then the fluid with a cooler temperature returns to the underground loop through the previous paths and completes the flowing circle. In the cooling mode, the operation is the reverse of that of heating. The heat collected from buildings or infrastructures is transferred into the underground by a circulation pump, heat pump,

and the circulating fluid, and is operated as borehole thermal energy storage (BTES) that can be reutilized for heating operations in the winter.

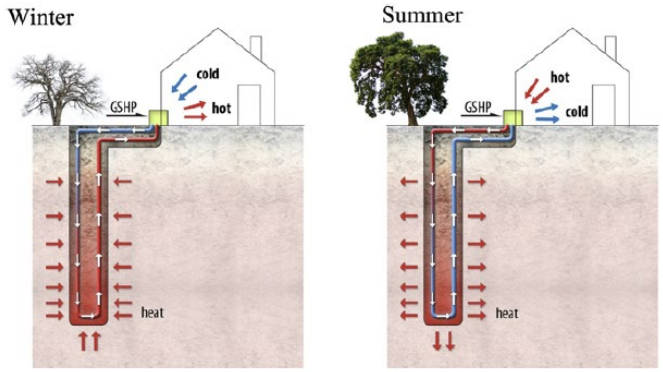

(a)

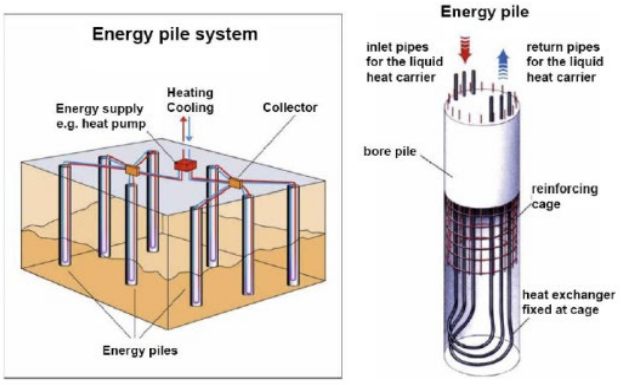

(b)

Figure 2-2. (a) Schematic of a GSHP for space heating and cooling, (b) energy pile system (Johnston et al. 2011)

This technology still encounters a series of challenges, the most significant of which is that the fluid temperature extracted from the underground should remain constant, but may vary with time due to the excessive consumption of geothermal energy for either heating or cooling, which affects its performance. Additionally, the temperature fluctuation may reduce the soils' compressibility and strength, which impairs the stability of the buildings' or infrastructures' foundation (Abdelaziz Sherif L. et al. 2015). This limitation is primarily a problem in areas with

extreme climates. Methods such as thermal energy storage or energy injection into the ground can be effectively utilized to alleviate this unbalanced energy extraction from the underground. Therefore, a combination of effective shallow geothermal energy systems and selective thermal energy storage can create an optimized system performance.

2.2.2 Geothermal Energy Piles

Energy piles' deep foundation elements are constructed by precast, pre-stressed concrete piles, or cast-in-place concrete piles and are integrated with circulation loops for use as heat exchangers to access geothermal energy from the soil surrounding foundations. Much research has been conducted globally in recent years on using energy piles for buildings' heating and cooling systems (Amayta et al. 2012; Bourne-Webb et al. 2009; Knellwolf et al. 2011; Laloui et al. 2006). Due to the deep foundations required for bridge support, the extraction of shallow geothermal energy using energy piles plays a dominant role in bridge deck heating/deicing operations, as the already-constructed deep foundations, combined with energy piles, can provide structural support for bridges and heat exchanger function with the ground. The heat carrier fluid extracted from the underground is supplied to the bridge deck for deicing in the winter. In the summer, the system can be utilized as a solar energy collector that stores the energy in the ground. Fig. 2-3 illustrates a schematic of ground-source bridge deck deicing with energy piles.

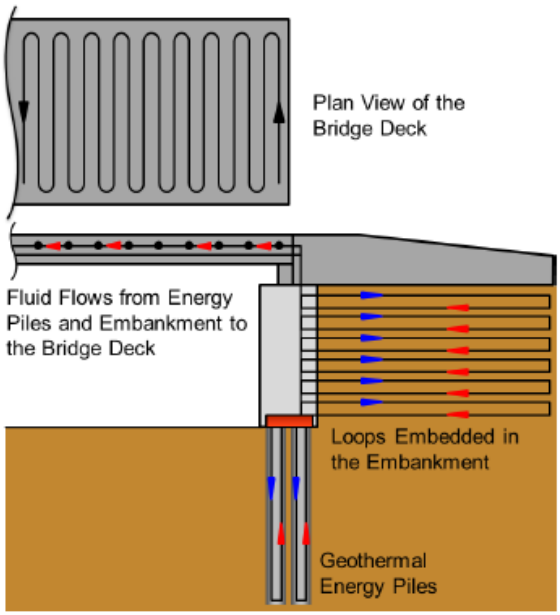

Figure 2-3. Schematic of ground-source bridge deck deicing, utilizing energy piles (Bowers 2016)

2.2.3 Conceptual Design of Hydronic Geothermal Heating System

The conceptual design of a geothermal bridge deicing system consists of the four components shown in Fig. 2-4. The first one is the ground loop heat exchanger (GLHE), which can extract heat from the underground fluid. The fluid flows out of the ground loops and enters the circulation pump and heat pump. In an extreme winter event, the heat pump is used to heat the water and provide extra energy for snow melting. Then, the warm fluid is pumped to the bridge deck loops to supply enough heat flux at the bridge deck's surface for snow removal. The control system is used to control the operation.

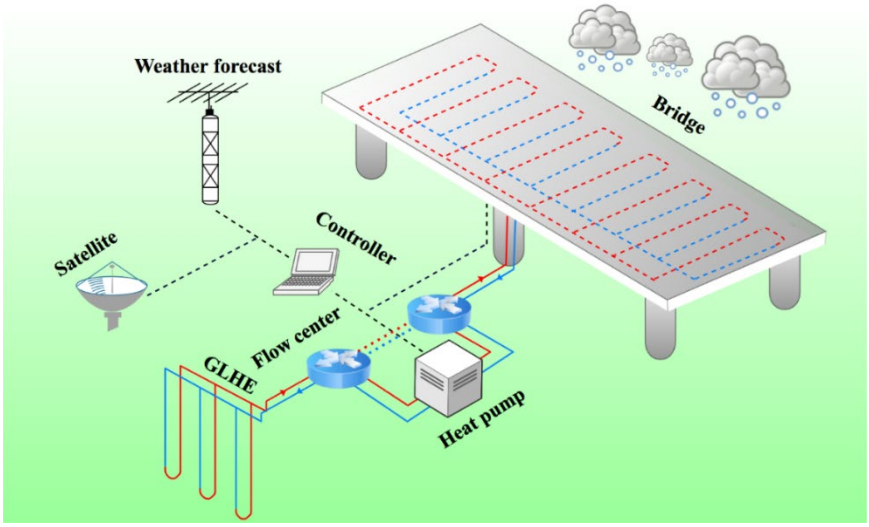

Figure 2-4. Conceptual design of a geothermal bridge deicing system

The design process of the geothermal bridge deicing system consists of four phases (Chiasson and Spitler 2001b): (1) determination of how much heat flux needs to be transferred to the bridge surface for deicing; (2) evaluation of the bridge heating loads; (3) estimation of how much energy can be recharged in the ground in summer.; and (4) the design the GLHE system, including all configurations for the number, spacing, depth, and diameter of the boreholes. The design process is summarized by the flow chart shown in Fig. 2-5, and detailed descriptions for each phase are provided in the following subsections.

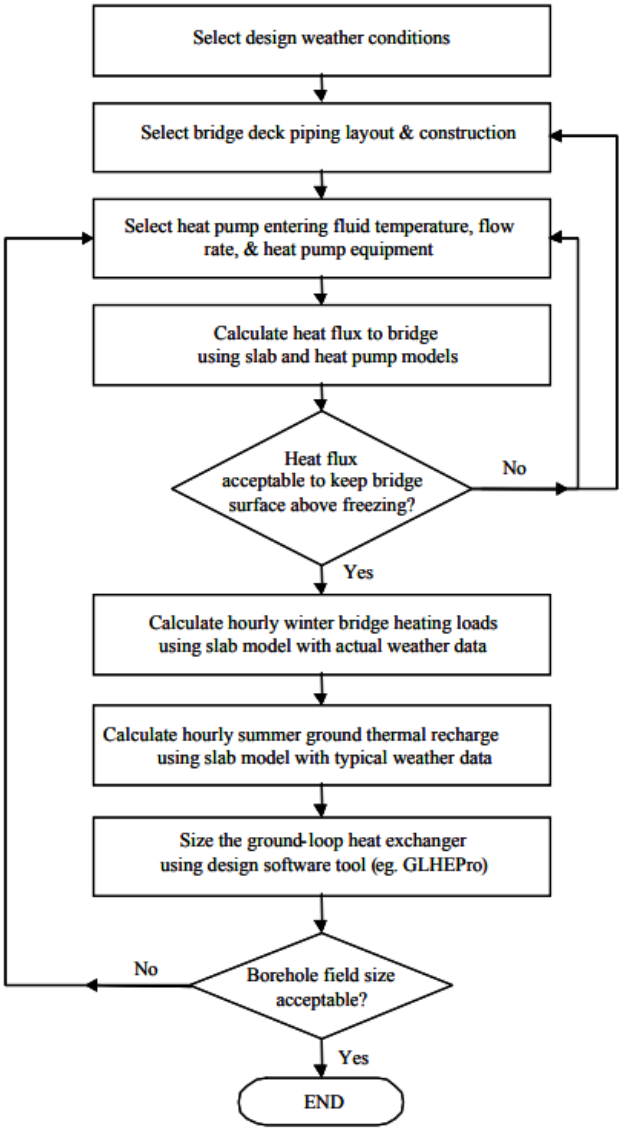

Figure 2-5. Flow chart of the design process for a ground-source heat pump bridge deck heating system (Chiasson and Spitler 2001b)

(1) Heat flux to the bridge

A heat flux is the standard method that is used to meet a heating system's requirements for melting ice and snow. Its design aims to ensure that the average temperature of the bridge deck surface can be heated above the freezing temperature to avoid ice accumulation. Various factors play important roles in the heating behavior of a hydronically geothermal heated bridge deck

system: (1) The heat transfer processes involved in a hydronically heated bridge deck and its surrounding environment; (2) the bridge deck configurations, consisting of material properties of the bridge deck, deck thickness, and orientation; (3) the material properties of the hydronic pipe, including the pipe shape, pipe diameter, pipe spacing, the thermal conductivity of the pipes, and the depth into which the pipes are embedded in the bridge deck; (4) the properties of the circulating fluid, such as the related thermal properties, flow rate, and inlet temperature; (5) the thermal properties of the underground soils incorporated in thermal conductivity, diffusivity, and heat capacity; and (6) the heat pump system design, including the number and arrangement of the heat pumps. Additionally, the weather conditions, including ambient temperature, wind speed and direction, snowfall, humidity, and solar radiation, also have a remarkable effect on the efficiency of the heating performance and the heat transfer behaviors within the bridge deck. To provide a comprehensive and accurate estimate of the heating requirement for snow melting, a system modeling approach can couple the bridge deck model and the heat pump model by inputting all of the parameters mentioned previously.

(2) Bridge Heating Loads

The prior determination of the required heat flux is the maximum system performance output due to the inputs of the extreme weather conditions; however, it cannot reasonably estimate the system's actual energy use for bridge deck deicing. Fig. 2-5 indicates that the GLHE system's design depends on the transient thermal loads on the heat pumps. Therefore, a more reliable and cost effective GLHE system can benefit from a reasonable evaluation of the heat pumps' hourly heating loads.

(3) Ground Thermal Recharge

Thermal recharge of the ground in summer can be described as the reverse of the heating operation process for buildings or infrastructures in the winter. It is capable of providing a cost reduction of the construction of the GLHE system due to fewer requirements for the number or size of boreholes. In summer, the bridge deck's temperature is supposed to be greater than the ambient temperature since the bridge deck is operated as a solar energy collector that injects energy into the ground. The amount of energy supplied by the bridge deck can be determined, based on an analysis of the energy balance of the circulating heat carrier fluid, by calculating the temperature deviator between the top surface of the bridge deck and the surrounding air. This can be utilized to estimate the hourly thermal recharge rate of the ground by employing numerical modeling of the bridge model.

(4) Design of GLHE systems

The GLHE system was established by using the design software GLHEPro 4.1, developed by Spitler (2000). The numerical analysis was performed by inputting the related parameters into the software and using the minimum designed inlet fluid temperature to the heat pump, with and without thermal energy storage in the summer, to determine the required number of boreholes. The parameters included the heating loads, thermal recharge loads, borehole configurations, thermal properties of the ground soils, thermal properties of the heat carrier fluid, and the description of the selected heat pumps. An optimum practical solution of the GLHE system design can be found through the numerical outputs. Modeling and experimental investigations of hydronic snow melting systems have been rapidly developed to maintain pavement slabs and bridge decks in the winter to increase traffic and public safety, as described in Sections 2.3 and 2.4.

2.3 Modeling Analysis of Hydronic Snow Melting Systems

Hydronic heating is one of the most popular snow-melting techniques used for internally heated bridge decks /pavements (U.S. Department of Transportation). Heat carrier fluid extracted from the ground supplies the required heat energy for snow melting to the bridge deck's surface/pavement by the circulation of fluid within the heating elements that are embedded in the bridge decks/pavements. The modeling analyses account for the heat transfer behaviors within the bridge deck/pavement and between the slab and the surrounding environment. Due to the snow-melting processes that are only on the bridge deck/pavement surface, the heat and mass transfer occurring on the surface of bridge decks/pavement plays a dominant role. The development of the hydronic snow-melting models can be grouped into steady-state and transient approaches.

2.3.1 Steady-State Model

Steady-state models were developed based on the assumption that the heating system is in steady state. Hence, the discontinuous operation and various environmental circumstances are not considered in this analysis. The most-accepted steady state snow melting models depicted in this section are divided into two groups: 1-D and 2-D models. The 1-D steady-state methods mainly focus on analyzing the required heat flux at the surface, including convection, radiation, evaporation, the sensible fluxes, and the latent fluxes related to snow-melting processes. For 2-D models, computational support is necessary for the modeling analysis.

2.3.1.1 Chapman (1952, 1956): One-Dimensional Steady-State Model

Chapman (1952) developed a one-dimensional steady-state method for a snow melting system. He stated the heating requirements for snow-melting at the bridge deck/pavement surface can be estimated by the mass and heat transfer mechanisms that occur at the surface, including the heat of fusion, sensible heat utilized for the snow melting, heat attributable to evaporation, heat

transfer associated with convection and radiation, and heat loss from the back. He indicated that the condition of the snow accumulation can have a significant insulating effect on the bridge deck/pavement surface, which decreases the heat loss associated with radiation, convection, and evaporation heat transfer occurring at the surface. To further depict how the accumulated snow insulates the surface from heat loss, a concept of an equivalent snow-covered area and a ratio of equivalent snow-free area to the total surface area (equivalent snow-free area ratio) were defined by Chapman (1956). This concept provides a more accurate understanding of the heat flux analysis of a snow-melting bridge deck/pavement surface and was recommended by American Society of Heating Refrigerating and Air-Conditioning Engineers (ASHRAE) as a steady-state method to perform the heat flux design for snow melting at the surface (ASHRAE Handbook 2013). The heating requirements can be expressed in terms of energy balance.

$$q_o = q_s + q_m + A_r(q_h + q_e) \tag{2-1}$$

Where,

q_o is heat flux required at the snow-melting surface, Btu/hr.ft^2 or W/m^2.

q_s is the sensible heat flux to raise the snow temperature to the melting point, Btu/hr.ft^2 or W/m^2.

q_m is the latent heat flux associated with melting snow, Btu/hr.ft^2 or W/m^2.

A_r is the equivalent snow-free area ratio, dimensionless.

q_h is the convective and radiative heat flux from the snow-free surface Btu/hr.ft^2 or W/m^2.

q_e is the heat flux attributable to evaporation from the snow-free area, Btu/hr.ft^2 or W/m^2.

Sensible heat flux q_s to raise the snow temperature to the melting point can be presented in the following equation.

$$q_s = \rho_w \cdot s \cdot c_p \cdot (T_f - T_a) \tag{2-2}$$

Where,

ρ_w is the density of water equivalent of snow, taken as 62.4 lb./ft^3 or 1000 kg/m^3.

s is the snowfall rate (inch of water equivalent per hour), in/hr. (m/s).

c_p is the specific heat of snow, taken as 0.5 Btu/(lb.^{o}F) or 2100 J/(kg·°C).

T_f is the water film temperature, ^{o}F or °C.

T_a is the ambient temperature, ^{o}F or °C.

The latent heat flux associated with melting snow Snow-melting heat flux q_m is calculated by Eq. (2-3).

$$q_m = s \cdot h_{if} \cdot \rho_w \tag{2-3}$$

Where:

h_{if} is the enthalpy of fusion for water, usually taken as 143.5 Btu/lbs. or 3.3×10^5 J/kg.

The heat flux attributable to radiation and convection q_h from the snow-free surface is formulated by Eq. (2-4).

$$q_h = C_1 \cdot (aV + b) \cdot (T_f - T_a) \tag{2-4}$$

Where:

a is a constant, taken as 0.0201 hr^2/(mile/ft) or 530.84 s^2/m^2.

b is a constant, taken as 0.055 hr./ft or 649.61 s/m.

C_1 is a constant, taken as 11.4 Btu/(hr^2·ft·°F) or 0.005476 W/(m·s·K).

V is wind speed, mph or m/s.

The heat flux attributable to evaporation from the snow-free area q_e is given by Eq. (2-5).

$$q_{e.} = h_{fg} \cdot (aV + b) \cdot (P_{wv} - P_{av}) \tag{2-5}$$

Where:

h_{fg} is the heat of evaporation at the film temperature, usually taken as 1075 Btu/lb. or 2.5×10^6 J/kg.

p_{wv} is the partial presser of water vapor in saturated air film on the surface vapor pressure of moist air, in. Hg or Pa.

p_{av} is the partial presser of water vapor in the surrounding air, in. Hg or Pa.

The water film temperature related to Eqs. (2-2) and (2-4) is assumed to be uniformly distributed on the entire surface. (It should be noted that the heating system's uneven layout is not considered in this analysis.) The equivalent snow-free area ratio in Eq. (2-1) can be viewed as an insulation factor that can deal with the insulating effect of the accumulated snow on the surface and the snow-melting performance of the heating system. Based on the research findings from Chapman (1956), the equivalent snow-free area ratio can be classified into three classes, as listed below.

Class 1 (residential): The energy supply cannot melt the falling snow that accumulates on the entire bridge deck surface and insulates the deck surface ($A_r = 0$), in which case a Neumann boundary condition is presented and indicates that the heat flux at the respective boundary is 0.

Class 2 (commercial): Although the supplied energy can melt the falling snow, 50% of the bridge deck/pavement surface is covered by snow ($A_r = 0.5$), in which case the radiative and convective heat fluxes are eliminated due to insulation effect of snow.

Class 3 (industrial): The energy supplied by the circulation tubes is adequate for melting the falling snow, and no snow accumulates on the surface of the bridge deck ($A_r = 1$). Radiative and convective heat fluxes are presented in this case.

Chapman (1956) indicated that weather condition analysis plays an important role in estimating the required heat flux for snow melting. All four environmental factors, including wind

speed, air temperature, relative humidity, and snowfall rate, were taken into account in the analysis of the heat output. However, some critical weather conditions, such as sky temperature and sky cover, were not considered; nor was the uneven temperature distribution at the bridge deck/pavement surface that is caused by the circulation tubes' configuration and layout.

2.3.1.2 Schnurr and Rogers (1970): Two-Dimensional Steady-State Model

Schnurr and Rogers proposed a two-dimensional steady-state model using a finite difference method that can account for the uneven temperature distribution caused by the discrete layout of heating elements within the bridge deck/pavement. In their study, the energy balance analysis was based on the model developed by Chapman (1956) and was presented by using simplified correlations to estimate the heat flux associated with different components, as expressed in the following equation.

$$q_o = q_s + q_m + q_e + h_c(C_2 - T_a) \tag{2-6}$$

Where,

h_c is the combined coefficient attributable to convective and radiative heat transfer, Btu/(ft^2·°F) or W/(m^2·K).

C_2 is a constant, taken as 32 °F or 0 °F.

Square grids spaced one-half of the pipe radius apart were utilized to generate the model domain in this FD analysis, as shown in Fig. 2-6, which indicates that only the areas that have a distance to the pipe with a multiple of the pipe radius can be analyzed. This model was only concerned with the snow-free surface condition; therefore, only the heated bridge decks/pavements with Class 3 of the equivalent snow-free area ratio can be investigated by this method. The model dealt with the impact of the heating system layout on heat transfer behaviors within bridge decks/pavements, and the maximum and minimum temperatures, respectively located over the

heat source position and between the pipes, can be verified by this model. The model still has limitations, however, due to assumptions of steady-state and snow-free surface conditions.

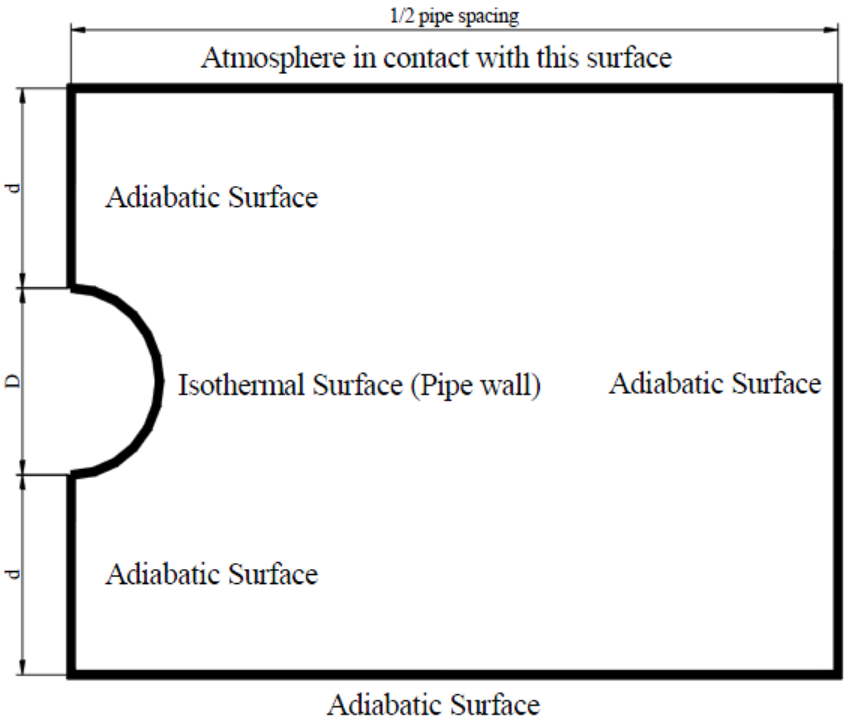

Figure 2-6. FD model geometry and boundary condition setup (Liu 2005)

2.3.1.3 Kilkis (1994a, 1994b): One-Dimensional Steady-State Model

A general energy balance equation was developed, based on Chapman's 1956 contributions, to estimate the heating requirements at the bridge deck/pavement surface. Kilkis (1994a) improved this equation by using updated correlations for the convection, radiation, and evaporation heat losses. An empirical correlation, established by using a snow-melting surface area of 16 ft^2, was proposed by Williams (1976) to deal with the convective contribution of the heat loss, which was formulated in Eq. (2-7). It was noted that the recorded wind speeds need to be adjusted to the surrounding terrain and the height of the snow-melting surface from ground level since the altitude of the location for measurement is different from that of the actual application.

$$q_{conv} = (C_3 \cdot U + C_4) \cdot (T_f - T_a) \quad (2\text{-}7)$$

Where:

C_3 is a constant, taken as 0.14 Btu/(mi·ft^2·°F) or 1.78 W/(m^3·°C).

C_4 is a constant, taken as 0.39 Btu/(ft^2·°F) or 2.22 W/(m^2·°C).

U is the corrected wind velocity, mph or m/s.

q_{conv} is the heat loss attributable to convective heat transfer, Btu/hr.ft^2 or W/m^2.

In the case of the radiative investigation, the effects of net longwave radiation under various sky conditions, including cloudy and clear skies, respectively stated by Williams (1976) and Williamson (1967), was depicted in terms of the two following updated correlations, as respectively given in Eqs. (2-8) and (2-9) below.

$$q_{rad} = C_5 + C_6 \cdot \left[\left(T_f + T_a\right)\right]^3 \cdot \left(T_f - T_a\right) - C_7 T_a^4 \quad (2\text{-}8)$$

$$q_{rad} = C_8 + C_9 \cdot (T_f - T_a) \quad (2\text{-}9)$$

Where,

C_5 is constant, taken as 10.3 Btu/(hr·ft^2) or 32.49 W/m^2.

C_6 is constant, taken as 8.14×10^{-10} Btu/(hr·ft^2·°F^4) or 2.695×10^{-8} W/(m^2·K^4).

C_7 is constant, taken as 7.316 Btu/(hr·ft^2·°F^4) or 2.423×10^{-9} W/(m^2·K^4).

C_8 is constant, taken as 30.15 Btu/(hr·ft^2) or 95.11 W/m^2.

C_9 is constant, taken as 0.74 Btu/(hr·ft^2·°F) or 4.2 W/(m^2·K).

q_{rad} is the heat loss due to radiative heat transfer, Btu/hr·ft^2 or W/m^2.

The heat loss associated with evaporation can be estimated by using the analysis of convective heat loss and Bowen's ratio.

$$q_e = \frac{q_c}{R} \cdot \frac{P_{wv} - P_{av}}{T_f - T_a} \quad (2\text{-}10)$$

$$R = \frac{P_a}{C_{10}} \tag{2-11}$$

Where,

P_a is atmospheric pressure, in. Hg or Pa.

R is the Bowen's ratio, in. Hg/°F or Pa/°C.

C_{10} is constant, taken as 2990 °F or 1643 °C.

Similar to previous studies, the configurations of the bridge deck/pavement slab and the layout of the heating elements were a concern in this model (Kilkis 1994b). With the help of the geometric information and a composite fin model proposed by Kilkis (1992), the maximum/minimum surface temperature of the slab can be predicted and utilized to evaluate the snow-melting performance of a heating system under given weather scenarios. A FEM validation for this model presented that a model error of 10% can be expected when using numerical analysis under a steady-state approach. However, this model has never been verified by experimental data, and it can only be performed under a steady-state condition.

2.3.1.4 Ramsey et al. (1999): One-Dimensional Steady-State Model

The one-dimensional steady-state model developed by Ramsey et al. (1999) was viewed as the current design methodology of a hydronic snow-melting system presented in the ASHRAE Handbook (2013), which essentially dealt with an energy balance at the bridge deck/pavement surface based on the previous remarkable efforts (Chapman 1952, 1956; Kilkis 1994a, 1994b). This goal was for the model to propose a design tool that could provide calculation results with enough accuracy for practical engineering. It is assumed that only the snow-free area of the slab surface can experience heat losses due to convection, radiation, and evaporation. The places where snow cover exists require a Neumann boundary condition, which indicates that the heat flux at the respective boundary is 0.

The significant difference between Kilkis's (1994a) work and Ramsey et al. (1999)'s model is how to estimate the heat losses. It is suggested that the value of the desired snow-free area ratio plays a dominant role in the model calculation. When a specific snow-free area ratio was selected, the heat loss analysis was performed with the specified value. For example, if the selected A_r is equal to 0.7, only 70% of the slab surface needs to be considered to calculate the heat losses, and the heating system is operated according to this condition.

The heat losses attributable to convective and radiative heat transfers can be calculated with the help of Eq. (2-12). The convective contribution is estimated in terms of the turbulent flow through the exposed area of a slab surface under a specific wind speed, as presented in Eq. (2-13), which can provide a reasonable calculation accuracy for an exposed surface. In the radiative case, the heat loss is affected by the mean radiant temperature related to the sky temperatures under clear and cloud-covered sky conditions.

$$q_h = h_c \cdot \left(T_f - T_a\right) + \sigma\varepsilon \cdot (T_f^4 - T_{MR}^4) \tag{2-12}$$

$$h_c = 0.037 \cdot (\frac{k_{air}}{L}) \cdot Re_L^{0.8} \cdot Pr^{1/3} \tag{2-13}$$

$$T_{MR} = [T_{cloud}^4 \cdot F_{sc} + T_{clear}^4 \cdot (1 - F_{sc})^{1/4}$$

Where,

h_c is the convective heat transfer coefficient, Btu/(ft^2·°F) or W/(m^2·K).

σ is the Stephan-Boltzmann constant, taken as 5.6705×10-8 W/(m^2·K^4) or 1.7123×10^9 Btu/(ft^2·°F^4).

ε is the emissivity of the surface, dimensionless.

T_{MR} is the mean radiant temperature, °F or °C.

k_{air} is the air's thermal conductivity at, Btu/(hr·ft·°F) or W/(m·K).

L is the characteristic length of the surface, ft or m.

Re_L is the Reynolds number, dimensionless.

P_r is the Prandtl number of air, taken as 0.7, dimensionless.

T_{cloud} is the sky temperature under cloud-covered condition, °F or °C.

T_{clear} is the sky temperature under clear sky conditions, °F or °C.

F_{sc} is the fraction of radiation exchange between surface and clouds, dimensionless.

The correlation utilized to describe the evaporative heat loss is given below.

$$q_e = \rho_a \cdot h_m \cdot (W_f - W_a) \cdot h_{fg} \quad (2\text{-}14)$$

Where,

ρ_a is the density of dry air, lb_a/ft^3 or kg_a/m^3.

h_m is the mass transfer coefficient, ft/s or m/s.

W_f is the humidity ratio of saturated air at the film surface temperature, lb_w/lb_a or kg_w/kg_a.

W_a = Humidity ratio of ambient air, lb_w/lb_a or kg_w/kg_a.

h_{fg} = Heat of vaporization, Btu/lb_w or J/kg_w.

In this model, the insignificant heat losses at the back and sides were not considered, and the model was not validated by experimental data.

2.3.2 Transient Model

The hydronic heating design of transient models has been developed more recently based on the advances made in computer technology and science. Due to the variations of weather events, the heating system is operated in intermittent scenarios. The time-dependent heating responses that occur within a bridge deck/pavement can be described by a transient model through the new

solution solver with boundary-fitted grids. Transient models can provide a more comprehensive and accurate understanding of various surface conditions on a heated bridge deck/pavement surface under a snowy event than can be provided by the steady state models.

2.3.2.1 Chiasson et al. (2000): Two-Dimensional Finite Difference Model

Leal and Miller developed a two-dimensional finite difference model in 1972 that was based upon work performed by Schnurr and Rogers (1970). The model depicted the heat transfer attributable to conduction within bridge deck/pavement under transient conditions, but it was limited to analysis for phase change processes. Schnurr and Falk (1973) improved this work by using a more advanced finite-difference model to perform the time-dependent conduction heat transfer in bridge deck/pavement. Despite this, however, it is still challenging to describe and accurately predict the snow-melting process that occurs on a slab surface via a transient analysis.

Based on the contributions from Schnurr and Rogers (1970), Leal and Miller (1972) and Schnurr and Falk (1973), an updated transient model with new algorithms for the heat flux analysis on the domain boundary was developed by Chiasson et al. (2000), which pertained to the thermal effect of solar radiation on the energy balance of the bridge deck/pavement surface. In this study, the evaluations of the heat fluxes, due to convection and radiation, were performed differently from the previous combining method. The selected convective coefficient was the greater value between the forced and nature convective coefficient. The radiation analysis focused on the estimate of the sky temperature that was dependent on the dry-bulb and dew point temperatures of the environment; however, the correlation between the radiation heat transfer and the cloud cover was included in this study. Another novelty is that a pipe wall analysis was not considered in terms of a uniform temperature distribution rather than an application of the Neumann boundary

condition that dealt with the heat flux transit from the circulating fluid that was attributable to convection.

The track of the snow's mass accumulated on the surface is available in the transient model since the heat flux associated with snow melting is dependent on the mass and heat balance on each surface node. The actual time-stepping mass flow rate was viewed as the smaller value of the potential snow-melting rate and the accumulated snow mass. The related equations are given below.

$$in''_{melt-actual} = \min\left(in''_{melt-potential}, \frac{m''_{accumulated-current}}{\Delta t}\right) \quad (2\text{-}15)$$

$$in''_{melt-potential} = \max\left(in''_{melt-HB}, 0\right) \quad (2\text{-}16)$$

$$in''_{melt-HB} = \frac{q_{solar} + q_{rad} + q_{conv} + q_s + q_e + q_{cond,surf}}{h_{if}} \quad (2\text{-}17)$$

Where,

$in_{melt\text{-}actual}$'' is the actual mass flow rate for each time step, lb./ft^2 or kg/m^2.

$in_{melt\text{-}potential}$'' is the potential snow-melting rate mass, lb./ft^2 or kg/m^2.

$in_{melt\text{-}HB}$'' is the accumulated mass of snow from the heat balance on the surface on this time, lb./ft^2 or kg/m^2.

$q_{cond,\ surf}$ is the conductive heat flux transferred to the surface, Btu/hr.ft^2 or W/m^2.

h_{if} is the latent heat of fusion of ice, Btu/lb. or J/kg.

With the combined information from each final node temperature in the model domain calculated in the last time step and the given environmental circumstances on the current time step, it is possible to estimate the transient heat transfer behaviors that occur on a snow-melting slab

surface. However, unreasonable computational results will be exported from this method if it is applied to a slab surface with a warm temperature. Specifically, the melted snow can rapidly lower the warm surface temperature close to freezing, and the heat losses that should have occurred are remarkably reduced. The conductive heat flux has a corresponding increase due to the great temperature gradient distributed on the slab surface that will result in an inaccurate estimate of the heat fluxes on the surface. This model does not consider the insulating effect of the snow layer and, similar to most of the previously mentioned models, it was not validated with snow-melting tests.

2.3.2.2 Rees et al. (2002): Two-Dimensional Finite Volume Model

Melting snow on the surface of a hydronically heated bridge deck/pavement is a complicated process that involves a series of heat transfer mechanisms, including solar radiation, the phase change of water (snow melting and water evaporation), heat transfer components due to radiation and convection on the heated surface, and the conductive heat flux transferred from the heat source to the slab surface. When accumulated snow on the surface was melted, the melted water evaporates, is drained, or permeates the slab due to the capillary action. The rate of snowfall determines the amount of heat flux required for snow melting. The melted snow (water) from the pavement depends on the wind speed and the difference in the vapor pressure between the air and the melted snow. Convection and radiation loss from the melted snow are based on the film coefficient and the temperature difference between the surface and air. Due to the uneven layout of heating elements, the various environmental circumstances, and different drainage conditions on the slab surface, the distribution of surface conditions is presented in terms of spatial and temporal variations during a snow-melting phase (Fig. 2-7.).

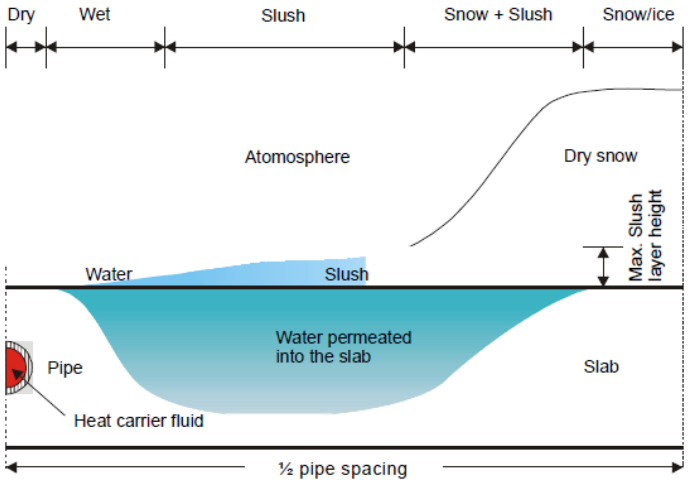

Figure 2-7. Variation of surface conditions during a snow-melting process under a cross-sectional view of the slab (Liu and Spitler 2004)

Base on the finite difference model domains presented in Fig. 2-6**,** Rees et al. (2002) proposed a 2-D finite volume model by using an updated grid generation with blocks of cells that could handle the complex model geometries, including the modeling of a round pipe in a square solid domain. (See Fig. 2-8.) This model was viewed as a transient tool that was capable of analyzing the effects of deicing processes on the system's performance. The development of a computer tool made it possible to explain how snow/ice accumulates and melts, using a boundary conditions model. The control system modeled in this program can be turned on automatically as soon as snow falls. The most significant innovation of this transient analysis is that it can provide an accurate prediction of the various surface conditions existing on the heated slab surface during a snow event. In general, the surface boundary conditions performed by a surface boundary model in this analysis can be classified into seven possible types: dry, wet, dry snow, slush, snow and slush, solid ice, and solid ice and water, which are depicted below.

- **Dry:** No liquid or ice are retained on the surface, which may have a temperature above or below freezing.

- **Wet:** Some liquid exists on the surface. The surface temperature is above freezing, and no ice is retained on it.
- **Dry Snow:** Freshly fallen snow exists on the surface but does not change to a liquid state. Instead, it remains on the surface in the form of a porous icy matrix. The snow does not melt because the surface temperature is below freezing.
- **Slush:** Ice with snow crystals that are fully saturated with water is retained on the surface. Water penetrates through the bottom surface of the porous icy matrix to its upper surface, and the surface is a freezing temperature.
- **Snow and slush:** Partial snow melting occurs on the surface. As shown in Fig. 2-7, the lower part is viewed as snow with full-water saturation, and the upper part is dry snow. The surface temperature is at freezing.
- **Solid ice:** Water is frozen on the surface in a solid- state form, and the temperature of the surface is below the freezing point.
- **Solid ice and water:** Solid ice and water can form on the surface when there is an occurrent ice melting or when rain has fallen over ice.

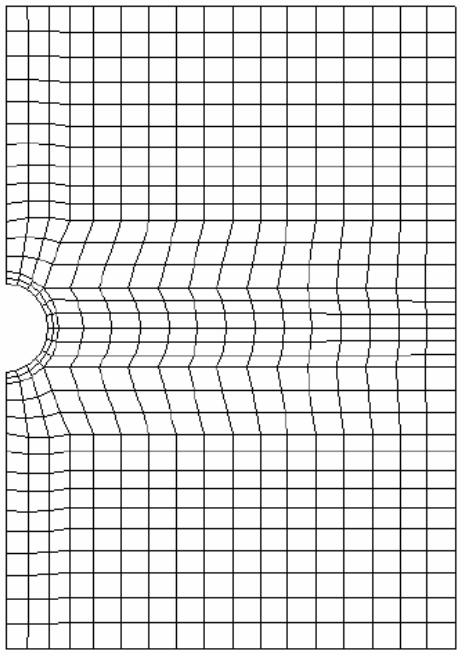

Figure 2-8. Grid generation for a hydronic heated slab (Rees et al. 2002)

This study used a three-node model to emphasize the heat transfer mechanisms for snow and slush conditions. The surface condition, which is the most difficult to model, is schematically presented in Fig. 2-9. Three nodes were located at the top surface of the snow layer: at the center, within the snow layer, and within the saturated (slush) layer. It was assumed that the snow processes were viewed as a one-dimensional analysis; therefore, the heat transfer contributions from the lateral direction within the slush layer were not a concern. The snow only melted at the lower node, which was located in the saturated (slush) layer. The heat transfer attributable to conduction was supplied from the hydronic heating elements and went through both layers of slush and snow. Due to the snow layer's insulating effect, only the upper node experienced the impacts of convection and radiation. The slush layer's considerations of convection and evaporation were not included since the slush layer was covered with a dry snow layer. Solar radiation analysis was neglected, and the model assumed that the temperature in the saturated (slush) layer was uniformly distributed.

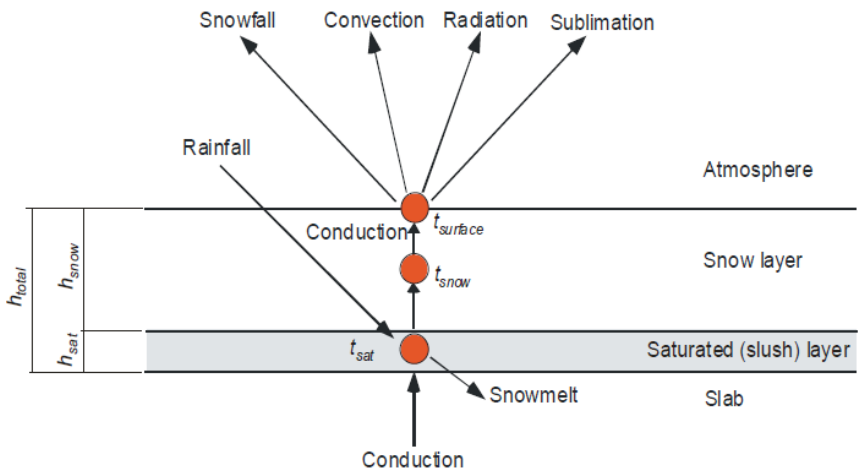

Figure 2-9. Schematic representation of heat transfer mechanisms in the three-node model (Rees et al. 2002)

This model provided five primary equations for the mass and energy balance under the snow and slush surface condition depicted above. The equations consist of two mass balances for the solid ice and liquid water, and three energy balances for the snow layer surface, within the center of the snow layer, and in the saturated (slush) layer corresponding to the three nodes from upper to lower, respectively. The correlations and algorithms utilized in this study to estimate the heat fluxes attributable to convection, radiation, and evaporation are identical to those used by Ramsey et al. (1999). The balance equations are shown below.

a. Mass balance on the solid ice:

The difference of the mass in falling and melted snow accounts for the rate change of the mass of ice crystals, which can be expressed in terms of the following equation:

$$\frac{dm_{ice}}{d\theta} = in''_{snowfall} - in''_{melt} \tag{2-18}$$

Where,

m_{ice} is the mass of ice crystals per unit area in the snow layer, lb./ft^2 or kg/m^2.

θ is the time, hr. or s.

$in_{snowfall}''$ is the rate of snowfall mass per unit area, lb./(ft^2·hr) or kg/(m^2·s).

in_{melt}'' is the snow melting rate per unit area, lb./(ft^2·hr) or kg/(m^2·s).

b. Mass balance on the liquid water:

The mass of melted snow, rainfall, and water runoff on the surface determines the mass of liquid water, as shown below:

$$\frac{dm_l}{d\theta} = in''_{melt} + in''_{rainfall} - in''_{runoff} \quad (2\text{-}19)$$

Where,

m_l is the mass of liquid water per unit area in the saturated (slush) layer, lb./ft^2 or kg/m^2.

$in_{rainfall}''$ is the rate of rainfall mass per unit area, lb./(ft^2·hr) or kg/(m^2·s).

in_{runoff}'' is the water runoff rate per unit area, lb./(ft^2·hr) or kg/(m^2·s).

In this equation, the runoff rate depends on the amount of extra water on the saturated (slush) layer that occurs during the snow melting. A simple heuristic method, utilized to evaluate the amount of runoff, stated that the runoff is less than 10% of the rate of the snow melting, due to the capillarity action, until the thickness of the saturated (slush) layer is 2 inches (5.04 cm). After that, an increase in runoff rate occurs to accelerate the water drainage from the surface of the slush layer. When a balance is attained between the capillary and gravitational forces, this phenomenon is complete, as validated by experiments conducted by Hockersmith (2002).

c. Energy balance on the snow layer surface:

The energy balance analysis didn't take into account the heat flux associated with evaporation and sublimation. With the help of a node heat balance on the snow layer surface, the temperature at the snow layer's top surface can be determined by Eq. (2-20):

$$q_{conv} + q_{rad} = k_{snow} \cdot \frac{T_{center,snow} - T_{surf,snow}}{0.5 \cdot h_{snow}} \quad (2\text{-}20)$$

Where,

q_{conv} is the convective heat flux at the snow layer surface Btu/hr.ft^2 (W/m^2).

q_{rad} is the convective heat flux at the snow layer surface Btu/hr.ft^2 (W/m^2).

k_{snow} is the thermal conductivity of the snow, Btu/(hr·ft·°F), or W/(m·K).

h_{snow} is the thickness of the snow layer, ft or m.

$T_{center,\ snow}$ is the temperature at the center of the snow layer, °F or °C.

$T_{surf,\ snow}$ is the temperature at the top surface of the snow layer, °F or °C.

The thickness of the snow layer h_{snow} in this equation is the difference between the total height h_{total} and the thickness of the saturated (slush) layer h_{sat}, as respectively shown in Fig. 2-7. Both of the layers can be calculated by the following two equations, respectively:

$$h_{total} = \frac{m_{ice}}{\rho_{ice} \cdot (1 - n_{eff})} \tag{2-21}$$

$$h_{sat} = \frac{m_l}{\rho_l \cdot n_{eff}} \tag{2-22}$$

Where,

h_{total} is the sum of the thickness of the snow and saturated (slush) layers, ft or m.

ρ_{ice} is the density of ice, lb./ft^3 or kg/m^3.

n_{eff}: effective porosity of the matrix of liquid/ice for snow and saturated (slush) layers, dimensionless.

h_{sat} is the thickness of the saturated (slush) layers, ft or m.

ρ_l is the density of water in a liquid state, lb./ft^3 or kg/m^3.

d. Energy balance at the center of the snow layer:

The energy balance equation aims to calculate the temperature at the center of the snow layer:

$$m_{snow} \cdot C_P \cdot \frac{dT_{center,snow}}{d\theta} = k_{snow} \cdot \frac{T_{slush} - T_{center,snow}}{0.5 \cdot h_{snow}} - q_{snowfall} k_{snow} \cdot \frac{T_{center,snow} - T_{surf,snow}}{0.5 \cdot h_{snow}} \quad (2\text{-}23)$$

Where,

m_{snow} is the mass of dry snow per unit area in the saturated (slush) layer, lb./ft^2 or kg/m^2.

T_{slush} is the temperature within the saturated (slush) layer, lb./ft^2 or kg/m^2.

$q_{snowfall}$ is the heat flux utilized to raise the snow temperature from the ambient temperature to the temperature at the center of the snow layer, Btu/hr.ft^2 (W/m^2).

e. Energy balance within the saturated (slush) layer:

It is assumed that the mixture of liquids and ice reaches a thermodynamic steady state, which indicates that the temperature is uniformly distributed at the melting temperature. The energy balance equation that is utilized to determine the temperature within the saturated (slush) layer is given by

$$in''_{melt} \cdot h_{if} = q_{cond,slab} + q_{rainfall} - k_{snow} \cdot \frac{T_{slush} - T_{center,snow}}{0.5 \cdot h_{snow}} \quad (2\text{-}24)$$

Where,

$q_{cond,\ slab}$ is the conductive heat flux transferred from the deck to the slush layer, Btu/hr.ft^2 or W/m^2.

$q_{rainfall}$ is the heat flux utilized to raise the rainfall temperature from the ambient temperature to the temperature within the saturated (slush) layer, Btu/hr·ft^2 or W/m^2.

This model is dependent upon a powerful computational tool because of the large number of equations and the iteration process required, coupled with the boundary condition model and the finite volume solver for converged analysis of heat fluxes and slab temperatures. Due to the

complex computations, it is difficult for this model to perform for long-term operations, and it can only be employed for heat transfer estimates for single snow scenarios. There are several concerns about the accuracy of the computations. First, due to the insulating effect of the snow with a low thermal conductivity of 0.03 W/m·K or 0.02 Btu/hr·ft·°F (Liu 2005), the small heat losses associated with convection, radiation, and evaporation on the surface may cause inaccurate evaluations of the energy balance on the upper surface and at the center of the snow layer. Second, the heuristic method's limitations to determine the runoff rate and the use of the effective porosity of the liquid/ice matrix in snow and slush layers in this study increase the potential for errors in estimating the heat flux in the slush layer. Third, water permeated into the slab was not incorporated into this model, which can negatively affect the mass balance of water in a liquid state on the slab surface**.** To conclude, this model was only partially verified with the laboratory data provided by Hockersmith (2002), and no further model verification was published.

2.3.2.3 Liu et al. (2007a; 2007b): Two-Dimensional Finite Difference Analysis

A series of models that account for the heat transfer mechanisms involved in hydronically heated bridge decks/pavements were described in previous sections and were classified as steady state and transient models. The steady state models developed by Schnurr and Rogers (1970), Kilkis (1994a, 1994b), and Ramsey et al. (1999) can be used to calculate the heat fluxes that are required for instantaneously melting all accumulated snow. However, due to an uneven distribution of snow on the surface, they cannot be employed for practical operations. The transient analyses performed by Leal and Miller (1972), Schnurr and Falk (1973), and Chiasson et al. (2000) also have significant limitations, including a lack of consideration of the phase change of the accumulated snow on the surface and the insulating effect of the snow layer. The application of the model developed by Rees et al. (2002) is limited by the expensive computational effort,

although it can track the processes of temperature and mass change on the surface.

Based on the contributions from Rees et al. (2002), an updated two-dimensional finite-difference study was performed by Liu et al. (2007a) on predicting the surface conditions under various snowy scenarios, using a more efficient computational consumption but still retaining sufficient accuracy. Their model was validated by experimental data collected from a hydronic snow-melting bridge deck during several snow events (Liu et al. 2007b), and can be employed in the practical design and operation of hydronically heated bridge decks/pavements. The experimental validation analysis provided a reasonably good agreement between the measured results and model predictions.

This model assumes that the snow and slush layers are homogeneous and isothermal, respectively. Solar radiation absorbed by the snow layer was considered to contribute to snow melting, which occurred only at the bridge deck's upper surface/pavement. The drainage was assumed as perfect; therefore, no melted water was retained on the slab surface. Similar to the model developed by Rees et al. (2002), the snow processes were considered in terms of a one-dimensional treatment. The heat and mass transfers from the lateral direction within the saturated (slush) layer were not targeted in this study. The classification of surface conditions was similar to that of Rees et al. (2002). The model didn’t consider the surface condition under solid ice and water but used hoarfrost to depict a surface whose temperature was below freezing and was covered with frost. The calculation procedure for the identification of surface conditions is summarized in Fig. 2-10. It can treat the heat balances through the estimate of surface temperatures under given environmental circumstances, regardless of whether or not water is retained on the surface.

Liu et al. (2007a) proposed a one-node model that accounted for the snow melting

processes only under slush surface conditions, as presented in Fig. 2-11(a). The heat transfer attributable to conduction within the slush layer was not considered in this model due to the assumptions of relatively small thickness and uniform temperature distribution of the slush layer. For the analysis of the snow and slush surface condition, Liu et al. (2007a) formulated a two-node approach, which considered the calculation of conductive heat transfer in the snow layer and estimated the mass balance at the lower node, as schematically shown in Fig. 2-11(b).

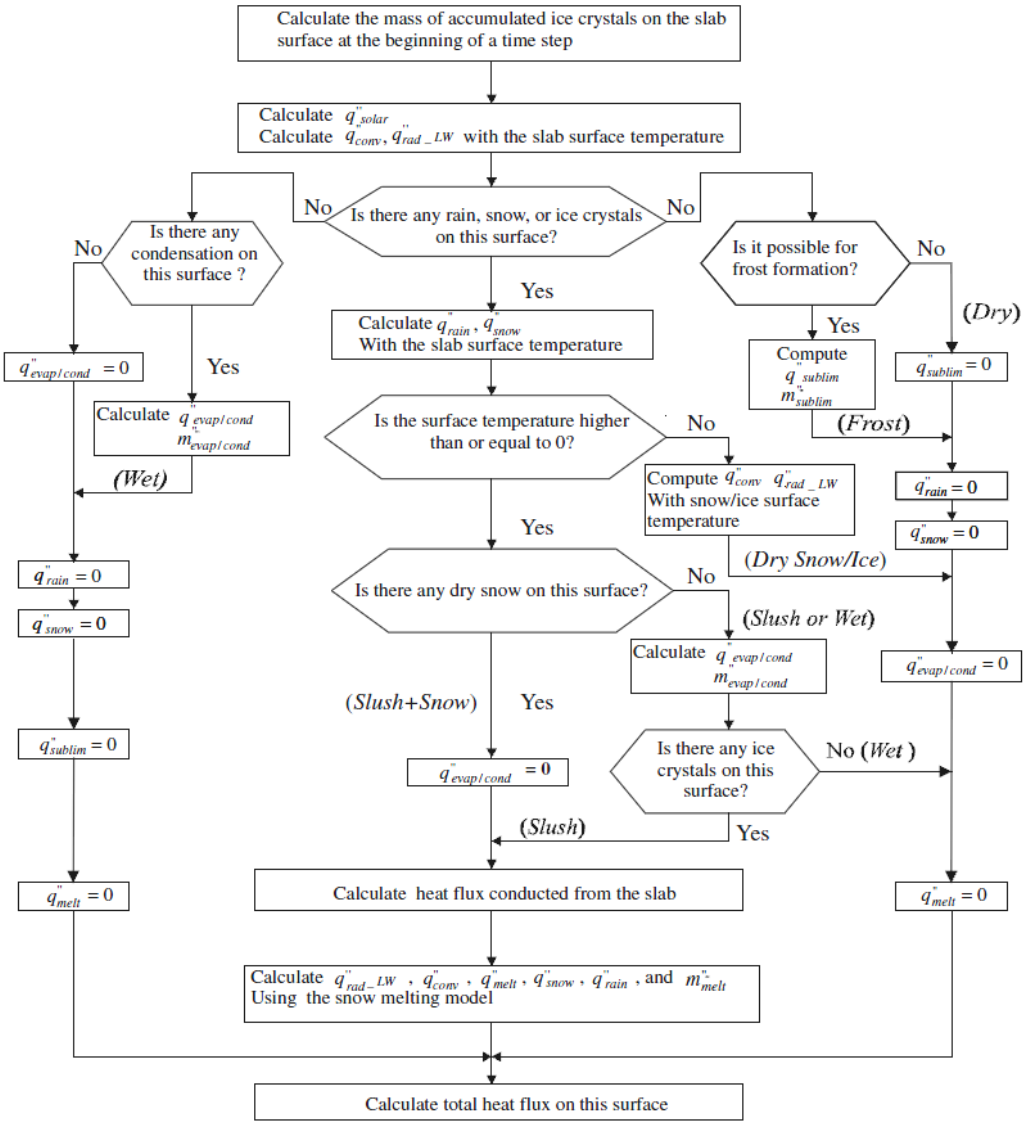

Figure 2-10. Flow chart of the calculation procedure for the snow melting processes (Liu et al. 2007a)

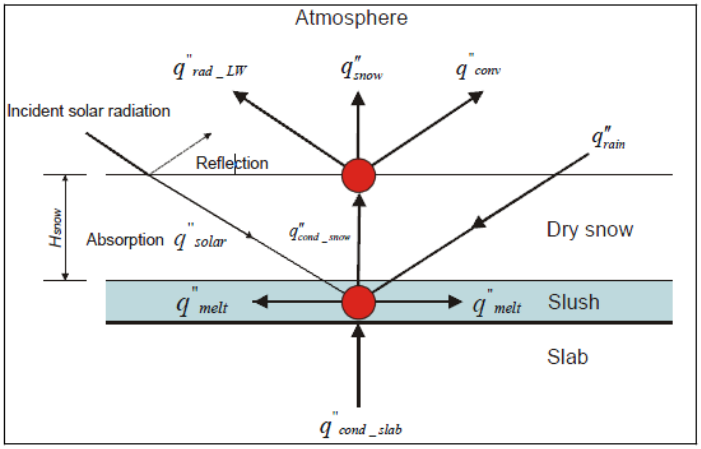

(a)

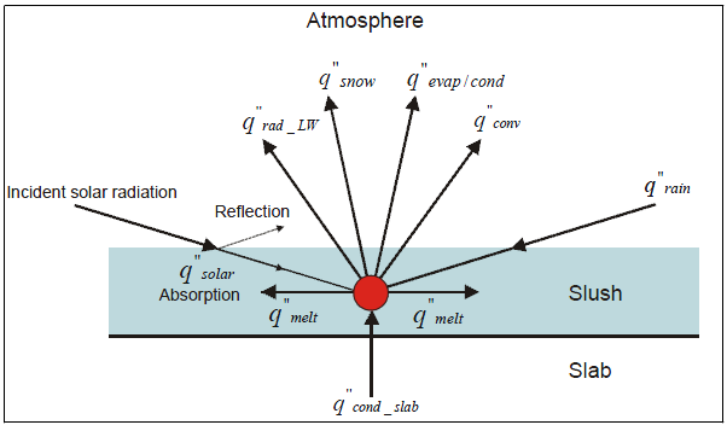

(b)

Figure 2-11. Schematic representation of heat transfer in (a): two-node snow and slush model, (b): one-node slush only model (Liu et al. 2007a)

The description of the snow melting process in the two-node snow and slush model was presented in terms of a mass balance of the solid ice crystals within both dry snow and slush layers and two energy balances respectively occurring on the surface of the dry snow layer and within the slush layer. The mass balance formulation was expressed the same as Eq. (2-18), which dealt with the correlation of the rate change of the mass of ice crystals, the snowfall rate, and the snow melting rate. The energy balance, considering the effect of solar radiation within the slush layers, is formulated below:

$$in''_{melt} \cdot h_{if} = q_{cond,slab} + q_{solar} + q_{rainfall} - q_{cond,snow} \quad (2\text{-}25)$$

$$q_{solar} = \alpha \cdot I \quad (2\text{-}26)$$

Where,

$q_{cond,\ snow}$ is the conductive heat flux transferred from the bottom surface of the snow layer to its top surface, Btu/hr.ft^2 or W/m^2.

α is the absorptivity coefficient of the slab surface, which is dependent on the surface conditions. For concrete, its value ranges from 0.5 to 0.8, dimensionless.

I is the direct radiation incident to a horizontal surface, which will change at any time.

Based on the energy balance at the upper node, the conductive heat transfer transferred within the snow layer is equal to the sum of the practical heat flux for raising snow temperature to the environment and the heat losses associated with convection and thermal radiation. The dry snow layer was assumed to have high porosity. The solar irradiation was not absorbed by this upper surface, but by this layer; therefore, solar radiation was not concerned with the energy balance analysis at the dry snow layer's upper surface in this model, as formulated in Eq. (2-27). The one-dimensional Fourier's Law of conduction heat transfer expressed in Eq. (2-28) can estimate how much heat was transferred within the dry snow layer.

$$q_{cond,snow} = q_{conv} + q_{rad} + q_{snowfall} \quad (2\text{-}27)$$

$$q_{cond,snow} = k_{snow} \cdot \frac{T_{snow,bottom} - T_{snow,top}}{h_{snow}} \quad (2\text{-}28)$$

Where,

$T_{snow,\ bottom}$ is the temperature at the bottom surface of the snow layer, °F or °C.

$T_{surf,\ snow}$ is the temperature at the top surface of the snow layer, °F or °C.

The node's energy balance at the surface of the slush layer is given below for the one-node slush only model schematically represented in Fig. 2-11(b).

$$in''_{melt} \cdot h_{if} = q_{cond,slab} + q_{solar} + q_{rainfall} - q_{conv} - q_{rad} - q_{snowfall} - q_{evap} \qquad (2\text{-}29)$$

The transient and two-dimensional finite difference model provided a comprehensive and accurate understanding of how to replicate the complex heat transfer mechanisms during the snow melting. It is also capable of predicting the various surface conditions and surface temperatures under inputs of environmental circumstances and the inlet fluid temperature or the heat flux supplied from the hydronic heat source. Compared to the model proposed by Rees et al. (2002), this model is more computationally efficient, as it uses a somewhat coarser mesh that does not decrease the accuracy of the calculation. Therefore, this model can be employed in the hydronic heating design for long-term operations. The model was experimentally validated by Liu et al. (2007a), which indicated that it was promising and feasible for applying the hydronic heated bridge deck/pavement.

2.4 Experimental Investigations of Hydronic Heating Systems for Bridges/Pavements

Many experimental investigations of hydronic heating systems for bridges/pavements that are based on the theoretical background of the developed numerical models are listed and described in this section. Some experimental studies are intended to determine the practical feasibility of hydronic snow melting through a series of parametric studies under various winter events, and some actual snow-melting applications can be viewed as experimental validations for previously developed models. This section will introduce these experimental investigations to provide an overall understanding of the development of the experimental analysis of hydronic heating systems for bridges/pavements.

Experimental investigations of bridge/pavement heating systems have been conducted for many years in the US. As early as the 1970s, Bienert et al. (1974) designed a test at the Fairbank Highway Research Station in McLean, Virginia, and indicated that it was technically feasible for the earth's heat to remove snow and ice from pavement/bridge deck surfaces. The focus of the study conducted by Ferrara et al. (1976) was to investigate the application of the earth's heat to prevent the freezing of pavements'/bridge decks' surfaces. In Colorado, Griffin (1982) conducted a study to develop a new heating system in which fossil fuel was not employed as the heat source. Conceptual designs, heating performance, life expectancy, and cost evaluation, were also studied.

In the 1990s, experts focused on the performance of heating systems. Minsk (1999) designed tests for a bridge located in the north fork of Silver Creek in Oregon, based on the supply of well water, combined with a ground source heat pump (GSHP), to heat the bridge deck. In 2000, a hydronic heating system for a bridge deck was implemented on an interstate highway in Oklahoma by Chiasson and Spitler (2001b), who described the typical constructional layout of a hydronic heating system and the heat transfer mechanism within a bridge deck, as respectively shown in Figs. 2-12 and 2-13. Due to the excellent feasibility of drilling and earth trenching, a vertical, closed-loop GSHP system was selected as the heat exchanger component to meet the heating needs. It was noted that the heat carrier fluid was also circulated from the bridge deck directly to the GLHE (ground-loop heat exchanger) in the summer, which made it possible to "recharge" the ground. Numerical simulation was utilized to analyze the heat transfer in the heated bridge deck by using two numerical environments: TRNSYS and HVACSIM+. The final system design, including 16 heat pumps with a performance capacity of nominal 30 tons and 250 boreholes with a single length of 76 m, was determined after completion of the combined experimental and numerical investigations.

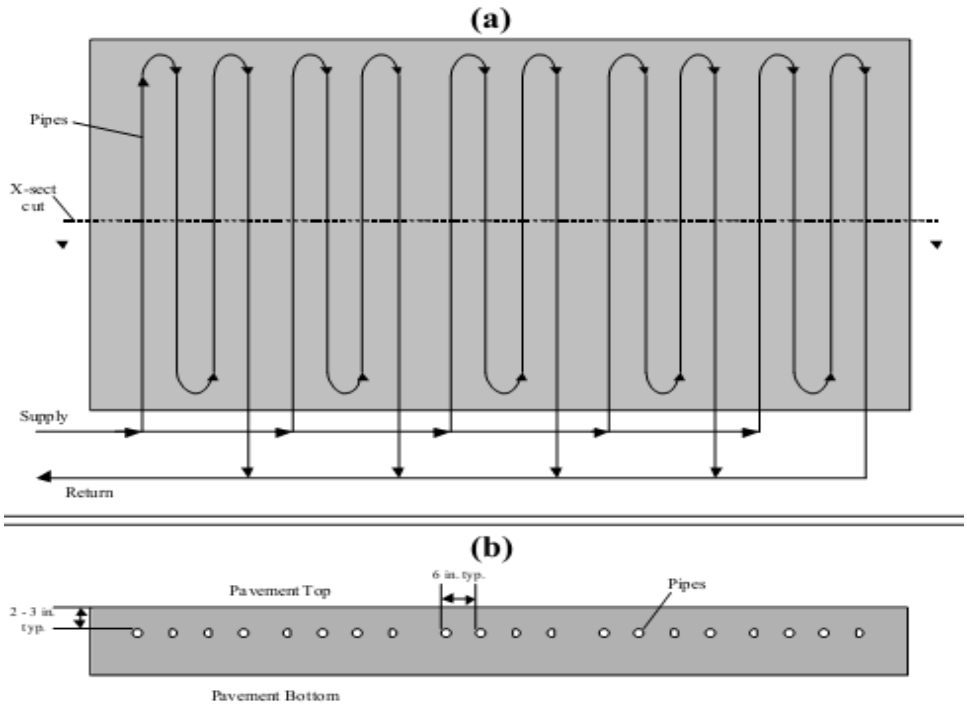

Figure 2-12. Typical hydronic loop layout of a geothermally heated bridge deck/pavement: (a) plan view, (b) cross-sectional view (Chiasson and Spitler 2001b)

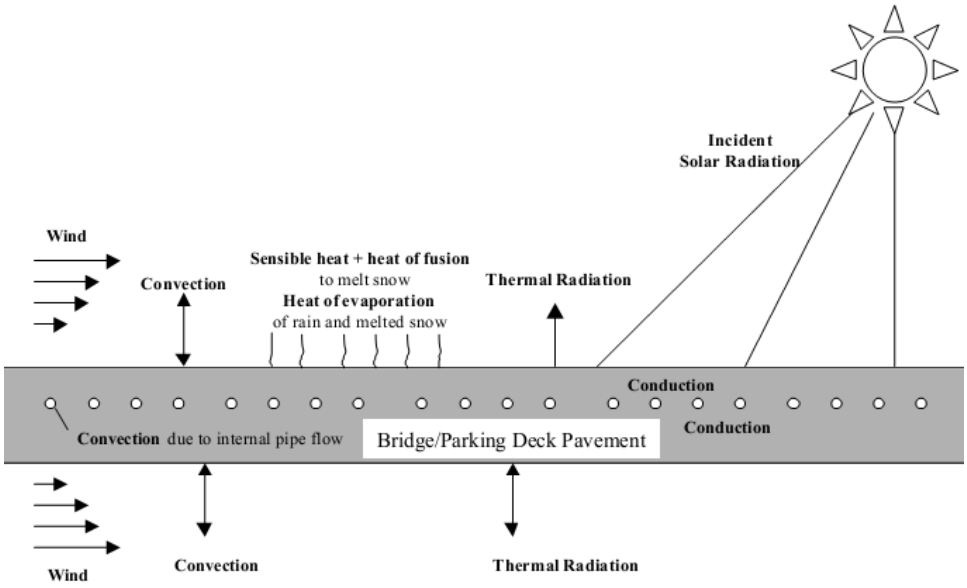

Figure 2-13. Cross-sectional view of the heat transfer mechanisms in an internally heated bridge deck (Chiasson and Spitler 2001b)

Based on the snow-melting theory developed by Rees et al. (2002), an experimental investigation was conducted by Hockersmith (2002) that accounted for the snow metamorphism of the shape of snow crystals during the melting process. A 0.91 m x 0.91 m (3 ft. x 3 ft.) concrete slab, shown in Fig. 2-14, was utilized for the study, and electricity served as the heat source that warmed the bottom of the slab so that the snow-melting test could be performed in an enclosed area. With the aid of various electrically thermal supplies, a series of experimental analyses were conducted to estimate the variations in the heating and snow-melting performances of the system. The analyses included water runoff, the maximum height of the slush layer (shown in Fig. 2-7), the size of the snow crystals, and the temperature responses on the plate surface. The results of the tests were employed in the experimental validation with the transient model proposed by Rees et al. (2002). Under the environment provided by the experimental chamber and snow-making apparatus, the interactions between the time for snow melting and the range of the supplied heat

flux can be predicted with moderate accuracy by this transient model. Another important finding was a rough prediction of water runoff, decreasing the deviation between the numerical and experimental results from 20% to 5% by using a simple runoff correction under the same experimental conditions. Unexpected uncertainties of this model were caused by the accuracy level of the experimental results (15% of the difference between simulated outputs and measurements) due to the inhomogeneities that take place during the snow-melting process, and led to an under-prediction of the simulated melt time compared to the experimental measurements. The heat loss from the sides and bottom were not of concern in this study.

Figure 2-14. Concrete slab for tests (Hockersmith 2002)

Based on the newly developed transient and two-dimensional FD model for the snow-melting process that takes place on a pavement surface heated by a hydronic loop system (Liu et al. 2007a), a geothermally heated bridge deck with dimensions of 18.3 m × 6.1 m (60 ft. × 20 ft.) and an embedded hydronic heating system with cross-linked polyethylene pipes was fabricated and installed at Oklahoma State University for experimental validation (Liu et al. 2007b). To

maintain a snow-free bridge deck, a vertical closed-loop GSHE, including six 13 cm (5.25 in.) diameter boreholes, was employed to transport geothermal heat.

The experimental results of the numerical model presented a satisfying prediction, including the surface temperature and conditions, and the amount of snow cover on the deck surface under given thermal supplies and environmental circumstances. It was concluded that this validated model can be utilized to estimate the snow-melting performance of a hydronic loop system under various snow events. The study emphasized that reasonably accurate information pertaining to weather data and operational parameters, including ambient temperature, wind speed, snowfall, solar radiation, fluid flow rate, and thermal properties of concrete slabs play a dominant role in the computational accuracy of this model. Although an over-prediction of the surface temperature occurred during water evaporation due to the exclusion of water penetration into the slab in this model, sufficient prediction accuracy can be provided during the heating. Snow-melting processes were the major concerns of this model.

A ground-source heat pump (GSHP) system was employed in the experimental analysis of the heating and snow-melting processes performed by Balbay and Esen (2010). The effect of various borehole depths (30, 60, and 90 m) on the heating efficiency of the system that included a hydronic heat pump and pipe loops embedded beneath the bridge and pavement slabs was estimated. Figure 2-16 illustrates the initial and intermediate snow melting process on these slabs.

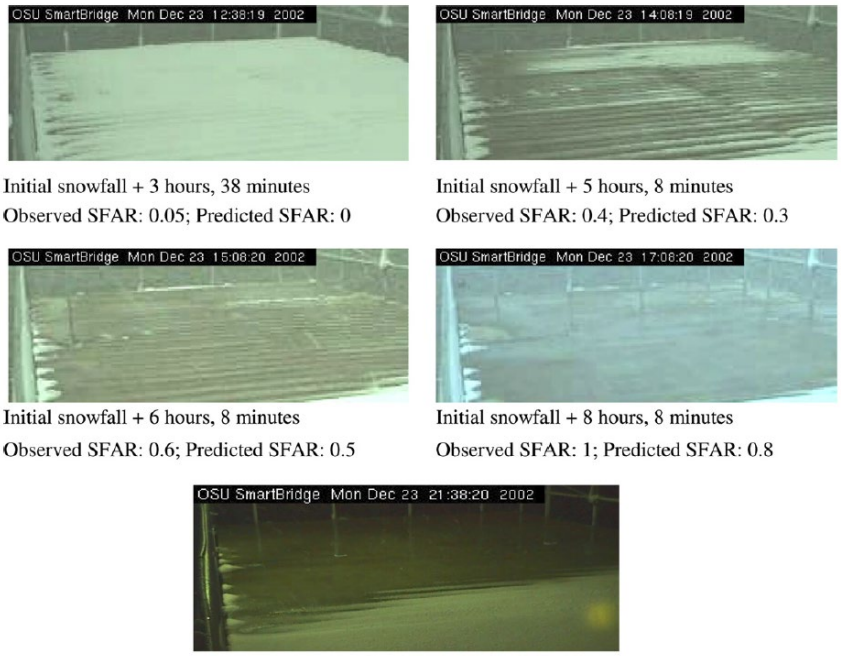

,

Figure 2-15. Surface conditions of the bridge, with estimates of snow-free area ratio (Liu et al. `2007b)

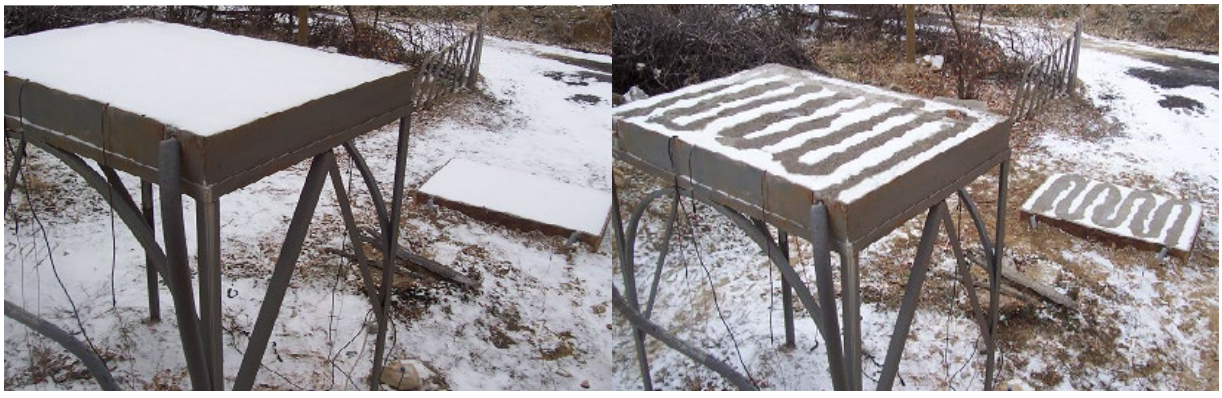

(a) **(b)**

Figure 2-16. Initial and intermediate snow-melting process on slabs: (a) initial state (t=0) for bridge and pavement slabs; (b) intermediate state (t=30 min) for bridge and pavement slabs (Balbay and Esen 2010)

Yoshitake et al. (2011) proposed a bridge deck heating system in Japan, where an underground water storage tank was the heating source. The ground heated the water to approximately ground temperature, then the water was circulated through the hydronic loops embedded in the bridge deck. The heat carrier water was circulated without hydronic power supplied by a heat pump; it was total self-sufficient. When the lowest temperature in the bridge deck, measured by the data collection system, was less than 0.5 °C (32.9 °F), the system operated automatically and heated the bridge deck.

2.5 Case Studies

This section provides several real-world applications of a geothermally heated bridge deck that have been used worldwide for snow melting/deicing the surfaces of bridge decks and pavements.

(1) SERSO bridge in Switzerland

In Switzerland, the SERSO heating project was the first geothermally heated bridge deck/pavement that utilized shallow geothermal energy as the heat source for melting snow (Eugster, 2007). The SERSO bridge, which is viewed as the most famous bridge deck/pavement heated geothermally, was designed in early 1990 and is still working today. This system can heat a bridge/pavement area larger than 1300 m^2 by a typical average heat output of 100 W/m^2, providing good road conditions on the bridge deck/pavement during winter events. The estimated installation and operation costs were 2500 $euro/m^2$ and 4 $euro/m^2$ for electricity and maintenance. Similar to the typical bridge deck/pavement heated with geothermal energy, the system can collect and store solar energy in the underground soils of the bridge deck/pavement, which increases the heating efficiency of the system in the winter and lowers the temperature at the deck surface in the summer, thus stabilizing the temperature responses within the bridge deck/pavement. In the winter,

the heat carrier fluid extracted from the underground circulates within the hydronic loop system embedded in the bridge deck/pavement for the deicing requirement. Figs. 2-17, 2-18, and 2-19 present the schematic of this SERSP heated bridge/pavement project, the road surface temperature controlled by the SERSO system, and the surface conditions after the SERSO system operation, respectively.

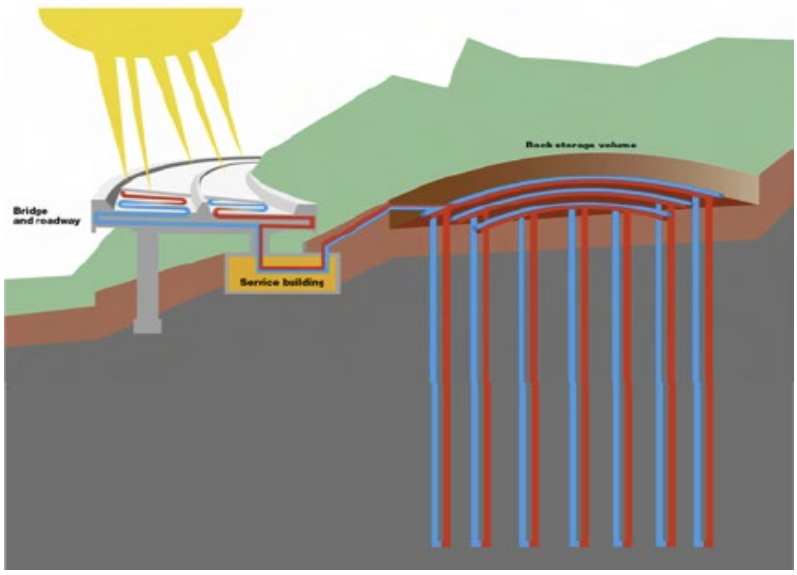

Figure 2-17. Swiss solar storage system (Eugster, 2007)

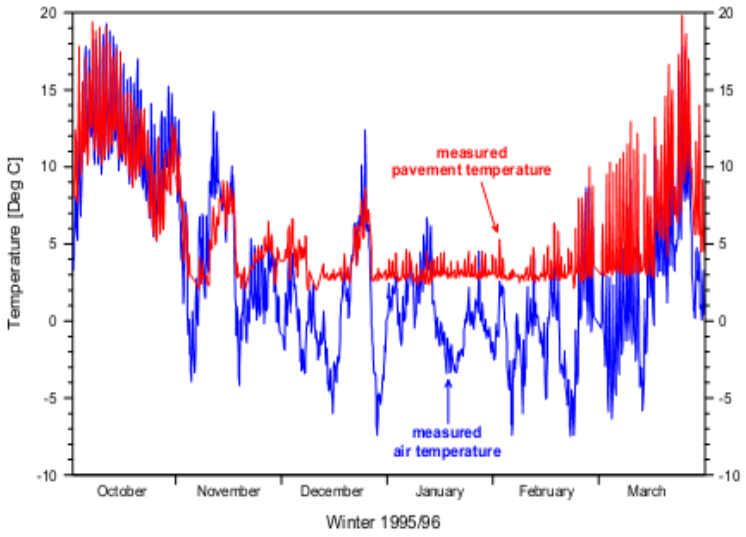

Figure 2-18. Road surface temperature controlled by the SERSO system (Eugster, 2007)

Figure 2-19. SERSO system in operation (Eugster, 2007)

(2) Case in Amarillo, Texas

Amarillo's project consisted of a north-bound two-lane bridge and a south-bound two-lane bridge on US 287 in Amarillo, over N. 15th Ave. The box beam bridges were 58 feet wide and 146 feet long, as shown in Fig. 2-20. The heated area on each bridge was 8600 ft^2. The design objective was to prevent the forming of ice (anti-icing) by using a heat flux of 129 W/m^2 or 41 Btu/ft^2-hr

(Minsk 1999). In this hydronic system, 50 geothermal wells for each structure provided the heat source. For each bridge, 11,355 L (3,000 gallons) of 50% propylene glycol-deionized water served as the deck circulating fluid. Minsk (1999) indicated that the heating system meets the snow-melting requirement and has experienced no problems. More hydronic loop design details are presented in Tab.1-1.

Figure 2-20. Heating hoses in place ready for concrete pour; hoses are on 152 mm (6-in.) centers placed 76 mm (3 in) under the top of the slab, affixed below #4 rebar

(3) Case in Weatherford, Oklahoma

This geothermally heated bridge is located on Interstate Highway 40 (I-40), just east of Weatherford, Oklahoma. The bridge is approximately 213 m long and 12 m wide; the heated area is 2475 m^2. For the hydronic loops design, the pipe, crosslinked polyethylene, is embedded in a serpentine configuration, as shown in Fig. 2-21 (Spitler and Ramamoorthy, 2000). The design objective was to ensure that the average bridge surface temperature remains above freezing. The heat transfer fluid (42% propylene glycol) circulated throughout the bridge deck. More details of the design hydronic loops design are provided in Table 1-1.

Table 2-1. Hydronic Loops Design Considerations for Previous Geothermal Heated Bridge Systems (Spitler and Ramamoorthy 2000; Minsk 1999)

Design Considerations	Case 1 (Weatherford, Oklahoma)	Case 2 (Amarillo, Texas)
Pipe diameter (in.) or (mm)	0.71 or 18	0.75 or 19
Pipe depth below road or bridge surface (in.) or (mm)	2.95 or 75	3 or 76
Pipe center spacing (in.) or (mm)	11.8 or 300	6 or 152
Pipe material	polyethylene	-
Road or bridge deck thickness (in.) or (mm)	7.9 or 200	48 or 1219.2
Deck area (ft^2) or (m^2)	26640 or 2475	17200 or 1600
Heat transfer fluid	42% propylene glycol	50% propylene glycol-deionized water
Heat flux (Btu/hr*ft^2) or (W/m^2)	From 136.5 or 430 to 168.3 or 530 based on different entering fluid temperature from 2 °C to 10 °C	41 or 130
Design objective	Snow melting (deicing) [1)]	Ice prevention (anti-icing) [2)]

Note: [1)] **Deicing** is the application of ice-control products to melt snow and ice. Deicing practices take place after snow-removal operations to melt the remaining snow and ice. (From We Scapes, Water & Earth Landscape Design)

[2] **Anti-icing** is the application of products that help prevent snow and ice from bonding to the pavement, to facilitate easy shoveling of surfaces. Anti-icing can create safe winter conditions and is a cost-effective alternative to deicing. (From We Scapes, Water & Earth Landscape Design)

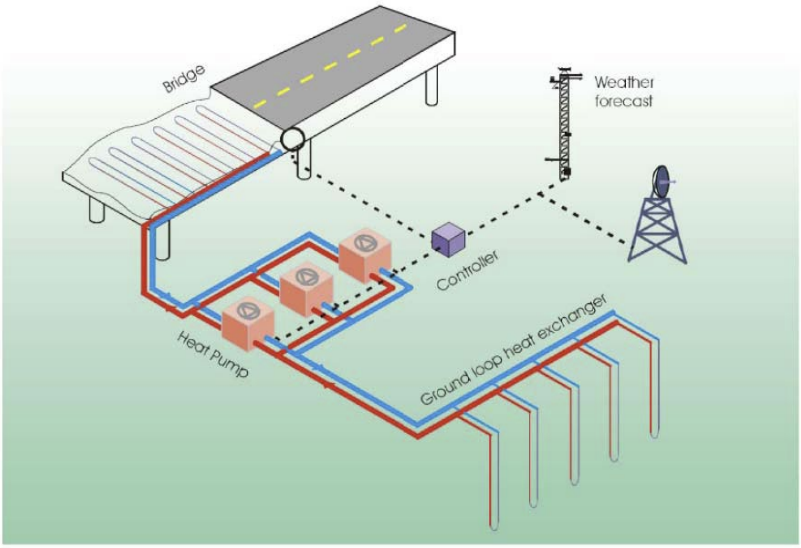

Figure 2-21. Oklahoma State University's geothermal bridge

(4) Geothermal heating projects in Japan

Geothermal energy snow-melting systems have been popular in Japan since the 1990s, and most of them are still working. After the 1990s, the concept of thermal recharge, based on collecting solar energy during the summer for snow-melting in the winter, began to be applied to bridge decks/pavements. Kamimura et al. (2000) took advantage of the shallow layer of geothermal energy to deice a pedestrian walkway in Nagaoka City. A geothermal heat exchange well (GHEW), shown in Fig. 2-22, was employed in this heating system to deliver the warm water from the ground to the snow/melting panels. By investigating the performance of this snow-melting system over two winter seasons, it was concluded that the system is capable of melting snow.

A hydronic loop heating system proposed by Yoshitake et al. (2011) utilized groundwater as the heat source for snow melting, as it provided a relatively constant temperature. An essential advantage of this heating system is the significant economic benefit, as it costs approximately half of other systems, and the cost of operating it is 10% less than other similar systems. Figure 2-23 compares the surface conditions of bridge decks/pavements with and without heating capabilities during snow events. It was observed that the practical feasibility of the geothermally heated bridge deck had been confirmed, and it was concluded that the system can meet the demands for deicing or snow melting in the winter. Consequently, the economical and practical system is up to the task of preventing snow/ice accumulation on bridge deck/pavement surfaces.

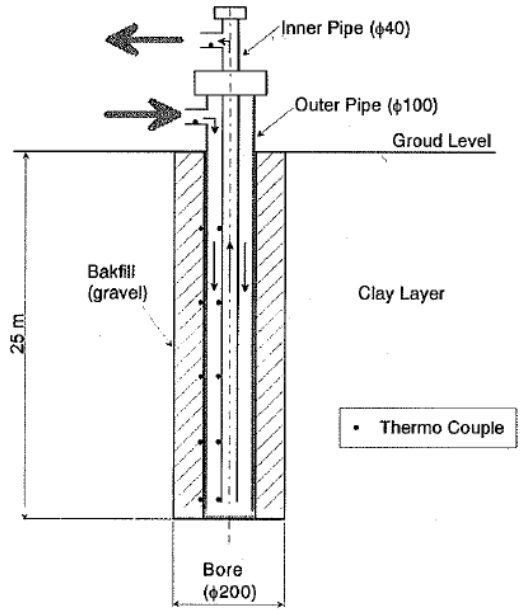

Figure 2-22. Schematic of geothermal heat exchange well (GHEW)

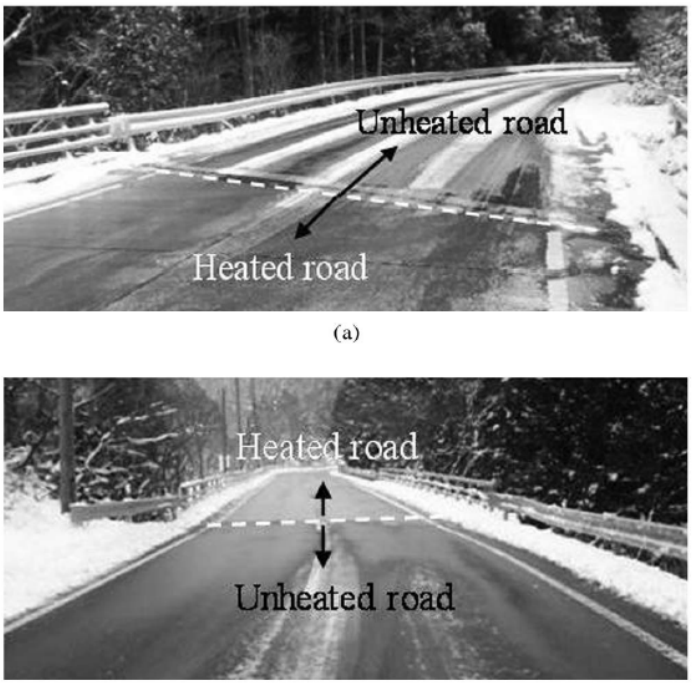

Figure 2-23. Example of road condition in snowy season ((Yoshitake et al. 2011)

2.6 Geothermal Bridge Decks Externally Heated

A series of experimental investigations and practical case studies verified the feasibility of applying geothermal energy to bridge deck deicing. It can be a more sustainable, renewable, and environmental-friendly alternative; however, most of the previous experimental and practical contributions of geothermal heating systems focused on an internal heating source design, which can only be applied to new bridges/pavements. Existing bridges, for which deicing is most in demand, cannot be heated by this design to prevent surface accumulation of snow. Therefore, a new heated bridge deck/pavement design with an external heating system was developed and has been successfully used for several years to increase the utilization of geothermal energy for deicing during winter events. Several studies have been developed through both numerical and experimental investigations to account for the feasibility of this external heating design, as described in this section.

2.6.1 Comparison of Designs of Internally and Externally Heated Geothermal Decks

A great many of TxDOT's overpass bridges have to be deiced. CIP-PCP bridge decks, including precast, prestressed concrete panels (PCPs), and cast-in-place (CIP) concrete decks account for approximately 85% of the bridges in Texas; consequently, the heated bridge deck design is often used on CIP-PCP bridge decks. The heat that is utilized to deice bridge decks is supplied from two sides of the bridge deck. The heating systems are directly installed in the concrete deck during the construction of new bridges, as shown in Fig. 2-24(b). To facilitate an easier installation and as little disturbance to the traffic flow as possible, the external heating source attached to the bottom of the bridge deck is intended to be treated as an alternative, as it is not the most efficient design. A schematic of the external hydronic heating loop design for a heated bridge deck consisting of hydronic pipes and foam insulation materials is presented in Fig. 2-24(a) and is compared to the internal heat source bridge deck illustrated in Fig. 2-24(b).

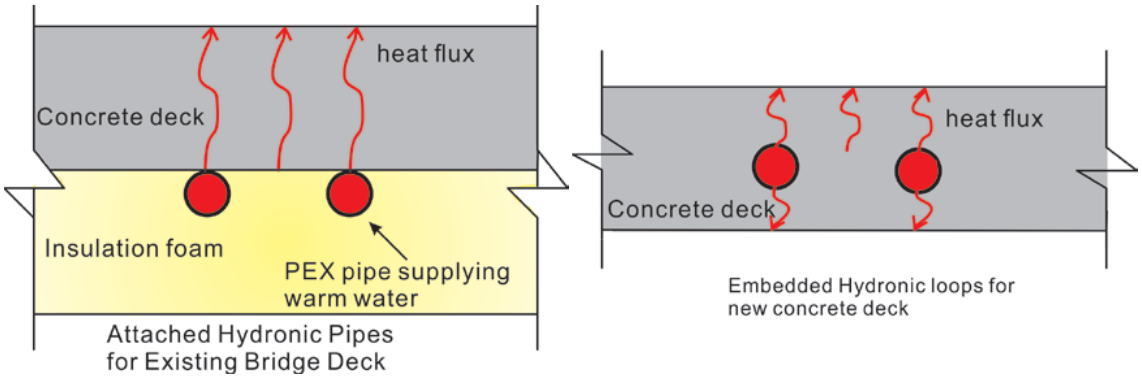

(a) **(b)**

Figure 2-24. Schematics of heated bridge decks: a) external heating source, b) internal heating source (Yu et al. 2020)

2.6.2 Research Contributions of Externally Heated Bridge Decks

Most geothermal heating studies have focused on an internal heat source that consists of hydronic loops embedded in the concrete deck during the construction of the bridge. Since this

heat source is only applicable to new construction, a novel design of an external heating system was developed that can be applied to existing bridges. Several numerical and experimental studies have been published to analyze the feasibility of the newly developed external heating design.

Zhang et al. (2017) created a finite element model of an externally heated bridge deck with a single hydronic loop to perform a series of parametric studies to investigate the new design's heating performance. They concluded that the ambient temperature, inlet fluid temperatures, and concrete thickness significantly affect the heating efficiency of the system. Wind speed at a low level cannot dominate the system performance due to a slight heat loss associated with the convective heat transfer, and variations in the flow rate can be neglected based on the simulated results. This study didn't consider the snow-melting or deicing process on the deck's surface, and the FEM model was not validated by experimental data.

Based on the findings of Zhang et al. (2017), Li et al. (2018) used Multiphysics COMSOL to develop finite element models of both internally and externally heated bridge decks with a single hydronic loop. A series of numerical parametric analyses, including ambient temperature, fluid velocity, inlet fluid temperature, and wind speed, were performed on the two models to estimate the numerical feasibility of the external heating design under various thermal supplies and environmental conditions through comparison with an internal heat source. They concluded that an externally heated geothermal bridge deck could reach above-freezing temperatures during mild winter events, but that it takes about 20 times longer than it takes the internal design. Lei et al. (2018) modeled an externally heated bridge deck with multi-loops in COMSOL. They conducted parametric studies on ambient temperatures, inlet fluid temperatures, flow velocities, wind speeds, and foam thicknesses under mild winter weather scenarios. The results were similar to those of Zhang et al. (2017), as both FEM models were based on the literature's thermal properties, were

not validated with experimental results, and neglected the thermal contact at the attached loop and concrete deck interface.

To examine the experimental feasibility of this external system, a series of heating tests under several different thermal scenarios were performed on an externally heated deck in which the hydronic heating system, sealed in a geofoam slab for heat insulation, was attached to the base of a concrete slab (Yu et al. 2020). An empirical equation can provide reasonably accurate temperature predictions at 2.54 cm (1 inch) below the slab surface under local freezing tests performed on the slab surface. By using the experimental data, Li et al. (2020) eveloped a validated FE model of the externally heated bridge deck, which was capable of providing a comprehensive understanding of heat transfer mechanisms within the bridge deck and accurately predicting the external heating system's performance under given ambient temperatures below freezing. The numerical study is described in detail in Chapter 3. The studies were performed under controlled temperatures in a laboratory and didn't consider the deicing process. Therefore, a real-world hydronic bridge deck needs to be constructed and fabricated in the field to evaluate the external heating design's deicing capabilities under various environmental circumstances. A series of heating tests were performed to estimate the system's performance.

2.7 Summary

This chapter provides a comprehensive understanding of the analyses of a geothermal snow-melting system, including numerical modeling, experimental investigation, and case studies. The comparisons of internal and external heating designs are described as well. Because of its sustainability, renewability, and non-pollution, geothermal energy has played a considerable role in geotechnical engineering products, such as ground-source heat pumps (GSHPs), geothermal energy piles (GEPs), and borehole thermal energy storage (BTES) (Amayta et al. 2012; Nam and

Chae 2014; Sterpi et al. 2018; Zhang et al. 2017). Due to its relatively constant temperature and heat storage capacity, the ground can be considered a heat source for deicing bridge decks in the winter, resulting in significantly fewer corrosive effects on bridge structures than applications of snow-melting agents (Bowers and Olgun 2014). Another benefit is that with the application of ground-source heating technology, the temperature of the bridge deck can be decreased during early concrete curing to minimize cracking (Bowers and Olgun 2014).

A large number of numerical models for deicing geothermally heated bridge decks/pavements have been developed. They include 1D, 2D, and 3D models of steady state and transient models, with considerations of initial and boundary conditions defined by specific operations or environmental scenarios. Early numerical models recommended by ASHRAE (ASHRAE Handbook 2013) were1-D steady-state, which provided calculations of the required heat flux on bridge/pavement surfaces related to the snow-melting process (Adlam 1950; Chapman 1956; Kilkis 1994a, 1994b). Ramsey et al. (1999) developed a 1-D steady state analysis model that could calculate the heat flux, in terms of energy balance, at the top surface of a bridge deck/pavement; however, they did not consider intermittent system operations or dynamic weather conditions. Some early studies also focused on developing transient models (Regis et al. 1973; Schurr and Falk 1973); however, they could not accurately estimate how the deicing process would perform under transient state or 2-D conditions and did not account for the snow accumulated on the surface. More recently, transient studies and 2-D numerical models have been developed, using a hydronic heating design. Chiasson and Spitler (2001b) created a two-dimensional finite difference model that could track the mass of snow accumulated on the surface during a snow event; however, it did not account for the insulating effect of the snow layer. Like most of the previously mentioned models, it was not validated by snow-melting tests. Rees et al. (2002)

reported a 2-D numerical method that included a transient tool that could analyze the effects of deicing processes on system performance and predict various surface conditions during a winter event. This method's expensive computational requirement makes it impractical for long-term operations, however, so it can only be performed for single winter events. Laboratory tests conducted by Hockersmith (2002) were only able to partially validate this model, and no other published studies focused on further validation. Based on the contributions of Rees et al. (2002) and Liu et al. (2003), a parametric study conducted by Liu and Spitler (2004) demonstrated how pipe spacing, slab insulation, idling time, and control strategies affect heating performance. It was noted that preemptive heating was one of the preconditions necessary for achieving the expected snow-melting performance. An updated numerical model that can account for the surface conditions under various snowy events was proposed by Liu et al. (2007a). Their newly designed model was more computationally effective than the model developed by Rees et al. (2002), and it had reasonably accurate simulation. Furthermore, it was comprehensively validated by experimental data (Liu et al. 2007b), which stated that the simulated results agreed with the experimental measurements.

Over the years, experimental investigations and case studies on bridge/pavement heating systems have been developed globally. Through a series of experimental investigations, the experimental and practical feasibility of applying geothermal energy to bridge decks for deicing was verified by Griffin (1982), Chiasson and Spitler (2001b), Hockersmith (2002), Liu et al. (2007b), Balbay and Esen (2010), and Yoshitake et al. (2011) and by case studies that were investigated in Europe, Japan, and the U.S. Geothermally heated systems have been touted as a more sustainable, renewable and environmental-friendly alternative; however, most of the experimental investigations focused on the internal heating source design, which can only be used for new

bridges/pavements. Therefore, a novel design of an external heating system, in which the hydronic loops system was attached to the bottom of the concrete deck and encapsulated in a geofoam layer for heat insulation was developed to be applied to existing bridges for snow melting/deicing.

Several numerical analyses accounted for interactions between various design parameters and the heating performance of an externally heated bridge deck model, which indicated that the external heating system could meet the demand for snow-melting under mild winter scenarios (Lei et al. 2018; Li et al. 2018; Zhang et al. 2017). However, these FEM models were limited to perfect contact assumptions at all module interfaces and were not validated by experimental data. To evaluate the externally heated bridge deck's experimental feasibility, an externally hydronically-heated concrete slab was developed and tested under different ambient and inlet temperatures in an environmental chamber (Yu et al. 2020). An empirical equation provided a reasonable evaluation of the temperature prediction at 2.54 cm (1 inch) below the local freezing tests' slab surface. By using the experimental data, Li et al. (2020) developed a fully laboratory-validated FEM model of a externally heated bridge deck that provided a comprehensive understanding of heat transfer mechanisms within the bridge deck and compared the heat transfer efficiency of the external heating design with experimental measurements and numerical outputs. These two limited studies were performed under controlled temperatures in a laboratory, and deicing behaviors were not involved.

CHAPTER 3 NUMERICAL ANALYSES OF A LABORATORY TEST OF A GEOTHERMAL BRIDGE DECK EXTERNALLY HEATED UNDER CONTROLLED TEMPERATURE

3.1 Introduction

As mentioned in Chapter 2, most previous studies relied on an internal heat source installed inside the bridge's construction concrete deck. This internal heating source design is not applied to existing bridges, which have the most critical demand for deicing. Recently, several numerical models were developed to analyze the numerical feasibility of the external heating design. However, these researches were not validated with experimental results and neglected the attached loop and concrete deck interface's thermal contact. Therefore, an external hydronically-heated deck, in which the hydronic loops system was attached to the bottom of the concrete deck and encapsulated in a geofoam layer for heat insulation, was fabricated and tested in an environmental chamber (Yu et al. 2020). A series of heating tests were conducted under various heating scenarios to examine the heating and heat transfer efficiency of the external heating design. A 3D FEM model of the externally heated deck was created in COMSOL Multiphysics (COMSOL 2016), and its transient simulation was calibrated using the experimental results acquired in the environmental chamber. The calibrated finite element model was further verified by the steady-state results of 15 environmental chamber tests. A comprehensive analysis of the heat transfer mechanism and energy balance was performed with the aid of the FEM model. The calibrated model can be a useful tool for heat transfer analyses and the design of externally heated hydronic bridges.

3.2 Laboratory Testing Program of a Heated Concrete Slab

This section presents a general description of the materials, design, instrumentation, fabrication, and data acquisition of externally heated bridge decks, followed by a discussion of the heating response test programs. In order to study the heating performance of the external heating source, a series of heating tests were conducted on a hypothetical bridge deck that was fabricated and installed in an environmental chamber at the structural lab at the University of Texas at Arlington (UTA). The measured temperature responses within the bridge deck are presented in this section, and the numerical results are presented in the next section, to validate the analysis of the finite element method (FEM) model.

3.2.1 Externally Heated Bridge Deck

3.2.1.1 Materials, Design, and Instrumentation

A standard 1.8 m × 1.2 m × 0.1 m (6 ft. × 4 ft. × 4 in.) TxDOT PCP panel was acquired from BEXAR Concrete Works, LTD, to function as the heated deck. Cross-linked polyethylene (PEX) tubing with an oxygen barrier layer was selected for hydronic heating because it is capable of preventing air/oxygen from infiltrating the radiant heating system. A PEX pipe with an inner diameter of 13 mm (0.5 in.) and an outer diameter of 19 mm (0.75 in.) was employed to circulate heat-carrying fluid within the bridge deck. In order to minimize heat loss from the exposed PEX pipe, a layer of thermal insulation material, such as geofoam and polyurethane foam, was installed under the deck. Expanded polystyrene (EPS) geofoam, comprised of approximately 2% polystyrene and 98% air, is considered an appropriate heat insulation material that has a poor thermal conductivity range of 0.035 – 0.037 W/(m· K) (0.24-0.26 BTU·in./(h·ft^2·°F)).

The geothermally heated bridge deck involves hydronic loops and geofoam as heat insulation. A serpentine hydronic loop system, consisting of 10 parallel pipes with centerline spacing of 152 mm (6 in.), and 9 turns with an internal radius of 3 inches was designed for this

PCP slab. The dimensions of the geofoam block were 1.5 m × 1.2 m × 127 mm (5 ft. × 4 ft. × 5 in.). The hydronic loops were secured to the bottom of the bridge deck and encapsulated in a geofoam block to minimize heat loss from the bottom. More detailed information on this externally heated bridge deck is presented in Figs. 3-1(a) and (b), along with top and cross-sectional views.

In this study, type T thermocouples from National Instruments, with an accuracy of +/-1°C (2°F), were employed to acquire the temperature responses of the testing system. To obtain the heat transfer behaviors within the panel, six type-T thermocouples (B-1 to B-6) were installed by drilling 1 inch above the concrete bottom surface, and another six identical thermocouples (T-1 to T-6) were installed by drilling 1 inch below the concrete top surface. Before the drilling, a mark of 1 inch was made on the drill bit to control the depth of the drilled hole. Then, the hole was cleaned with air and thermocouple was placed into it, which rested on the bottom. Finally, fine cement paste was carefully applied to seal the hole to facilitate good contact with the concrete. Although special care was taken to maintain the thermocouple depth during the thermocouple installation, it is possible the actual measurement depth may not be exactly as planned. To evaluate the thermal insulation performance of the geofoam block, two thermocouple sets (G-1, G-2, and G-3) and (G-4, G-4, and G-5) were installed in the geofoam block. The thermocouple layout within this heated bridge deck is illustrated in Figs. 3-1(a) and (b), which show where the specific spatial coordinates of each thermocouple location can be obtained. The origin of the coordinate system presented in Figs. 3-1(a) and (b) are located at the lower-left corner of the deck's top surface. The X and Y axes are respectively along the length and the width of the top surface, and the Z-axis is along with the depth of the deck, with a negative downward.

3.2.1.2 Test Setup of the Heated Slab

The heated bridge deck was fabricated and installed in an environmental chamber in which a minimum temperature of 4.4 °C (40 °F) could be attained. Two 1.1 m (3.5 ft.) high concrete pedestals, each with 6 inches of landing space, supported the concrete slab, as shown in Fig. 3-2. The geofoam block encapsulating the hydronic heating system was directly attached to the bottom surface of the concrete slab by straps and wood. A flat interface zone, created by covering the pipe system with a fine cement paste, made the heat transfer at the base of concrete slab more uniform and efficient. The loop inlet was connected to a water pump that was submerged in a water tank and capable of providing a constant flow rate of 0.13 kg/s (2 gallons/min); the loop outlet was connected to a water tank that could provide warm water at the desired temperature.

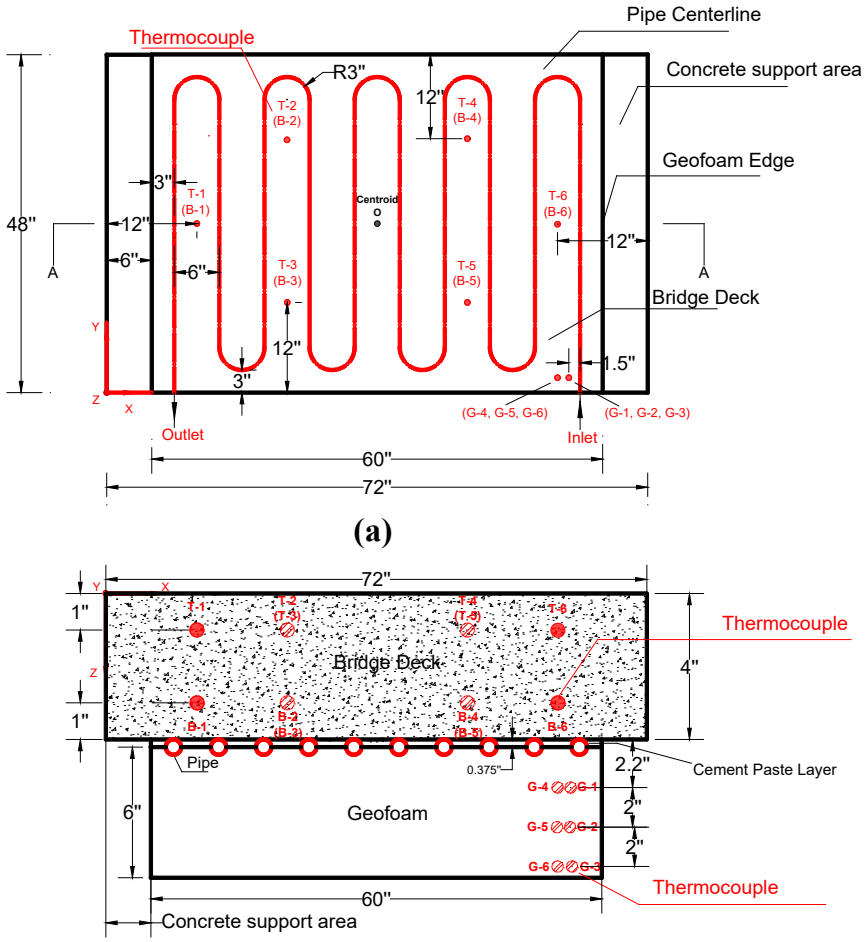

Figure 3-1. Thermocouple locations within the heated bridge deck and geofoam block: (a) Top view, (b) A-A cross-sectional view (not to scale, 1” = 2.54 cm)

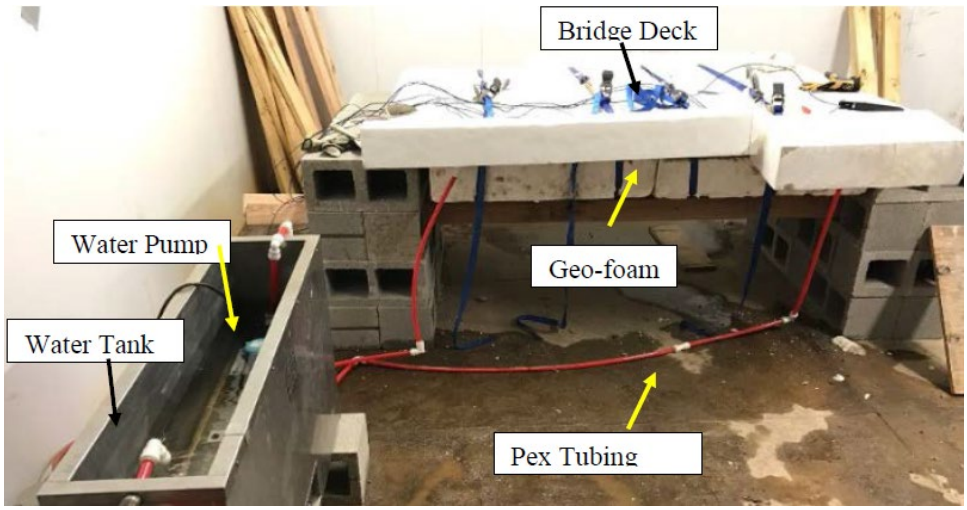

Figure 3-2. Photo of the laboratory setup for the heated bridge deck panel test inside an environmental chamber

3.2.2 Experimental Program

Sixteen (16) heating response test programs were conducted under various water and ambient temperatures to evaluate the heat transfer performance of this external design and to determine the steady-state temperature of the heated slab, as shown in Table 3-1.

The water tank in Case 1 did not supply the fluid with the temperature of 21.1°C (70 °F) to the bridge deck until the temperature of the bridge deck was in equilibrium with the freezer box temperature (ambient temperature) that was set to 4.4 °C (40 °F). Case 1, as shown in Table 1, was selected as an example to illustrate the heating test procedure. The freezer box temperature was first set to 4.4 °C (40 °F), and the concrete slab was cooled from the initial room temperature until an equilibrium with the room temperature was reached. While the concrete slab was cooling, the water tank was turned on to reach the desired water temperature of 21.1°C (70°F). When the concrete slab was cooled to the room temperature and the water tank reached 21.1°C (70°F), the water pump was turned on to circulate 21.1 °C (70 °F) water to the bridge deck. Thus, the heating test was initiated and continued until a steady-state of the concrete slab was reached. It should be

noted that Case 1 was the only case in which the heating was started with the slab at the set room temperature and water at the set temperature. For the remaining tests, the heating test was initiated when the room and water tank temperature controls were adjusted to the set temperatures, to avoid the initial equilibrium process and save time. The tests were still terminated when the slab reached a steady state. For cases 2-5, a constant ambient temperature of 4.4 °C (40 °F) was provided, and five water tank temperatures incrementally increased from 23.9 °C to 37.8 °C (75 °F to 100 °F). For cases 6-10, the ambient temperature was held constant at 45 °F, and the water tank temperature increased incrementally from 70 °F to 100 °F. Each of the two remaining test sequences, cases 11 to 13 and cases 14 to 16, included 3 sub-tests, in which the ambient temperature was respectively constant at 12.8 °C (55 °F) and 16.9 °C (62.5 °F), and the water tank temperatures of 21.1 °C (70 °F), 29.4 °C (85 °F), and 37.8 °C (100 °F) were incrementally supplied.

It was noted that due to the temperature fluctuations in the environmental chamber and the decrease of the water temperature during the transfer from the water tank to the bridge deck, the actual ambient and inlet fluid temperatures were not the same as the specific desired temperatures. They are respectively named "adj. inlet temperature" and "adj. ambient temperature" in Table 3-1. These adjusted temperatures were inputted to the COMSOL program to validate the FM model. Comparisons of the temperature responses of the experiments and numerical analyses listed in Table 3-1 are presented in detail in the next section.

Table 3-1. Test Program Summary of the Environmental and Numerical Steady-State Temperatures in Different Heating Scenarios

Test Sequence	Case	Desired Ambient – Water Temp. (°C)	Adj. of Ambient Temp. (°C)	Adj. of Inlet Temp. (°C)	Average Steady-State Temperature at 1 inch Below the Bridge Deck Surface (°C)		
					Test	FEM	Deviation
1	1	4.4(↔) – 21.1(↔)	4.4	19.7	8.2	8.3	0.1
	2	4.4(↔) – 23.9(↑)	4.4	23.0	9.3	9.0	0.3
	3	4.4(↔) – 26.7(↑)	4.7	26.6	10.1	9.7	0.4
	4	4.4(↔) – 32.2(↑)	4.2	31.8	11.2	11.1	0.1
	5	4.4(↔) – 37.8(↑)	4.7	36.9	12.6	12.4	0.2
2	6	7.2(↔) – 21.1(↓)	7.2	20.5	11.1	10.9	0.2
	7	7.2(↔) – 29.4(↑)	7.2	28.4	13.2	13.0	0.2
	8	7.2(↔) – 32.2(↑)	7.3	32.8	14.0	13.7	0.3
	9	7.2(↔) – 35(↑)	7.3	34.8	14.5	14.4	0.1
	10	7.2(↔) – 37.8(↑)	7.8	36.5	15.6	15.1	0.5
3	11	12.8(↔) – 21.1(↓)	15.6	21.1	15.1	14.8	0.3
	12	12.8(↔) – 29.4(↑)	12.5	29.5	17.3	16.9	0.4
	13	12.8(↔) – 37.8(↑)	12.6	38.6	19.1	18.9	0.2
4	14	16.7(↔) – 21.1(↓)	14.4	20.8	18.1	17.9	0.2
	15	16.7(↔) – 29.4(↑)	17.0	29.6	20.3	20.0	0.3
	16	16.7(↔) –37.8(↑)	16.9	36.2	22.4	22.1	0.3

Note: ↔ represents the constant temperature during the test, ↑ represents that the temperature increased to the temperature shown before the bracket, and ↓ represents that the temperature decreased to the temperature shown before the bracket.

3.3 Numerical Study

This section details the development of the finite element model of the externally heated bridge deck that was replicated by using COMSOL Multiphysics®, and describes the theoretical bases governing the heat transfer mechanisms. The model was validated with the corresponding laboratory heating response tests through the transient and steady-state approaches. Heat flux and energy balance analyses also are included in this section to provide a comprehensive understanding of the performance of the external heating system during heating operations. Due to the lack of experimental data under ambient temperatures below freezing temperatures in the environmental chamber, this model was employed to predict and estimate the performance of this heating system under severe winter weather conditions. The predicted results provide an approach to evaluating the interactions between thermal supplies and the system's heat transfer performance under given environmental circumstances.

3.3.1 Heat Transfer Mechanisms in an Externally Heated Bridge Deck

A comprehensive understanding of the heat transfer mechanisms in an externally heated bridge deck is crucial to creating an accurate and useful model. Many different heat transfer processes are involved in the heating and deicing of a bridge deck, as summarized in Figs. 3-3 and 4.

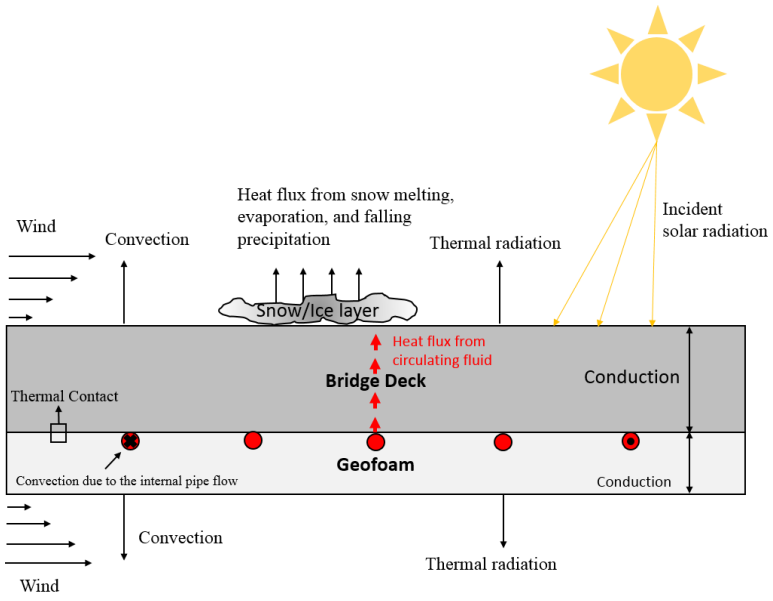

Figure 3-3. A cross-sectional view of heat transfer mechanisms in an externally heated bridge deck

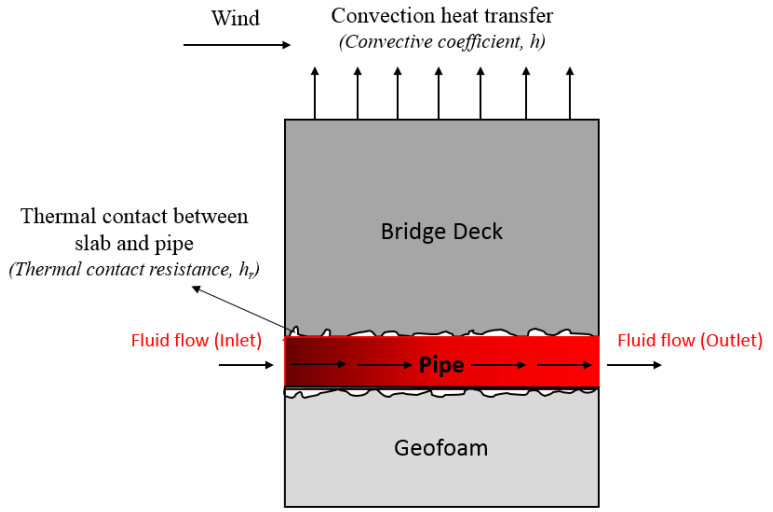

Figure 3-4. A side view of interface heat transfer in an externally heated bridge deck

The heat transfer mechanisms incorporating the conduction from the concrete slab, the phase change of water (snow melting and water evaporation), solar radiation, thermal radiation, and convective heat transfer on the surface of an internally hydronically heated bridge deck have

been detailed by a number of studies (Adlam 1950; Chapman 1952; Chen et al. 2019; Chiasson and Spitler 2001a; Kilkis 1994b; Liu et al. 2007a; Liu et al. 2007b). In externally heated bridge decks, the heating fluid supplied from an underground loop circulates inside the PEX pipe, and provides the heat sources for the bridge deck. The heat flux flows start with the circulating fluids and end at the bridge deck surface through a series of complex heat transfer mechanisms. The heat transfer processes along the path from the fluids to the bridge deck surface include fluid-solid conduction at the pipe, conduction in the pipe, thermal contact at the pipe-from-deck interface, and conduction inside the concrete. At the concrete and air interface, multiple processes occur, including convection, phase changes of ice/snow, thermal radiation, and incident solar radiation.

In solid domains consisting of the concrete slab, pipes, and geofoam block, the conductive heat transfer occurring in and between circulation tubes, the concrete slab, and the geofoam block dominates. Conduction also occurs between falling precipitation and either the bridge deck or accumulated precipitation on the bridge deck. The conduction heat transfer can be evaluated by the following equations (COMSOL 2016):

$$\rho C_p \frac{\partial T}{\partial t} + \nabla \cdot \boldsymbol{q} = Q \tag{3-1}$$

$$\boldsymbol{q} = -k \cdot \nabla T \tag{3-2}$$

Where, ρ is the solid density (kg/m^3), C_p is the solid heat capacity at constant pressure (J/(kg·K)), Q is the inner heat generation rate per volume (W/m^3), k is the solid thermal conductivity (W/(m·K) (a scalar or a tensor if the thermal conductivity is anisotropic).

Eqs. (3-1) and (3-2) assume that no heat is generated internally. When the temperature within the bridge deck no longer changes with time, the first term on the left-hand side can be negligible. A Neumann boundary condition occurs when several boundary conditions are applied

to adiabatic surfaces of the bridge deck, and there is no heat flux at such surfaces, indicating that Eq. (3-2) is equal to 0.

Based on Eq. (3-2), the conductive heat flux occurring in the tube wall can be described in the following equation:

$$q = -k\frac{\partial T}{\partial r} = \frac{k}{r\ln(r_2/r_1)}(T_{s,1} - T_{s,2}) \tag{3-3}$$

Where, k is the thermal conductivity of the pipe (W/(m·K)); r is the distance from the pipe center to the expected area within the pipe (unit: m); r_1 and r_2 are the inner and outer diameters of the pipe, respectively (m); and $T_{s,1}$ and $T_{s,2}$ are the surface temperatures at the inner and outer surfaces of the pipe (K).

Heat transfer in the water flow along the pipe can be solved by convection. The momentum and continuity equations proposed by Barnard et al. (1966) solve the fluid flow problem. For the water convection heat transfer, three contribution terms are added to Eq. (3-1) to address the fluid temperature field in terms of energy balance, as expressed in Eq. (3-4). The fluid and solid heat transfer are solved by utilizing the conjugate approach available in COMSOL.

$$\rho C_p\frac{\partial T}{\partial t} + \rho C_p\boldsymbol{u}\cdot\nabla T = \alpha_p T\left(\frac{\partial p_A}{\partial t} + \boldsymbol{u}\cdot\nabla p_A\right) + \tau : S + \nabla\cdot(k\cdot\nabla T) + Q \tag{3-4}$$

Where u is the velocity field of fluid (m/s), α_p is thermal expansion coefficient (1/K), P_A is absolute pressure (Pa), τ is viscous stress tensor (N/m^2), S is strain rate tensor (1/s). In Eq. (4), the convective contribution describing the energy transport caused by fluid motion is expressed by the second term on the left-hand side, which indicates that the convection dominates in heat transfer in a fluid. The first term on the right-hand side, viewed as a pressure work term, only needs to be considered when fluid density is temperature-dependent. The second term on the right-hand side describes the fluid heating that results from the viscous effect of fluid flow. This contribution is

remarkable only for viscous fluids with a fast flow, and is not pertinent to this study. The flow regimes, material properties, heat transfer modes, and model configurations in this equation play a considerable role in the temperature field and heat transfer in fluids (Dorfman and Renner 2009).

When two solid materials are in direct contact, heat is transferred from the hotter body to the colder one. Due to the surface roughness, gaps between the two contacting materials are usually filled with air, which has a much lower thermal conductivity than other common solid materials. Only a small portion of the apparent area has real contact between the solid spots. The conduction of heat transfer occurring in the remaining area is dominated by air, which leads to an increased temperature drop across the interface between the contacting materials, as shown in Fig. 3-5. The representation of this temperature change is viewed as thermal contact resistance, which is the inverse of thermal contact conductance. At the thermal contact interface, the thermal contact conductance h_c (W/(m^2·K)) can be utilized to evaluate the thermal contact behaviors at this interface zone. In order to obtain accurate simulation results that correspond to the experiments, the thermal contact between the top surface of the cement layer and the base of the concrete slab needs to be considered in this study.

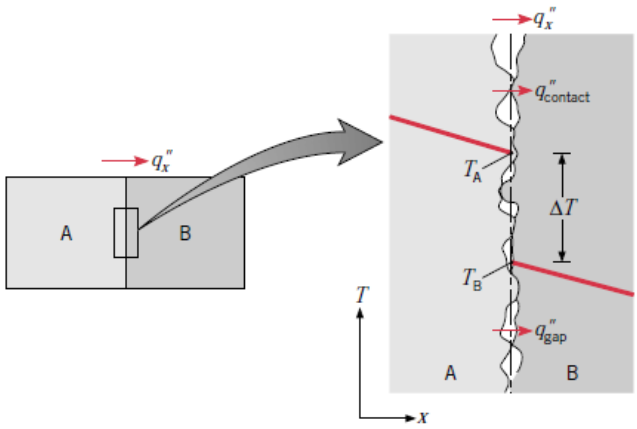

Figure 3-5. Temperature drop due to thermal contact resistance (Incropera et al. 2007)

In COMSOL, thermal contact is described by the term "micro-contact heat transfer," which includes micro-contact parameters, such as microhardness, surface roughness, surface roughness slope, the microscopic distance between mean planes, and gas rarefaction. This type of thermal contact model has been extensively studied in many studies (Fieberg and Kneer 2008; Lee et al. 1993; Liu et al. 2015; Madhusudana 1975; Vyas and Nirmal 2016). In order to simplify the micro-contact heat transfer, this study doesn't involve the microcosmic parameters mentioned above but hypothesizes that the interface between the top surface of the cement layer and the base of the concrete slab can be viewed as "pseudo-material" that has no thickness, and a much lower heat transfer efficiency than concrete and cement paste. Therefore, only the constriction conductance h_c and gap conductance h_g at the thermal contact interface mentioned in Eq. (3-5) were employed to evaluate the thermal contact feature in this study, which can be defined as inputs in COMSOL.

There are four types of convection: forced, natural, boiling, and condensation (Bowers 2016). Natural and forced convection heat transfers are needed at the bridge deck surface. Natural convection occurs because of buoyancy forces that are caused by temperature differences in the fluid. Forced convection results from external means, such as wind. All surfaces of a bridge deck experience both convection and radiation heat transfer, which is dependent on the exposure to the environment. The heat transfer equations for convection are formulated below (COMSOL 2016):

$$q_0 = h(T_{ext} - T_s) \tag{3-5}$$

$$h = \begin{cases} 2 \cdot \dfrac{k}{L} \cdot \dfrac{0.3387 Pr^{1/3} Re_L^{1/2}}{(1 + (\frac{0.0468}{Pr})^{2/3})^{1/4}} & if\ Re_L \leq 5 \cdot 10^5 \\ 2 \cdot \dfrac{k}{L} \cdot Pr^{1/3}\left(0.037 Re_L^{4/5} - 871\right) & if\ Re_L > 5 \cdot 10^5 \end{cases} \tag{3-6}$$

$$R_e = \frac{\rho u L}{\mu} \tag{3-7}$$

Where, h is convection heat transfer coefficient ($W/(m^2 \cdot K)$), T_{ext} is the external surrounding temperature (K), T is the solid surface temperature (K), k is the thermal conductivity of the fluid ($W/(m \cdot K)$), L is a characteristic linear dimension (m), P_r is the Prandtl number (for air, it is around 0.72), R_e is the Reynolds number, ρ is the fluid density (kg/m^3), u is the velocity of the fluid with respect to the object (m/s), and μ is the kinematic viscosity of the fluid (m^2/s).

In this study, external convection occurred due to the circulation of air created by a fan in the evaporator coil in the environmental chamber that simulated a bridge deck, where the airflow originates from external winds. Eq. (3-7) shows that wind velocity plays a remarkable role in the determination of the Reynolds number. By utilizing the Reynolds number as an indicator, the flow regime (laminar or turbulent flow) can be characterized in Eq. (3-6), which also indicates that a convection heat transfer coefficient is crucial for accounting for the effect of wind velocity on the temperature of the bridge deck. With the help of Eq. (3-5), the heat flux at each exposed surface of the bridge deck can be determined to carry out further heat flux analysis, based on validation of the model with experimental data.

The energy from radiation is emitted in the form of electromagnetic waves of all surfaces with a finite temperature. All surfaces of a bridge deck experience radiation heat transfer that is affected by surface emissivity and is dependent upon materials. The energy exchange, in the form of radiation, between the bridge deck and the environment can be expressed in Eq. (3-8). The simplified correlation among T_{sky}, T_{air}, and T_{dew} expressed in Eq. (3-9) was derived in Duffie and Beckmann (Duffie and Beckman 2013).

$$-\boldsymbol{n} \cdot \boldsymbol{q} = \varepsilon\sigma(T_{sky}^4 - {T_s}^4) \tag{3-8}$$

$$T_{sky} = T_{air}(0.004T_{dew} + 0.8)^{0.25} \tag{3-9}$$

Where, ε is the surface emissivity of the concrete bridge deck, whose value is 0.9 (Incropera et al. 2007); σ is the Boltzmann constant of 5.6710^{-8} W/m^2·K^4; T_{sky} is the sky temperature (K); T_s is the slab surface temperature (K); T_{air} and T_{dew} are respectively dry-bulb and dew-point temperatures (K), which are available from local weather stations.

For solar radiation, the incident heat flux can be accounted for:

$$-\boldsymbol{n} \cdot (-k\nabla T) = \alpha \cdot I \tag{3-10}$$

Where, α is the absorptivity coefficient of the concrete slab surface. Research conducted by Xiao et al. (2013) stated that the α value of a concrete slab surface ranges from 0.5 to 0.8. I is the direct radiation incident to a horizontal surface, which can change at any time. ASHRAE Handbook (2013) described how to determine the angle of incidence to a horizontal surface. In this study, the solar radiative effect is not considered, since the bridge deck was fabricated and installed in an interior chamber.

3.3.2 3D Multiphysics FEM Model of the Externally Heated Bridge Deck

A three-dimensional finite element bridge deck model was developed in COMSOL to replicate the laboratory deck in the environmental chamber shown in Figs. 3-1(a) and (b). The concrete, cement layer, geofoam, and pipe were modeled and defined as corresponding domains. The effects of rebar can be ignored, based on the FEM models of concrete slabs with and without rebars (Bowers and Olgun 2014); therefore, to increase computational efficiency, rebar was not modeled in this study. Ozudogru et al. (2014) and Bowers (2016) used a pipe flow module to evaluate the transfer of thermal energy along the pipe axis. This simplified the process, by changing the 3-D pipe model to a 1-D approximation without modeling the pipe's cross-section, but this simplification cannot be applied in numerical studies of interface heat transfer between two different material domains; nor is it available for analyzing the temperature distribution along

the radial direction of the pipe. In order to overcome these two problems, the conjugate heat transfer module was utilized in this study to couple heat transfer and fluid flow with a multiphysical interface. A transient model was employed to analyze the heating processes with the time change and steady-state model to obtain the final temperature at equilibrium state.

The heat transfer that occurs within the pipe domain plays a predominant role in the numerical analysis; therefore, a sufficiently accurate mesh is necessary. Different methods can be used to generate the mesh for the FE model. In this study, free tetrahedral mesh elements were utilized to generate the domains of concrete, cement layer, and geofoam. In order to optimize the computations, without a significant reduction of accuracy, the model used a swept mesh method with triangular elements to develop the pipe domain. The finite element mesh of the bridge deck model is presented in Figs. 3-6(a) and (b). Mesh sensitivity analysis was performed in this study to evaluate the effects of mesh quality on computational accuracy. Compared with the mesh quality shown in Figs. 3-6(a) and (b), finer mesh elements do not provide a considerable improvement of numerical results but cause a significant increase in computational time. Therefore, the “finer level” of geofoam mesh and “fine level” of the other domains were applied in this numerical study, as illustrated in Figs. 3-6(a) and (b).

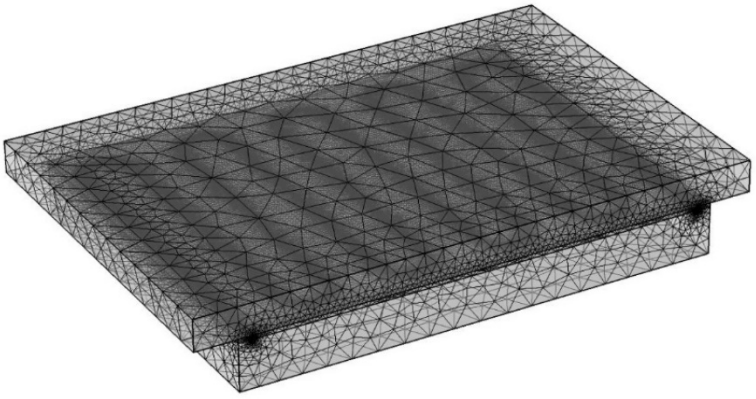

(a)

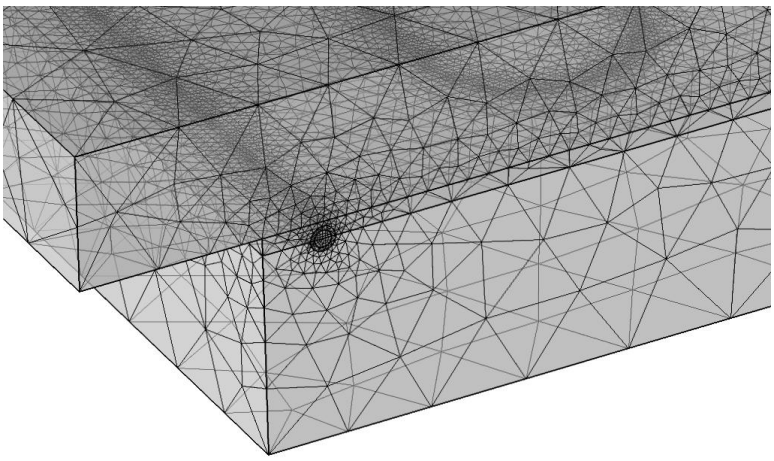

(b)

Figure 3-6. Finite element mesh of the bridge deck model: (a) Entire slab, (b) Zoom of pipe elements

3.3.3 Initial and Boundary Conditions

The adjusted inlet fluid temperatures presented in Table 3-1 are the average of the measured temperatures in the environmental chamber, and were utilized as the boundary condition of the inlet in the COMSOL model. The measured mass flow rate of 0.13 kg/s was assigned to the inlet of the PEX pipe. The initial temperature of the heated slab, including the concrete slab, geofoam, and PEX pipe, was set the same as the adjusted room temperature. In COMSOL, the module interfaces of the pipe-concrete slab, pipe-geofoam slab, and pipe-inlet fluid were set as perfect surface contacts due to the excellent bonding of these interfaces. A thermal contact was created in COMSOL to simulate the gap between the concrete bottom surface and the cement paste layer, which was evident from a thermal image study and matching of the temperature gradient, along with the deck thickness (Yu et al. 2020). The phase change of materials, such as the melting of snow and ice, was not considered in the simulated heat transfer processes. The properties of

materials adopted in the COMSOL model were determined either from previous studies (Acharya et al. 2014; Ruttanaporamakul et al. 2016; Yu et al. 2020) or the reference values provided in COMSOL (2016), and are summarized in Table 3-2.

Heat transfer processes, including conduction, convection, and radiation heat transfer, were modeled in these numerical analyses. Eq. (3-5) indicates that convection heat transfer is in proportion to the convective coefficient. The values of the convective coefficient applied at each boundary surface were estimated, based on Eqs. (3-6) and (3-7), using the corresponding properties of the materials, wind speed flowing through each surface measured in the environmental chamber, and the characteristic linear dimension. It should be noted that the characteristic linear dimension is defined as the longest side length of each boundary surface, as shown in Figs. 3-1 (a) and (b). In this study, all of the surfaces shown in Fig. 3-5 (a) were modeled with convective heat transfer, the convective coefficient of 1.4 W/(m^2·K) was selected for all exposed geofoam surfaces, and the h value of 6 W/(m^2·K) was selected for all exposed concrete and cement surfaces, except for the top deck surface. A convective coefficient of 38 W/(m^2·K) was chosen due to its direct exposure to circulation airflow and a study reported by (Chávez-Galán et al. 2014). The bottom surface seated on the CMU block was modeled identical to the side area in terms of heat loss. The above-selected h-values were verified, based on a trial and error approach, for the best match of lab measurements. As the tests were conducted inside an environmental chamber, the radiative heat losses on the model surfaces were modeled following Eqs. (3-8) and (3-9) with the sky temperature equal to the environmental chamber temperature. Eqs. (3-8) and (3-9) and the solar radiative effect determined by Eq. (3-11) are for field conditions and were not considered in this study.

Table 3-2. Summary of Properties of the Material Considered in Numerical Simulations (Acharya et al. 2014; Ruttanaporamakul et al. 2016; Yu et al. 2020)

Material	Property	Value	Unit
Water (liquid)	Dynamic viscosity	0.00273	Pa·s
	The ratio of specific heat	1.0	-
	Heat capacity at constant pressure	4180	J/(kg·K)
	Density	1000	kg/m^3
	Thermal conductivity	0.61	W/(m·K)
Concrete	Density	2300	kg/m^3
	Thermal conductivity	1.92	W/(m·K)
	Heat capacity at constant pressure	1000	J/(kg·K)
	Surface emissivity	0.91	-
Cement	Density	1860	kg/m^3
	Thermal conductivity	1.92	W/(m·K)
	Heat capacity at constant pressure	780	J/(kg·K)
PEX pipe	Density	938	kg/m^3
	Heat capacity at constant pressure	950	J/(kg·K)
	Thermal conductivity	0.51	W/(m·K)
Foam	Density	21.6	kg/m^3
	Thermal conductivity	0.035	W/(m·K)
	Heat capacity at constant pressure	1300	J/(kg·K)
	Surface emissivity	0.60	-

This section describes the simulation of the heating process for the heated bridge deck under a given inlet fluid temperature and ambient temperature. The heated slab and the ambient air were set to have the same temperature. The water flow model was initiated with the same measured temperature input at the inlet. The model was solved with a transient method, with the simulation time the same as that of the lab test. The simulated time-dependent heating curves were verified with the laboratory-measured data at the thermocouple locations. Comparisons of the temperature responses of the inlets, outlets, and ambiance for thermocouples T-1 to T-6, located 1 inch below the concrete top surface; thermocouples B-1 to B-6, located 1 inch above the concrete bottom surface; and thermocouples G-1 to G-6, installed in geofoam, are shown in Figs. 3-7 to 3-11, respectively. To validate the numerical outputs, the thermocouple locations determined in the COMSOL-Model were identical to those in the laboratory. Case 1, which has well-defined initial and final temperature conditions, was selected for model validation.

3.3.4 Transient Simulation of Slab Heating at Constant Ambient and Water Temperature and Model Validation

3.3.4.1 Comparison of Variations of Inlet, Outlet, and Ambient Temperatures

Fig. 3-7 shows the recorded and simulated temperature variations of the inlet, outlet, and ambient temperatures. Before the test was initiated, the heated bridge deck in the environmental chamber had a uniform temperature distribution of approximately 4.4 ºC (40 °F) (Fig. 3-8). During the heating process, warm water at 19.2 ºC (67.5 °F) was supplied to the bridge deck to gradually increase the temperature. The fluctuations of the inlet temperature at 19.2 ºC (67.5 °F) and ambient temperature at 40 °F may have resulted from the variations of the heat dissipation rate and performance of the heating control system in the environmental chamber. The ambient temperature was set as a constant at 4.4 ºC (40 °F) in the simulation to increase the numerical stability in

COMSOL. It was noted that the simulated inlet temperatures were in agreement with the measured data, and the COMSOL outputs of the outlet temperature were slightly larger than that of the experiments.

3.3.4.2 Comparison of Temperature Variations in the Concrete Slab

(1) Thermocouple set T-1 to T-6

Fig. 3-8 depicts the recorded and simulated temperature responses of the thermocouple set T-1 to T-6, which was installed 1 inch below the top of the concrete. The temperature response variations of experimental and numerical cases were less than 1 ºC (2 ºF) and 0.5 ºC (1 ºF), respectively, which signified a uniform heat distribution at the top surface of the concrete slab. The differences between the experimental and numerical average final temperature responses were less than 0.5 ºC (1 ºF). Nevertheless, compared to numerical outputs, the variation range of the recorded temperatures' response of T-1 to T-6 in the laboratory was larger, as shown in Fig. 8. One possible reason for this may be that the selected materials in COMSOL are viewed as perfectly homogeneous; therefore, the distribution of thermal conductivity within one material is perfectly uniform. However, due to the porosity and non-uniformity of the materials, the thermal conductivity applied to the experiments represents the general heating performance known as average thermal conductivity, which may lead to non-uniform temperature distribution during the heat transfer. In addition, the installed loop geometry deviates the design. The actual bonding of the cement and the concrete slab varies, as shown in the photo (Fig. 3-10). Details of the bonding surface and its effects are discussed in the following sections.

It was also noted that compared to the laboratory case, the thermocouple temperature increases from numerical analyses were significantly rapid during the first seven hours. The possible reasons for this include the resistance of the air gap between the cement paste and the

concrete slab, and inaccurate thermal diffusivity used in the model. Further improvements can be made by conducting more tests of the thermal properties and refining the thermal diffusivity; however, the overall accuracy of the model is satisfactory. The time required for the simulation to reach the peak temperature agreed well with the lab results, and the final steady-state temperatures of the simulation and experiment closely matched.

(2) Thermocouple Set B-1 to B-6

Fig. 3-9 illustrates the temperature increases from the initial value to the final response for thermocouple set B-1 to B-6, installed 1 inch above the concrete bottom surface, for both the experiments and numerical simulations. The final temperature responses of B-2 to B-5 from laboratory and numerical results varied from 11.1 °C to 12.2 °C (52 °F to 54 °F) and from 10.6 °C to 11.1 °C (51 °F to 52 °F), respectively. The maximum temperature deviation of B-1 to B-6 from experimental data was 1.9 °C (3.5 °F), which was much larger than that of T-1 to T-6 (0.9 °C [1.6 °F]). The temperature distribution was more uniform in the areas near the concrete top surface. Due to the closer proximity to the heat source supply, the difference in the increase of temperature between the experimental and numerical cases of B-1 to B-6 was not as significant as it was for the thermocouples installed 1 inch below the concrete top surface. As shown in Fig. 3-9, the average thermocouple temperature difference between experiments and numerical simulations was less than 1 °F, which indicates that numerical outputs can match the laboratory data. In both experiments and numerical analyses, the time required to reach the peak temperature was almost identical (about 23 hours) for thermocouples T-1 to T-6 and B-1 to B-6.

The final temperature responses of B-1 and B-6 from the experiment were lower than B-2 through B-5. This may have resulted from the poor bonding in the middle, which was due to the sagging of the geofoam that was strapped to the concrete slab. Fig. 3-10 shows the geofoam with

a cement paste layer on the top, after the heated slab was disassembled. The project's thermocouple locations are also shown in the figure. The two edges highlighted by red are the front and backside, to which additional cement paste was applied to seal the gap after the geofoam block was strapped to the slab. Extra cement was not applied to the short edges that are highlighted by blue, because they were not accessible due to the CMU blocks. This could explain the air gaps near thermocouples B-1 and B-6 and their lower temperature readings.

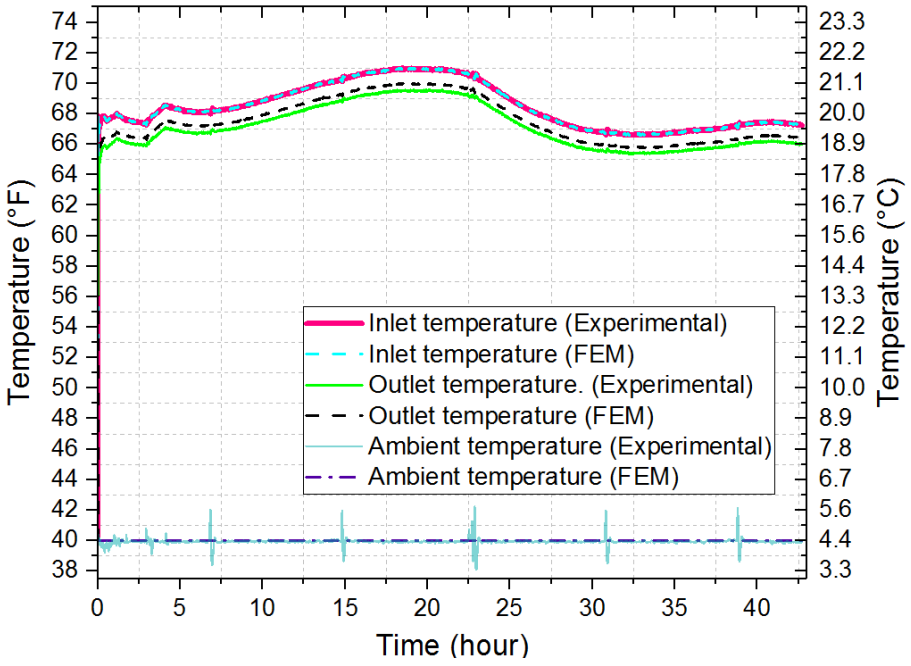

Figure 3-7. Comparisons of laboratory and numerical results of the inlet, outlet, and ambient temperatures

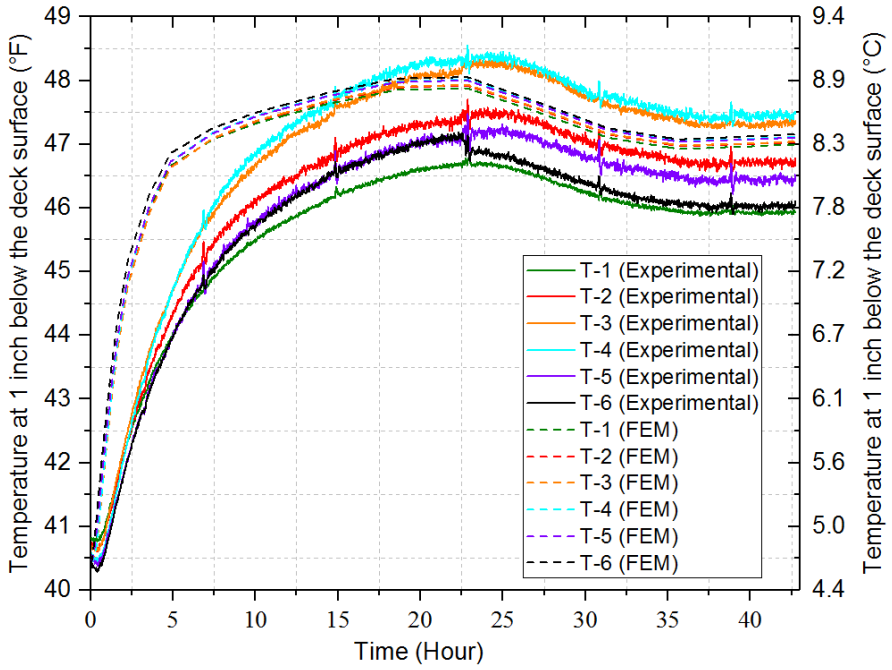

Figure 3-8. Comparison of experimental records' and numerical analyses' temperature responses for thermocouples T-1 to T-6

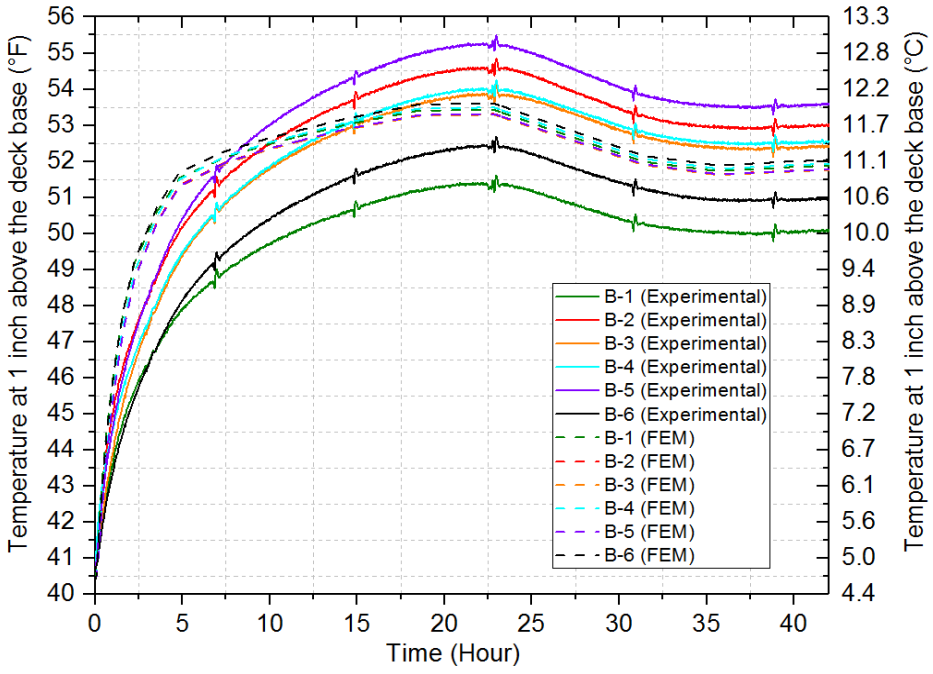

Figure 3-9. Comparison of experimental results' and numerical analyses' final temperature responses for thermocouple set B-1 to B-6

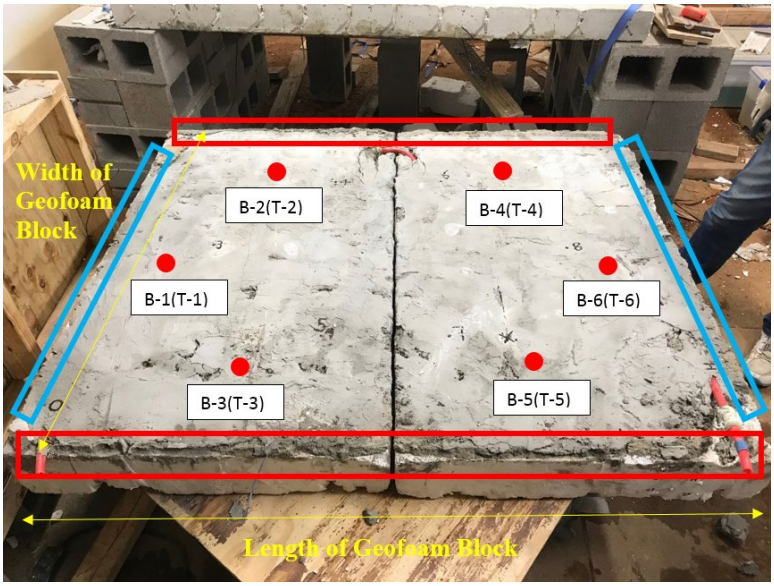

Figure 3-10. Cement mortar-bound layer after disassembly of the heated deck

3.3.4.3 Comparison of Temperature Variations for Thermocouple Set G1-G6 in Geofoam

Fig. 3-11 shows the time-dependent thermocouple temperature heating curves inside the geofoam, based on experiments and numerical analyses. The farther the thermocouple is from the heat source, the more rapidly the temperature decreases. Due to the shorter distance from the thermocouple to the circulation fluid inlet, the three final temperature responses of thermocouple set G-1 to G-3 were higher than thermocouple set G-4 to G-6. The temperatures of thermocouples G-3 and G-6, located in the outer layer, were close to the ambient temperature, which signifies that the geofoam block provides effective thermal insulation, and hinders heat loss.

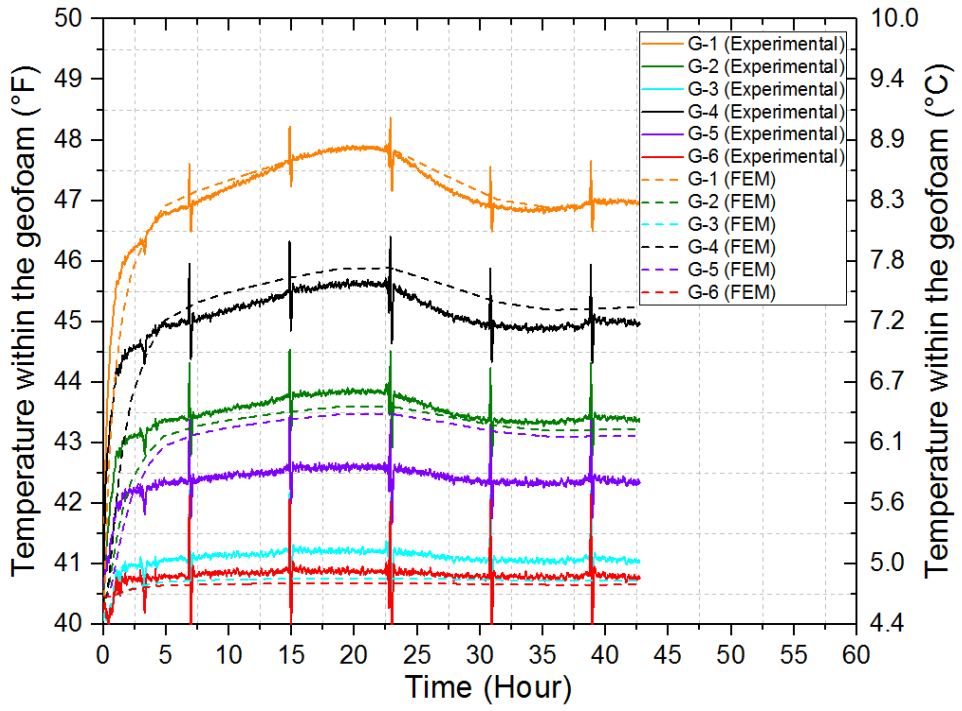

Figure 3-11. Comparison of experimental results and numerical outputs of final temperature responses for thermocouple set G-1 to G-6

3.3.5 Vertical Temperature Profile

3.3.5.1 Temperature profile comparisons between experimental records and numerical analyses, based on Case 1

Figs. 3-12 (a) and (b) illustrate the temperature profiles along the vertical path defined by the installed thermocouples that were obtained from the lab measurements and simulation counterparts. Each thermocouple location defined in COMSOL was identical to the corresponding spatial coordinates presented in Figs. 1(a) and (b). The thermocouple pairs were grouped into two sets: the middle four thermocouple pairs (2, 3, 4, and 5), as shown in Fig. 3-12 (a); and the two side thermocouples (1 and 6) and geofoam thermocouples (G-1 and 2), as shown in Fig. 3-12 (b). In general, the top thermocouples, located 1 inch below the surface, were in agreement with the measured values. The simulated temperature gradients of the middle four thermocouples were

slightly higher than the measured temperature gradients. The temperature gradients at the two side locations closely agreed with the measured values. The possible causes for the deviation of the simulation from the measurement include mismatched thermocouple locations due to installation errors, and lack of uniform bonding of the cement paste with the concrete slab. The measured temperatures had more substantial lateral variations than the simulations, particularly for the lower thermocouples in the concrete slab. The simulated temperature in the geofoam agreed well with the measured values. Despite all that, a reasonably good agreement was observed between the measured and simulated temperatures, and the temperature gradients.

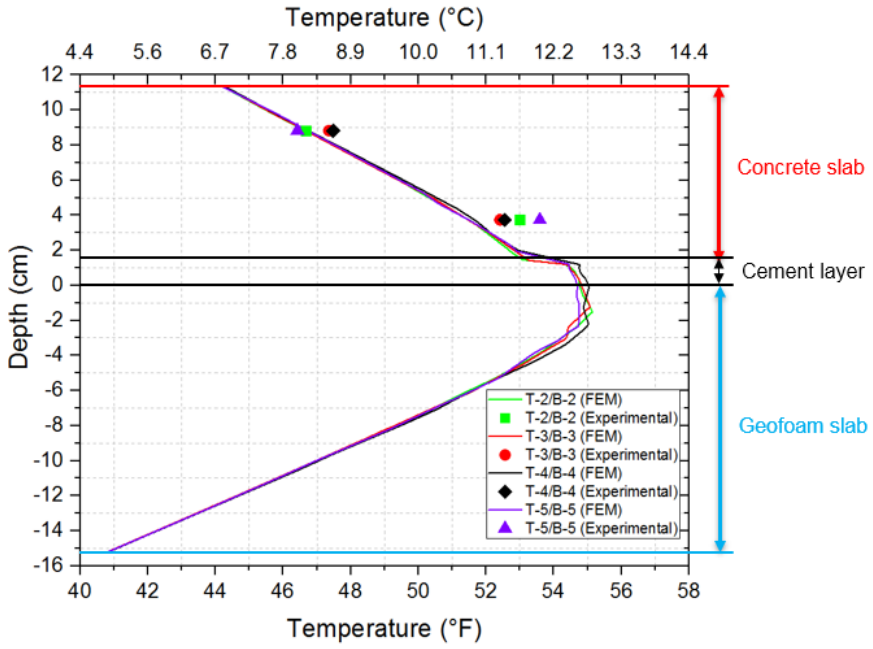

(a)

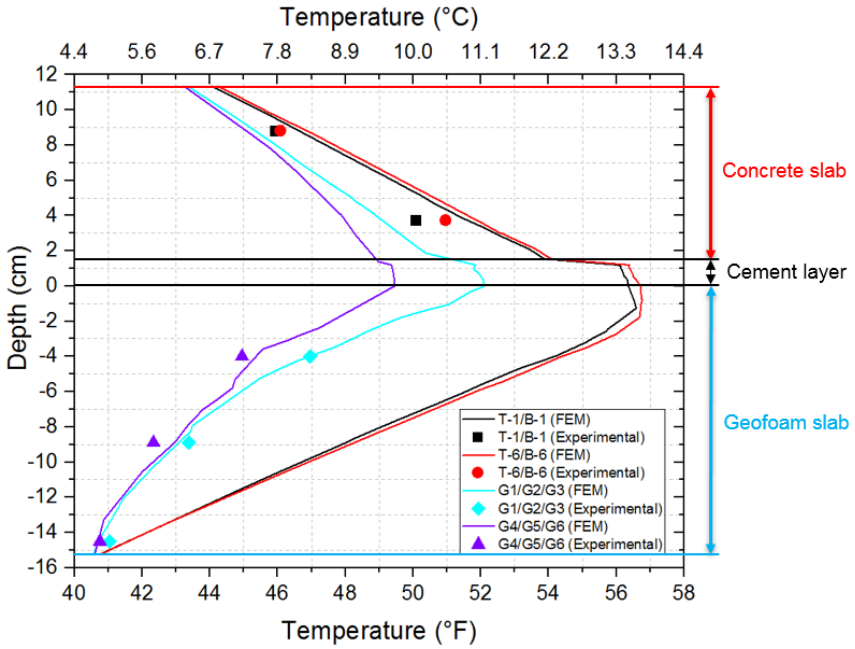

(b)

Figure 3-12. Temperature profile comparisons between experimental records and numerical analyses: (a) T-2/B-2, T-3/B-3, T-4/B-4, T-5/B-5 (b) T-1/B-1, T-6/B-6, G1/G2/G3 and G4/G5/G6

3.3.5.2 Vertical temperature profile along the vertical axis through the centroid O

Fig. 3-13 illustrates the temperature profile along the vertical axis through centroid O of the concrete slab at different chosen time intervals for Case 1 (see Fig. 3-1). The pipe centerline was located at 0 cm, i.e., the interface between the cement paste layer and the geofoam block. The temperature profiles show the heating process vertically from the PEX pipe to the top and bottom surfaces. The temperature rose much faster at the base of the bridge deck than at the top surface of the bridge deck or the bottom surface of the geofoam block. Due to the significant fluctuations of the inlet temperature during the heating test, the recorded temperature responses were not constant with time, from 15 hours to 30 hours, as shown in Figs. 3-7, 3-8, 3-9, and 3-11. After 33 hours of heating, the measured inlet temperature was approximately constant, and the temperature profiles

within the bridge deck remained the same as those after 43 hours (the end) of the heating test, which signified steady equilibrium. A sudden temperature drop occurred near 1.2 cm, the interface between the cement paste layer and the concrete slab, as the result of thermal contact. Thermal contact was essential for obtaining a close match with the measured temperatures from thermocouple group B. The optimized h_c value of 1.5 W/(m^2·K) and h_g value of 78.5 W/(m^2·K) were used for the thermal contact model in the calibrated FEM model. The temperature at the bottom of the geofoam block was approximated as the same as the ambient temperature, and indicated good thermal insulation. The top concrete surface had a final temperature response that was about 2.5 ºC (4.5 ºF) higher than the ambient temperature.

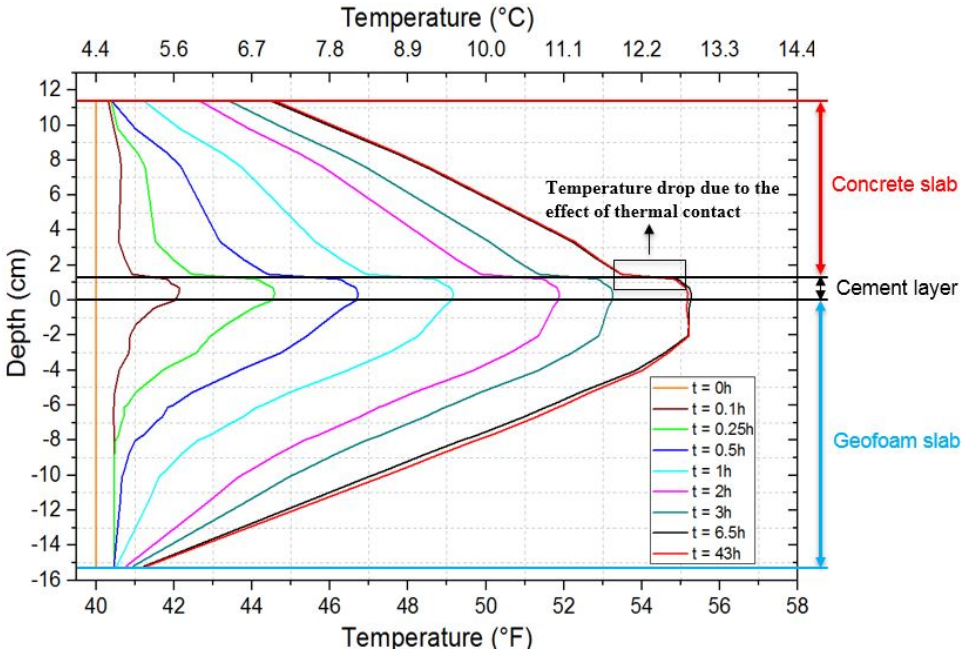

Figure 3-13. Temperature profiles along the vertical section of the centroid O of the concrete slab at different selected time intervals for simulation, based on Case 1

3.3.6 Model Error Analyses

A regression analysis was performed on the steady-state temperatures obtained from the last thermocouple readings for Case 1, as shown in Fig. 3-14. The last thermocouple temperatures were determined from Figs. 3-8, 3-9, and 3-11, at 43 hours (the final data readings), and are considered as the steady-state temperatures. The corresponding steady-state temperatures of the simulation were determined from the simulations shown in Figs. 3-8, 3-9, and 3-11 at the same time. The x-axis and y-axis are respectively represented for numerical and experimental steady-state temperatures of all thermocouples mentioned in this section (T-1 to T-6, B-1 to B-6, and G-1 to G-6). The R-square value of 0.95 was obtained for the best-fit line "y=x," which indicated a close match between the FEM results and the experimental results. It was also observed that the bottom thermocouples (B-1 to B-6) had larger variations than the thermocouples located at the top and in the geofoam. Further validation of the FEM model under different heating scenarios is presented in the following section.

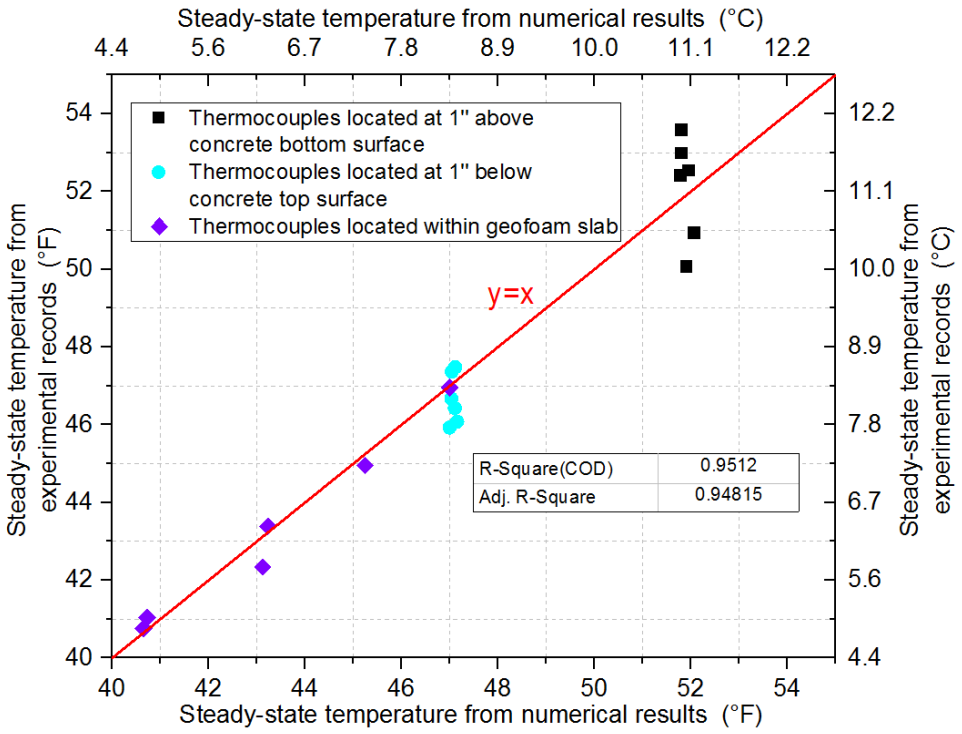

Figure 3-14. Regression analysis of the numerical model for Case 1

3.3.7 Steady-State Simulations and Verifications of Slab Heating Under Various Heating Scenarios

In order to further investigate the heating performance of the external heating system, a series of 16 heating response lab tests, including those for Case 1, were conducted under various hydronic thermal supply conditions and ambient temperatures, as shown in Table 3-1. All 16 cases were simulated with the model calibrated from Case 1, using steady-state analyses. Only the first case was simulated with transient analyses. The steady-state simulation of Case 1 agreed well with the final temperatures obtained from the transient analyses. This section compares the steady-state results obtained from the FEM with those of the lab test results.

3.3.7.1 Simulation Results and Verification

The previous section described the laboratory and numerical time-dependent temperature variations of thermocouples T-1 to T-6 that were located 1 inch below the concrete top surface,

thermocouples B-1 to B-6 located 1 inch above the concrete bottom surface, and thermocouples G-1 to G-6 installed in geofoam. This section focuses on the steady-state temperatures near the surface; therefore, only temperatures 1 inch below the concrete top surface are presented. To reduce the computational time, the steady-state simulation method was utilized in this parametric analysis.

Similar to the simulation of Case 1, adjusted ambient and inlet temperatures were used as the boundary conditions in the FEM model. A total of 16 cases were simulated, and the simulated average steady-state temperature at 2.54 cm (1 inch) below the surface is reported in Table 3-1. The simulation results and lab results are plotted in Fig. 3-15. The average temperature is the average of the temperatures at the six thermocouple locations. A close agreement was observed. It is interesting that the slopes of each of the best-fit lines were reasonably close. The surface temperature was directly proportional to the water temperature. More discussion of this plot (gridline) is presented in the next section. The differences between the lab test and the FEM results were less than 0.5 °C (1 °F).

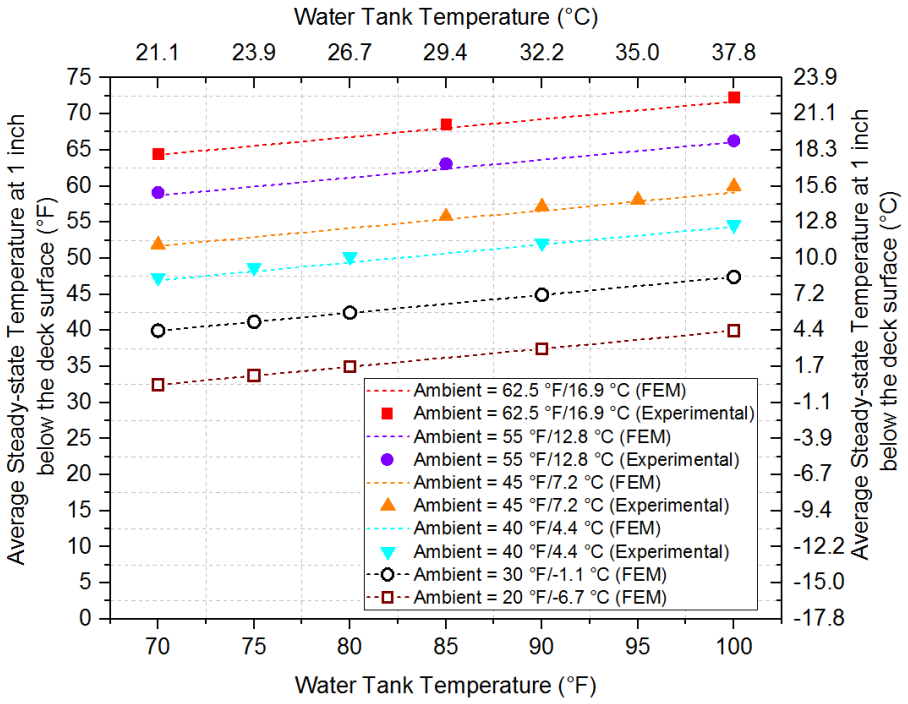

Figure 3-15. Average steady-state temperatures at 1 inch below the deck surface, based on different ambient and water tank temperatures

Fig. 3-16 illustrates the regression analysis results of steady-state temperatures derived from the experiments and numerical analyses shown in Table 1. The R-square in this analysis was 0.999, which signifies that the numerical model was validated and could be utilized to evaluate the heating performance of the external heating hydronic system.

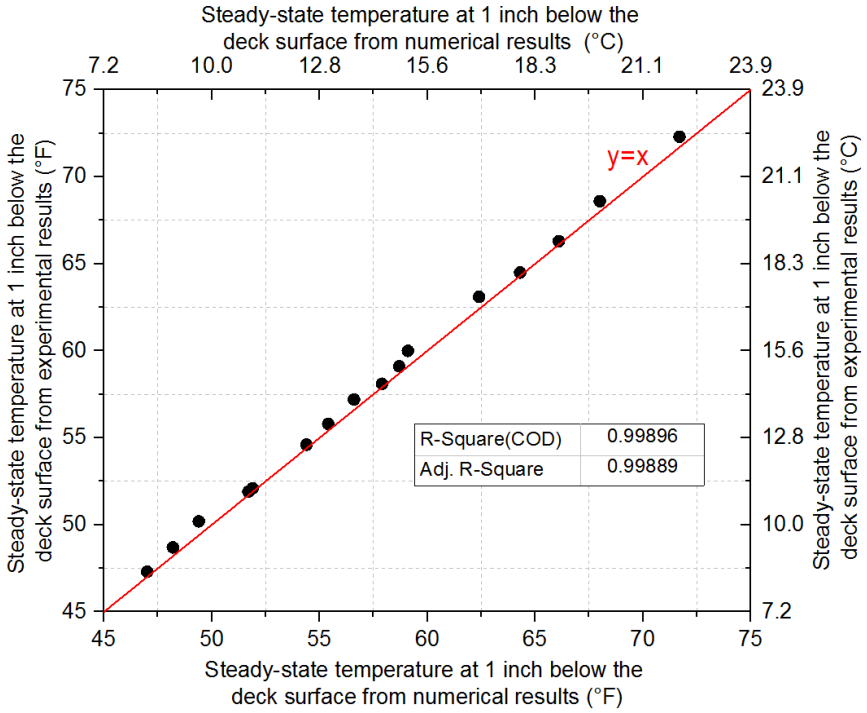

Figure 3-16. Regression analysis for the numerical model under different heating scenarios

3.3.7.2 Prediction of Steady-State Temperature Under Freezing Conditions

The slopes of the gridlines (Fig. 3-15) obtained from best-fit of the numerical simulations at ambient temperatures 4.4 °C (40 °F), 7.2 °C (45 °F), 12.8 °C (55 °F), and 16.9 °C (62.5 °F) matched those from the laboratory results. The simulations had the same slope (0.2471), regardless of the ambient temperature, which was very close to the average slopes of the experiments (0.2502). There were 4.3%, 6.5%, 2.9%, and 5.5% slope errors between the numerical and experimental cases with ambient temperatures at 4.4 °C (40 °F), 7.2 °C (45 °F), 12.8 °C (55 °F), and 16.9 °C (62.5 °F), respectively. The numerical model was validated and can be used to predict the heating performance of the hydronic external system under other environmental circumstances. Due to the limitations of the environmental chamber, experiments below 0 °C (32 °F) were not possible. Hence, in the absence of laboratory data, a series of numerical analyses with constant ambient temperatures of -6.7 °C (20 °F) and -1.1 °C (30 °F) and various heating inputs were performed to

predict and evaluate the heating performance below freezing temperatures. As is shown in Fig. 3-15, two numerical predicted gridlines, with ambient temperatures of minus 6.7 °C (20 °F) and minus 1.1 °C (30 °F), indicated that the external heating system is capable of supplying an average steady-state temperature above freezing, 1 inch below the concrete top surface when the ambient temperature and the water temperature are higher than -6.7 °C (20 °F) and 21.1 °C (70 °F), respectively.

3.3.8 Heat Flux Analysis

3.3.8.1 Line Heat Flux Supplied Along the PEX Pipe Loop

The heat supplied from the water tank to the bridge deck is calculated by using the following equation that is based on the given inlet and outlet temperatures.

$$Q_{supplied} = m \cdot c \cdot (T_{inlet} - T_{outlet}) \quad (3\text{-}11)$$

By using the measured and simulated inlet and outlet water temperatures summarized in Table 3-3, the amount of heat supplied along the length of the pipe from experiments and numerical analyses can be determined, respectively. Then, the line heat flux, which is equal to the ratio between the supplied heat and the total pipe length, can be established, as shown in Fig. 3-17. In this heat flux analysis, the ambient and inlet water temperature inputs in COMSOL were identical to the adj. temperatures recorded in experiments. The thermal load is defined as the temperature difference between inlet water and ambient temperatures. Fig. 3-17 indicates that the line heat flux from numerical analyses was directly proportional to the supplied thermal load since the R^2 of the trend line was 1. The calculated line heat flux is more scattered with much less R-value 0.8, which highlights the measurement errors caused by the thermocouple and flow meter accuracies. However, based on the data distribution presented in Fig. 3-17, the line heat flux from experimental data was still approximately proportional to the supplied thermal load, as expected. The difference

between the line heat flux obtained from COMSOL and experiments is caused by the mismatch of the outlet temperature. Although the mismatch is much smaller than 1 ºC, it is multiplied by the heat capacity. To minimize this error, thermal sensors with higher accuracy such as the PT100 sensor, are recommended for temperature measurement.

3.3.8.2 Vertical Heat Fluxes

Vertical heat fluxes can be estimated, using one-dimensional Fourier's law of heat conduction (Lienhard IV 2011), from the measured thermal gradients and thermal conductivity. Four additional thermocouples were installed on the surface of the concrete slab, directly above thermocouples T-2, T-3, T-4, and T-5, and named S-2, S-3, S-4, and S-5, respectively. These four locations provided less lateral temperature variations and were selected to determine measured heat flux. Heat fluxes at the surface were calculated as the product of thermal conductivity and the average temperature gradient determined from thermocouples pairs, i.e., T-2/S-2, T-3/S-3, T-4/S-4, T-5/S-5. The heat flux at 1 inch was calculated from the thermocouple pairs from 1 inch to 3 inches below the bridge deck surface, i.e., B-2/T-2, B-3/T-3, B-4/T-4, and B-5/T-5 (Yu et al. 2020). Only the thermal supply and environmental circumstances from cases 1, 3, 4 and 5 presented in Table 3-3 were considered in this heat flux analysis.

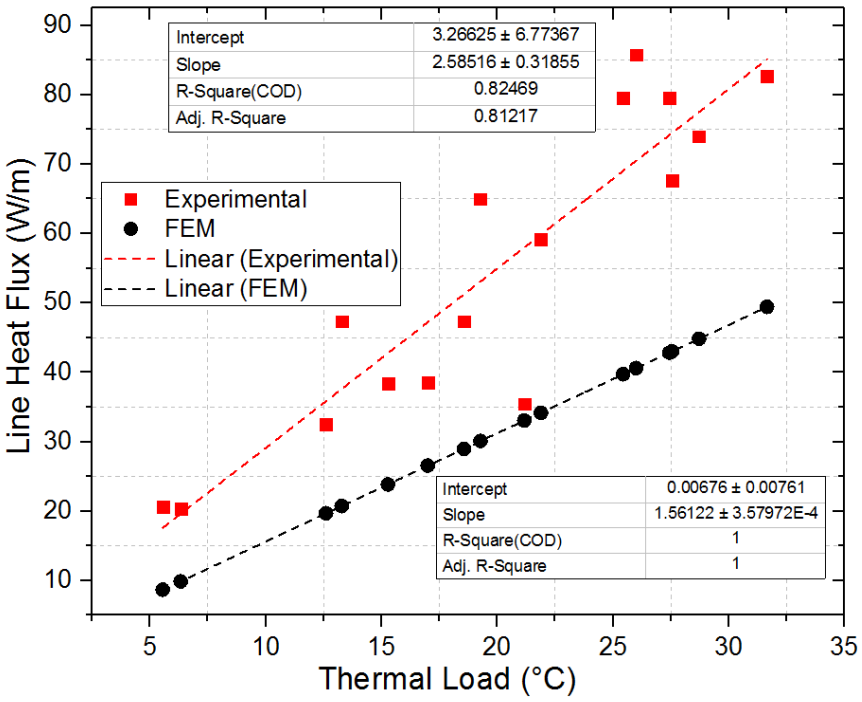

Figure 3-17. Experimental and numerical results of line heat flux along with the attached hydronic loops

Fig. 3-18 illustrates the average experimental and numerical heat flux through four thermocouples (T-2 to T-5) installed 1 inch below the concrete top surface, and the average estimated heat flux at the top surface of the concrete. The heat fluxes at these two surfaces were appropriately the same, which signifies that the heat transfer was one-dimensional upward. Figs. 3-19(a) - (d) plot the heat flux vectors at different depths. The heat fluxes gradually become more uniform and oriented upward as they approach the surface. The simulated heat fluxes along the vertical depth verify the 1-D heat transfer assumption near the surface. Fig. 3-18 also shows that the heat flux from the experimental and numerical cases, similar to that described above, was in direct proportion to the thermal load.

Table 3-3. Summary of Line Heat Flux Analyses from Experimental and Numerical Results

Case	Ambient Temp. (°C)	Experiments				Numerical Simulations			
		Inlet (°C)	Outlet (°C)	Thermal Load (°C)	Line Heat flux (W/m)	Inlet (°C)	Outlet (°C)	Thermal Load (°C)	Line Heat flux (W/m)
1	4.4	19.7	19.0	15.3	37.3	19.7	19.3	15.3	24.0
2	4.4	23.0	22.1	18.6	47.9	23.0	22.5	18.6	28.8
3	4.7	26.6	25.5	21.9	58.6	26.6	26.0	21.9	34.1
4	4.2	31.8	30.5	27.6	69.3	31.8	31.0	27.6	43.2
5	4.7	36.3	34.8	31.6	79.9	36.3	35.4	31.6	49.5
6	7.2	20.5	19.6	13.3	47.9	20.5	20.1	13.3	20.8
7	7.2	28.4	27.7	21.2	37.3	28.4	27.8	21.2	33.0
8	7.3	32.8	31.3	25.5	79.9	32.8	32.0	25.5	40.0
9	7.3	34.8	33.3	27.5	79.9	34.8	34.0	27.5	42.6
10	7.8	36.5	35.1	28.7	74.6	36.5	35.7	28.7	44.8
11	15.6	21.1	20.7	5.5	21.3	21.1	21.0	5.5	8.5
12	12.5	29.5	28.8	17.0	37.3	29.5	29.0	17.0	26.6
13	12.6	38.6	37.0	26.0	85.2	38.6	37.9	26.0	40.5
14	14.4	20.8	20.4	6.4	21.3	20.8	20.6	6.4	10.1
15	17.0	29.6	29.0	12.6	32.0	29.6	29.2	12.6	19.7
16	16.9	36.2	35.0	19.3	63.9	36.2	35.7	19.3	30.4

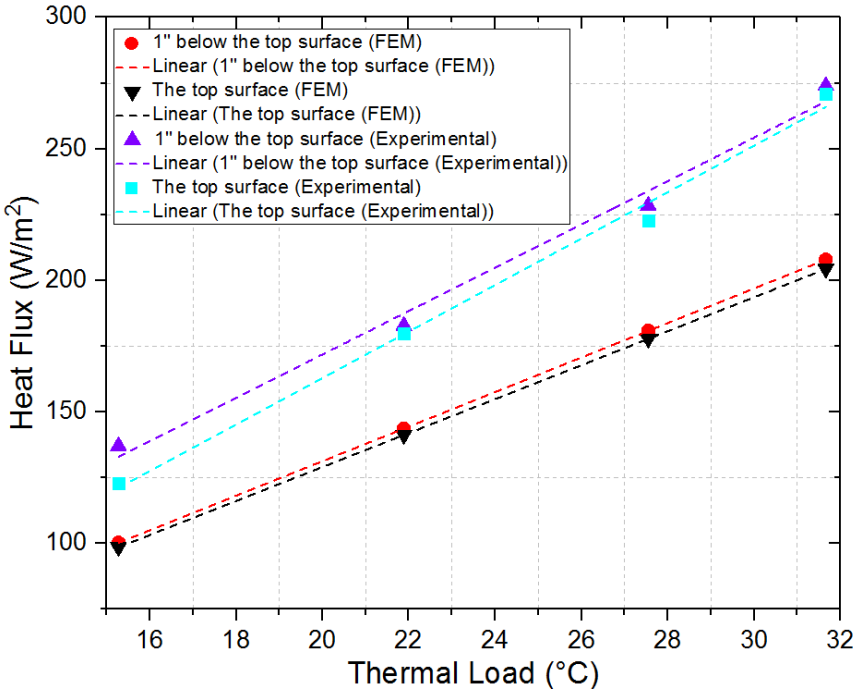

Figure 3-18. Average heat flux through four thermocouples (T-2 to T-5) installed 1 inch below the concrete's top surface, and estimated heat flux at the concrete's top surface derived from experimental data and numerical outputs

3.3.9 Numerical Energy Balance Analysis

An energy balance analysis, based on the post-processing of a series of variables involved in the energy balance equation in COMSOL, was needed to estimate the accuracy of this numerical simulation.

In the conjugate heat transfer module utilized to perform this simulation, the energy balance equation is presented in the following expression (COMSOL 2016).

$$\frac{d}{dt}\int_{\Omega} \rho E_0 dV + \int_{\partial\Omega} \boldsymbol{e}_{tot} \cdot \boldsymbol{n} dS = Q_{tot} + W_{tot} \tag{3-12}$$

Here, the first term on the left side is the accumulated energy rate; the second one is the total net energy rate, which is the integral form of total energy flux (e_{tot}). On the right side, Q_{tot} is the term of the total heat source. W_{tot}, defined as pressure work, can be neglected since the

problems of temperature-dependent fluid density and vicious effect of fluid flow aren't involved in this numerical analysis. Therefore, Eq. (3-12) can take the following form.

$$\frac{d}{dt}\int_{\Omega} \rho E_0 dV + \int_{\partial\Omega} \boldsymbol{e}_{tot} \cdot \boldsymbol{n} dS = Q_{tot} \tag{3-13}$$

In Eqs. (3-12) and (3-13), e_{tot} is defined as the total energy flux existing on all external boundaries, which can be expressed in the following equation (COMSOL 2016).

$$\boldsymbol{e}_{tot} = \rho \boldsymbol{u} E_0 - \boldsymbol{k}\boldsymbol{\nabla}\boldsymbol{T} + \boldsymbol{q}_{rad} - \sigma \boldsymbol{u} \tag{3-14}$$

Here, $E_0 = E + 1/2\mathbf{u}\cdot\mathbf{u}$ is the total internal energy. The right terms of $\rho\mathbf{u}E_0$, $-\mathbf{k}\boldsymbol{\nabla}\mathbf{T}$, and $\mathbf{q}_{rad}$ are convective, conductive, and radiative heat flux, respectively, which states that the total heat flux takes into account all three types of heat transfer modes. Two additional terms, including the convective kinetic energy, $\rho\mathbf{u}/2(\mathbf{u}\cdot\mathbf{u})$ and the convective stress energy, σu are accounted for in the total energy flux as well.

Since the stationary study was used in this numerical analysis, the accumulated energy rate vanished, as long as the steady state had been reached. Therefore, Eq. (3-13) can reduce to

$$\int_{\partial\Omega} \boldsymbol{e}_{tot} \cdot \boldsymbol{n} dS = Q_{tot} \tag{3-15}$$

In COMSOL, the term on the left side in Eq. (3-15) can be calculated by the total heat on all external boundaries, which is the sum of heat transferred to the deck surface $Q_{surface}$, heat dispersed from deck sides (including all the sides of the cement layer) Q_{sides}, and heat dispersed from geofoam Q_g, as listed in Table 3-4. The study of heat dispersed from lateral boundaries and geofoam is important for the heating performance evaluation of the real-world geothermal heated bridge deck design. The total heat source on the right side can be obtained from Eq. (3-11) and Table 3-3. Due to the disappearance of the accumulated energy rate term in the stationary study, the total net energy rate and the total heat source must balance. The numerical results for 16 cases

under different heating scenarios are shown in Fig. 3-20 and Table 3-4. The error between the total net energy rate and the total heat source is around 0.2% for each case, which signifies that the total heat dissipation occurring at all boundary surfaces of the bridge deck model created in COMSOL and the total heat source from this model match perfectly.

In order to evaluate the heating efficiency of this external system, the ratio between the total heat energy transferred to the concrete top surface and the total heat supplied along the pipe length is viewed as the heat transfer efficiency which can be determined by the following equation.

$$Heat\ Transfer\ Efficiency\ (\%), e_{heat} = \frac{Q_{Surface}}{Q_{supplied}} \tag{3-16}$$

The heat transfer efficiency for each simulated case was calculated based on the COMSOL outputs for each as shown in Table 3-4. Approximately 76% of total supplied heat is transferred to the concrete top surface, which implies that 24% of heat is dissipated along with the exterior areas of the bridge deck including the cement and deck sides and geofoam slab. Based on the experimental evaluation of heat flux at concrete top surface and total supplied heat under specific heating scenarios of case 1, 3, 4, and 5 listed in Table 3-3, the experimental heat transfer efficiencies of the bridge deck in the environmental chamber are approximately 60% (Yu et al. 2020). The discrepancy can be attributed to the poor bonding between the cement layer and the concrete slab, errors of the measured heat flux, and material uncertainties.

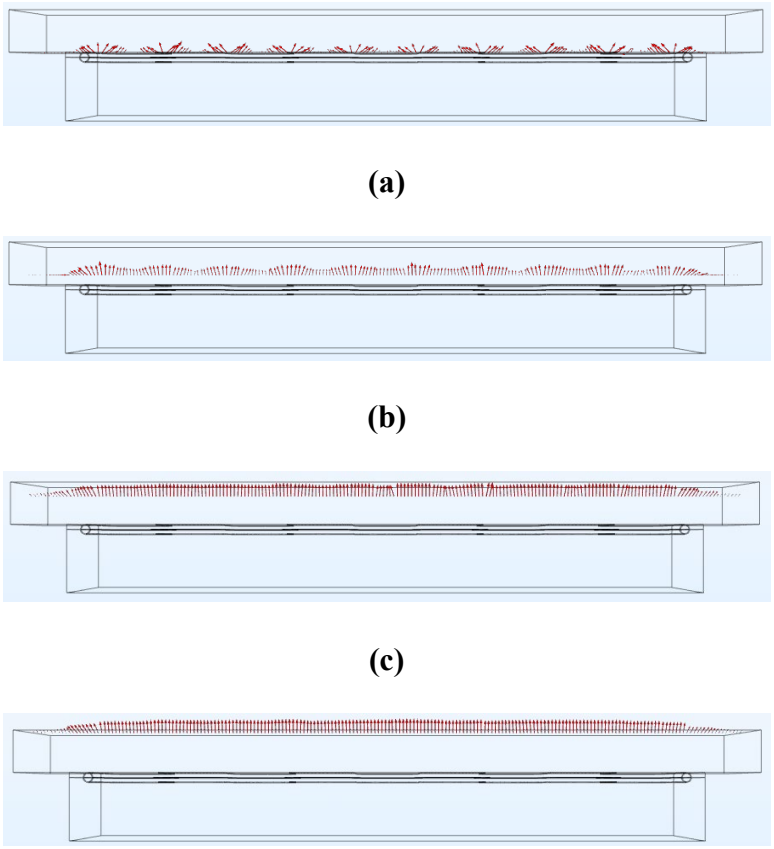

Figure 3-19. Heat flux transfer direction distribution at (a) concrete's bottom surface, (b) 1 inch above concrete's bottom surface, (c) 1 inch below concrete's top surface, and (d) concrete's top surface

Table 3-4. Summary of Numerical Energy Balance Analysis for Each Test Case

Case	Total net energy rate (W), Q_{tot}	Total heat source (W), $Q_{supplied}$	Heat transferred to the deck surface (W), $Q_{surface}$	Heat transfer efficiency (%), e_{heat}	Heat dispersed from deck sides (W), Q_{sides}	Heat dispersed from geofoam (W), Q_g	Error (%), e
1	242.8	243.3	184.8	75.96	45.5	12.5	0.21
2	294.9	295.5	224.4	75.94	55.3	15.2	0.20
3	347.9	348.5	264.8	75.98	65.2	17.9	0.17
4	437.9	438.7	333.3	75.97	82	22.6	0.18
5	503.2	504.2	383.0	75.96	94.2	26.0	0.20
6	211.1	211.5	160.6	75.93	39.5	10.9	0.19
7	336.4	337.1	256.0	75.94	63	17.4	0.21
8	404.4	405.2	307.8	75.96	75.7	20.9	0.20
9	436.2	437.1	332.0	75.96	81.7	22.5	0.21
10	456.5	457.4	347.4	75.95	85.5	23.6	0.20
11	88.4	88.6	67.2	75.85	16.6	4.6	0.23
12	270.3	270.9	205.7	75.93	50.6	14.0	0.22
13	413.4	414.2	314.6	75.95	77.4	21.4	0.19
14	100.6	100.8	76.6	75.99	18.8	5.2	0.20
15	200.6	201.0	152.6	75.92	37.5	10.4	0.20
16	306.6	307.2	233.3	75.94	57.4	15.9	0.20

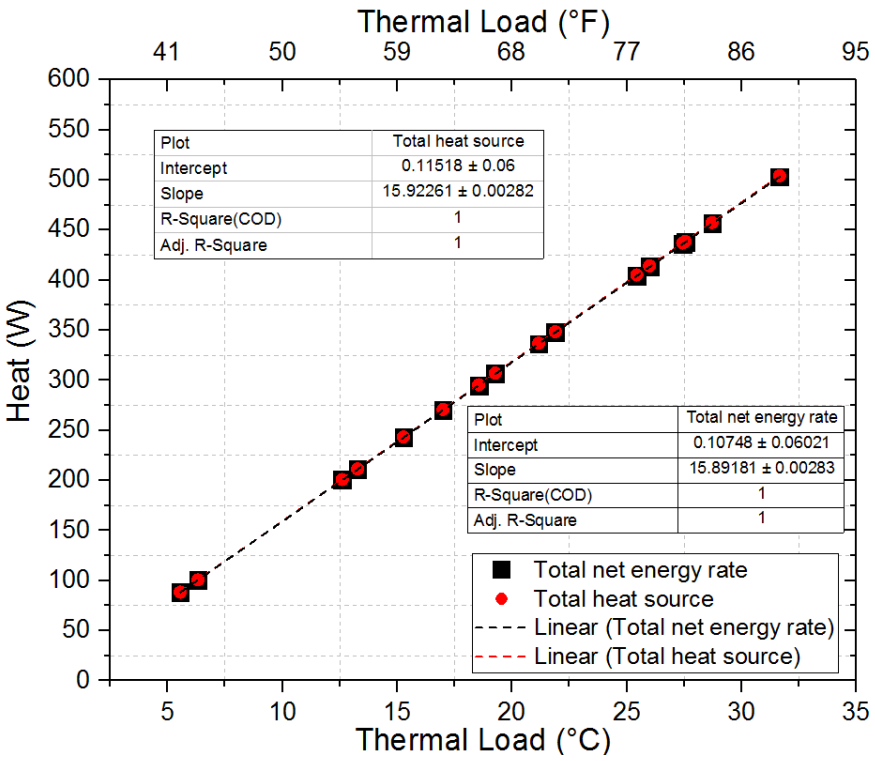

Figure 3-20. Energy balance analysis for 16 cases under different heating scenarios, based on numerical analysis

3.4 Summary and Conclusions

A 3-dimensional finite element model was created to simulate the heating tests of a newly developed externally heated hydronic bridge deck at controlled water temperatures and ambient temperatures. The complete heat transfer process in the hydronic heating system was modeled, which included coupled fluid flow and convection heat transfer, conduction from fluid to solid and solid to solid, heat loss at the air-concrete interface, and solid-solid thermal contact. The finite element model was first calibrated using transient analyses, and the results closely matched the thermocouple readings in the concrete slab, geofoam, and outlet. Then the steady-state analysis of the finite element model was performed for 16 cases, and the results were verified with their lab counterparts. The maximum error of the average simulated temperature at 2.5 cm below the deck

surface is less than 0.5 ºC. A gridline plot was presented to correlate the deck surface temperature with the supplied water temperature and ambient temperature at a steady state.

A solid-to-solid thermal contact model was created to simulate the poor cement paste-concrete slab contact with an optimized h_c value of 80 W/(m^2·K). A convective coefficient of 38 W/(m^2·K) was found to be satisfactory to estimate the convection heat loss at the slab deck surface. Simulations of the heating tests can capture the measured temperature gradient profile, and were performed under freezing ambient temperatures. They showed a relationship similar to that observed in test results of above-freezing temperatures. The bridge deck temperature is proportional to the supplied temperature of the hydronic loop and the proportion remains constant regardless of the ambient temperature. Heat flux and heat energy balance tests were also performed on the externally heated bridge deck. The heat flow close to the bridge deck surface can be assumed as a one-dimensional vertical flow with reasonable accuracy. The surface heat flux is linearly related to the temperature difference between the inlet of the hydronic loop and the ambient. Energy analyses of simulations show the heated deck had a relatively constant heating efficiency of 76% regardless of the ambient temperature, which is higher than the 60% heating efficiency obtained from lab results. The difference is attributed to the heat loss at the cement and deck interface due to their poor bonding, measurement errors, and material uncertainties. In this study, snow/ice melting processes were not considered. The fully calibrated FEM model provides calibrated heat transfer models that are needed for modeling the newly developed hydronically heated deck using attached loops. This study is the first attempt to develop a numerical tool for design analyses of hydronic bridge decks heated externally. In future laboratory tests and numerical simulations, the effects of snow, ice, and wind will be considered.

CHAPTER 4 ELEMENT-SCALE HEATING TEST TO STUDY INTERFACE HEAT TRANSFER MECHANISMS

4.1 Introduction

Two critical parameters of the heat transfer mechanism had to be determined in order to understand bridge deck heating. Experimental data was used to find the convection heat transfer coefficient h and the thermal contact conductance h_r between the concrete bottom surface and geofoam/spray top surface (external heating) or PEX pipe (internal heating). To decrease the difficulty of experimental construction and computational time in numerical analysis, two concrete blocks, one with an internal heating system and one with an external single-loop heating system, were employed to replace the previous slab-scale bridge deck model. The two internally and externally heated concrete blocks were respectively cast and fabricated in the structures lab at the University of Texas at Arlington (UTA). A series of heating response tests were performed in a freezer box that had a minimum temperature of -10 °C (15 °F), and comparative analyses were conducted of the heat transfer behaviors and efficiency of the internal and external heating designs. Two replicated experimental measurements validated the 3D FEM models of the internally and externally heated blocks developed in COMSOL Multiphysics (COMSOL 2016) through transient and steady-state approaches. A comprehensive analysis of the heat transfer mechanism, especially the two interface heat transfer mechanisms, was performed using the calibrated finite element models to obtain more accurate and reasonable numerical outputs. The updated FEM models can be viewed as novel numerical tools for predicting the heat transfer and the design of externally heated hydronic bridges.

4.2 Development of Insulated PEX Pipe Loops Adhered to Base of the Bridge Deck to Minimize Bridge Inspection Interference

The goal of this research was to develop a geothermal deicing system that can be added to existing bridges. The research team fabricated a heated concrete slab, installed hydronic heating loop panels to the slab, and tested the heated slabs inside the lab, under a controlled temperature in an environmental chamber. There was concern about the conduction of bridge inspections for such geothermally heated bridges because of the fully insulated bottom surface, and that, as well as other implementation issues, required comprehensive research. An insulated loop design was developed to refine the external heating system and to facilitate bridge inspections, and it was tested on an externally heated concrete block inside a freezer box under various environmental conditions. The internal heated block was utilized to conduct contrast experiments to compare the heating performance and efficiency of the two heating designs. This section provides a report on the development of an insulated PEX pipe loop for heated blocks installed in a freezer box.

4.2.1 Design of Insulated PEX Pipe Loops

As described in Chapter 3, hydronic loops for a heated bridge deck were attached to the bottom surface of the bridge deck with complete insulation coverage to minimize heat loss. Although the test results proved this design to be efficient for providing sufficient heat deicing, the bottom of the bridge deck was completely covered by the insulation material and was not accessible for underside bridge inspections. Therefore, a new insulation design, in which only the pipe loop was insulated, as schematically shown in Fig. 4-1(a) and (b), was employed for future analysis. A series of parametric studies were performed on the numerical 3D model, using COMSOL simulations, to determine the optimal design that would supply enough heat to the heated deck for deicing under design winter events. Results of the numerical parametric study

showed that the cross-section dimensions of the new insulated PEX pipe loops should be 6.4 cm × 9.5 cm (2.5 in. × 3.75 in.), as shown in Fig. 4-1(b). This design was intended for testing heated blocks in the freezer box. The insulated loops were fabricated in one piece to facilitate an easy installation, and the casing was made from a commercially available HDPE pipe to minimize the fabrication costs. The PEX pipe loop was secured to the aluminum heat transfer plate attached to the HDPE housing to form a confined pipe conduit for the injection of polyurethane insulation foam.

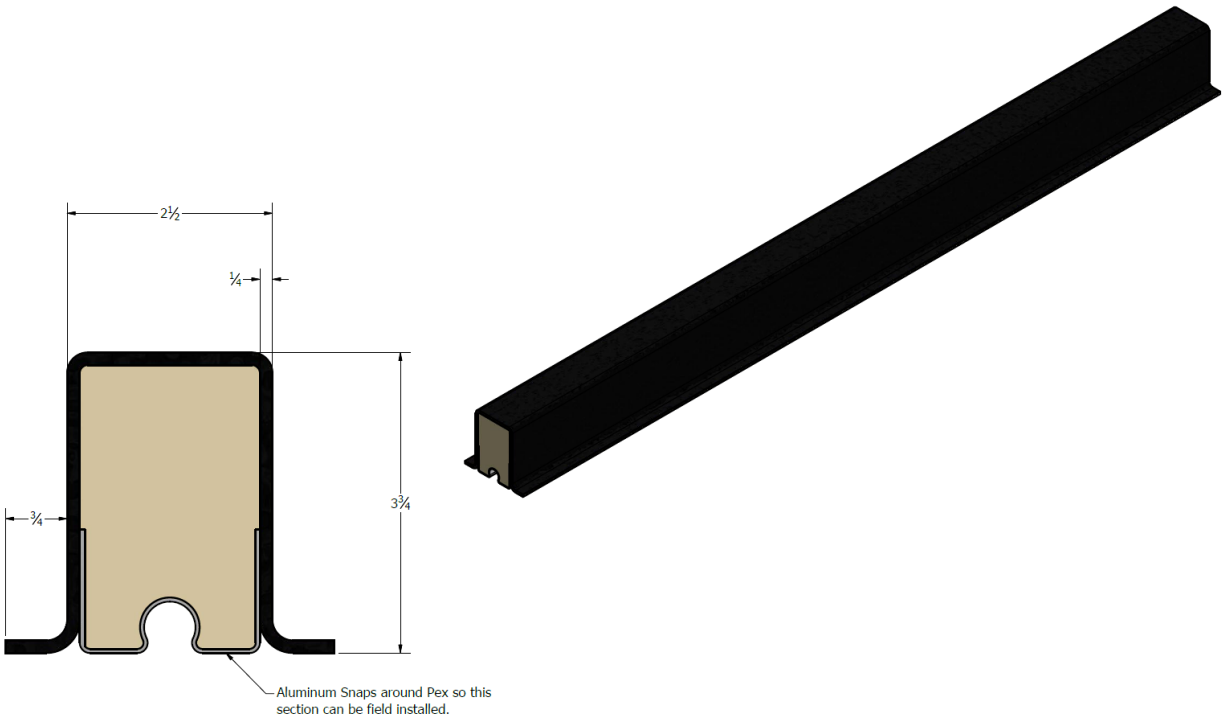

(a) **(b)**

Figure 4-1. Schematic of insulated pipe loops for externally heated bridge deck: (a) 3-D view, (b) plane view (provided by Thermador Process)

(a) **(b)**

Figure 4-2. Final product of prefabricated insulated loops: (a) aluminum pipe holder, (b) molded HDPE channel jacket

4.2.2 Insulation and Heat Transfer Enhancement

In previous tests of the heated slabs, air gaps were observed between the PEX pipe and the concrete slab that were caused by the uneven pipe and concrete interface and resulted in a drastic increase in thermal resistance and a reduction in the heat transferred to the bridge deck surface. To minimize this negative impact, an aluminum heat transfer plate with much higher thermal conductivity (237 W/m*K) than that of concrete (2.8 W/m*K) and air (0.0239 W/m*K) was applied to cover the interface between the concrete and the pipes. It was also helpful in increasing the thermal conductance at this interface and minimizing the difficulty in installing the pipe attachment. The new contact design also increased the contact area between the PEX pipe and the concrete deck, and improved the efficiency of the heat transfer. The width and thickness of the aluminum plate were 2 in. and 0.06 in., respectively.

4.3 Laboratory Setup and Testing Program of the Heated Concrete Blocks

This section presents the laboratory setup of an internally heated concrete block and a concrete block with an attached external insulated PEX pipe loop and instrumentations that were placed inside a freezer box. Heating tests were conducted on the block inside the freezer box, and the measured temperature responses within the bridge deck were used to perform a validation analysis of the FEM models developed by COMSOL that are presented in the next section.

4.3.1 Implementation of the Heated Concrete Blocks

4.3.1.1 Casting and Curing of the Concrete Blocks

Two 30.5 cm × 20.3 cm × 20.3 cm (12 in. × 8 in. × 8 in.) concrete blocks were cast with TxDOT class-S concrete mix, a commonly utilized mix in Texas, in two pre-fabricated molds. Pre-embedded thermocouples were attached on steel rods and installed at predefined locations within the molds to capture the temperature response distribution within the concrete blocks, as shown in Figs. 4-3(a) and (b). A sufficient distance between the tip of the thermocouple and the steel rods was reserved to prevent the contact. A total of 13 thermocouples were pre-embedded in each of the blocks. The instrumentation plan is depicted in Section 4.3.2. Figs. 4-4(a) and (b) depict the casting of the two concrete blocks.

(a) **(b)**

Figure 4-3. Prefabricated molds: (a) internally heated concrete block, (b) externally heated concrete block

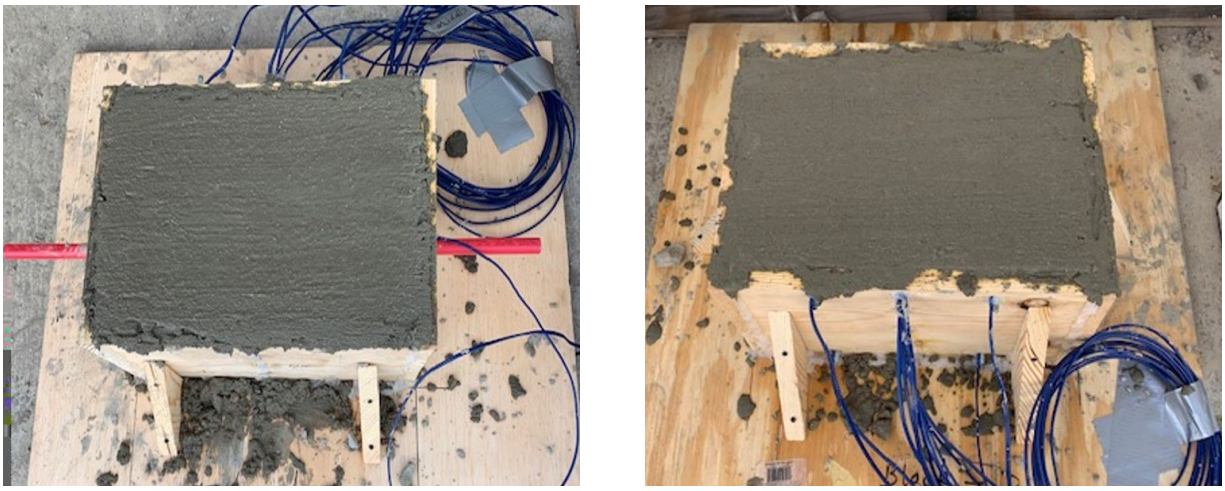

(a) **(b)**

Figure 4-4. Casting of concrete block: (a) internally heated concrete block, (b) externally heated concrete block

Both concrete blocks were placed in a curing room where the temperature and humidity were set to 25 °C (77 °F) and 100%, respectively. During the early stages of the curing, water was sprayed manually on the block's surface to minimize cracking that might occur due to hydration. After 28 days, the curing was complete and the molds were removed, as shown in Figs. 4-5(a) and (b).

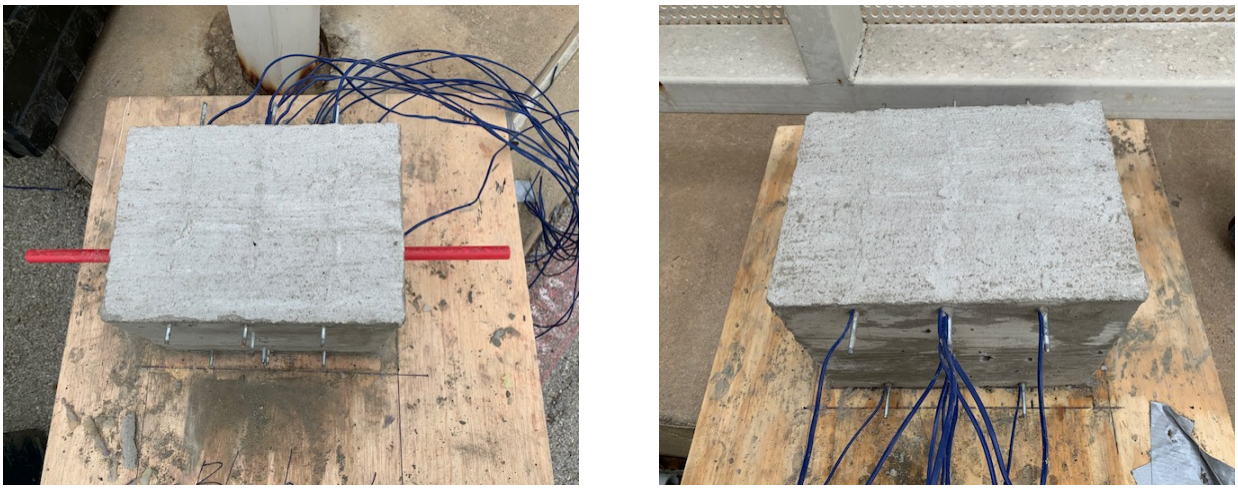

(a) **(b)**

Figure 4-5. Heated concrete blocks: (a) internal, (b) external

4.3.1.2 Installation of New Insulated PEX Pipe

The concrete block without a pre-embedded PEX pipe was selected for the installation, and the installation plan is shown in Fig. 4-6. A layer of thermally conductive paste (thermal mastic) was applied on the PEX pipe and aluminum plate to ensure proper contact with the bridge deck and higher heat transfer efficiency. The insulated PEX pipe loops were then installed to the longer centerline of the concrete block's bottom surface, using 8-10 one-inch ribbed plastic anchors and screws, as shown in Fig. 4-6.

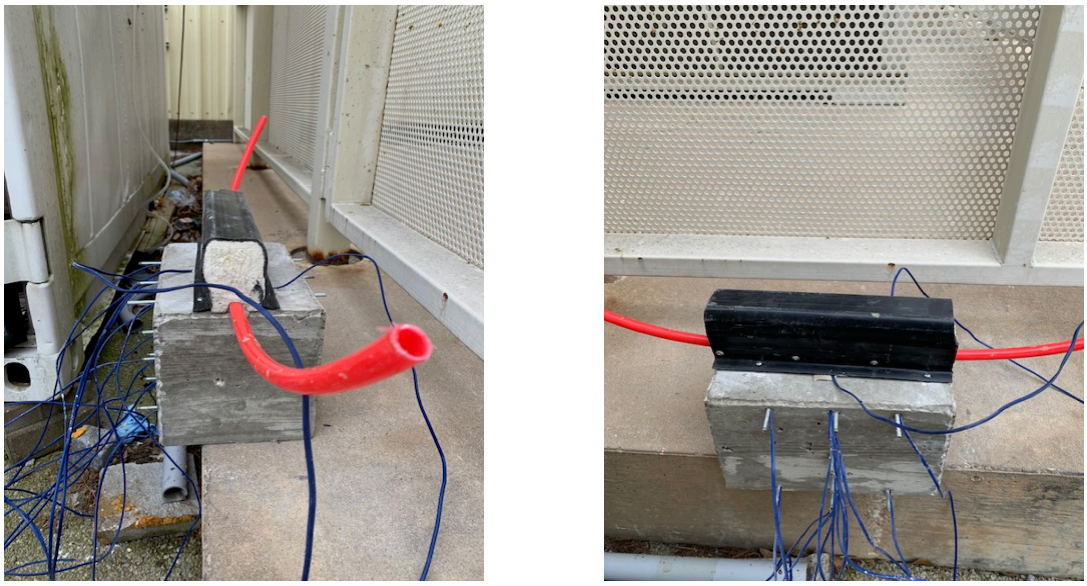

(a) **(b)**

Figure 4-6. Installation of insulated PEX Pipe on the externally heated concrete blocks: (a) front view, (b) side view

4.3.1.3 Experimental Setup of Both Internally and Externally Heated Concrete Blocks

The two pre-cast concrete blocks with TxDOT class S concrete were placed inside a freezer box that is capable of providing a constant temperature below freezing. The concrete blocks were placed on a concrete slab by using small pieces of wood and bricks. The concrete blocks were only supported at the four corners to minimize any interference on the heat transfer resulting from the contact between the bottom surface and the support materials. Figs. 4-7(a) and (b) show that the two concrete blocks were connected in series so that the supplied fluid could circulate through the two concrete blocks at an approximately constant flow rate. Two layers of fiberglass with a total thickness of 7.6 cm (3 in.) were strapped to the side surfaces of both concrete blocks to minimize the amount of heat loss attributed to convection, as shown in Fig. 4-7(b). To evaluate the performance of the insulation, two Type-T thermocouples from National Instruments were installed in the fiberglass layers of both the internally and externally heated blocks to monitor the

transient temperature responses of the insulation materials. In the externally heated concrete block, two Type-T thermocouples were attached to the PEX pipe and aluminum plate to perform the temperature measurement at the interface zone, and one thermocouple was embedded in the geofoam to evaluate the performance of the thermal insulation.

After the concrete insulation was completed, rubber self-stick pipe insulation was employed to wrap the exposed PEX pipes shown in Fig. 4-7(a) to prevent heat loss during circulation of the fluid. A water tank (PolyScience: WBE05A11B) with a 5-gallon capacity that was used as the heat source, was capable of providing a constant temperature in a range of 5 °C to 100 °C (41 to 212 °F). A hydronic water pump with a constant mass rate of 0.16 kg/s (flow rate of 2.5 gallons/min) was submerged in the water tank to connect the insulated PEX loop inlet and outlet.

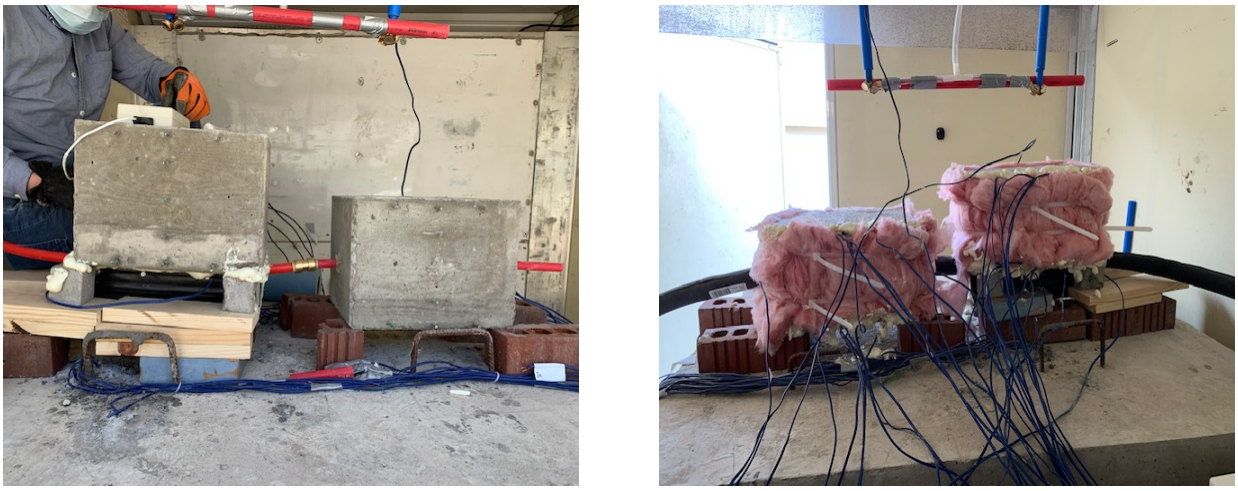

(a) **(b)**

Figure 4-7. Photos of the laboratory setup for both internally and externally heated concrete blocks: (a) before concrete insulation, (b) After concrete insulation

4.3.2 Instrumentation Plan

National Instruments provided the data acquisition system that recorded the temperature responses within both the internally and externally heated concrete blocks. Type-T thermocouples with an accuracy of +/-1 °C (2 °F) were employed to capture the temperature responses at specific locations within the blocks by thermocouple junctions. To evaluate the two blocks' heat transfer behavior, five thermocouple sets, named T1 to T5, were embedded in each of the blocks. Set T1 included five thermocouples that were installed at depths of 1.3 cm, 5.1 cm, 10.2 cm, 15.2 cm, and 19.1 cm (0.5, 2, 4, 6, and 7.5 in.), respectively, to obtain a detailed vertical temperature response profile through the centroid of the block and to evaluate the convective coefficient at the block's surface (described in Section 4.3.1.3). Two thermocouples from each set T2 to T5 were respectively embedded at depths of 1.3 cm and 19.1 cm (0.5 and 7.5 in.) and were capable of providing a general temperature distribution in the heated blocks. Two index numbers and one letter were utilized to identify the thermocouples. The two index numbers corresponded to the thermocouple set number and depth, respectively, and the letter indicated the type of block. For example, in set T1, the thermocouple embedded at a depth of 1.3 cm (0.5 in.) within the externally heated concrete block was defined as E0.5T1, with "E" representing "Externally." If it was installed in the internally heated block, I0.5T1would represent the thermocouple, with "I" representing "Internally." The thermocouples employed to measure the temperature responses of the PEX pipe, aluminum plate, and geofoam block of the externally heated block were referred to as P-1, Al-1, and G-1, respectively. The specific spatial locations of each thermocouple installed within both the externally and internally heated blocks are illustrated in Figs. 4-8 and 4-9; the origins of the coordinate systems shown in Figs. 4-8(a) and 4-9(a) are located at the top surfaces' lower-left corner. The X and Y axes are respectively along the short side and the long side of the top surface,

and the Z-axis has a negative downward trend along the blocks' depth. The inlet and outlet portions of the pipe are labeled in Figs. 4-8 and 4-9 as inlet and outlet, respectively.

In this experimental study, two data loggers, AM25T & CR1000X (Campbell Scientific) and TC-08 (PICO Technology), were utilized to acquire the temperature responses measured by the thermocouples, as respectively shown in Figs. 4-10.

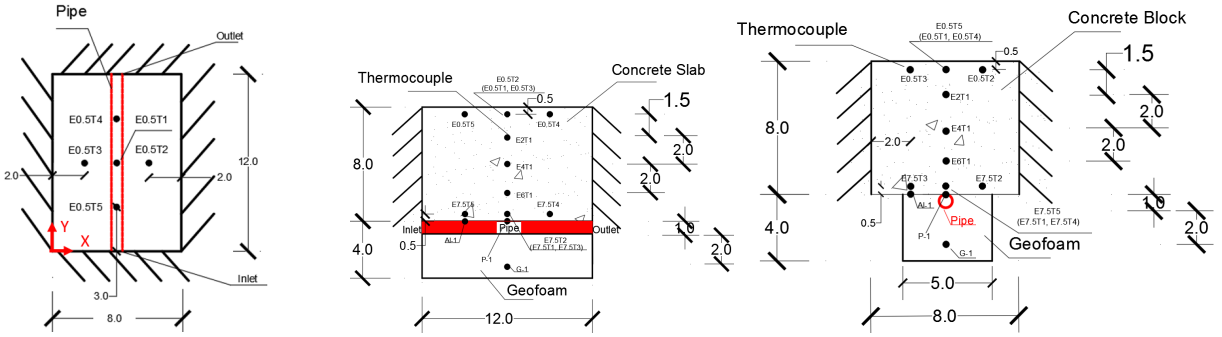

Figure 4-8. Thermocouple layout within the externally heated concrete and geofoam blocks: (a) top view, (b) side view, (c) cross-sectional view (unit: inch; 1" = 2.54 cm)

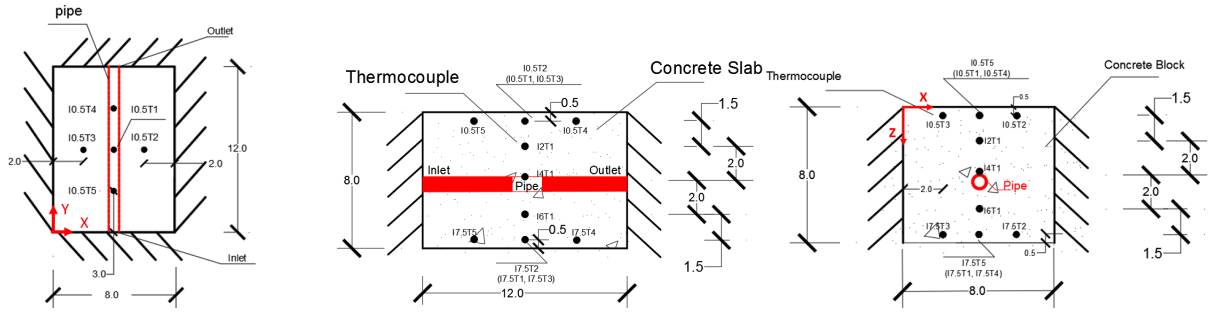

Figure 4-9. Thermocouple layout within the internally heated concrete and geofoam blocks: (a) top view, (b) side view, (c) cross-sectional view (unit: inch; 1" = 2.54 cm)

(a) **(b)** **(c)**

Figure 4-10. Data loggers involved in the study: (a) & (b) AM25T & CR1000X, (c) TC-08

4.3.3 Experimental Program

The concrete blocks were heated by supplying 40 °C (104 °F) water to the PEX pipe at two different freezer box temperatures (-3.8 °C and -6.6 °C (25 °F and 20 °F), which were chosen to respectively represent the typical and severe winter temperatures for the Dallas/Fort Worth (DFW) area in Texas. The 40 °C (104 °F) temperature represents the average temperature output from a typical geothermal heat pump.

Six heating response tests were performed with various thermal supplies and under different environmental circumstances to analyze the performance and heat transfer efficiency of the external and internal heating systems. Cases 1-3 and 4-6 were conducted at the set ambient temperatures of -3.8 ºC (25 ºF) and -6.6 ºC (20 ºF), respectively. The heating tests shown in Table 4-1 were conducted following the test procedure described below. The freezer box temperature was initially in equilibrium with the outside ambient temperature during the experimental setup, then was adjusted to -3.8 °C (25 °F). Both concrete blocks were allowed to cool from the initial freezer box temperature and reach an equilibrium with the set freezer box temperature. The water tank was turned on with a set water temperature of 40 °C (104 °F) during the phase of block cooling. It took approximately 20 minutes for the water tank to research the set temperature, and then it was on standby. When the concrete blocks were in equilibrium with the set freezer box temperature,

the water pump was turned on to supply the warm water of 40 °C (104 °F) to the blocks to initiate the heating test. The heating process was maintained until stationary temperatures of the blocks were reached under the designated ambient and inlet water temperatures. To shorten the experimental duration and prevent repeating the equilibrium process every time, only Case 1 was performed in the heating process. The blocks' initial temperatures were in equilibrium with the set room temperature -3.8 °C (25 °F). For the remaining five heating tests, the blocks were heated by adjusting the ambient and inlet water temperatures to the desired set temperatures listed in Table 4-1 to obtain the steady-state temperature for each heating scenario.

It was noted that the measured ambient and inlet water temperatures were not identical to the specific set temperatures due to the temperature fluctuations in the freezer box and an unknown error from the thermocouples. Therefore, the measured ambient and inlet water temperatures, respectively named "adj. ambient temperature " and "adj. inlet water temperature" in Table 4-1 were viewed as initial conditions to be inputted to COMSOL to perform the validation analysis of the FEM models. Comparisons of the experimental measurements' temperature responses and numerical outputs summarized in Tables 4-1 and 4-2 are presented in the next section.

4.4 Numerical Study

This section describes the development of the finite element model of both the internally and externally heated concrete blocks, using COMSOL Multiphysics®, a finite element simulation environment. Comprehensive descriptions of the heat transfer mechanisms, including the two critical interface heat transfers (the thermal contact between the PEX pipe [spray foam] and the concrete and convection between the top surface and the environment) are presented as theoretical background. The models were validated with the corresponding heating response tests through time-dependent and stationary approaches, respectively. Detailed temperature profiles were

provided to account for the temperature distribution within the concrete blocks in a vertical direction. A comparison of the heat fluxes of the experimental measurements and numerical outputs are also provided in this section. The updated FEM models can be viewed as novel numerical tools for predicting heat transfer analyses and designing externally heated hydronic bridges.

Table 4-1. Test Program Summary of Measured and Numerical Steady State Temperatures of the Externally Heated Concrete Block under Different Heating Scenarios

Temperature Response Summary (External)							
Test sequence	Case	Set ambient – water temp. (°C)	Adj. of ambient temp. (°C)	Adj. of water temp. (°C)	Average steady-state temperature at 0.5" below the block surface (°C)		
					Test	FEM	Deviation
1	1	-3.8(↔) – 40(↔)	-3.2	41.0	6.9	7.0	0.2
	2	-3.8(↔) – 30(↓)	-3.2	30.8	5.0	4.8	0.2
	3	-3.8(↔) – 18(↓)	-3.2	19.1	2.4	2.2	0..2
2	4	-6.6(↔) – 40(↑)	-6.0	41.0	5.4	5.5	0.1
	5	-6.6(↔) – 32(↓)	-6.0	33.0	3.8	3.7	0.1
	6	-6.6(↔) – 21(↓)	-6.0	22.1	1.4	1.3	0.1

Table 4-2. Test Program Summary of Measured and Numerical Steady State Temperatures of the Internally Heated Concrete Block under Different Heating Scenarios

Temperature Response Summary (Internal)							
Test sequence	Case	Set ambient – water temp. (°C)	Adj. of ambient temp. (°C)	Adj. of inlet water temp. (°C)	Average steady-state temperature at 0.5" below the block surface (°C)		
					Test	FEM	Deviation
1	1	-3.8(↔) – 40(↔)	-3.2	41.0	13.1	13.0	0.1
	2	-3.8(↔) – 30(↓)	-3.2	30.8	9.3	9.2	0.1
	3	-3.8(↔) – 18(↓)	-3.2	19.1	4.7	4.6	0.1
2	4	-6.6(↔) – 40(↑)	-6.0	41.0	11.9	12.0	0.1
	5	-6.6(↔) – 32(↓)	-6.0	33.0	8.9	8.7	0.1
	6	-6.6(↔) – 21(↓)	-6.0	22.1	4.6	4.5	0.1

Note: ↔ represents the constant temperature during the test, ↑ indicates that the temperature increased to the temperature shown before the bracket, and ↓ indicates that the temperature decreased to the temperature shown before the bracket.

4.4.1 Modeling of Heat Transfer Mechanisms

The accuracy of an externally heated bridge deck developed by numerical analysis is heavily dependent on a comprehensive understanding of the heating and deicing processes. Figs. 3-3 and 3-4 show the schematic developed by Li et al. (2020) or the heat transfer mechanisms that move the circulating fluids to the concrete block surface. These include conductive, convective, and radiative processes within the bridge deck and between the deck and the environment. A turbulence model was developed to model the coupling with the fluid flow and heat transfer in a

pipe. The thermal contact analysis and the estimate of the convective coefficient were performed to improve the interface heat transfer.

4.4.1.1 Fluid flow analysis

All fluid flow can be categorized into two broad regimes, laminar flow and turbulent flow, based on the shape and type of the streamlines. Whether laminar or turbulent, the flow regime plays a remarkable role in the design and operation of any industrial engineering endeavor related to fluid dynamics. Laminar flow, also viewed as viscous flow, is a type of fluid flow in which the particles of fluid travel through smooth paths in layers. In contrast to laminar flow, the flow of the fluid particles follows an irregular or chaotic movement. In turbulent flow, the fluid motion is not in parallel layers; therefore, a disruption exists between the layers due to high lateral mixing.

The Reynolds number, the ratio of inertial forces to viscous forces, was utilized to distinguish the flow regime, which is expressed in the following equation.

$$R_e = \frac{\rho u L}{\mu} = \frac{Inertial\ forces}{viscous\ forces} \tag{4-1}$$

Where ρ is the fluid density (kg/m^3), u is the velocity of the fluid with respect to the object (m/s), μ is the dynamic viscosity of the fluid (kg/m·s), and L is a characteristic linear dimension (m). For practical purposes, fluid motion is classified as laminar flow if the Reynolds number is less than 2000. Turbulent flow is characterized by a Reynolds number that is greater than 4000. In this study, the calculated value of the Reynolds number was 1.4×10^6. Therefore, a turbulence model was utilized to perform the numerical analysis by coupling the heat transfer module through the Multiphysics interface in COMSOL.

The following Navier-Stokes equations account for the motion of incompressible and Newtonian fluids, which can be viewed as Newton's second law of motion for fluids.

$$\rho\frac{\partial \boldsymbol{u}}{\partial t}+\rho(\boldsymbol{u}\cdot\nabla)\boldsymbol{u}=\nabla\cdot[-p\boldsymbol{I}+\mu(\nabla\boldsymbol{u}+(\nabla\boldsymbol{u})^{T})]+\boldsymbol{F} \quad (4\text{-}2)$$

$$\rho\nabla\cdot\boldsymbol{u}=0 \quad (4\text{-}3)$$

Where **u** is the fluid velocity (m/s), p is the fluid pressure (Pa), ρ is the fluid density (kg/m^3), and μ is the dynamic viscosity of the fluid (kg/m·s).

By developing a great many elements of the fluids, the turbulent flow can be simulated by Navier-Stokes equations (Eq. (4-2)), which are capable of capturing the wide-scale fluid motion. In Eq. 4-2, the sum of the two terms on the left-hand side represents the inertial forces. The first and second term on the right-hand side formulate the viscous forces and the external forces applied to the fluid, respectively.

Eq. (4-2) is always solved with the continuity equation (Eq. (4-3). The Navier-Stokes equations (Eq. (4-2)) and continuity equation (Eq. (4-3)) express the conservation of momentum and mass, respectively.

There are many cases in engineering applications where the inertial forces are much greater than the viscous forces, i.e., the Reynolds number is very high. The solutions of such transient turbulent flow problems related to the size of the smallest eddies are heavily dependent on the quality of the fluid domains' mesh. However, most current computers are unable to complete the numerical simulation by using Navier-Stokes equations. Consequently, an updated Reynolds-averaged Navier-Stokes (RANS) expression of the Navier-Stokes equations, obtained by averaging the velocity and pressure fields in time, was inputted in COMSOL to develop the turbulence models, as formulated in the following equation:

$$\rho\frac{\partial \boldsymbol{U}}{\partial t}+\rho(\boldsymbol{U}\cdot\nabla)\boldsymbol{U}=\nabla\cdot[-P\boldsymbol{I}+(\mu+\mu_{T})\cdot(\nabla\mathbf{U}+(\nabla\mathbf{U})^{T})]+\boldsymbol{F} \quad (4\text{-}4)$$

Where, **U** and P are the time-averaged velocity and pressure, respectively. The term μ_T represents the turbulent viscosity, which can be estimated by the turbulence models. Eq. (4-4) accounts for the effect of the viscous stress tensor in a turbulent regime. Total of four turbulence models, including algebraic yPlus, L-VEL, k-ε, and low Reynolds number k-ε, are available for analysis of the turbulent flow. The k-ε turbulence model is one of the most common turbulent interfaces in industrial applications because it is stable and an easy model to solve with reasonable accuracy. However, its use is limited by its computationally expensive process. In this study, a detailed analysis of fluid flow in a pipe was not the primary major concern of the FEM model. Instead, the focus was on the heat transfer mechanisms within the concrete blocks and between the blocks and environment. Therefore, the algebraic yPlus turbulence model with the cheapest computational expense and good approximations for internal flow was selected as the fluid flow model to perform the numerical analysis. It should be noted, however, that it is not as computationally accurate as the k-ε turbulence model.

4.4.1.2 Thermal Contact Analysis

When heat flows transfer across a contact interface between any two solid materials, a considerable temperature drop can usually be measured in the region due to thermal resistance to the heat transfer. For two solid bodies in contact with each other, the contact interface is mostly filled with air since many rough elements existing on the material surfaces keep the interface separated, as shown in Fig. 4-10. A thermal contact model must be considered as a design factor if the air has a considerably lower thermal conductivity than the contact materials. In this heat transfer study, thermal contact conductance h_c ($W/(m^2 \cdot K)$) was viewed as an essential factor in specifying the heat transfer performance under consideration of the thermal contact model, which is the inverse of thermal contact. The thermal contact model developed in this numerical study

accounts for the significant variations of heat transfer behaviors between the concrete and PEX pipe to reach a reasonable agreement between numerical outputs and experimental measurements for both internally and externally heated blocks.

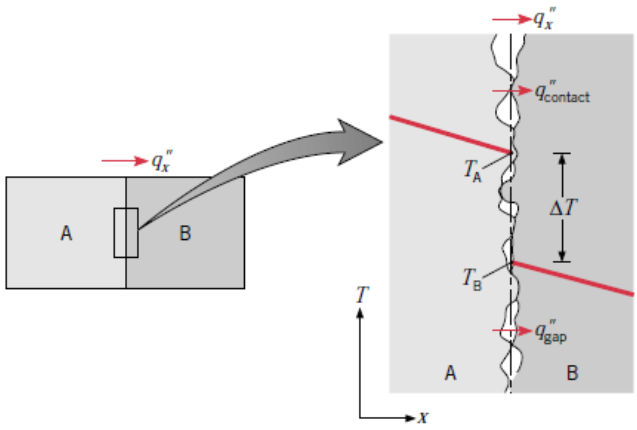

Figure 4-11. Temperature drop due to thermal contact resistance (Incropera et al. 2007)

Many studies have provided a comprehensive understanding of thermal contact theory (Fieberg and Kneer 2008; Lee et al. 1993; Liu et al. 2015; Madhusudana 1975; Vyas and Nirmal 2016). A series of parameters, including surface morphology, gas rarefaction, thermal interface material, the microscopic distance between mean planes, and material hardness, have critical influences on thermal contact conductance and were utilized to develop and specify the thermal contact model in terms of "micro-contact heat transfer" in COMSOL. However, it is very difficult, or even impossible, to accurately measure the parameters mentioned above in laboratory tests. Therefore, a newly hypothesized thermal contact model was developed that simplifies the micro-contact heat transfer and specifies the gaps between the concrete and the PEX pipe, where a "pseudo-material" has no thickness and a much worse heat transfer performance. Compared to the external heating system, the thermal contact conductance h_t utilized in an internally heated block was greater than that of an external heating system, due to the stronger binding conditions between the concrete and PEX the pipe. It should be noted that this study is the first attempt ever made to

develop a thermal contact model for an internal heating system that can improve the accuracy of numerical analyses and obtain a more reasonable match with experimental measurements. Based on a trial and error approach, the optimized h_c values for internally (183) (W/(m^2·K)) and externally (122) (W/(m^2·K)) heating systems were respectively validated for the best agreement with experimental results. The selected values of thermal contact conductance were inputted in COMSOL to evaluate the interface heat transfer mechanisms.

4.4.1.3 Calculation of Convective Coefficient

Previous research works performed to estimate the convective heat transfer coefficient were classified into three groups: heat plates (Sartori 2006), flat plate solar collectors (Sharples and Charlesworth 1998), and buildings (Chávez-Galán et al. 2014). Lienhard IV (2011) espoused that some of the factors, including the physical properties of the fluid flowing to the surface, the surface conditions and configuration, the velocity and direction of the flowing fluid, and the difference between the flowing fluid and surface temperature, play dominant roles in estimating the h value. Experimental analysis is the method most commonly used to evaluate the h value of the heat transfer mechanism for complex surface geometries with satisfactory accuracy.

In this study, the h value was estimated based on steady state laboratory data acquired by thermocouple sets E0.5T1 to E7.5T1 (externally heated block) and I0.5T1 To I7.5T1 (internally heated block), as shown in Figs. 4-8 and 4-9. The heat transfer within the concrete blocks was simplified to a one-dimensional model, as shown in Fig. 4.12. The finite difference method (FDM) was utilized to derive the equation for calculating the convective coefficient h at the block surface, as expressed in Eq. (4-5), that was fully calibrated by Lei et al. (2020). Thus, the h value for each test that can be calculated as listed in Table 4-3.

$$h = \frac{12152.86T_5 - 110.24T_4}{(273.15 - T_{ambient}) \times 110.24 + 110.24T_4 - 220.4T_5} \quad (4\text{-}5)$$

Where, $T_{ambient}$ is the measured ambient temperature. T_4 and T_5 are the corresponding measured thermocouple temperatures within the concrete blocks.

Table 4-3. Calculated Convective Coefficients at the Top Surface Utilized in COMSOL

Test sequence	Case	Measured ambient temp. (°C)	Measured water temp. (°C)	Calculated h value
1	1	-3.2	41.0	18.74
	2	-3.2	30.8	17.37
	3	-3.2	19.1	17.56
2	4	-6.0	41.0	17.13
	5	-6.0	33.0	17.17
	6	-6.0	22.1	16.47

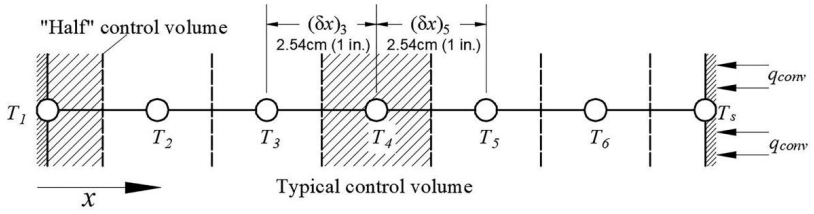

Figure 4-12. Schematic of a 1D heat conduction with uniform control volumes

4.4.2 Development of Finite Element Models

Two three-dimensional finite element models were created in COMSOL to replicate the internally and externally heated concrete blocks that were tested in the freezer box (Figs. 4-13). Based on Bowers and Olgun's (2014) contributions, the effects of rebar can be ignored; therefore, to increase computational efficiency, the embedded steel rods were not modeled in this study. The concrete, aluminum plate, geofoam, and PEX pipe of the externally heated block were modeled and defined as corresponding domains. For the internal block, only the concrete and PEX pipes

were developed as solid domains. To investigate the interface heat transfer mechanisms between the different material domains and the radial temperature distribution of the PEX pipe, the conjugate heat transfer module with a turbulence model was utilized in this study to couple the heat transfer and the fluid flow with a Multiphysics interface. Time-dependent and stationary models were respectively employed to simulate the transient heating processes and to acquire the final temperature responses at a steady state.

Sufficiently accurate mesh elements are crucial for FEM analysis of the heat transfer that occurs within concrete blocks and between the surrounding environment. In this study, the free tetrahedral mesh method was employed to develop concrete, aluminum plate, and geofoam domains. The domain of the PEX pipe was generated by a swept mesh method. A mesh sensitivity analysis was conducted to obtain an optimized balance between the computational expense and accuracy. Figs. 4-13 presents the developed finite element mesh for both internally and externally heated block models. The mesh elements with a fine level were utilized to generate the domains of concrete and geofoam. The other domains, including the aluminum plate and the PEX pipe, were developed by mesh elements with a finer level since they were associated with interface heat transfer mechanisms. A better quality of finite element mesh at the interface zone is necessary for improving computational accuracy.

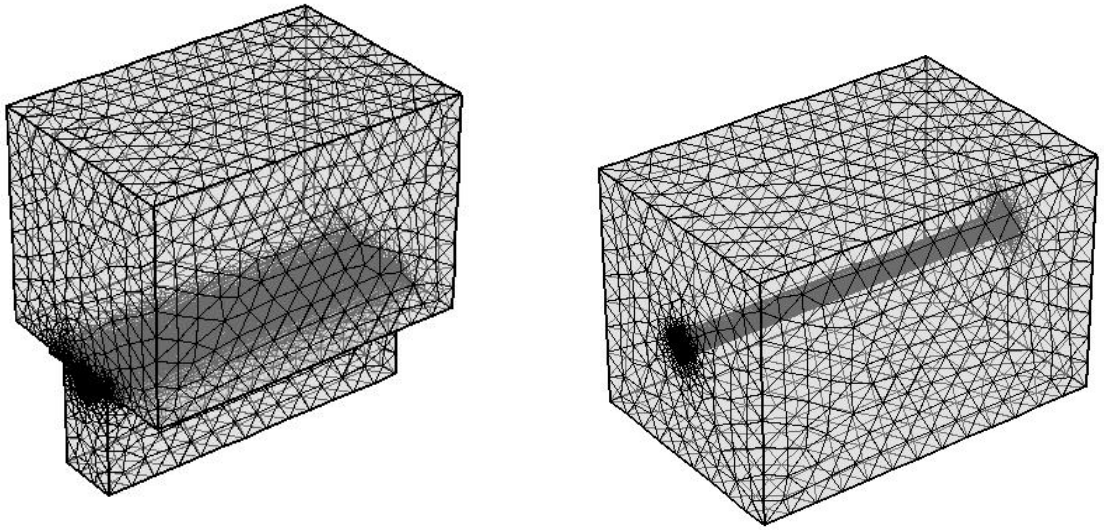

(a) **(b)**

Figure 4-13. Finite element mesh of the finite element models: (a) internally heated block, (b) externally heated block

4.4.3 Initial and Boundary Conditions

The adjusted inlet water temperature responses listed in Table 4-1 were utilized as an inlet boundary condition to be interpolated in COMSOL. In this study, the fluid flow regime in the pipe flow module was turbulent since the Nusselt number calculated by Eq. (4-1) was greater than 4000. Therefore, the turbulence model was selected to couple with the heat transfer module to perform the conjugate heat transfer mechanisms. The adjusted ambient temperatures depicted in Tables 4-1 and 4-2 were set as the initial temperatures for the heated concrete blocks incorporated in the concrete, geofoam, aluminum plate, and hydronic loops and indicate that a state of temperature was reached between the concrete blocks and the interior of the freezer box before the numerical investigation was initiated. For the externally heated block, a thermal contact model was utilized to develop the gaps between the concrete bottom surface and geofoam top surface to account for the interface zone's thermal contact feature. Based on the research method proposed by Li et al. (2020) the optimized h_c value of 122 W/(m^2·K) was used for the thermal contact model. For the

internally heated block, the optimized value of the hc value of 184 W/(m2·K) was greater than that of the external one since the binding between the pipe and the concrete in the internal heating design was much better than that of the external one. The phase change of materials, consisting of snow and ice melting, is described in Section 4.6. To decrease the computational expense, module interfaces incorporated in the pipe-concrete slab and pipe-geofoam slab were set as perfect surface contacts. The properties of the materials utilized in the COMSOL model were determined either from previous studies (Acharya et al. 2014; Ruttanaporamakul et al. 2016; Yu et al. 2020) or from the reference values in COMSOL (2016) that are listed in Table 4-3.

Heat transfer processes, including conduction, convection, and radiation heat transfers, were developed in COMSOL. The conductive heat transfer within the solid domains is dependent on the thermal conductivity of utilized materials, as presented in Table 4-3. All of the surfaces, except those of the four insulated side surfaces of the concrete blocks shown in Fig. 4-13 (a) and (b), were modeled with convective heat transfer. The convective coefficient at the top surface utilized in COMSOL was based on the calculation results summarized in Table 4-2. The convective coefficient of 10 W/(m^2·K) was selected for all of the exposed geofoam surfaces, and the h value of 3 W/(m^2·K) was chosen for the two concrete bottom surfaces. Radiative heat transfer was modeled through a boundary condition of diffused surface to all of the exposed surfaces with the different surface emissivity of utilized materials, as shown in Table 4-4. It was noted that the sky temperature associated with radiative heat transfer was defined as the adjusted ambient temperature since the concrete blocks were tested in an interior freezer box. The solar radiative effect was not considered for the same reason.

Table 4-4 Summary of Properties of the Materials Considered in Numerical Simulations (Acharya et al. 2014; Ruttanaporamakul et al. 2016; Yu et al. 2020)

Material	Property	Value	Unit
Water (liquid)	Dynamic viscosity	0.00273	Pa·s
	The ratio of specific heat	1.0	-
	Heat capacity at constant pressure	4180	J/(kg·K)
	Density	1000	kg/m^3
	Thermal conductivity	0.61	W/(m·K)
Concrete	Density	2300	kg/m^3
	Thermal conductivity	2.8	W/(m·K)
	Heat capacity at constant pressure	900	J/(kg·K)
	Surface emissivity	0.91	-
PEX pipe	Density	938	kg/m^3
	Heat capacity at constant pressure	950	J/(kg·K)
	Thermal conductivity	0.51	W/(m·K)
Geofoam	Density	21.6	kg/m^3
	Thermal conductivity	0.028	W/(m·K)
	Heat capacity at constant pressure	1300	J/(kg·K)
	Surface emissivity	0.60	-
Thermal mastic	Density	2000	kg/m^3
	Thermal conductivity	6	W/(m·K)
	Heat capacity at constant pressure	900	J/(kg·K)
Aluminum plate	Density	2700	kg/m^3
	Thermal conductivity	237	W/(m·K)
	Heat capacity at constant pressure	910	J/(kg·K)

4.4.4 Time-dependent Insulation of both Internally and Externally Heated Blocks under Heating Case 1

This section describes the simulation of the heating process for both internally and externally heated blocks under the given thermal supply and environmental circumstances in heating case 1. The numerical setup was based on the description provided in Section 4.4.3 for the

initial and boundary conditions. The FEM models solved a transient method using the same simulation time as was used for heating case 1 to develop a series of simulated time-dependent heating curves that were validated with the laboratory-measured data at the thermocouple locations. The thermocouple locations determined in the COMSOL program were identical to those in the laboratory that were used to validate the numerical models. Comparisons of the inlets, outlets, and ambiance; thermocouples located 1.3 cm (0.5 in.) below the block top surface; and thermocouples located 1.3 cm (0.5 in.) inch above the block bottom surface are presented in Figs. 4-12 to 4-14, respectively, which depicts the experimental validation of both internally and externally heated FEM models under heating case 1.

4.4.4.1 Comparison of variations of inlet, outlet, and ambient temperatures

Fig. 4-14 presents the recorded temperature variations of the inlet, outlet, and ambient temperatures. Before initiating heating case 1, an approximate equilibrium stage was set to allow the two blocks to reach the same temperature as the freezer box. The block temperatures were monitored continuously, and this stage was terminated when the entire slab temperature converged to the freezer box temperature, approximately -3.2 °C (26.2 °F). During the heating process, the two blocks were heated by a supply of warm water. Temperature spikes were observed for all of the thermocouple readings except the inlet, outlet, and water tank, which had a controlled temperature. The spikes were caused by the defrosting cycle of the freezer box. The water tank temperature rose to the set temperature in approximately 20 minutes and then remained stable regardless of the ambient temperature. In this numerical analysis, both the inlet and ambient temperatures were set as identical to the laboratory-measured data to be interpolated in COMSOL as initial conditions. Both measured inlet and outlet temperatures were constant and had a slight temperature difference of 0.4 ºC (0.2 ºF), which signified the water tank's good heating and

insulation performance. The measured and simulated outlet temperatures were constant and had a slight temperature difference of 0.2 ºC (0.1 ºF), which proved that they were in reasonable agreement; the outlet temperature exported from COMSOL was slightly higher than that of the experimental measurements.

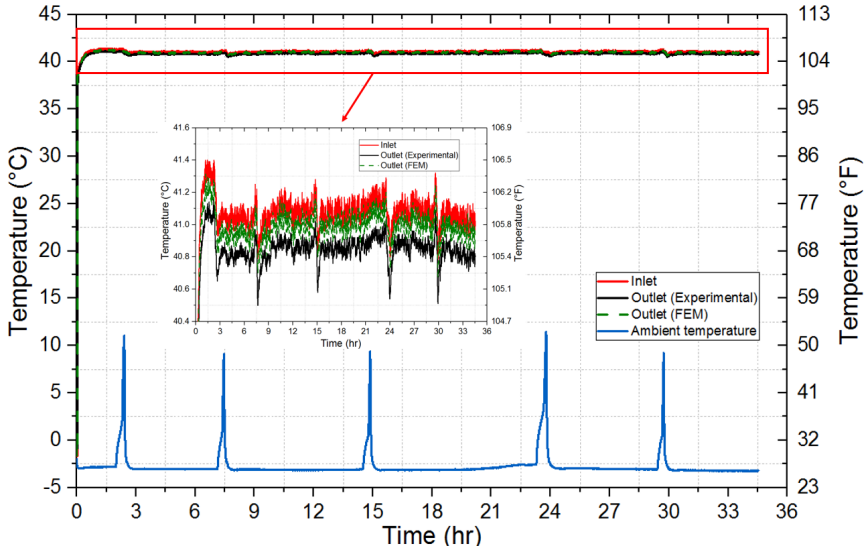

Figure 4-14. Temperature variations of the inlet, outlet, and ambient temperatures during heating case 1

4.4.4.2 Comparison of Temperature Variations Within Both Concrete Blocks

(1) Thermocouple Sets E0.5T1 to E0.5T5 (Externally Heated Block) and I0.5T1 to I0.5T5 (Internally Heated Block)

Figs. 4-15(a) and (b) illustrate the time-dependent thermocouple temperature heating curves for thermocouple sets E0.5T1 to E0.5T5 and I0.5T1 to I0.5T5 installed 1.3 cm (0.5 in.) below the block top surface. The temperatures within both concrete blocks reached a steady state after heating for 35 hours. In Fig. 4-15(a), the temperature responses of E0.5T2 were lower than those of the other thermocouples. This may have been caused by the somewhat smaller distances between the locations of E0.5T2 and the air outlet inside the freezer box, which led to more convective heat loss. For the internally heated block (Fig. 4-15(b)), thermocouples I0.5T2 and

I0.5T3 not located directly above the heating PEX pipe recorded relatively lower temperature responses. For both internally and externally heated blocks, the variations of the temperature responses of experimental measurements and numerical outputs were less than 1 °C (2 °F) and 0.5 °C (1 °F), respectively, which indicated that a uniform temperature distribution near the top surface was reached. The differences between the experimental and numerical average temperature responses for both internally and externally heated blocks were respectively limited to 0.2 °C (0.1 °F) and 0.1 °C (0.05 °F), which showed that the simulated temperatures agreed with the experimental measurements. The increases in the thermocouple temperature in the numerical analyses also agreed well with the laboratory results. All of the thermocouple readings were greater than 0 °C (32 °F) after reaching the equilibrium state, which signified that the newly installed PEX pipe design was capable of providing sufficient energy to maintain the surface temperature above freezing on the bridge deck.

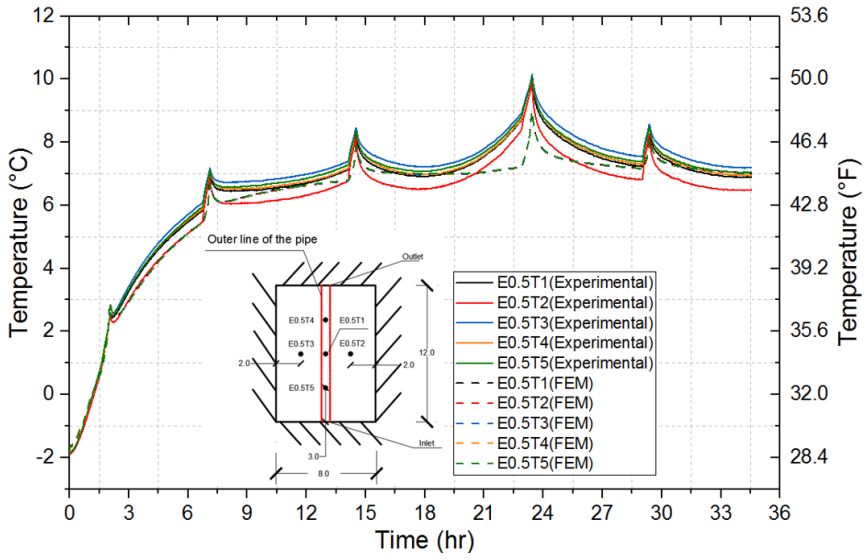

(a)

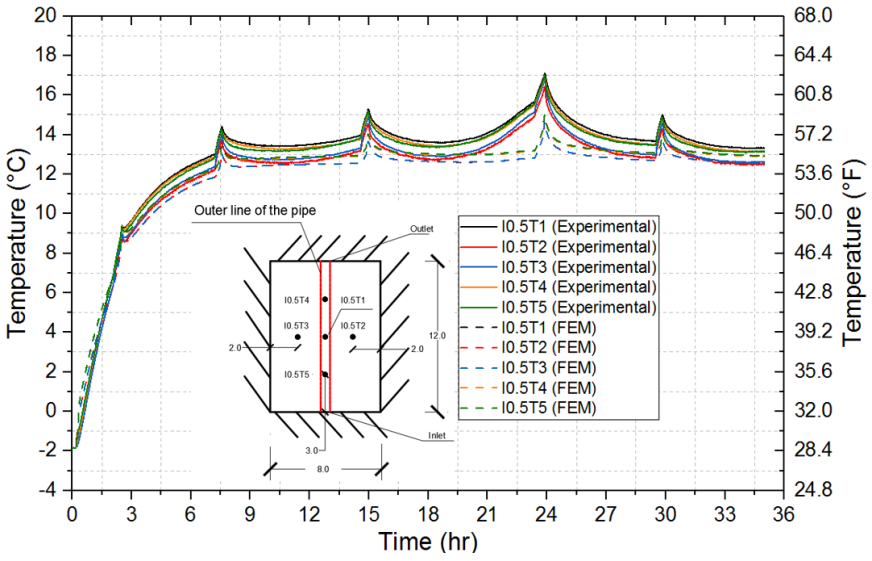

(b)

Figure 4-15. Comparison of experimental measurements' and numerical simulations' temperature responses for thermocouple sets: (a) E0.5T1, E0.5T2, E0.5T3, E0.5T4, and E0.5T5 (externally heated block); (b) I0.5T1, I0.5T2, I0.5T3, I0.5T4, and I0.5T5 (internally heated block)

(2) Thermocouple Sets E7.5T1 to E7.5T5 (Externally Heated Block) and I7.5T1 to I7.5T5 (Internally Heated Block)

Figs. 4-16(a) and (b) compare the simulated temperature responses of thermocouple sets E7.5T1 to E7.5T5 and I7.5T1 to I7.5T5 located 1.3 cm (0.5 in.) above the block's bottom surface with those measured experimentally for both internally and externally heated blocks. For the externally heated block, both measured and simulated temperature responses were divided into two groups. The thermocouples from the group with higher temperature responses, E7.5T1, E7.5T4, and E7.5T5, were located right above the PEX pipe, which has the shortest distance to the heat source and the least convective heat loss to the environment. The remaining two thermocouples, E7.5T2 and E7.5T3, installed on both sides of the PEX pipe, recorded lower temperatures, as presented in Fig. 4-16(a). The ranges of the final temperature responses E7.5T1

to E7.5T5 for both measured and simulated results were from 16.0 °C to 20.9 °C (60.8 ºF to 69.6 ºF) and from 16.5 °C to 20.6 °C (61.7 ºF to 69.1 ºF), respectively. The maximum temperature difference of 4.9 °C (8.8 ºF) from E7.5T1 to E7.5T5 was much greater than that of 0.7 °C (1.3 ºF) from E0.5T1 to E0.5T5, which signified that a more uniform temperature distribution was reached near the concrete's top surface. Fig. 4-16(a) shows that the average thermocouple temperature deviation between the experimental measurements and the numerical investigations was less than 0.2 ºC (0.4 ºF), which indicates that numerical outputs can match the laboratory-measured results. In both experimental and numerical analyses, the time required to reach the steady-state temperature was almost identical (about 23 hours) for thermocouples E7.5T1 to E7.5T5.

In Fig. 4-16(b), the maximum final temperature deviations from the experiments and numerical simulations were much smaller than those presented in Fig. 4-16(a). One possible reason for this may be that insulation materials did not cover the bottom surface of the internally heated block, resulting in an approximately uniform effect of convective heat transfer on the bottom surface and no significant temperature difference on the surface. The numerical outputs and experimental data were in agreement, similar to the external one, since the average deviation of the thermocouple temperature between the two measurement approaches was less than 0.1 ºC (0.2 ºF). The time required to reach the steady-state temperature was approximately 23 hours, similar to the external heating design.

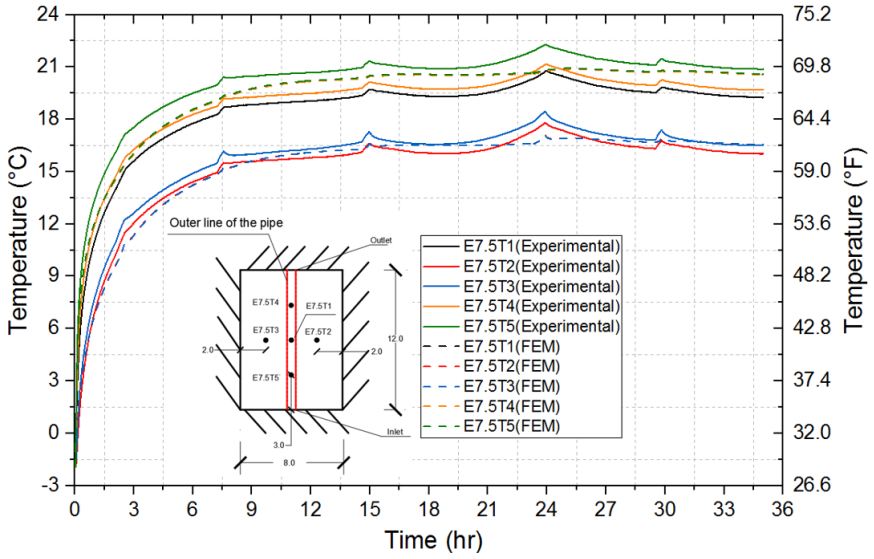

(a)

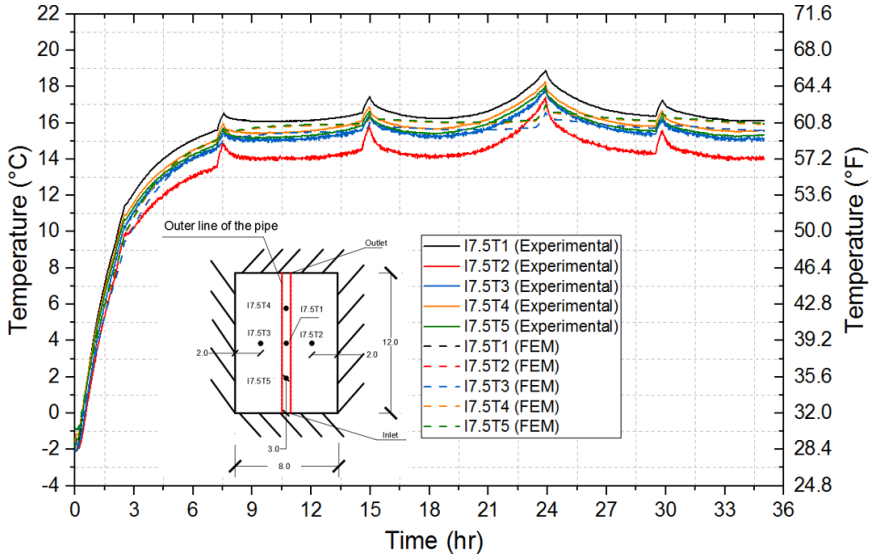

(b)

Figure 4-16. Comparison of laboratory and numerical temperature responses for thermocouple sets: (a) E7.5T1 E7.5T2, E7.5T3, E7.5T4, and E7.5T5 (externally heated block); (b) I7.5T1, I7.5T2, I7.5T3, I7.5T4, and I7.5T5 (internally heated block)

(3) Thermocouple Sets E0.5T1 to E7.5T1 (Externally Heated Block) and I0.5T1 To I7.5T1 (Internally Heated Block)

The temperature distributions and vertical temperature variations within the heated blocks, and plots of temperature variations, along with the depth from the top of the block to the bottom surface, are presented in Figs. 4-17(a) and (b). Thermocouple sets E0.5T1 to E7.5T1 and I0.5T1 to I7.5T1 were analyzed since their good thermocouple readings could provide an even temperature distribution along the vertical direction. It was observed that the closer the thermocouple was to the heat source, the more rapidly the temperature increased. For both the internal and external heating designs, the simulated temperature responses from thermocouples installed at each depth (1.3 cm, 5.1 cm, 10.2 cm, 15.2 cm, and 19.1 cm below the top surface) were in agreement with those from experimental measurements. Similar to the records from the thermocouple sets located near the top and bottom surfaces, it took 23 hours for the thermocouples vertically distributed to record the steady-state temperature.

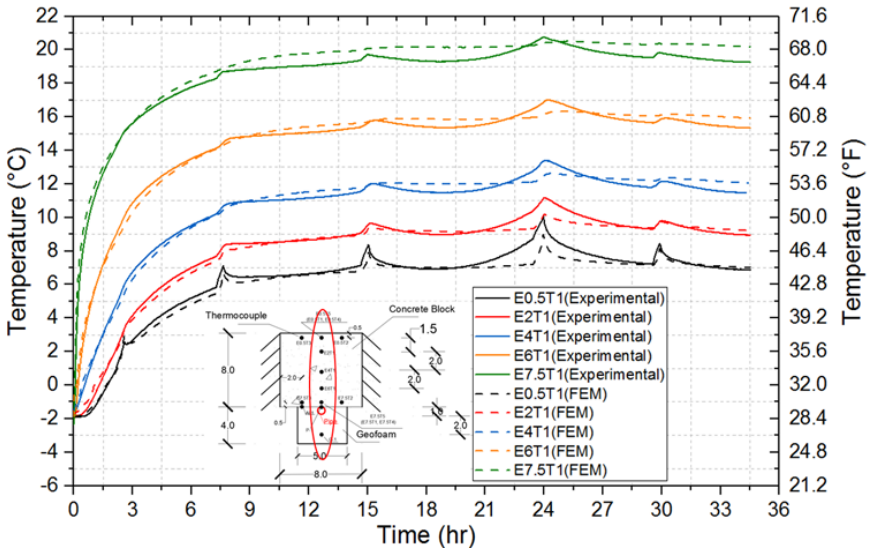

(a)

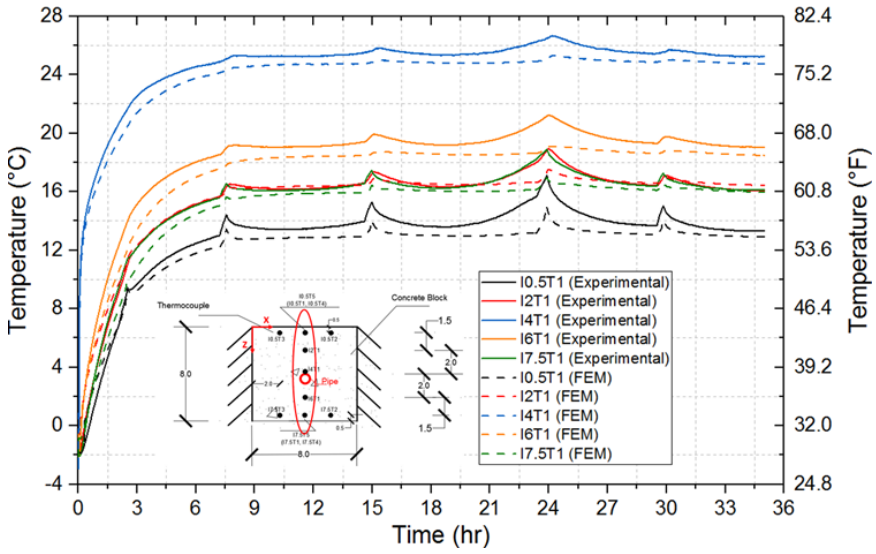

(b)

Figure 4-17. Comparison of experimental results and numerical outputs of temperature responses for thermocouple sets: (a) E0.5T1, E2T1, E4T1, E6T1, and E7.5T1 (externally heated block); (b) I0.5T1, I2T1, I4T1, I6T1, and I7.5T1 (internally heated block)

4.4.4.3 Comparison of Experimental and Numerical Vertical Temperature Profiles along the Vertical Direction at the Steady State

Figs.4-18 (a) and (b) illustrate the experimental and numerical temperature profiles along the vertical axis for both internally (I0.5T1 to I7.5T1) and externally (E0.5T1 to E7.5T1) heated blocks. The thermocouple temperatures for both the experimental and numerical cases are the final temperatures obtained from the transient analyses. The PEX pipe centerlines of internally and externally heated blocks were respectively located at -0.95 cm (Fig. 4-18(a)) and 10.16 cm (Fig. 4-18(b), where the peak temperature responses (supplied water temperature) were obtained and presented in the two temperature profiles, as shown in Figs 4-18. The temperature profiles relate to the vertical heating process from the PEX pipe to the top and bottom surfaces, for both internally and externally heated blocks. Due to the shorter distance to the supplied fluid inlet for the externally heated block, a significantly faster temperature increase occurred at the bottom, rather

than the top surface of the concrete blocks. As a result of the consideration of thermal contact models depicted in Section 4.4.3, significant temperature drops occurred near 0 cm and 11.1 cm for the internally and externally heated blocks, respectively, i.e., the interface between the concrete block and the PEX pipe (for internal heating) or geofoam (for external heating), which made a remarkable contribution to obtaining close agreement between the measured and simulated temperature responses, as shown in Fig. 4-18(a) and (b). The temperature gradients at steady equilibrium had a nearly linear relationship with the depth within the concrete and geofoam block, which matched the theory of conductive heat transfer in solids. In Fig. 4-18(a), a close approximation between the temperature at the bottom of the geofoam block and the ambient temperature indicated that the insulted PEX pipe was capable of providing a good insulation performance. The steady-state temperatures at the top concrete surfaces were greater than freezing, which proved that the heating designs satisfied the heating performance.

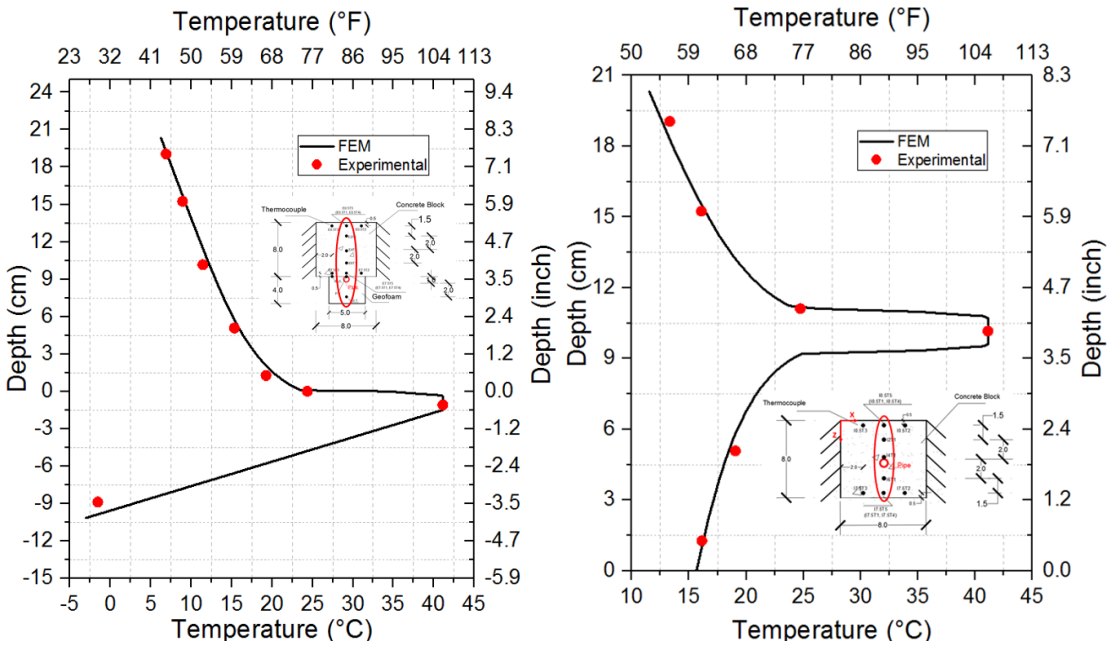

Figure 4-18. Comparison of experimental and numerical vertical temperature profiles along the vertical direction for thermocouple sets (a) E0.5T1, E2T1, E4T1, E6T1, and E7.5T1 (externally heated block); (b) I0.5T1, I2T1, I4T1, I6T1, and I7.5T1 (internally heated block)

4.4.5 FEM Model Verifications of Slab Heating Under Various Heating Scenarios

Section 4.4.4 dealt with the experimental and numerical transient temperature variations within both the internally and externally heated blocks under heating case 1. Numerical modeling was performed by a stationary approach to obtain the average steady-state temperatures at five different thermocouple locations that were 0.5 in. below the block's top surface (E0.5T1 to E0.5T5 and I0.5T1 to I0.5T5) under the various thermal supplies and environmental circumstances shown in Table 1. Stationary numerical simulations of all six cases were analyzed by the model calibrated from case 1. The adjusted ambient and inlet temperatures listed in Table 4-1 were set as initial conditions in the stationary FEM models. A comprehensive comparison of the steady-state results

were exported from COMSOL, along with those measured from laboratory tests, and were presented in this section.

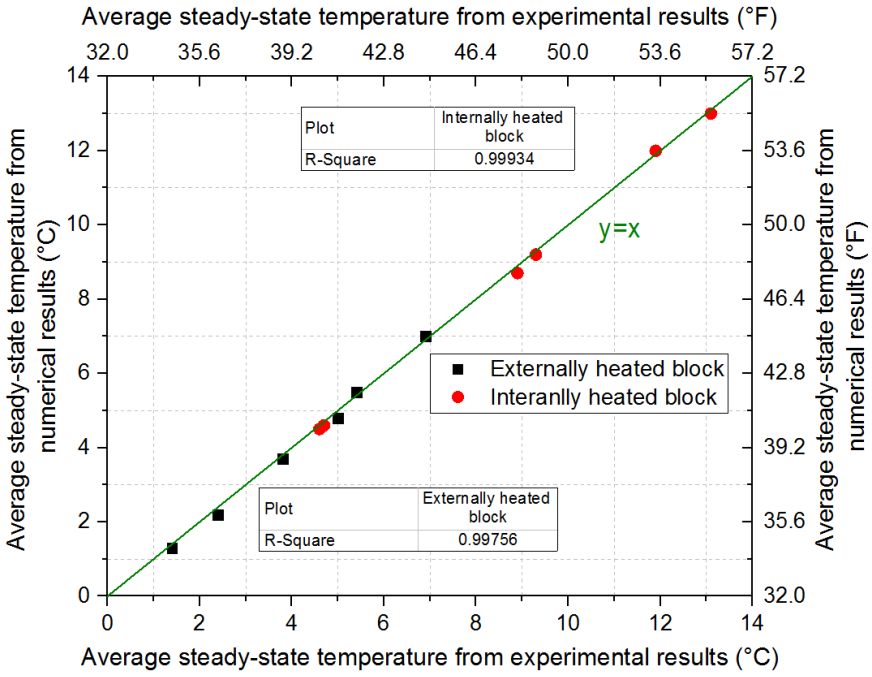

Figure 4-19. Regression analysis for the numerical model under different heating scenarios

Fig. 4-19 illustrates the regression analysis results of the steady-state temperatures measured from the experiments and the numerical analyses summarized in Table 1. The R-square of internally and externally heated blocks, calculated for the best-fit line "y=x," were respectively 0.999 and 0.997, which indicated that the numerical model was validated and could provide a reasonable estimate of the performance of both internal and external hydronic heating systems. The stationary models' steady-state temperatures were in reasonable agreement with the final temperatures outputted from the time-dependent approach.

The correlations between the average experimental and numerical steady-state temperatures of both the internal and external blocks recorded 0.5 in. below the block's top surface and the adj. inlet water temperatures, respectively, are listed in Table 4-1 and illustrated in Fig. 4-20(a) for six cases. It was observed that the numerical outputs agreed well with the laboratory

results. A comparison of the FEM results and experimental measurements revealed a close match of the slopes of the gridlines developed from FEMs at measured ambient temperatures -3.2 °C (26.2 °F) and -6.0 °C (21.2 °F) for both internal and external heating systems (Fig. 4-20(a)). The specific slope errors between the simulations and experiments with ambient temperatures at -3.2 °C (external), -6.0 °C (external), -3.2 °C (internal), and -6.0 °C (internal) were 6.2%, 5.0%, 1.2%, and 2.5%, respectively. Fig. 4-20(a) signifies that the temperature responses recorded 0.5 in. below the concrete surface were directly proportional to the inlet water temperature. The same slopes of internally (0.3849) and externally (0.2065) heated blocks from simulations were obtained independent of the variations in the ambient temperature. The temperature deviations between the experimental measurements and the numerical results were less than 0.2 °C (0.4 °F), which signified that the FEM models were experimentally validated and were capable of performing a series of parametric studies to estimate the heating performance of hydronic heating systems under various heating scenarios. Fig. 4-20(b) illustrates the gridlines of average steady-state temperatures under various ambient and water tank temperatures, which revealed that the block surface temperature is proportional to the supplied inlet temperature. The proportion remains the same in Fig. 4.20(a). Due to a shorter distance to the heat source, the temperature responses 0.5 in. below the block surface were higher than those at the block's surface.

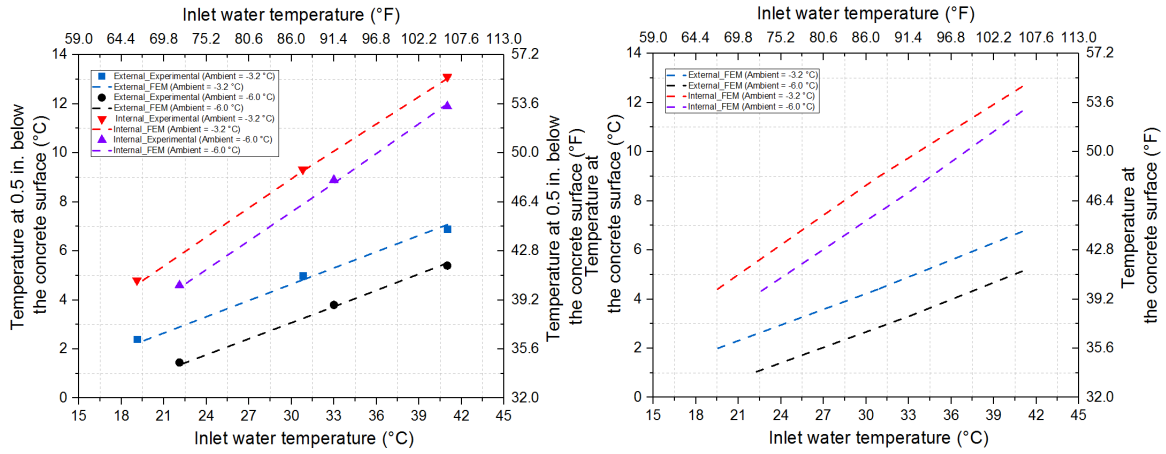

(a) **(b)**

Figure 4-20. Gridlines of average steady-state temperatures under various ambient and water tank temperatures: (a) at 0.5'' below the surface, (b) at the surface

4.4.6 Heat Flux Analysis

Applying the one-dimensional Fourier's law of heat conduction (Lienhard IV 2011) enabled the analysis of the vertical heat fluxes transferred from the heat source to the top surface by utilizing the measured thermal gradients and thermal conductivity, as shown in Eq. (4-6)

$$q = k \cdot \frac{dT}{dx} \tag{4-6}$$

Figure 4-21(a) illustrates the average experimental and numerical heat flux acquired at 1.27 cm (0.5 in.) below the concrete's top surface for both externally and internally heated blocks. The surface heat flux for the thermocouple sets can be calculated by using Eq. (4-6). The average thermal conductivity of the concrete deck was 2.8 W/(m·K) using the KD2 pro thermal analyzer. The heat flux corresponding to thermocouple sets T2 and T4 was calculated from the thermocouple pairs from 1.27 cm (0.5 in.) to 19.05 cm (7.5 in.) below the concrete surface, i.e., E7.5T2/E0.5T2, E7.5T3/E0.5T3, E7.5T4/E0.5T4, and E7.5T5/E0.5T5. The heat flux from thermocouple set T1 was calculated through the product of thermal conductivity (2.8 W/(m·K)) and the average

temperature gradient acquired from thermocouples pairs E7.5T1/E6T1, E6T1/E4T1, E4T1/E2T1, and E2T1/E0.5T1. For internally heated blocks, the heat flux at 0.5 inches was calculated from the thermocouple pair, 1.27 cm (0.5 in.) to 9.21 cm (3.6 in.) inches below the concrete surface, i.e., I4T1/I0.5T1. The heat fluxes were assumed to be transferred one-dimensionally upward, which can be verified from Figs. 4-22(a) and (b) by comparing the heat flux vectors at different depths. The heat fluxes along the vertical depth became more uniform and oriented upward as they approached the top surface. In Fig. 4-21(a), the heat flux from the FEM model was in agreement with the experimental cases. Experimental and numerical heat fluxes from both internally and externally heated blocks were directly proportional to the supplied thermal load, as expected. Fig. 4-21(b) illustrates the average heat flux derived from umerical outputs, which revealed that the block surface heat flux was proportional to the thermal load and the proportion remained the same as in Fig. 4.21(a). Due to a shorter distance to the heat source, the heat flux at 0.5'' below the block surface was greater than that at the block's surface.

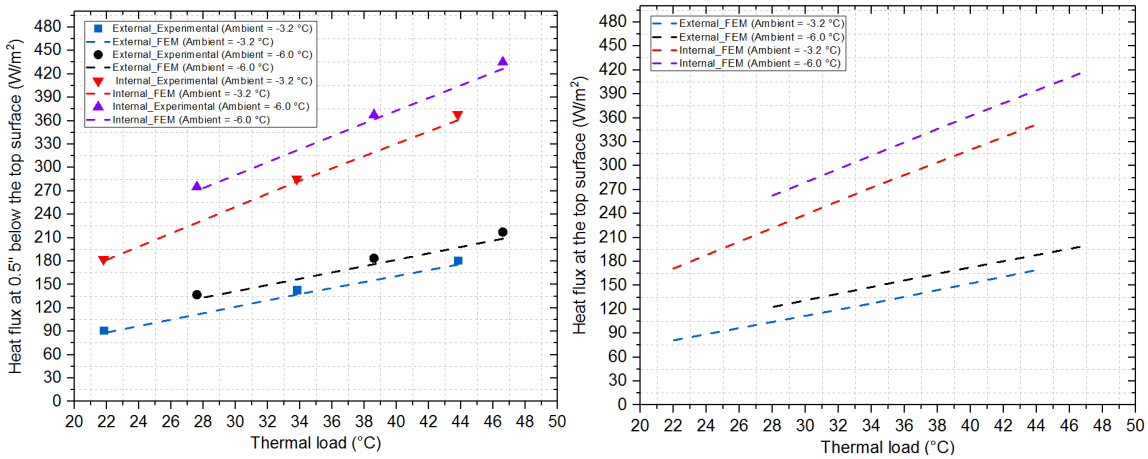

(a) **(b)**

Figure 4-21. Average heat flux derived from experimental data and numerical outputs: (a) at 0.5" below the block surface, (b) at the block surface (only numerical results)

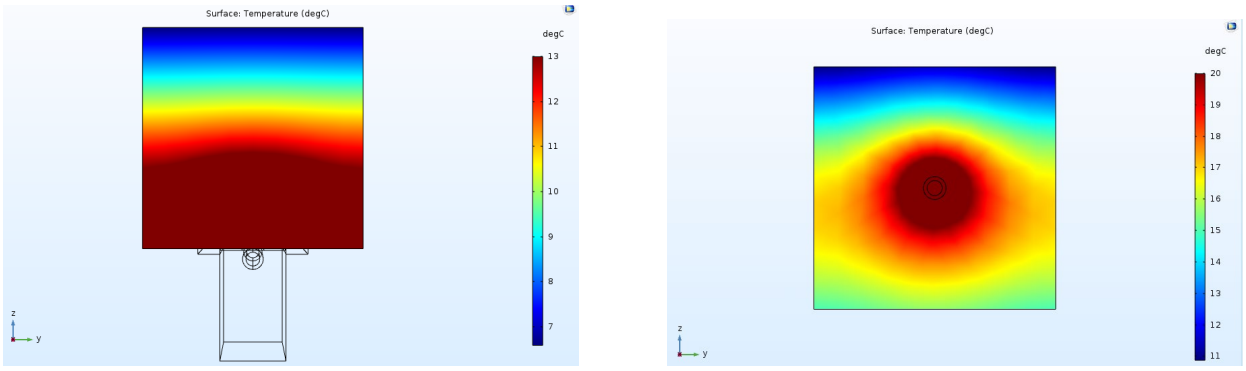

(a) **(d)**

Figure 4-22. Temperature contours for both block models at steady-state under heating test 1: (a) externally heated block, (b) internally heated block

4.5 Summary and Conclusions

Two concrete blocks were fabricated with internal and external heating systems and were installed in the structural lab at the University of Texas at Arlington (UTA) to investigate two important interface heat transfer mechanisms: surface convection with the environment and the thermal contact between PEX pipes and concrete. To decrease the difficulty of conducting bridge inspections of the bottom surface, an insulated PEX loop design that serves as a heating element was developed and attached to the externally heated concrete block. The thermocouples were pre-embedded within the molds before the blocks were cast, for the acquisition of temperature responses. The two concrete blocks were connected in a series to obtain the same flow rate. Six environmental response tests under various thermal supplies were performed to analyze the system performance and the efficiency of the heat transfer of the two different heating designs. Two 3-dimensional finite element models were developed in COMSOL to replicate both heated concrete blocks for a series of numerical studies. A comprehensive analysis was conducted of the heat transfer process that included conduction, convection, and radiation between the concrete and the

environment. Transient and stationary approaches were respectively utilized to obtain time-dependent plots and final temperature responses at a steady equilibrium. The FEM models were calibrated by experimental data measured at 0.5" below the deck surface with temperature deviations limited to 0.2 °C. For internally and externally heated blocks, the R-square values calculated for the best-fit line “y=x” were respectively 0.999 and 0.997, which signified that a reasonable agreement can be obtained between numerical and experimental results.

The convective heat transfer coefficient h at the blocks’ surfaces was evaluated, using the finite difference method based on the assumption of a one-dimensional heat transfer process. The average h value calculated from each test was 18.74 W/(m^2·K), 17.37 W/(m^2·K), 17.56 W/(m^2·K), 17.13 W/(m^2·K), 17.17 W/(m^2·K), and 16.47 W/(m^2·K), respectively. A solid-to-solid thermal contact model was developed to study the thermal resistance behavior between the concrete and PEX pipes. The optimized hc value of 184 (W/(m2·K) was obtained by experimental validation of the internally heated block. The external system's optimized hc value of 122 (W/(m2·K) was smaller than that of the internal system, since the external binding conditions were worse. Based on the improvement of the thermal contact models developed in this study, the numerical results of vertical temperature profiles have a much better agreement with experimental data than the study described in Chapter 3. The block surface temperature is proportional to the supplied inlet fluid temperature, independent of the variation of ambient temperature. In this study, the heat flux transferred near the surface can be assumed as a one-dimensional vertical flow. A linear relationship between the surface heat flux and thermal load can be observed as well.

The fully validated FEM models provide a comprehensive study of interface heat transfer mechanisms. Accurate evaluations of the convective heat transfer coefficient at the surface and vertical temperature profiles within the blocks can significantly improve the agreement between

numerical outputs and experimental data, which is expected to be widely applied to geothermally heated bridge deck design. In future laboratory tests and numerical investigation, the deicing behaviors, including phase change and energy balance at the surface, will be considered.

CHAPTER 5 HEATING PERFORMANCE OF A NOVEL EXTERNALLY-HEATED GEOTHERMAL BRIDGE DEICING SYSTEM: FIELD TESTS AND NUMERICAL SIMULATIONS SCENARIOS

5.1 Introduction

In Chapter 3, a series of heating tests and numerical simulations under different thermal scenarios performed on an externally hydronic heated deck have examined the experimental feasibility of this external system (Yu et al. 2020), provided a comprehensive understanding of heat transfer mechanisms within the bridge deck, and accurately predicted the performance of this external heating system under given ambient temperatures below the freezing (Li et al. 2020). In Chapter 4, two concrete blocks with internal and external single-loop heating systems were employed to improve two important interface heat transfer mechanisms: convection heat transfer between the deck surface and environment and the thermal contact between hydronic PEX pipes and concrete, which is capable of providing a more accurate agreement between experimental measurements and FEM outputs. The updated FEM models can be viewed as novel numerical tools for predictions of the heat transfer analyses and the design of externally heated hydronic bridges. However, these two studies were limited to be performed under controlled temperatures in a laboratory and didn't consider the deicing processes. Therefore, to estimate the practical feasibility of this external heating design for deicing under various environmental circumstances, a mock-up hydronic bridge deck was constructed and fabricated in the field. A series of heating tests were performed to estimate the system performance. In this chapter, a 3D FEM model of this externally heated mock-up bridge deck was developed in COMSOL Multiphysics (COMSOL 2016), which was respectively validated by the experimental data collected from three different practical operations: non-heating, heating, and heating and deicing. A numerical investigation by

using the validated FEM model under one of the most severe snowy events recorded in the Dallas/Fort Worth (DFW) area was conducted to estimate the practical feasibility of snow melting performance for the external heating system. The simulated results illustrated that this calibrated FEM model can be viewed as an accurate numerical framework for an estimate of heating performance of externally heated bridge decks under various weather conditions in snowy events.

5.2 A Full-Scale Externally-Heated Geothermal Bridge Deicing System

To estimate the feasibility of the practical application of the externally geothermal heating design for deicing, a mock-up hydronic bridge deck was constructed and fabricated by the UTA research team. A series of winter heating tests were performed on the mock-up bridge deck to evaluate the heating performance and heat transfer behaviors within the bridge deck under different severe winter weather scenarios. This section provides a general description of the geothermal mock-up bridge, hydronic heating system, and instrumentation system of the externally full-scale heated bridge decks.

5.2.1 Geothermal Mock-up Bridge

The selected site for constructing the mock-up bridge deck is located at West Division Street (SH 180) and Green Oaks Boulevard Bridge (Dottie Lynn Parkway) in Arlington. The site is on an abandoned asphalt pavement, which was used by TxDOT for storage of reclaimed asphalt pavement (RAP). A total of 12 standard 2.43 m × 1.82 m × 10.16 cm (8 ft. × 6 ft. × 4 in.) PCP panels, 3 I-beams, and 2 standard concrete traffic barriers (CTBs) were employed to construct the mock-up bridge deck to represent approximately 85% of Texas's bridges (Merrill 2002). The bridge deck was built on top of three standard I-beams fixed on two standard CTBs to increase its elevation. Figs. 5-1(a) and (b) present the plan and cross-sectional views in a schematic design of the hydronic snow-melting system, respectively. The dimensions of the entire mock-up bridge

deck were 10.97 m × 4.87 m × 20.32 cm (36 ft. × 16 ft. × 8 in.). Notably, only the externally heated zone with an area of 7.31 m × 4.8 m (24 ft. × 8 ft.) was used to perform the heating scenarios in this study. The remaining portion of the deck surface which was not set up to use the heating system is viewed as a control area that can be utilized to conduct contrast tests with the external heated zone to evaluate the heating performance of this newly developed design. The hydronic loops were covered by fine cement paste to increase the surface contact with the deck base and were attached to the bottom surface of the externally heated zone where they were encapsulated by a layer of spray foam for heat insulation, as shown in Figs. 5-2(a) and (b). Figs. 5-2(c) and (d) present the borehole heat exchanger (BHE) and the control room of the heat pump, respectively.

5.2.2 External Geothermal Bridge Deicing System

The purpose of the mock-up bridge deck design is to evaluate the feasibility of whether this external geothermal heating design is capable of being implemented on existing bridge decks. Doing so will meet the demand for deicing despite difficult environmental conditions in the field. The hydronic heating loop design for the mock-up bridge is shown in Fig. 5-1 as divided into two sections: an externally heated bridge deck area and a control zone for monitoring purposes. However, only the externally heated zone was tested in this study. The geothermal bridge deicing system consists of three different components. The borehole heat exchanger (BHE) which can extract heat through the fluid underground. In this study, a single borehole with a length of 132.5 m and a width of 14.6 cm was utilized to supply heat energy for snow melting/deicing on the mock-up bridge deck. Then, the fluid flows out of the ground loops and enters the circulation pump and heat pump which were kept in a control room built on-site, as shown in Fig. 5-2(d). The operation mode of a full load can get its heat from this system, showing the geothermal heat pump to be active under an extreme winter event. After circulating through the control room, the heat-carrier

fluid will be pumped to the hydronic loop system to supply the required heat fluxes at the bridge deck surface for snow/ice removal. For the externally heated zone, the extracted underground fluid is circulated within the bridge deck through a PEX pipe which has an inner diameter of 13 mm (0.5 in.) and an outer diameter of 19 mm (0.75 in.), respectively. Fig. 5-1(a) shows the external heating system with three inlets and three outlets, Based on Bowers (2016), the hydronic loop spacing was set as 20.32 cm (8 in.). The thermal conductivity of the concrete deck is 2.16 W/m·K, as measured by a KD2 pro thermal analyzer on site.

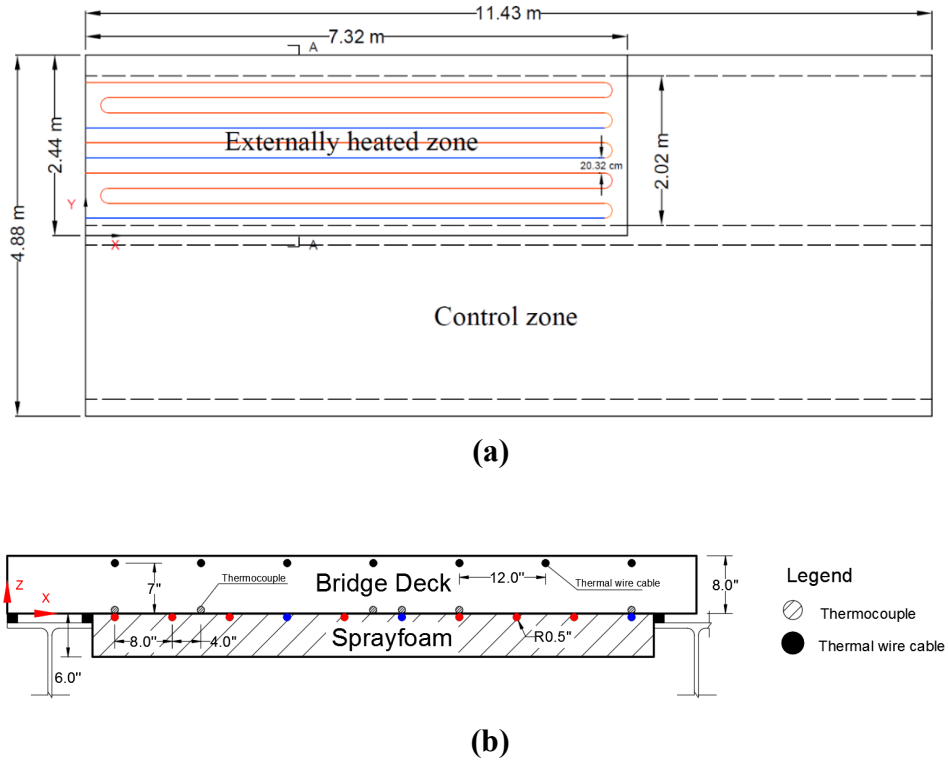

Figure 5-1. Geothermal mock-up bridge: (a) a plan view of the bridge deck (unit: m); (b) a cross-section view of the bridge deck with temperature sensor layout (unit: cm)

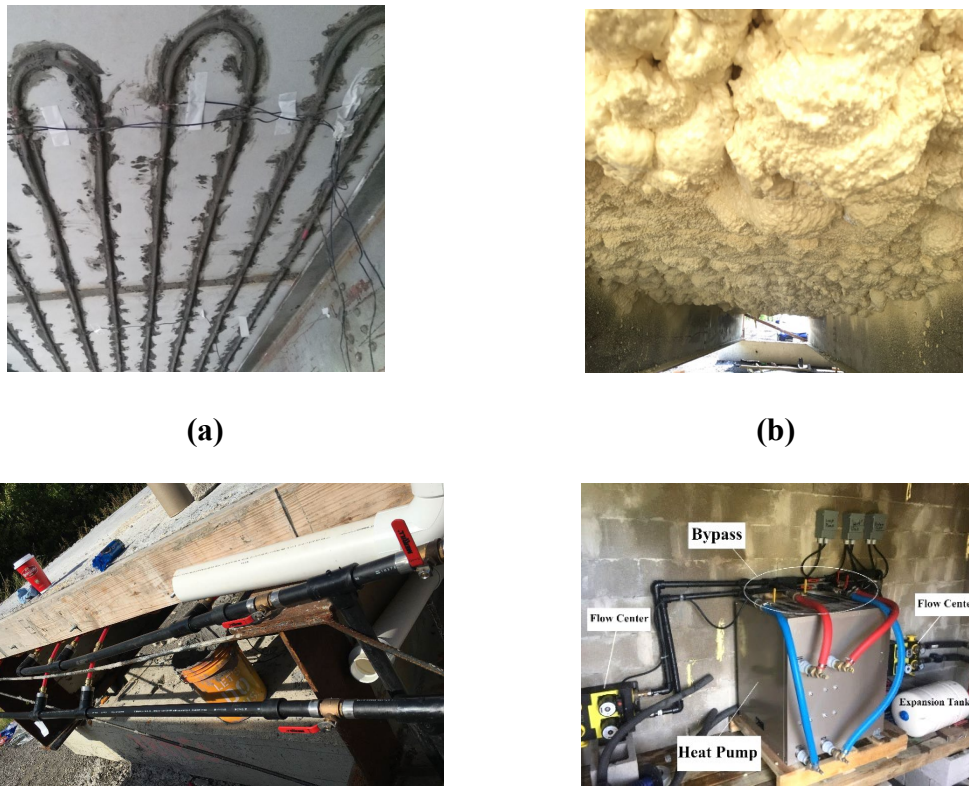

Figure 5-2. Installation of PEX pipe loops. (a) PEX pipe loops fastened to the bridge deck and covered with cement paste, (b) polyurethane foam insulation, (c) borehole heat exchanger (BHE), and (d) control room for heat pump

5.2.3 Instrumentation System

The data collection system for the mock-up bridge deck was provided by Pile Dynamics, Inc. (Cleveland, OH, USA) and National Instruments (now NI, headquartered in Austin, TX, USA) to record the heat transfer behaviors within the heated bridge deck. The utilized temperature sensors included thermal wire cable (Pile Dynamics) and Type-T thermocouples (NI). The former can provide multiple measurements along a cable, and the latter is capable of capturing the temperature response at a specific point. One solid-state thermocouple multiplexer and one Pile Dynamics Thermal Acquisition Port (TAP-Edge) unit were connected to the utilized temperature

sensors to conduct the data acquisition. All the sensors were calibrated internally in the data logger, and the temperature outputs were recorded directly into the data logger.

The sensors were placed in two general locations, in the deck's cross-section (at the concrete base) and one inch below the concrete surface, as illustrated in Fig. 5-1(b). A total of 10 Type-T thermocouples were installed at the bridge deck base to measure the temperature distribution at this surface, as shown in Fig. 5-3(a). The thermocouples were placed in two general locations in a plane view: on a circulation tube and between two circulation tubes. One thermal wire cable with a total of 53 pre-configured sensor nodes set at customized spacings was embedded one inch below the deck surface during concrete pouring to provide a comprehensive understanding of the heat transfer behaviors near the top surface of the bridge deck. as shown in Fig. 5-3(b). Additionally, two Type-T thermocouples were attached to the high-density poyethylene (HDPE) pipes to monitor the supplied fluid temperature in (via inlets) and out (via outlets) of the bridge. A thermocouple, utilized to measure the ambient temperature in the field, was placed on the roof of the control room constructed onsite approximately 5 m from the mock-up bridge deck. One thermocouple, installed in the foam slab about one inch above the foam bottom surface, was utilized to estimate the thermal insulation performance of the spray foam

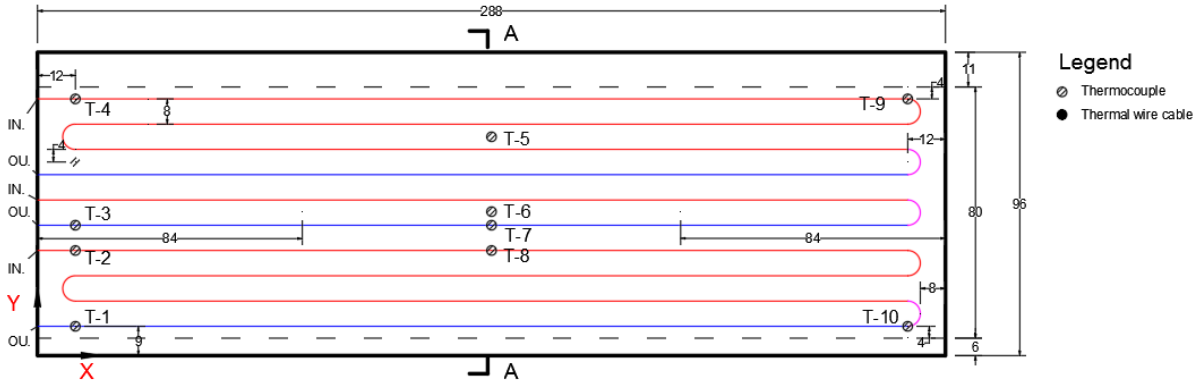

Plane View Z=0"

(a)

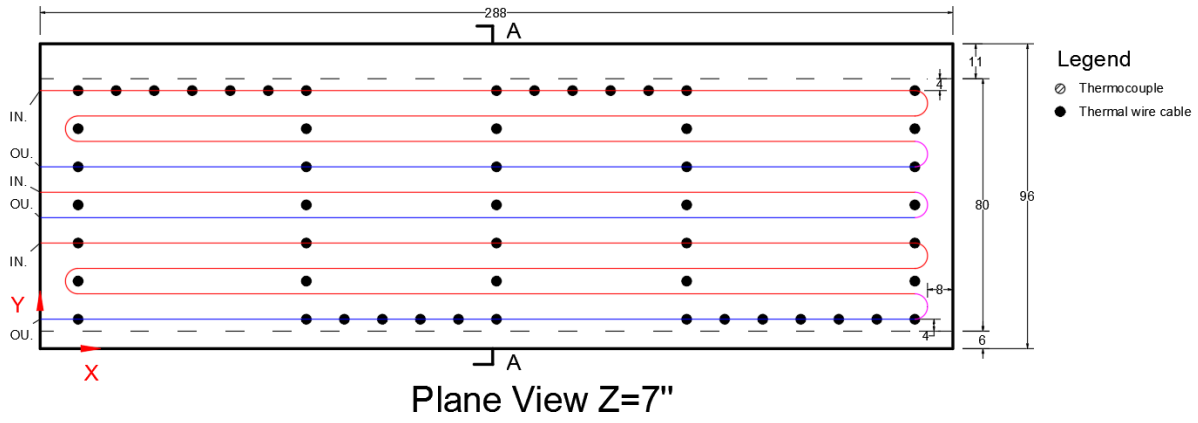

(b)

Figure 5-3. A plane view of sensor locations in the externally heated bridge deck. (a) at the concrete base and (b) 2.54 cm (1 inch) below the concrete surface

5.2.4. Winter Tests

As mentioned in Section 5.2.2, the hydronic system was operated in several modes based on the geothermal heat pump's operational conditions and the given weather conditions. Table 5-1 deals with three different operation tests performed in the winter of 2018 and 2019. The start and end times account for the operation period of the geothermal heating system. The number of freezing hours, minimum ambient temperature, and average ambient temperature were measured by the temperature sensor installed on site. The operation mode of each winter test and the heat efficiency of the heating and deicing test (Test #3) are described in Table 1 as well. The detailed description of each test is presented in Sections 5.2.4.1 to 5.2.4.3.

Table 5-1. Summary of Operation Tests and Weather Scenarios

Test	Start	End	Ambient temperature			Operation mode	Heating efficiency (%)	
			# Hr. of freezing	Average (°C)	Minimum (°C)		Measured	Simulated
#1	2/1/19 06:00	2/4/20 0:00	0	19.2	11.4	Non-heating	-	-
#2	1/24/19 01:00	1/29/19 12:55	14.90	-1.7	-3.7	Full load (heating)	-	-
#3	2/7/19 22:02	2/12/19 9:19	11.70	-2.4	-3.6	Full load (heating and deicing)	55	71.3

5.2.4.1 Non-heating Test (Test #1)

A non-heating test was operated from 6 a.m. on 2/1/2019 to 12 a.m. on 2/4/2019 to capture the temperature response variation within the bridge deck with the ambient temperature. During this operation, the circulation pump remained off, and no heat-carrying fluids were supplied to the bridge deck; thus, the geothermally heated bridge can be viewed as a conventional bridge. The ambient temperature was measured by a thermocouple which was installed on-site. Due to the absence of a weather station in the field during this test, the wind speed data were collected from another weather station located at the DFW International Airport, which is 15 miles from the research site. No snowy precipitation existed during the test. Detailed operation results are depicted in Section 5.3.4.1.

5.2.4.2 Winter Heating Test (Test #2)

A winter heating response test was initiated at 1 a.m. on 1/24/2019 since a minimum ambient temperature at −3.7 °C (25.4 ºF) was observed after 4 to 5 hours. The geothermal heat pump heated the circulating fluid underground to provide a pre-heating operation for the bridge deck in advance of the minimum freezing temperature. The pre-heat scenario is usually viewed as "idling." During the heating period, no rain/snow precipitation was observed to accumulate on the deck surface. Section 5.3.4.2 deals with the interpretation of the results for both experimental and numerical cases.

5.2.4.3 Winter Heating and Deicing Test (Test #3)

The winter heating and deicing test was carried out since the temperature responses measured by thermistors were available, and the observed ambient temperatures were as low as −3.6 °C (25.5 °F). This test ran from 10 p.m. on 2/7/2019 to 9 a.m. on 2/12/2019. Similar to Test #2, a pre-heating scenario was performed approximately seven hours before the arrival of the minimum ambient temperature. Unfortunately, no expected snow precipitation appeared during this test. Therefore, a snowmaking gun was utilized to initiate a snow simulation test at 5:40 a.m. on 2/8/2019 due to the lowest ambient temperature of −3.6 °C (25.5 °F), as shown in Fig. 5-4(a). Fig. 5-4(b) presents a uniform ice/snow layer accumulated on the non-heated zone's surface due to the absence of a pre-heating operation. This photo was taken after an expected snow simulation test was performed. Fig. 5-4(c) provides a clear contrast of the surface conditions between the heated and non-heated zone after the snow simulation, verifying the feasibility of a practical application for the external geothermal heating system under a snowy event. A comprehensive description of the measured and simulated temperature responses within the external heated zone is provided in Section 5.3.4.3.

(a) **(b)** **(c)**

Figure 5-4. Winter deicing and heating tests (a) snow simulation operation, (b) snow/ice formation accumulated on the non-heated zone, and (c) comparison of surface conditions between heated and non-heated zone.

5.3 FEM Analyses of the Externally Heated Bridge Deck

This section depicts the development of the finite element model of the externally heated mock-up bridge deck by using COMSOL Multiphysics®, a finite element simulation environment. The model was validated with the corresponding non-heating, heating, and heating and deicing response tests previously described in the transient approach. A numerical study using the validated FEM model under one of the most severe snow events recorded in the DFW area was performed to estimate the practical feasibility of snow melting performance for the newly developed external heating design. The numerical analysis provides desired results verifying that the new external hydronic deicing system can meet the demand for snow melting under one of the heaviest snowy weather conditions recorded in the DFW area.

5.3.1 Heat Transfer Models for Externally Heated Bridge Deck

An accurate and comprehensive theoretical background of heating and deicing processes plays a remarkable role in the numerical development of an externally heated bridge deck. Detailed heat transfer analysis from the circulating fluids to the bridge deck surface through a series of

complex heat transfer mechanisms consisting of conductive, convective, and radiative processes taking place within the bridge deck and between the surrounding environment has been developed by Li et al. (2020), as shown in Figs. 5-5 and 5-6. A new COMSOL module, the "pipe flow module," was employed in this paper to model the coupling with fluid flow and the heat transfer in a pipe. The new module proved capable of accurately analyzing the fluid flow, heat transfer, and the conservation of momentum as well as energy in pipes and channel networks. A description of the method follows.

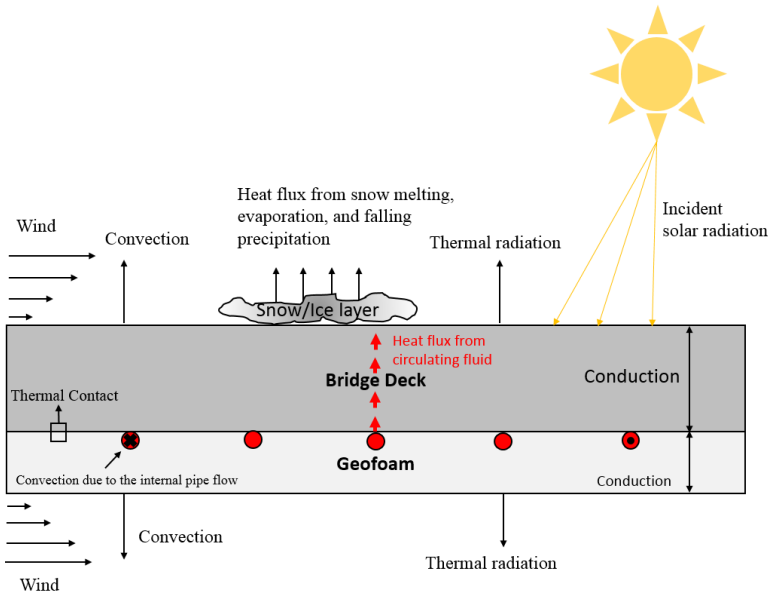

Figure 5-5. Cross-sectional view of heat transfer mechanisms in an externally heated bridge deck (Li et al. 2020)

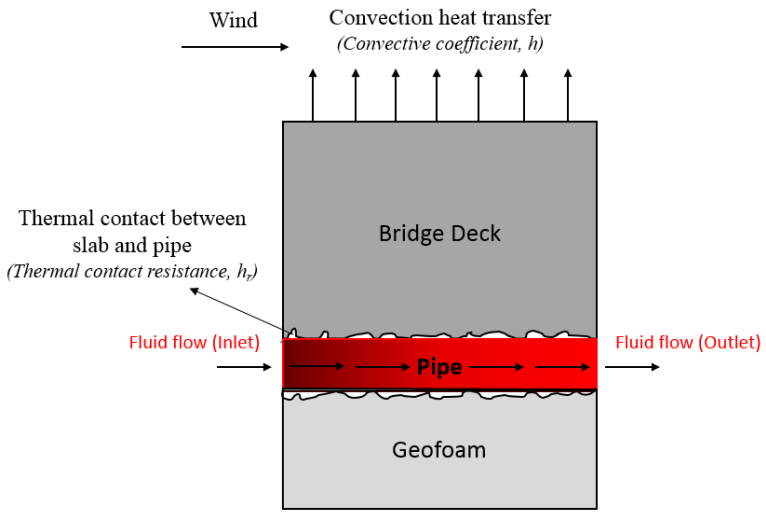

Figure 5-6. Side view of interface heat transfer in an externally heated bridge deck (Li et al. 2020)

5.3.1.1 Fluid Flow Analysis

Due to the larger size of the mock-up bridge deck model on-site, a pipe flow module was employed to model the heat transfer processes within the deck to increase the computational efficiency. Furthermore, this study's objectives seek to increase a comprehensive understanding of the thermal energy processes between the heat-carrying fluid and the bridge deck rather than directly modeling the fluid flow circulation in a pipe. After the pipe flow module application, the tangential cross-sectional average velocity along the edge is solved by using Edge elements instead of generating the full cross-sectional 3D mesh of the pipe. This indicates that pipe flow interface can use the line elements to simplify the 3D fluid flow equation to a 1D approximation, as shown in Fig. 5-7. Based on this assumption, only the variations of modeled variables occurring along the pipe length need to be considered in the pipe flow module, which avoids computationally expensive processes.

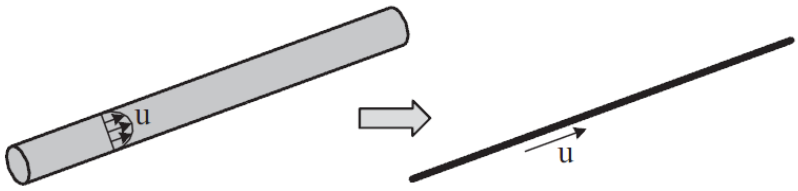

Figure 5-7. 1-D "pseudo-pipe" elements instead of 3D modeling of pipes (COMSOL 2016)

Heat transfer for an incompressible fluid flowing in a pipe can be expressed in the energy equation, calculated as (COMSOL 2016):

$$\rho A C_p \frac{\partial T}{\partial t} + \rho A C_p \mathbf{u} \cdot \nabla T = \nabla \cdot Ak\nabla T + f_D \frac{\rho A}{2d_h} |\mathbf{u}|^3 + Q_{wall} \quad (5\text{-}1)$$

The first term on the left-hand side is the cumulative contribution, which can be neglected when the temperature responses within the bridge deck reach an equilibrium state. Energy transport resulting from the fluid flow is depicted by the second term on the left-hand side, expressed as a convective. The second term on the right-hand side describes friction heat dissipated due to viscous shear. Q_{wall} corresponds to the external heat exchanger through the pipe wall, which can be expressed as (COMSOL 2016):

$$Q_{wall} = (hZ)_{eff} \cdot (T_{ext} - T) \quad (5\text{-}2)$$

Eq. (5-2) accounts for the radial heat transfer from the surroundings into the pipe, in which the internal film resistance h_{int} and the thermal resistance $1/k_p$ of the pipe dominate the effective value of the heat transfer coefficient $(hZ)_{eff}$. For a circular pipe with a non-layered cross-section, $(hZ)_{eff}$ can be expressed as (COMSOL 2016):

$$(hZ)_{eff} = \frac{2\pi}{\frac{1}{r_i h_{int}} + \frac{\ln(r_0/r\,i)}{k_p}} \quad (5\text{-}3)$$

The internal film resistance in Eq. (5-3) can be determined by:

$$h_{int} = Nu \cdot \frac{k_f}{2r_i} \tag{5-4}$$

The fluid flow regime is related to the Nusselt number. The laminar pipe flow is equal to 3.66. The following correction can be utilized to evaluate the Nusselt number for turbulent flow conditions (COMSOL 2016).

$$Nu = \frac{(f_D/8)(Re - 1000)Pr}{1 + 12.7(f_D/8)^{1/2}(Pr^{2/3} - 1)}, \qquad \begin{matrix} 0.5 < Pr < 2000 \\ 3000 < Re < 6 \times 10^6 \end{matrix} \Bigg\} \tag{5-5}$$

5.3.1.2 Evaluation of The Required Heat Flux for Deicing on The Deck Surface

The required heat flux for deicing the deck surface can be expressed in terms of energy balance, which is shown as:

$$q_o'' = q_{conv}'' + q_{rad}'' + q_{solar}'' + q_p'' + q_e'' \tag{5-6}$$

where, q''_o is the required heat flux geothermal power input to melt snow or ice (W/m^2); q''_{conv} is the convective heat flux (W/m^2); q''_{rad} is the heat flux associated with infrared radiation; q''_{solar} is the heat flux attributable to solar radiation (W/m^2); q''_p is the heat flux under the consideration of precipitation (snow) (W/m^2), and q''_e is the evaporation heat flux.

(1) Convective Heat Transfer

In this study, the convective heat flux is due to the externally forced airflow through the exposed deck surface and can be determined as (COMSOL 2016; Incropera et al. 2007)

$$q_{conv}'' = h \cdot (T_s - T_{air}) \tag{5-7}$$

$$h = \begin{cases} 2 \cdot \frac{k_{air}}{L} \cdot \frac{0.3387 Pr^{1/3} Re_L^{1/2}}{(1 + (\frac{0.0468}{Pr})^{2/3})^{1/4}} & if\ Re_L \le 5 \cdot 10^5 \\ 2 \cdot \frac{k_{air}}{L} \cdot Pr^{1/3}\left(0.037 Re_L^{4/5} - 871\right) & if\ Re_L > 5 \cdot 10^5 \end{cases} \tag{5-8}$$

$$Re_L = \frac{\rho u L}{\mu} \tag{5-9}$$

where, h is the convective heat transfer coefficient (W/(m^2·K)), which can be calculated by the pre-set equations in COMSOL; thus, T_s is the deck surface temperature (K). T_{air} is the absolute air temperature near the ground (K), which is equal to the ambient temperature in this study. k_{air} is the thermal conductivity of air (W/(m·K); L is the characteristic linear dimension (m); Re_L is the Reynolds number, and P_r is the Prandtl number (for air, it is around 0.72). ρ is the fluid density (kg/m^3); u is the velocity of the fluid with respect to the object (m/s), and μ is the dynamic viscosity of the fluid, kg/(m·s). In this study, the collected wind speeds were interpolated in COMSOL and applied to the exposed surfaces of the bridge deck to estimate the convective heat transfer between the bridge and the environment.

(2) Radiative Heat Transfer

Eqs. (5-10) and (5-11) express the heat fluxes attributable to the outgoing infrared solar radiation and incoming solar radiation, respectively. Therefore:

$$q''_{rad} = \varepsilon \cdot \sigma \cdot (T_s^4 - {T_{sky}}^4) \quad (5\text{-}10)$$

$$q''_{solar} = \alpha \cdot I \quad (5\text{-}11)$$

where, ε is the surface emissivity of the concrete bridge deck with a value of 0.9 (Incropera et al. 2007); σ is the Boltzmann constant of 5.6710^{-8} W/m^2·K^4; α is the absorptivity coefficient of the concrete slab surface, which is related to the property and condition of the concrete surface and ranges from 0.5 to 0.8 (Xiao et al. 2013). I is the direct radiation incident to a horizontal surface, which can change at any time. In this study, an inward heat flux (solar heat source) which changes with I was applied on all exposed surfaces of the bridge deck as the heat flux due to solar radiation. T_{sky} is the sky temperature (K), which is dependent on T_{air} and T_{dew} (dew-point temperatures near the ground (°C)), and cloud cover and can be calculated as (Duffie and Beckman 2013):

$$T_{sky} = T_{air} \cdot (0.004T_{dew} + 0.8)^{0.25} \quad (12)$$

(3) Consideration of Snow

Liu (2005) and Liu et al. (2007a) modeled an extremely complex snow melting process. In this research, the numerical models are not employed to replicate the snow melting process rather than provide an accurate evaluation of energy consumption required to melt falling or accumulated snow on the bridge deck's surface. Therefore, a good understanding of existing snow conditions on a bridge deck surface is necessary to achieve this goal.

Since the distribution of the heated zone at the bridge deck surface is not entirely uniform, three surface conditions may exist at the same time at different locations of the bridge deck surface where: no snow has accumulated, snow is beginning to be accumulated, and snow has accumulated on the deck surface. The following simple equation introduced by Bowers (2016) was applied to estimate the heat flux for deicing a deck surface:

$$q_p'' = \dot{m}_s \cdot \left[H_{f,s} + C_{p,s}(-T_a) + c_1 C_{p,w}\right]/A \quad (5\text{-}13)$$

Where, the heat flux is equal to the multifaction of the mass rate of snowfall, $\dot{m}_s$ (kg/s), and it is also the sum of the three right-side terms. The first right term, $H_{f,s}$ (334 kJ/kg), describes the required energy to melt the snow and represents the heat of fusion of snow. The multifaction of the heat capacity of snow, $C_{p,s,}$, and the temperature difference between the ambient temperature and 0 °C is the second term, thereby highlighting the energy needed to raise the snow's temperature to the freezing point. Here, we note that the falling temperature of the snow is assumed to be the same as the ambient temperature. The third term considers how much energy is required to raise the melted snow temperature to the liquid film temperature. c_1 is the conversion factor with the unit K. Based on Bowers (2016), c_1 was set to be 1/10 in this study. Notably, the perfect drainage on the deck surface was hypothesized in this study since Liu et al. (2007a) also utilized this

assumption in their complex snow melting models. Therefore, the heat flux associated with evaporation q''_e was neglected. A is the surface area of the bridge deck.

The snow melting flux was estimated by using Eq. (5-13) was set as a boundary condition outwardly applied on the deck surface to investigate the snow melting performance of this external heating system. The convective and radiative heat losses on the deck surface during a snow covering were also considered, which were reduced due to the insulation effect of snow/ice. The specific investigation is described in Section 5.3.4.3. Based on a perfect drainage assumption on the bridge deck surface (Liu et al. 2007a), the heat loss associated with evaporation is not considered in this study.

5.3.2 A 3D Multiphysics FEM Model for the Heated Bridge Deck

A 3D finite element bridge deck model was developed in COMSOL to replicate the mock-up bridge constructed in the field, as shown in Fig. 5-8. The bridge deck concrete slab and spray foam were modeled directly as a solid. The circulation loops were modeled using 1D line elements to simplify the 3D solid domain, with a thermal conductivity and wall thickness that was directly input in the wall heat transfer boundary condition as initial values. The 3D fluid flow through the pipes was simplified to a 1D approach, which was coupled with the temperature domains by use of the pipe flow interface. Weather conditions, including wind speed, ambient temperature, snow-melting heat flux, and heat flux due to solar radiation, were interpolated in COMSOL as initial values. A transient model was applied to analyze the time-dependent heating processes for the previously mentioned three system operations under corresponding weather conditions.

A sufficiently accurate mesh is critical to the reliability of the numerical analysis of the heat transfer that takes place within the bridge deck. In this study, the free tetrahedral mesh method was utilized to generate concrete and spray foam domains. The hydronic loops were not modeled

as a full cross-sectional 3D domain. Instead, 1D line elements were developed in the pipe flow module to simplify the geometric configuration. A mesh sensitivity analysis was conducted to balance the computational consumption and numerical accuracy under different mesh quality standards. The finest pre-defined mesh quality listed in COMSOL cannot provide a sufficiently accurate mesh system for the material domains of the bridge deck, while several faces within the narrow region are much smaller than the specified minimum element size. Therefore, a manual adjustment of the element size parameter was performed in this study to solve this issue. The optimized maximum and minimum element sizes for both concrete and spray foam domains were respectively input in COMSOL as 0.07 m and 0.0007 m, which generated the final mesh elements of the FEM bridge deck model, as illustrated in Fig. 5-8.

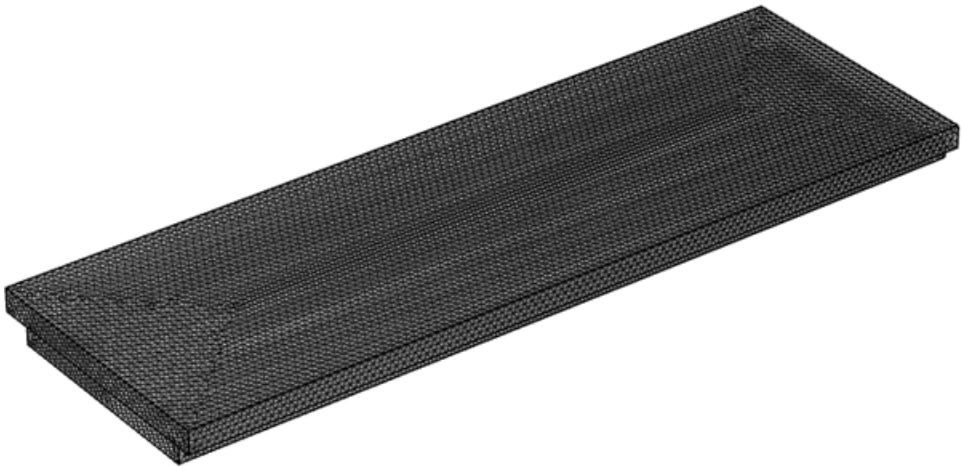

Figure 5-8. Finite element mesh of the bridge deck model

5.3.3 Initial and Boundary Conditions

The measured inlet fluid temperatures during the heating Test #2 and the heating and deicing Test #3 response tests viewed as a boundary condition of the inlet were interpolated in COMSOL. The fluid flow regime in the pipe flow module is dependent on the Nusselt number, which accounts for the ratio of heat transfer by convection to conduction through a boundary. Predefined equations can calculate the Nusselt number in COMOSL using the input thermal

properties and the flow rate of the circulating fluids plus the pipe configuration. With the help of Eq. (5-5), the fluid regime in the pipe can be determined automatically. The fluid flow was coupled with the heat transfer module by using a non-isothermal pipe flow interface. The measured ambient temperatures onsite were set as the initial temperatures for the heated bridge deck consisting of the concrete slab, spray foam, and hydronic loops, which indicated that the mock-up bridge deck could now reach an equilibrium state based on the environmental circumstances at the initiation of numerical simulation. Notably, sky temperatures calculated by the corresponding ambient and dew temperatures through Eq. (5-10) were interpolated in COMSOL for radiation heat transfer modeling. Module interfaces, including the pipe-concrete slab and the pipe-geofoam slab, were set as perfect surface contacts in this study to increase the computational efficiency. The internal film resistance and wall resistance mentioned in Eqs. (5-2) and (5-3) account for the interface contact between circulating fluid and the pipe by inputting the major parameters, including inner/outer radii and the thermal conductivity of the pipe. The existing gaps between the concrete bottom surface and spray foam top surface were developed as a thermal contact model in COMSOL to deal with the poor contact feature at the interface. Based on contributions from Li et al. (2020), we utilized the h_c (constriction conductance) value of 2.5 W/(m^2·K) and the h_g (gap conductance) value of 95 W/(m^2·K), which signifies a better surface contact in the interface zone. The phase change of snow/ice was not directly modeled in COMSOL but was investigated in terms of an outward boundary condition applied to the deck surface to estimate how much energy was required for snow/ice melting on the deck surface, as mentioned in Section 5.3.1.2. The material properties adopted in the COMSOL model were determined either from previous studies (Acharya et al. 2014; Ruttanaporamakul et al. 2016; Yu et al. 2020) or the reference values provided in COMSOL (2016) and summarized in Table 5-2.

Heat transfer processes, including conduction, convection, and radiation heat transfer, were developed in COMSOL. The conductive heat transfer within the solid domains is dependent on the pre-input thermal conductivity of utilized materials. Both convective and radiative heat transfer take place on all surfaces that are exposed to the environment. The bridge deck's top surface was subjected to significant heat exchange behaviors between the bridge deck and the environment. The convection heat transfer is dominated by recorded wind speeds that were interpolated in COMSOL. Radiation heat transfer was modeled by applying boundary conditions referred to as a "diffuse surface" to each exposed surface with different surface emissivity rates in utilized materials, as shown in Table 5-2. For solar radiation, an inward heat flux representing solar radiation was directly applied to the exposed surfaces.

5.3.4 Winter Test Simulations

This section describes the comparisons of temperature variations between experimental and numerical results for the mock-up heated bridge deck under three different field test scenarios, including non-heating, heating, and heating and deicing operations. The numerical investigations were performed to provide a comprehensive evaluation of the temperature responses and heating performance within the bridge deck through a transient approach using the corresponding measured data for the three practical operations. The comparison results were utilized to perform the model error analysis.

Table 5-2. Summary of material properties considered in numerical simulations (Acharya et al. 2014; COMSOL 2016; Ruttanaporamakul et al. 2016; Yu et al. 2020)

Materials	Properties	Values	Units
Water (liquid)	Dynamic viscosity	0.00273	Pa·s
	The ratio of specific heat	1.0	-
	Heat capacity at constant pressure	4180	J/(kg·K)
	Density	1000	kg/m^3
	Thermal conductivity	0.61	W/(m·K)
Concrete	Density	2300	kg/m^3
	Thermal conductivity	2.2	W/(m·K)
	Heat capacity at constant pressure	1000	J/(kg·K)
	Surface emissivity	0.91	-
PEX pipe	Density	938	kg/m^3
	Heat capacity at constant pressure	950	J/(kg·K)
	Thermal conductivity	0.51	W/(m·K)
Spray Foam	Density	21.6	kg/m^3
	Thermal conductivity	0.028	W/(m·K)
	Heat capacity at constant pressure	1300	J/(kg·K)
	Surface emissivity	0.60	-

5.3.4.1 Non-heating FEM Model (Corresponding to Test #1)

Numerical analysis with a transient method was performed to understand the temperature distribution within the mock-up bridge deck under a no-heat operation (Test #1). The measured

ambient temperature and wind speed were viewed as initial values and were interpolated in COMSOL. As mentioned in Section 5.2.3, the comparison results between numerical outputs and measured results including the 10 circled thermocouple temperature responses at the bottom surface of the externally heated zone in Fig. 5-3(a) and thermal wire cable embedded one-inch below the deck surface in Fig. 5-3(b) as illustrated in Figs. 5-9 and 5-10, respectively. During the installation of temperature sensors, special care was taken to maintain the actual locations of temperature sensors so as to carefully follow the instrumentation plan without error, as shown in Figs. 5-3(a) and (b). Therefore, the determined locations of temperature sensors in the FEM model based on the instrumentation plan were assumed to be identical to those in the existing mock-up bridge deck in the field. The comparison results are employed to perform the model error analysis in Section 5.3.5.

Fig. 5-9 presents the time-dependent experimental and simulated temperature variations at the base of the externally heated concrete along with the change of ambient temperature. Notably, both experimental and simulated temperature responses at the bottom surface of the bridge deck show a two-hour delay compared to the ambient temperature variations since it takes time for the ambient temperature to affect the deck bottom surface, which is encapsulated by spray foam for heat insulation. Fig. 5-9 shows a reasonably good agreement between the measured and computed temperature responses. The maximum difference between these two measurements for each thermocouple is 1.8 °C (3.2 °F), ranging from 10 to 16 hours.

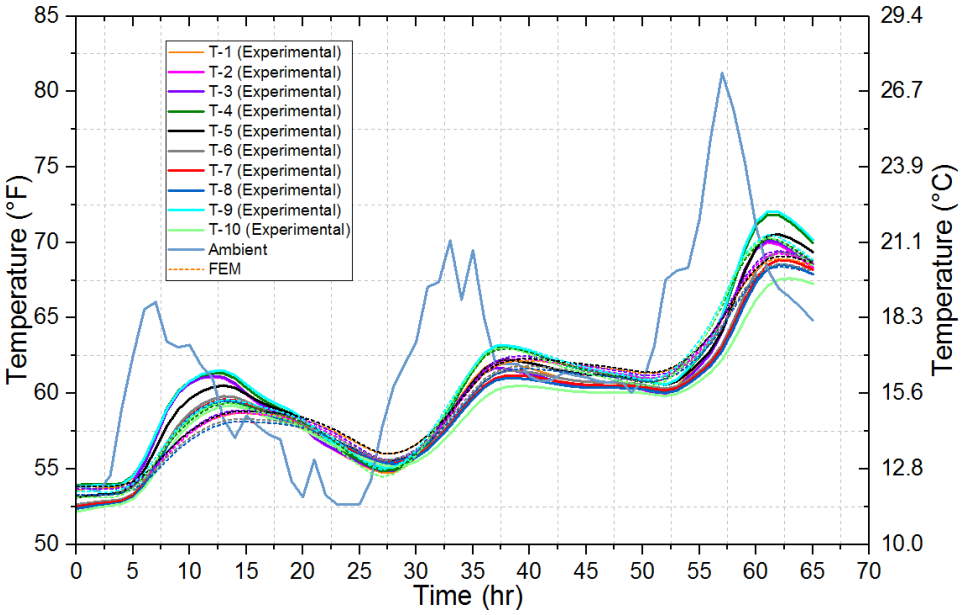

Figure 5-9. Comparisons of experimental and numerical results based on temperature variations at the base of the externally heated slab along with the change of ambient temperature during the no-heat operation

Since the temperature distribution was much more uniform in the areas near the concrete top surface than that near the bottom surface close to the heat source (Li et al. 2020), and in order to avoid too many temperature curves lumping together in a figure, the average values of transient temperature responses measured from 53 pre-configured sensor nodes in the thermal wire cable, which were checked for the general temperature variations one inch below the deck surface, as shown in Fig. 5-10. Compared to Fig. 5-9, the variation tendency of experimental and simulated temperature responses one inch below the deck surface can have an approximate synchronization with the change of ambient temperature due to the shorter distance to the exposed surface boundary. Fig. 5-10 shows the average temperature one inch below the deck surface from numerical outputs and provides a reasonable estimate of the experimental results since the maximum temperature deviator is within 1 °C (2 °F).

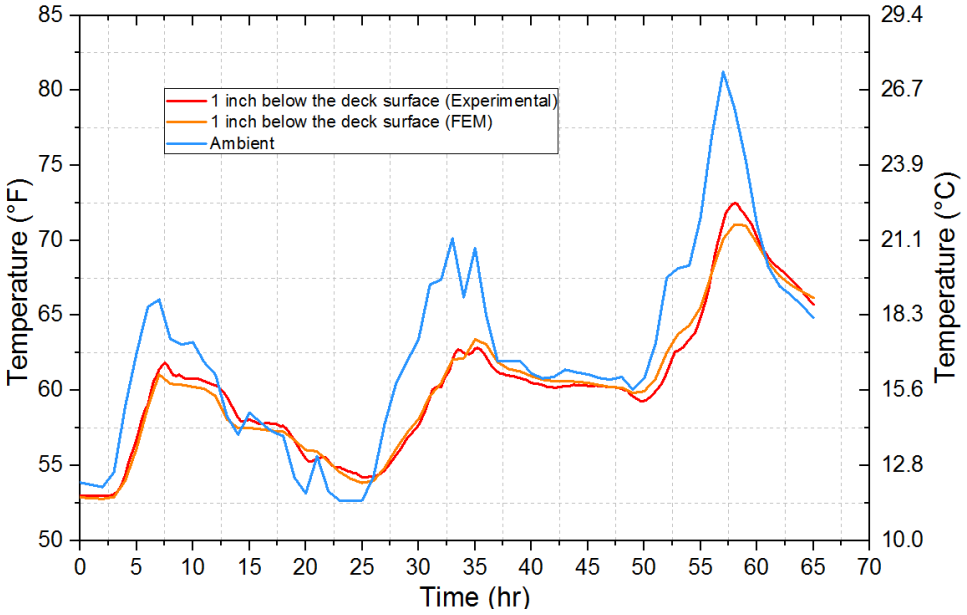

Figure 5-10. Comparison of experimental and numerical results based on temperature variations one inch below the deck surface along with changes in ambient temperature during no-heat operation

5.3.4.2 Heating FEM Model (Corresponding to Test #2)

This section describes a numerical analysis of the mock-up heated bridge deck heating processes in the field. The heated bridge deck and the ambient air were set to have the same temperature. The aforementioned environmental factors were interpolated in COMSOL as initial conditions. A transient method with a time duration identical to that of the field heating test was utilized to develop the computational time-dependent heating curves that were compared to the field-measured data from temperature sensors. Experimental and numerical comparisons were conducted to measure the temperature responses of the thermocouple inlets and outlets.Ten circled thermocouples were installed at the bottom surface of the externally heated zone, and the thermal wire cable with pre-configured sensor nodes placed one inch below the deck surface are shown in Figs. 5-11 to 5-13, respectively.

(1) Comparison of Variations of Inlet and Outlet Temperatures

Fig. 5-11 shows the measured and simulated temperature variation of the inlet and outlet heat carrier fluid within the bridge deck. It is noted that the temperature distribution within the heated bridge deck reached an approximate equilibrium with the ambient temperature before the heating test was initiated. The heating system was turned on after 36 hours. We observed that both inlet and outlet temperatures experience a rapid increase due to the operation of the heat pump. During the heating process, the fluctuations of the fluid temperature may have resulted from variations in the ambient temperature and output power of the heat pump. The variation tendency of inlet and outlet temperature experienced a reasonably good agreement. The measured heating fluid with an average temperature of 41.1 ˚C (inlet) was supplied to the bridge deck and had an approximate temperature drop of 3 ˚C (5 ˚F) after circulating through the deck, recorded as outlet temperature (38.3˚C). The simulated outlet temperatures had an acceptable match with the measured data, with an average temperature deviation of less than 0.5 ˚C (1 ˚F).

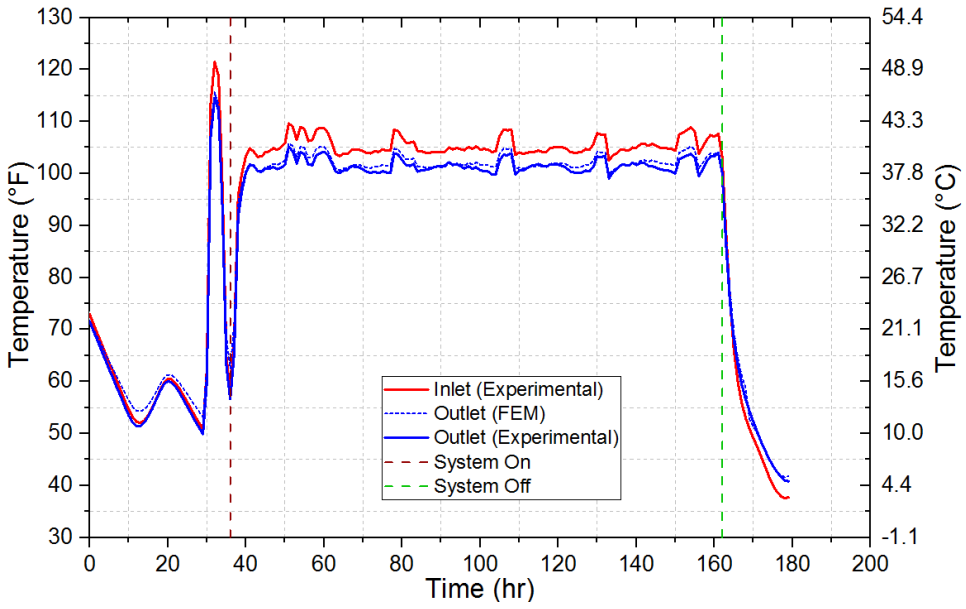

Figure 5-11. Comparisons of experimental and numerical results based on the inlet and outlet temperatures during the heating test

(2) Thermocouple responses from the bottom surface of the externally heated zone

Fig. 5-12 compares the simulated temperature responses of the thermocouple set T-1 to T-10 with those measured experimentally. Both measured and simulated temperature responses are divided into two groups. The thermocouples from the group with the relatively higher temperature responses, including T-10, T-11, T-12, are located in the bridge deck's middle section. One possible reason is that no significant external forced convective boundary conditions affect this zone. Compared to these three middle-zone thermocouples, T-9 recorded a much lower temperature since it has a shorter distance to the bridge deck side. T-16 also recorded higher temperatures since the bridge side near T-16 has the most incident solar radiation, which supplies more heat in this zone. The remaining five thermocouples with relatively lower temperatures (T-1–T-5) are located near the bridge deck side, where convective heat loss plays a dominant role. EZ0T16 is located in the middle-zone of the whole bridge deck, which does not have significant boundary effects resulting from convection heat loss. Therefore, its temperature readings are also reasonable.

Similar to the non-heating case, both measured and simulated temperature responses at the bottom surface of the bridge deck have two-hour delays compared to the ambient temperature variations. Notably, the lowest numerical outputs obtained during each cyclic variation of ambient temperatures were much lower than those from the measured results. One possible reason for this may be that the bonding between concrete and pipe as well as pipe and spray foam in COMSOL is better than the actual conditions, which can decrease the lateral heat losses from the gap between the slab bottom surface and the foam top surface. Therefore, a relatively higher temperature was recorded in COMSOL Besides, the better homogeneity of the utilized materials in the FEM model also contributes to increasing this heating system's performance. Despite that, the tendency

variations between the experimental measurements' and numerical simulations' temperature responses for each thermocouple from T-1 to T-10 proved compatible in their ability to provide a good match.

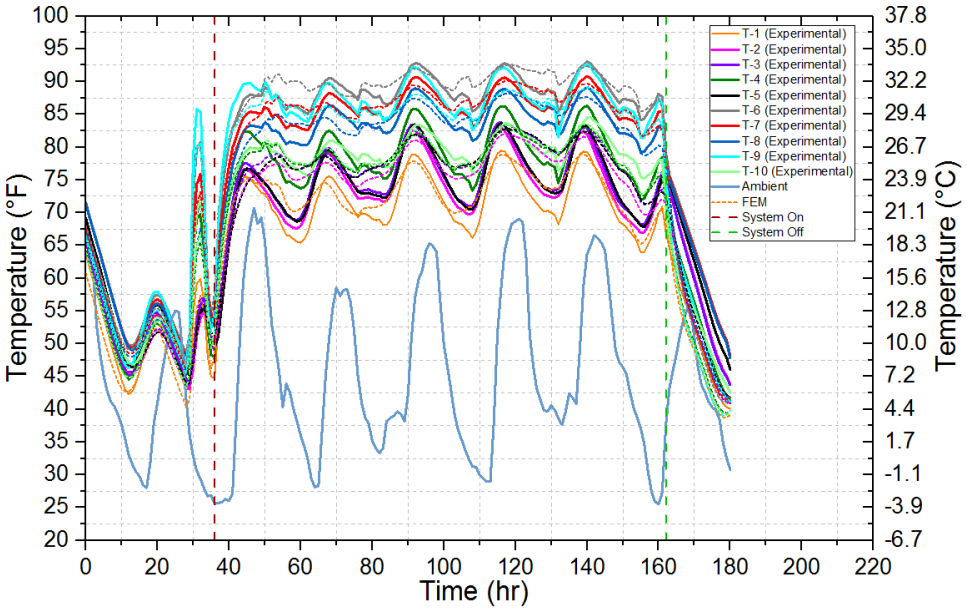

Figure 5-12. Comparison of temperature responses based on experimental records and numerical analyses of thermocouples T-1 to T-10 during the heating operation

(3) Thermal wire cable embedded one inch below the deck surface

Fig. 5-13 presents both average temperature responses from experimental results and numerical outputs one inch below the deck surface able to reach above the freezing temperature due to the contribution of the auxiliary heating unit, which was much higher than the recorded ambient temperature for each circle. Similar to temperature comparisons of the concrete bottom surface, the lowest numerical outputs for each cyclic variation of ambient temperatures were much lower than those from measured results due to the similar possible reasons mentioned in Section 5.3.4.1. Nevertheless, the tendency variations of numerical simulation temperature responses agree with those from experimental measurements.

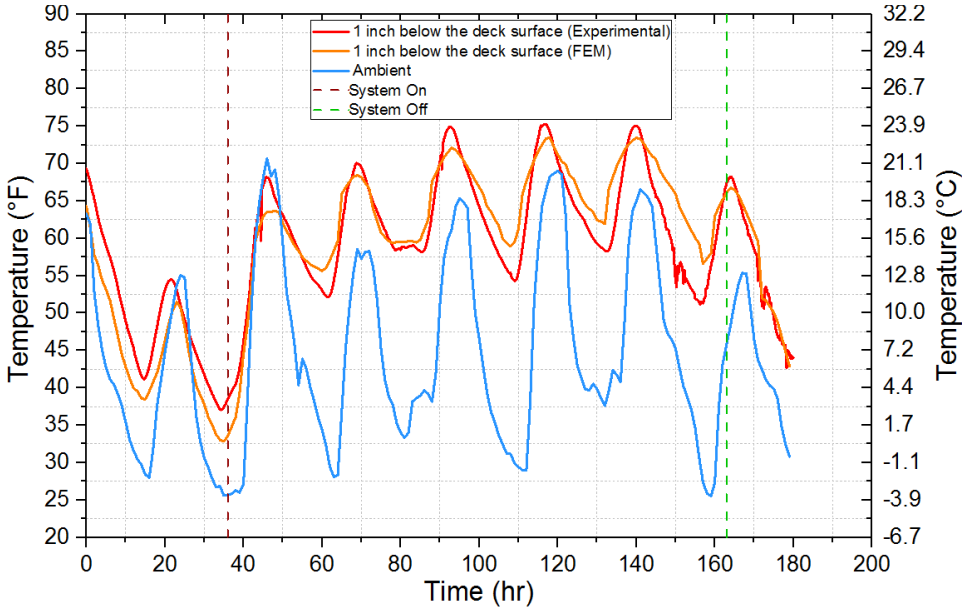

Figure 5-13. Comparison of temperature responses based on experimental results and numerical analyses of thermal wire cable during the heating operation

5.3.4.3 Heating and Deicing FEM Model Corresponding to Test #3

Liu (2005) and Liu et al. (2007a) performed comprehensive modeling of the snow melting process. In this study, numerical models are not employed to replicate the snow melting process. Instead, they provide an accurate evaluation of the energy requirement for snow/ice melting on the bridge deck surface. This section deals with the numerical investigation that focuses on the mock-up bridge deck's deicing and heating processes.

(1) Analysis of experimental data

Figs. 5-14 and 5-15 illustrate the experimental temperature response records for thermocouples T-1 to T-10 and the thermal wire cable during the heating and deicing operation, respectively. As mentioned in Section 5.2.4.3, the snow simulation operation was turned on at 5:40 a.m. on 2/8/2019. The surface of the externally heated zone became wet due to the melting of ice pellets while a uniform ice layer was accumulated on the non-heated surface. During and after the deicing phase (t = 59 hours), no significant drop occurred in temperatures acquired from

thermocouples T-1 to T-10 (installed on the concrete bottom surface) nor in the thermal wire cable embedded one inch below the concrete top surface. Instead both the temperatures from the thermocouples and thermal wire cable remained approximately constant, which indicates that the heat fluxes required to heat the bridge deck under a deicing operation are usually very similar or the same. The reason for these similarities is because the heat losses associated with convection and radiation will reduce during deicing processes due to the insulating effect of ice. The amount of decreased heat losses can approximately offset the heat fluxes utilized in deicing. Therefore, the temperature did not remarkably vary during and after the operation of the snow simulation. Notably, the melted snow disappeared rapidly due to a perfect drainage assumption on the bridge deck surface (Liu et al. 2007a), which is why the heat loss attributed to evaporation was not considered in this study. Figs. 5-14 and 5-15 also show the ambient temperature from 58 hours to 62 hours as approximately constant.

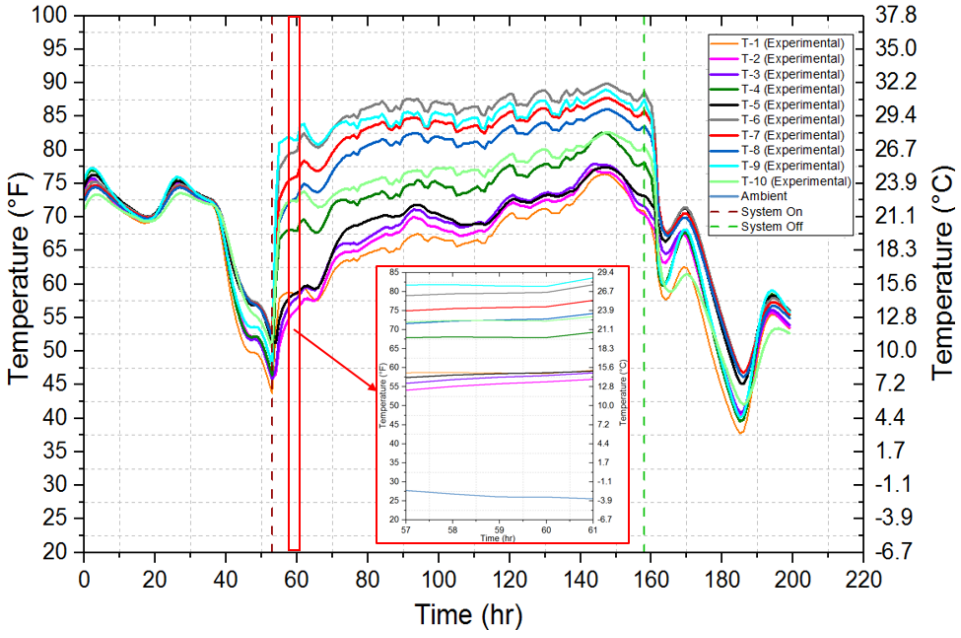

Figure 5-14. Temperature responses based on experimental records of thermocouples T-1 to T-10 measurements during the heating and deicing operation

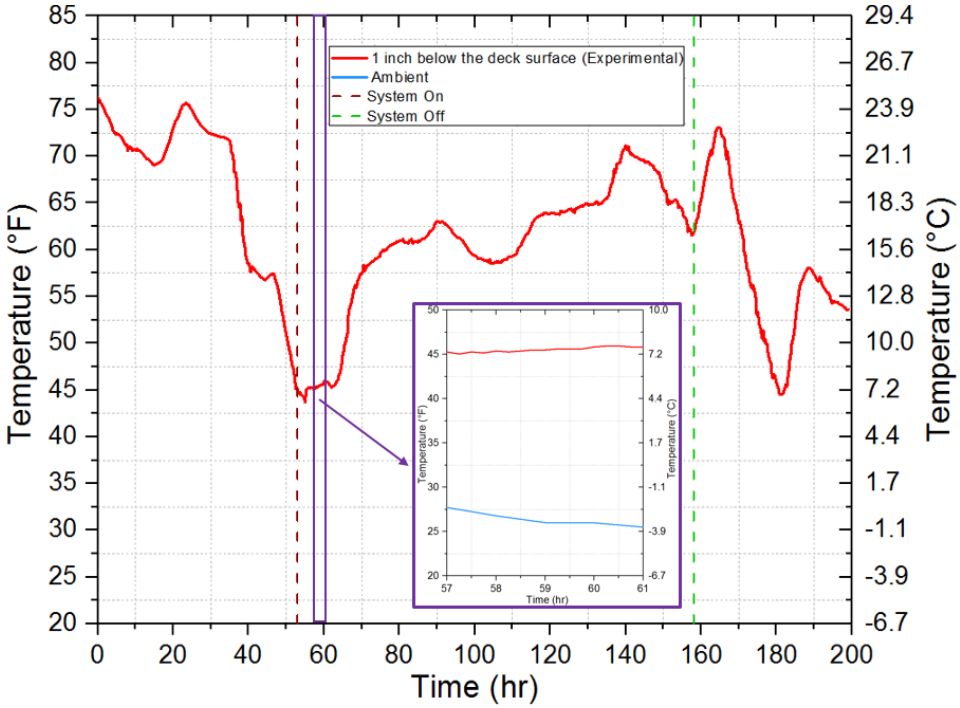

Figure 5-15. Temperature responses from experimental results for the thermal wire cable during heating and deicing operation

Because the surface of the heated zone remained wet for a couple of hours after the snow simulation test, we assumed that the heat flux attributed to evaporation was neglected during this deicing process. In addition, the heat flux from solar radiation was not considered either since the deicing test was performed before dawn. Thus, the only limited heat losses due to convection and radiation was balanced with the heat flux required for deicing, which can be expressed as:

$$(1 - A_r) \cdot (q''_{conv} + q''_{rad}) = q''_p \quad (5\text{-}14)$$

where, A_r is the equivalent ice-free area ratio which is viewed as an insulation factor that can deal with the insulating effect of the accumulated ice/water film on the surface, which stated that only the exposed surface areas experience the effects of convection (q_{conv}") as well as radiation (q_{rad}") heat transfer. q_p" is the required heat flux for deicing at the deck surface (W/m^2).

With the assistance of Eq. (5-14) and a series of data input including the assumed rate of the icefall, the thermal properties of air, wind speed, and ambient temperature during the operation of snow simulation, the approximate A_r value of 0.23 can be estimated. Based on Eq. (5-13), the calculated value of 20.4 W/m^2 under a mass rate of icefall (0.001 kg/s) is utilized as a boundary condition outwardly applied on the deck surface to represent the heat flux needed for deicing. Compared to convective heat loss, the radiative contribution plays a minor role in the combined heat flux since there is no significant difference in surface emissivity between water and concrete. Besides, the ambient temperature and dew point remained approximately constant during the deicing operation, which did not result in a remarkable variety of radiation. Therefore, the convective contribution dominated the heat loss on the deck surface. During the deicing operation, the wind speed utilized in COMSOL was reduced from 2 m/s to 0.5 m/s to limit the convective heat loss. The amount of the decreased convective heat loss contributed to the primary heat flux requirement for deicing.

Similar to the heating operation, the initial temperatures of the heated bridge deck and the ambient air were set to reach an equilibrium state. The interpolated environmental factors were viewed as initial conditions. Time-dependent approaches were utilized to perform the heat transfer analysis between the experimental results and numerical outputs, as depicted in the next section.

(3) Comparison of Inlet and Outlet Temperature Variations

Fig. 5-16 shows the measured and simulated temperature variations of the inlet and outlet heat carrier fluid circulating within the bridge deck during the deicing and heating test. The heating system was turned on after 52 hours. Similar to the heating case, the variation tendency of inlet and outlet temperatures had good agreement. The average outlet temperature difference between

measured results and numerical outputs is limited to 1 ˚C (2 ˚F), which means that the simulated outlet temperatures can reasonably match the experimental measurements.

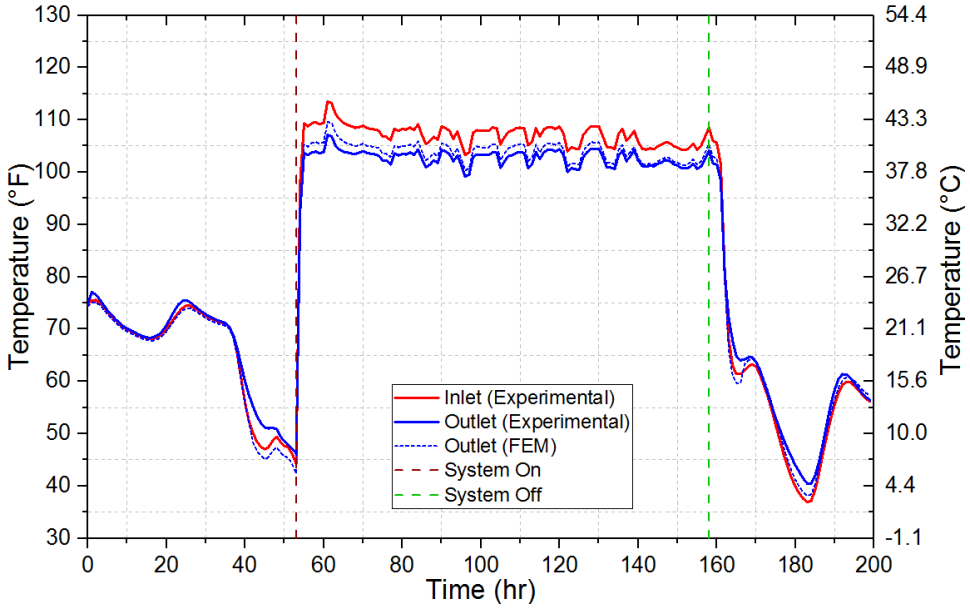

Figure 5-16. Comparison of experimental and numerical inlet and outlet results, as well as temperatures during the deicing and heating test

(4) Thermocouple responses located at the bottom surface of the external heated zone

Fig. 5-17 shows the heating curves of transient thermocouple temperatures at the bottom of the externally heated zone, based on experiments and numerical analyses. In general, the simulated temperature curves are in good agreement with the experimental measurements. Similar to the case of the heating operation described in Section 5.3.4.2, the thermocouples located in the middle of the bridge deck captured relatively higher temperatures, including T-10, T-11, and T-12. The temperatures acquired near the deck sides, such as T-1, T-2, T-3, and T-5, are lower due to the more significant convective boundary conditions. During the deicing operation (t = 59 hours), the temperature variation from numerical outputs is similar to that of the experimental results and does not experience a significant temperature drop.

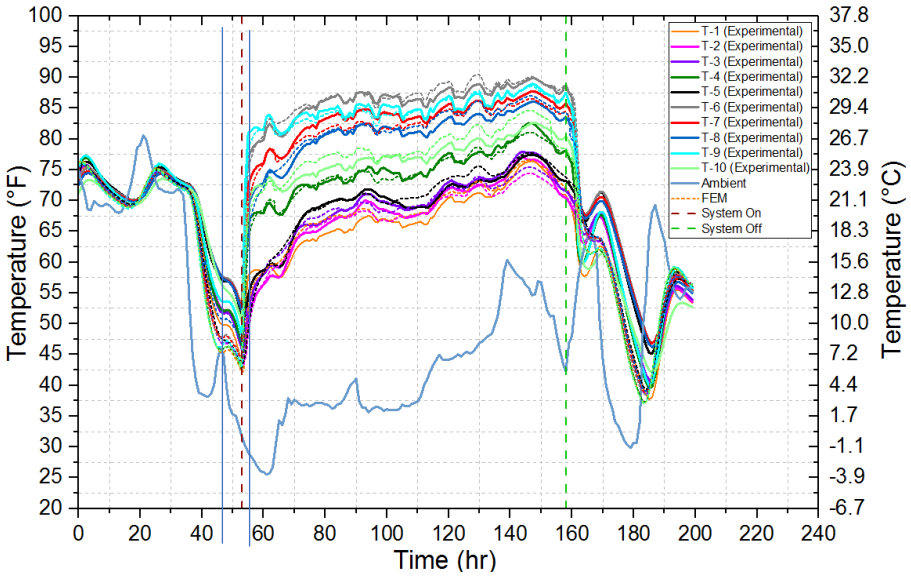

Figure 5-17. Comparison of experimental records and numerical analyses results on temperature responses for thermocouples T-1 to T-10 during the heating and deicing operation

(5) Thermal wire cable embedded one inch below the deck surface

Fig. 5-18 presents the average measured and computed temperature variations of the thermal wire cable embedded one inch below the deck surface. When the heat pump is turned off, the temperature responses from the externally heated zone can attain a close agreement with the measured ambient temperature from the thermocouple installed on site. After the onset of the heating system, the temperature responses in the heated zone one inch below the deck surface started to rise and went above the freezing temperature due to the effective heating contribution. During the deicing period (t = 59 hours), the simulated temperature responses were relatively higher than those from experimental results, similar to the results in Fig. 13 due to the lower lateral heat losses and better material homogeneity in COMSOL. However, a reasonable agreement was obtained between the recorded and simulated temperature responses during this heating and deicing operation.

(6) Heat Flux and Heating Efficiency Analysis

The following equation evaluates how much heat was transported from the hydronic heating system to the deck with the given inlet and outlet temperatures.

$$Q_{supplied} = m \cdot c \cdot (T_{inlet} - T_{outlet}) \quad (5\text{-}15)$$

Based on the contributions from Yu et al. (2020) and Li et al. (2020), the heat transfer efficiency of the external heating system, the ratio between the heat transferred to the deck surface, and the total heat supplied from the heat source were expressed as:

$$Heat\ Transfer\ Efficiency\ (\%), e_{heat} = \frac{Q_{surface}}{Q_{supplied}} \quad (5\text{-}16)$$

The numerical outputs of the total supplied heat and heat transferred to the deck surface were 4,514.4 W and 3,220.12 W, respectively. Based on Eq. (5-16), the heat transfer efficiency under the heating and deicing operation was 71.3%, which is greater than the experimental efficiency of 55% (Habibzadeh-Bigdarvish et al. 2020) measured from the thermocouples installed within the deck. One possible reason for that is the mismatch of the outlet temperatures between experimental measurements and numerical outputs, as shown in Fig. 5-16. Although the outlet temperature match is reasonable, it is multiplied by the heat capacity to calculate the supplied heat using Eq. (5-15). Compared to published results from Li et al. (2020), the system efficiency in the field (71.3%) is relatively lower than that in a laboratory (76%) since more heat losses associated with snow melting were analyzed in this study.

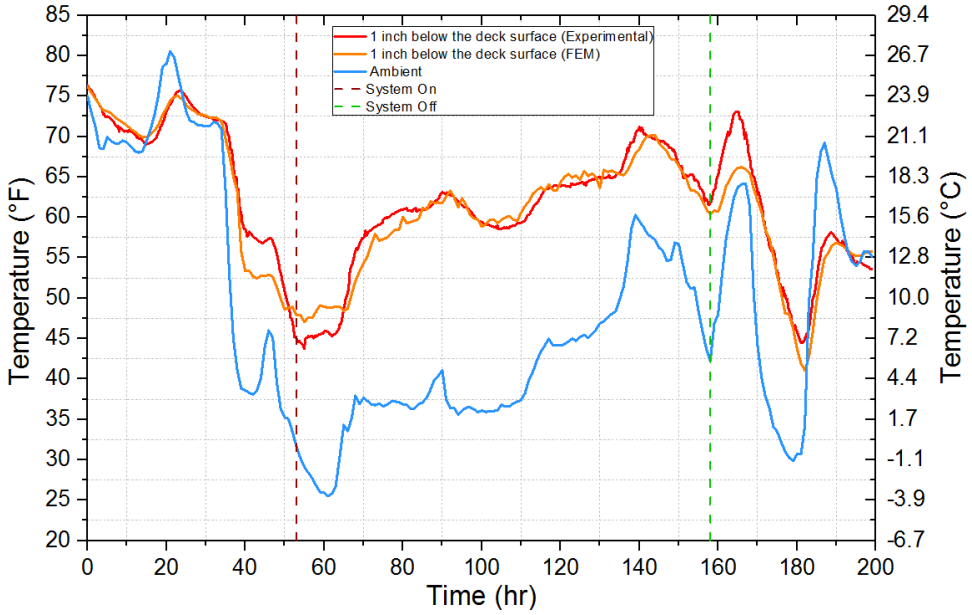

Figure 5-18. Comparison of experimental and numerical temperature responses for thermal wire cable during the heating and deicing operation

5.3.5 Model Error Analysis

Regression analyses were conducted on the experimental and numerical temperature responses captured from the non-heating, heating, and heating and deicing tests, as shown in Figs. 19(a) and 19(c), respectively. Ten temperature sensor nodes located near the boundary and in the middle of the slab were selected from the thermal wire cable embedded one inch below the deck surface to represent the general temperature distribution of this zone.

In Fig. 5-19(a), the transient temperature responses obtained at t = 6 hours and 57 hours were selected to perform this regression analysis. The x-axis and y-axis are respectively represented for transient experimental and numerical temperatures collected at t = 6 hours and 57 hours for each temperature sensor mentioned in Section 5.4.4.1. An R-square value of 0.926 determined to be the best-fit line "y=x" is illustrated in Fig. 5-19(a), which indicates the FEM results are in good agreement with the experimental results. Compared to the measured temperature responses at the concrete base, the variation range of the experimental results one inch

below the deck surface was larger since the latter was closer to the convective boundary on the deck surface. The differences in temperature distributions one inch below the deck surface between experimental measurements and numerical outputs indicate that this FEM still can be improved in future research since not all heat transfer boundary conditions were considered in this numerical investigation, such as variations in the direction of wind speed. Another possible reason for this may be that the materials utilized in the field were not as homogeneous as those selected in COMSOL, which resulted in uneven heat transfer within the actual bridge deck.

Similar to Fig. 5-19(a), Fig. 5-19(b) also presents the regression analysis results of transient temperatures derived from the experiments and numerical analyses for heating operation at t = 78 hours and t = 101 hours. The 10 selected temperature sensors from the thermal wire cable embedded one inch below the deck surface are identical to those in the no-heat case. The corresponding R-square value of 0.957 calculated for the best-fit line "y=x" states that a good match can be obtained between the experimental data and numerical results. In both cases, the maximum temperature deviations one inch below the deck surface from the two selected time points are relatively smaller than those at the deck bottom surface, which states that a more uniform temperature distribution occurred in the areas near the deck top surface.

Fig. 5-19(c) illustrates the model validation results for heating and deicing operation at t = 66 hours and t = 153 hours. The R-square value of 0.978 calculated for the best-fit line "y=x" concludes that this numerical model can provide an accurate heat transfer analysis under deicing conditions.

Through the model validation analysis, this verified numerical model could be utilized as a FEM tool that designers can use to design other similar external heating systems and evaluate

the systems' performance under various environmental circumstances and geometric configurations.

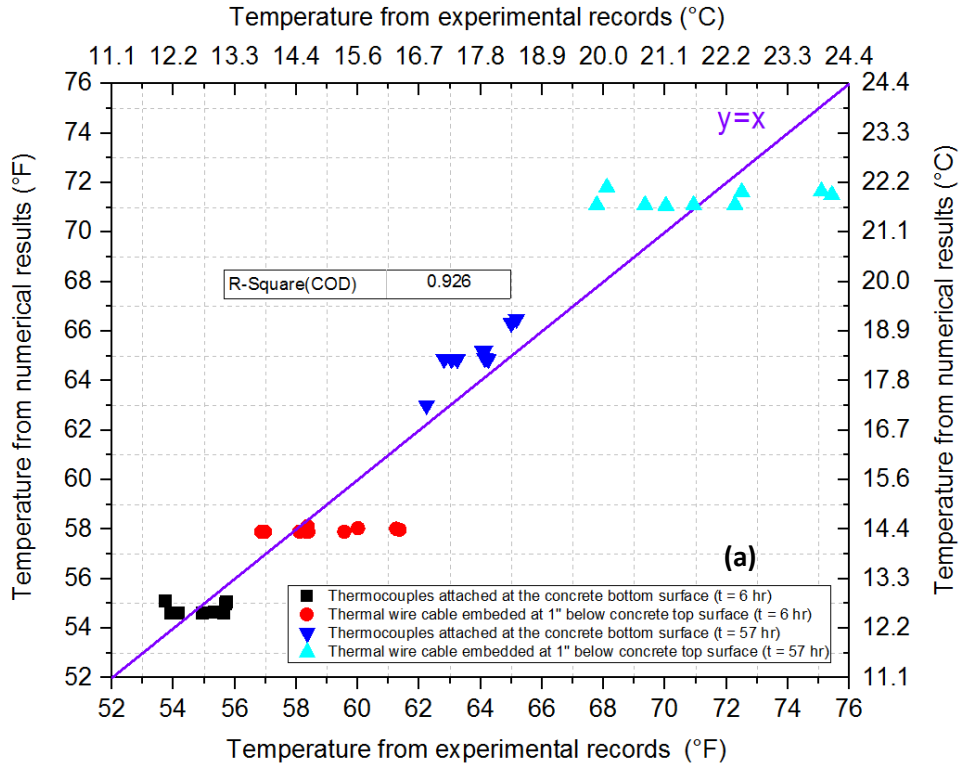

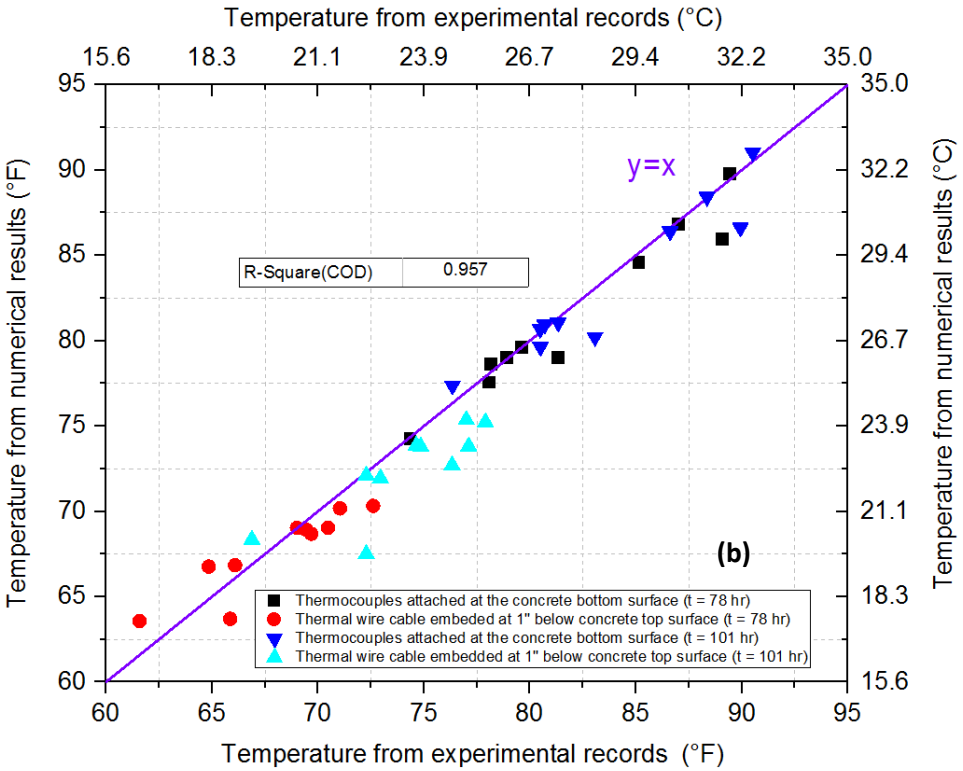

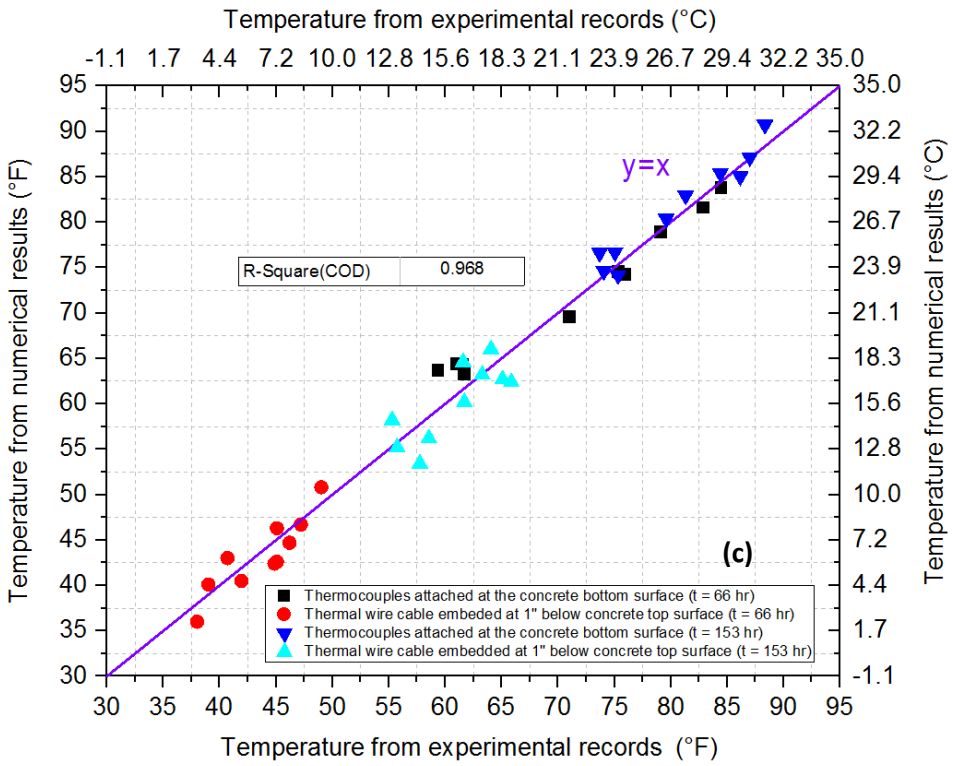

Figure 5-19. Regression analyses for the numerical model: (a) non-heating operation (Test #1), (b) heating operation (Test #2), and (c) heating and deicing operation (Test #3)

5.3.6 Case Study for a Severe Snow Event in the DFW Area in March 2015

The Dallas-Fort Worth area (DFW) climate is classified as a humid subtropical climate, with eight months above 68 ºF and dry winters. The climate experiences four seasons. Although mild winters are conventional in the region, it has also experienced one severe snowstorm on March 4 and 5, 2015, which was the fourth largest ever recorded during March in the DFW area. Altogether, 3.5 inches (9 cm) of snow fell within 6 hours. Due to a lack of exact snowfall measurements for each hour, an average rate was set at 1.5 cm/hr for this study. A numerical investigation used the validated FEM model of the mock-up bridge deck under this severe snow event, which was performed as a case study to estimate the practical feasibility of snow melting performance for the external heating system. Based on weather data obtained from *Weather Underground*, the ambient temperature and wind speed recorded from 2 p.m. on 3/4/2015 to 2 p.m.

on 3/5/2015 are presented in Fig. 5-20 and respectively interpolated in COMSOL as environmental inputs. The heat-carrying fluid with a constant inlet temperature of 43.3 °C (110 °F) circulating at a flow rate of 15.1 L/min (4 gallons/min) was supplied to the bridge deck model by using a boundary condition of the inlet in the FEM model to provide a pre-heating operation starting from 2 p.m. on 3/4/2015. A heat flux of 71 W/m^2 required for snow-melting can be calculated by Eq. (5-13) under a mass rate of snowfall of 0.0037 kg/s (equivalent to a snowfall rate of 1.5 cm/hr). Based on previous experience, the heating system provided the surface of the heated bridge a pre-heating operation of 8 hours before the bridge deck experienced the snowfall.

In this numerical study, it was assumed that fresh snow was immediately melted as soon as it fell on the deck surface due to pre-heating operation rather than being accumulated on it, which noted that the convection and radiation heat losses due to the insulating effect of ice layer on the deck surface were not reduce and kept constant. Then, the melted snow disappeared rapidly based on an assumption of perfect drainage on the bridge deck surface (Liu et al. 2007a). Therefore, the heat flux attributable to evaporation were not considered in this model. This model dealt with the worst conditions. If the external heating system can be feasible under the worst scenarios, it will work under milder cases as well.

The initial temperature of the heated bridge deck, including the concrete slab, cross-linked polyethylene (PEX) pipe, and spray foam, was set the same as ambient temperature at 2 p.m. on 3/4/2015 to reach an equilibrium state with the environment. The setting of other boundary conditions incorporating thermal contact, convection, and radiation was identical to that described in Section 5.3.3. The authors (representing the UTA research group) also deployed a time-dependent model to analyze the transient heat transfer behaviors on the deck surface, which is described below in detail.

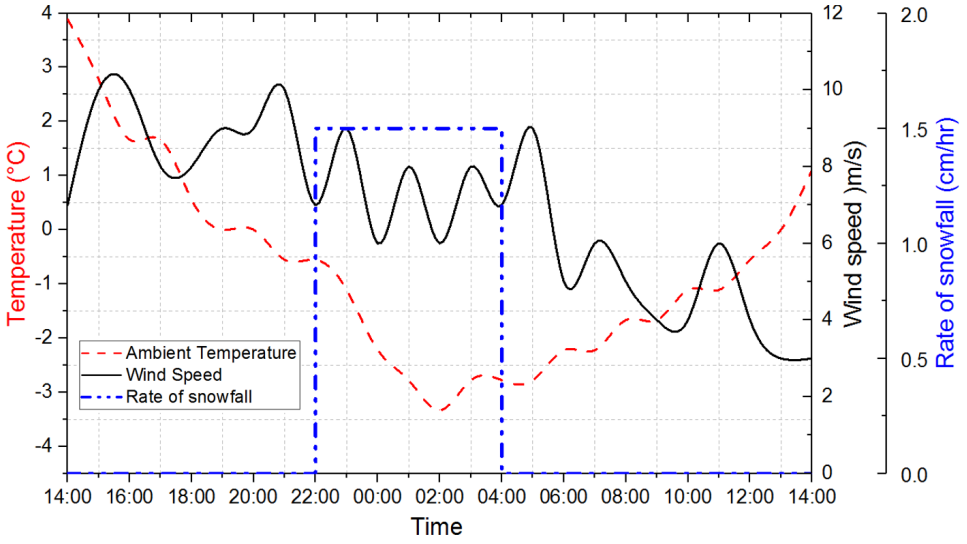

Figure 5-20. Recorded ambient temperature, wind speed, and rate of snowfall during a severe snow event recorded from 2 p.m. on 3/4/2015 to 2 p.m. on 3/5/2015

Fig. 5-21 compares the average surface temperature of the externally heated bridge deck under scenarios of no snow and a snow event with a snowfall rate of 1.5 cm/hr. During the absence of snowfall, the simulated temperature responses from these two scenarios had a close agreement. We observed that the surface temperature responses under the snowfall rate of 1.5 cm/hr started to decrease at 10 p.m. on 3/4/2015 due to application of the outward heat flux required for snow-melting on the deck surface. During this snow-melting period, the lowest temperature (0.3 °C (32.6 °F) on the deck surface occurred at 3 a.m. on 3/5/2020, which indicates this external heating design is promising and feasible for the practical application of snow-melting on the mock-up bridge deck under one of the most severe snowstorm conditions recorded in the DFW area. After the snow-melting operation was terminated, the temperature responses under the snowfall rate of 1.5 cm/hr rose after 4 a.m., 3/5/2015, indicating good agreement with the simulation temperatures under the scenario of no snow.

Fig. 5-22 compares the simulated required heat flux on the deck surface under these two scenarios. Similar to Fig. 21, the required heat flux on the deck surface under these two scenarios

can have a reasonable match when the additional outward heat flux is not applied. From 10 p.m. on 3/4/2015/2015 to 4 a.m. on 3/5/2015, more heat fluxes were needed on the deck surface compared to the case of no snow due to the additional energy requirement for snow melting. Based on the results of Figs. 5-21 and 5-22, it is concluded that an approximate heat flux of 220 W/m^2 had to be transferred to the deck surface to heat the average surface temperature to 0.3 °C (32.6 °F) under the specific weather conditions of this snow event. This external heating system can meet the desired demand for snow-melting under one of the heaviest severe snow events recorded in the DFW area using this designed thermal supply.

Fig. 5-23 presents the temperature contour of the bridge deck at 3:00 p.m. on 3/5/2015 when the lowest surface temperature was simulated. It was observed that the temperature at the heated area of the deck surface was greater than the freezing point, which also signified that the externally heated bridge deck could meet the deicing requirements under severe winter events in the DFW area.

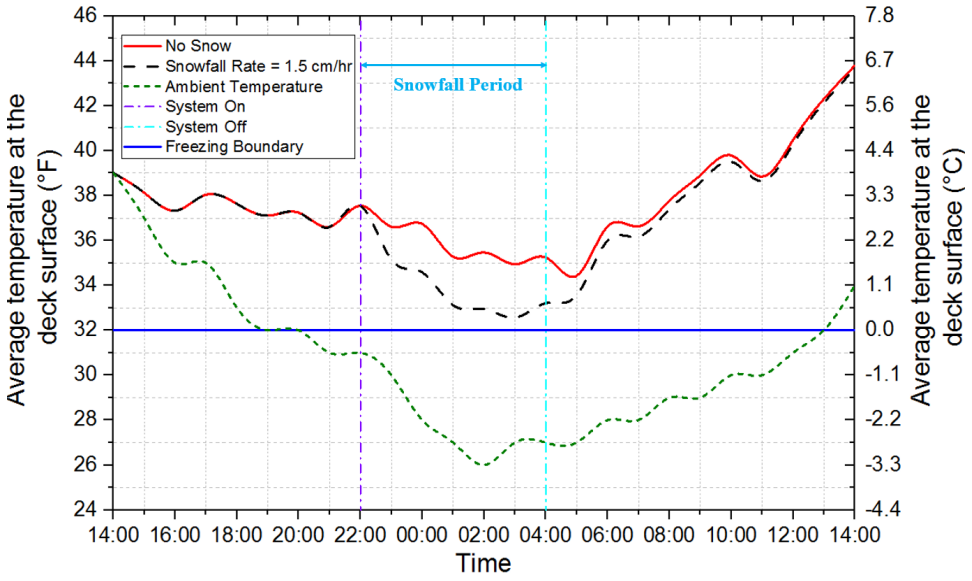

Figure 5-21. Comparison of average temperature responses at the deck surface under scenarios of no snow and a snowfall rate of 1.5 cm/hr

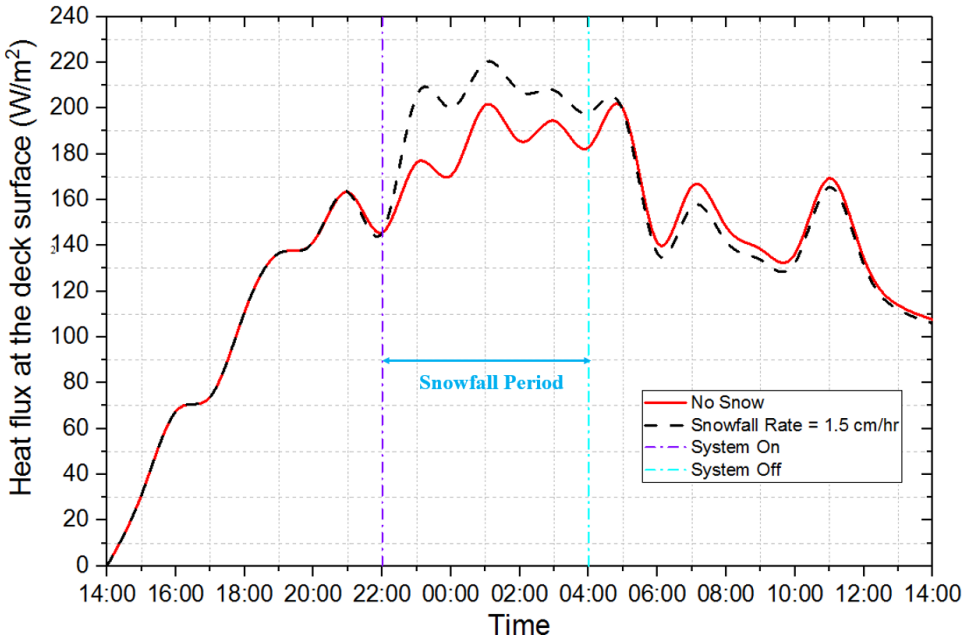

Figure 5-22. Comparison of required heat flux at the deck surface under scenarios of no snow and a 1.5 cm/hr snowfall rate

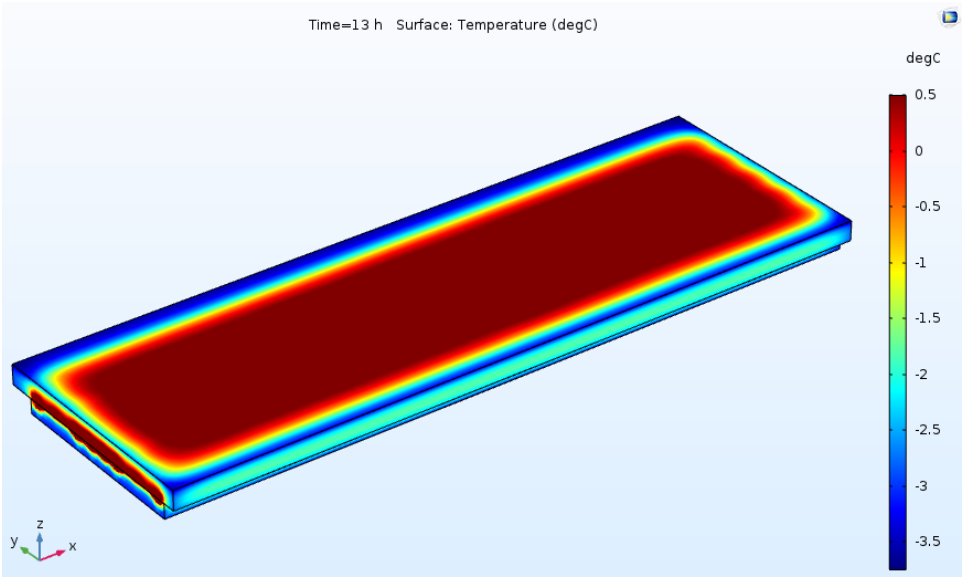

Figure 5-23. Temperature contour of the bridge deck at 3:00 p.m. on 3/5/2015

5.4. Summary and Conclusions

A 3-D FEM was created to simulate the field tests of a newly developed externally heated hydronic mock-up bridge deck under different operation scenarios, including non-heating, heating, heating, and deicing tests. The heat transfer process from the supplied heat-carrying fluid to the deck surface was modeled using a pipe flow module to couple fluid flow and heat transfer. A thermal contact model with an optimized combination of the h_c value of 2.5 W/(m^2·K) and the h_g value of 95 W/(m^2·K) was developed in COMSOL to account for the poor contact feature at the interface between concrete and spray foam. The numerical model was fully calibrated by the test data acquired in the field using transient analyses, which states that the numerical outputs can have a reasonable agreement with experimental measurements. In this study, the complete snow melting process was not replicated in COMSOL to avoid the computational expense of the energy requirement. Therefore, the phase change of snow/ice was analyzed in terms of an outward heat flux applied to the deck surface to estimate the amount of required energy for snow/ice melting on the deck surface, which increased the computational efficiency of numerical work.

In heating and deicing operation of Test #3, an outward heat flux of 20.4 W/m^2 calculated by Eqs. (5-13) and (5-14) was applied to the deck surface for snow melting. Although simulated temperatures were relatively higher than those from experimental measurements due to the lower lateral heat losses and better material homogeneity in COMSOL, a reasonable agreement can be observed between numerical and experimental results. The numerical heat transfer efficiency (71.3%) of the heating and deicing operation is much higher than the experimental result (55%). The difference is attributed to the outlet temperature mismatch between simulated and measured data. Compared to the previous numerical study (76%), the system efficiency is relatively lower since the deicing process was considered in this paper. In the numerical case study, an outward heat flux of 71 W/m^2 applied to the deck surface for snow-melting was calculated by Eq. (5-13)

under a snowfall rate of 1.5 cm/hr based on severe snow events recorded in the DFW area. The temperature at the deck surface could be heated to 0.3 °C (32.6 °F) if the external heating system provided a minimum inlet temperature of 43.3 °C (110 °F). From the perspective of heat flux, a minimum heat flux of 220 W/m^2 was required to be transferred to the deck surface. The validated finite element model is the first developed numerical tool for estimating heating and deicing performance for externally heated bridge decks in the field.

In the future, a series of parametric studies, including environmental and operational factors, will be performed to provide a more comprehensive understanding of the heat transfer behaviors within the externally heated bridge deck.

CHAPTER 6 EXTERNALLY HEATED BRIDGE DECK DESIGN CREATED BY UTILIZING A SERIES OF DESIGN CHARTS DEVELOPED UNDER VARIOUS CONDITIONS

6.1 Introduction

Three-dimensional numerical models previously illustrated the heating and deicing processes within an externally heated mock-up bridge deck. They were created in COMSOL and validated by replicating the experimental tests performed on-site under non-heating, heating, and deicing operations. This chapter describes a series of parametric studies that were performed by utilizing the validated finite element models to provide a comprehensive understanding of the heat transfer behaviors within an externally heated bridge deck. Stationary models were employed under various environmental and operational conditions to analyze the interactions between the thermal supplies and the average steady-state temperatures on the deck surface, and the application of transient models was used to estimate the heating times required to raise the average temperatures at the deck surface above the freezing temperature (0 °C/32 °F). A detailed flow chart can depict the externally heated bridge deck design process in detail and is a useful design tool for an external heating system.

6.2 Numerical Analysis Methodology

6.2.1 Design Process of Externally Heated Bridge Decks

The design of an externally heated bridge deck aims to provide an optimized hydronic pipe system to meet the heating and deicing requirements of the bridge deck under winter events. Figure 6-1 shows a flow chart of the design process of an externally heated bridge deck that was developed by employing a series of design charts developed under parametric studies that are described in detail in Sections 6.3 and 6.4. First, the typical weather and bridge deck conditions including

average ambient temperature, wind speed, rate of snowfall, deck thickness, and bridge were selected as inputs. In this study, the weather and bridge data were based on actual conditions in the DFW area and provided an overall picture of the winter weather and bridge construction conditions. The heat flux required for heating and snow/ice melting at the bridge deck surface was calculated by using Eqs. (5-6 to 5-13) expressed in Chapter 5 that were based on the selected weather data. In the third step, the peak hourly heating loads were equal to the product of the heat flux calculated in the last step and the area of the bridge deck. The calculated results were utilized as a theoretical base to develop a FEM model that was validated by experimental data, as presented in Chapter 5. Then, a series of design charts were developed by using the validated FEM model. The specific methodology of developing the design charts is presented in Sections 6.3 and 6.4. The design charts were completed and were ready to be utilized for the design of an externally heated bridge deck.

Non-snowy and snow events were considered in the application of the design charts. For the former, design chart #1 was utilized to determine the minimum inlet fluid temperature under which the average steady-state surface temperature can be above the freezing under the selected pipe spacing. Then, design charts #2 and #3 were employed to determine the minimum inlet temperatures under the selected flow rate and deck thickness, respectively. Up to now, the inlet temperatures were determined based on the selected pipe spacing, flow rate, and deck thickness. Afterward, design weather conditions including ambient temperature and wind speed were selected by using the corresponding design charts. The inlet fluid temperatures were respectively determined by design charts #4 and #5 under ambient temperature and wind speed. Therefore, a total of five inlet temperatures under which the average temperature of the steady-state surface could be above freezing were determined by using various design chart combinations.

Through the mathematic knowledge of the set, it was confirmed whether the lower and upper limits of the required inlet fluid temperature could be determined by the ready design charts. If so, the required heat pump system, including numbers and arrangement, could be determined, and then a series of design outputs could be exported for bridge snow/ice melting. Otherwise, new numerical simulations would have to be performed by using the validated FEM model under the specific design conditions to determine the design outputs. For non-snowy conditions, the methodology is the same as described. An example of the design process is presented in the appendix to provide a better understanding of how to use the design charts for designing an externally heated bridge deck.

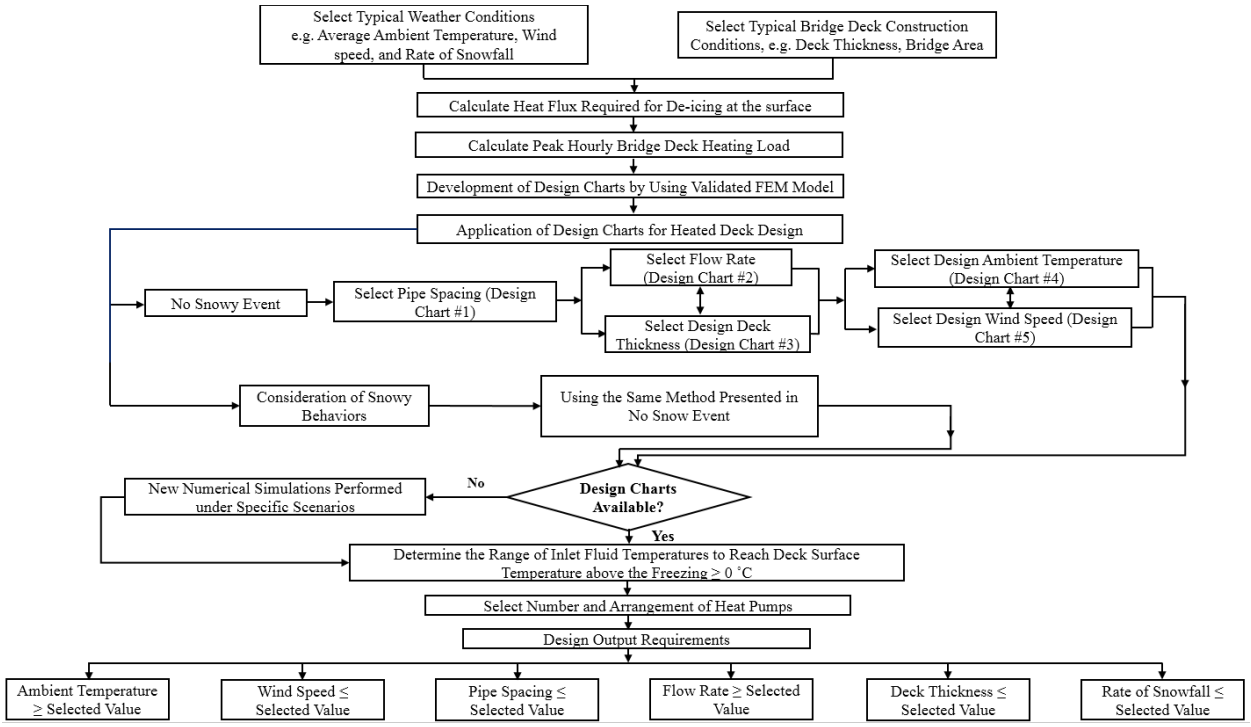

Figure 6-1. Flow chart of the design process for externally heated bridge decks, using a series of design charts developed from parametric studies

6.2.2 Numerical Test Program for the Development of Design Charts

Many parameters play important roles in the heating behavior of external bridge deck systems. Environmental factors including ambient temperature, wind speed, and rate of snowfall; and operational factors such as the bridge deck thickness, pipe spacing, and flow rate are the initial values that need to be inputted into the COMSOL program to analyze the heating systems' performance and implement and instrument the external heating design under various conditions. A series of numerical programs were conducted in this study to develop design charts for an externally heated bridge deck under different environmental and operational parameters, as summarized in Tables 6-1 to 6-2. Both non-snowy and snowy winter conditions were considered. It was noted that stationary and transient approaches were utilized to respectively analyze the interactions between the inlet fluid temperatures and the average steady-state temperatures at the deck surface, as well to determine the number of heating hours required to raise the average temperatures at the deck surface above freezing under different parameters. In the stationary approach, various inlet fluid temperatures were utilized as initial inputs in COMSOL to determine the minimum temperature under which the average steady-state surface temperature can be maintained above freezing under various conditions. For transient simulations, a constant inlet fluid temperature was determined based on previous on-site tests (the heat capacity of the borehole and the temperature of underground water) to evaluate the required heating time. In this study, the selected inlet fluid temperature under non-snowy and snowy conditions was 110 °F (43.3 °C) and 120 °F (48.9 °C), respectively.

Table 6-1 presents the environmental and operational parameters that were used in the numerical parametric studies for non-snowy conditions. The ambient temperature of -4 °C (24.8 °F), wind speed of 5 m/s, pipe spacing of 20.32 cm (8 inches), deck thickness of 20.32 cm

(8 inches), inlet temperature of 110 °F (43.3 °C) for stationary simulations, and flow rate of 15.1 L/min were respectively determined as basic values, based on the recorded severe weather conditions in Dallas from 2011 to 2019 and a previous on-site test experience described in Chapter 5. As shown in Table 6-2, the rate of snowfall was based on the research conducted by Bowers (2016), who classified snowfalls into three classes: mild (2 cm/hr), moderate (5 cm/hr), and severe (10 cm/hr). Due to few snowy events in Dallas, mild snowfall (2 cm/hr) was utilized in the base case. Except for the inlet fluid temperature for stationary simulations (120 °F (48.9 °C)), the values of the parameters were the same as those in Table 6-1.

Table 6-1. FEM Test Programs without Consideration of Snow Melting

Ambient Temperature (°C)	Wind Speed (m/s)	Pipe Spacing (cm)	Deck Thickness (cm)	Flow Rate (L/min)	Inlet Fluid Temperature (°C)		Number of Runs in Each Process	
					Stationary	Transient	Stationary	Transient
-4	5	20.32	20.32	15.1	-	43.3	2 (Base Case)	
-10, -6, -4, -2, -1	5	20.32	20.32	15.1	From 1.7 to 82.2	43.3	20	5
-4	1, 2, 5, 8, 12	20.32	20.32	15.1	From 1.7 to 82.2	43.3	20	5
-4	5	20.32, 25.4, 30.48	20.32	15.1	From 15.6 to 43.3	43.3	9	3
-4	5	20.32	20.32, 22.86, 25.4	15.1	From 15.6 to 43.3	43.3	9	3
-4	5	20.32	20.32	7.6, 11.4, 15.1, 18.9, 22.7	From 11.4 to 43.3	43.3	15	5

Table 6-2. FEM Test Programs with Consideration of Snow Melting

Ambient Temperature (°C)	Wind Speed (m/s)	Rate of Snowfall (cm/hr)	Flow Rate (L/min)	Pipe Spacing (cm)	Deck Thickness (cm)	Inlet Fluid Temperature (°C)		Number of Runs in Each Process	
						Stationary	Transient	Stationary	Transient
-4	5	2	15.1	20.32	20.32	-	48.9	2 (Base Case)	
-10, -6, -4	5	2, 5, 10	15.1	20.32	20.32	From 21.1 to 126.7	48.9	27	9
-4	4, 5, 8	2, 5, 10	15.1	20.32	20.32	From 4.4 to 126.7	48.9	27	9

Similar to the FEM model of the mock-up bridge deck, the free tetrahedral mesh method with optimized maximum and minimum element sizes of 0.07 m and 0.0007 was utilized to generate the domains of concrete and spray foam. The pipe flow module with 1-D line elements was selected as the hydropic loops to simplify the geometric configuration.

Both convective and radiative heat transfers existed on all of the surfaces that were exposed to the environment. The top surface of the bridge deck was subjected to the major heat exchange behaviors between the bridge deck and the environment. The initial temperature of the bridge deck domains was set as the ambient temperature. The boundary conditions, including the inlet fluid temperature, wind speed, flow rate, ambient temperature, and heat flux required for snow melting on the deck surface, based on the selected snowfall, were set as specific constant values to input into COMSOL. Based on the contributions from Chapter 5, the optimized h_c value of 95 W/(m^2·K) was utilized in the thermal contact model to account for the poor contact at the interface between the deck bottom surface and the top surface of the spray foam slab. The interface contact between the circulating fluid and the pipe was formulated by Eq. (5-3), which is related to the internal film resistance, the thermal resistance of the pipe, and the inner/outer radius of the pipe. The other

module interfaces, including the pipe-concrete slab, pipe-geofoam slab, and pipe-inlet fluid were set as perfect surface contacts in this study. The parametric studies were respectively performed by stationery and time-dependent approaches to estimate the performance of the external heating system under different weather conditions and geometric scenarios. Each of the numerical parametric analyses performed by COMSOL Multiphysics is described below in detail.

6.3 Development of Design Charts Without Consideration of Deicing Behaviors

6.3.1 Effect of Pipe Spacing

Pipe spacing is one of the primary design factors that affects the efficiency of the heat transfer of an external system. In previous studies, pipe spacing of 6 to 12 inches was recommended. In Chapters 3 and 5, the designed pipe spacings of the heated bridge deck in the environmental chamber and field were 15.24 cm (6 inches) and 20.32 cm (8 inches), respectively. From the perspective of the technical feasibility of construction, pipe spacings selected in this parametric study were 8, 10, and 12 inches (15.24cm, 20.32 cm, and 30.48 cm), and were investigated to evaluate the effect on the heating performance of the external heating system. The development of technical charts was intended to summarize the correlations between tube spacing and the supplied heat energy.

Figs. 6-2 (Design chart #1) and 6-3 show the transient and steady-state temperature response curves under various pipe spacings, respectively. By supplying the same inlet fluid temperature, it was indicated that the greater the pipe spacing is, the lower the surface temperature is. To prevent bridge deck surfaces from freezing, the minimum supplied inlet fluid temperatures are respectively required to reach 27.8 °C (82 °F), 32.8 °C (91 °F), and 39.4 °C (103 °F) under the three different pipe spacings. The bridge decks are required to be externally heated for at least 8.3, 10.2, and 18.5 hours, respectively.

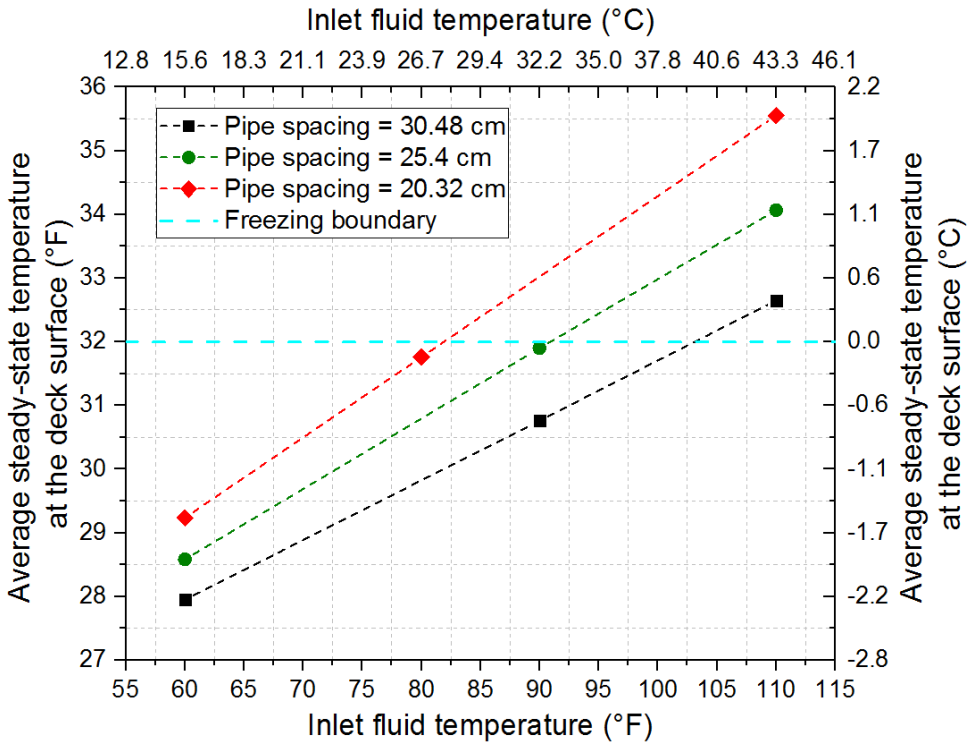

Figure 6-2. Design chart #1: Interactions between inlet fluid temperatures and average steady-state temperatures at the deck surface under different pipe spacing

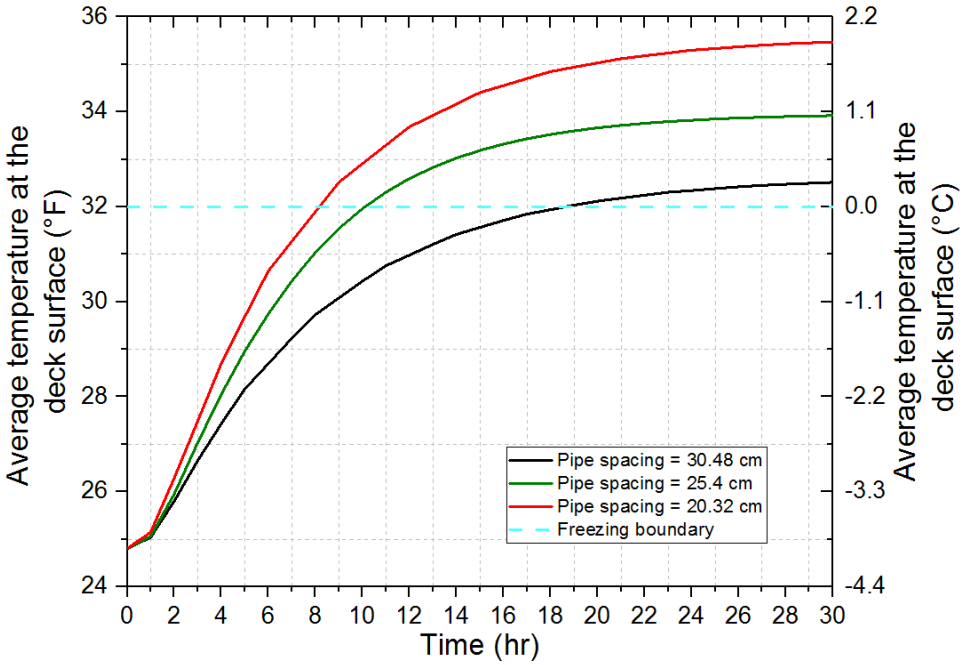

Figure 6-3. The number of heating hours required to raise the average temperatures at the deck surface above the freezing temperature under different pipe spacings

6.3.2 Effect of Flow Rate

Flow rate is another factor that controls the heating system's operation since it can affect the flow convective contribution, accounting for the energy transport resulting from the fluid flow inside the hydronic loops. Flow rates ranging from 7.6 L/min to 22.7 L/min were employed to perform the numerical analysis to obtain information about the effect of the flow rate on the system's performance. A flow rate of 15.1 L/min, utilized for the previous heating tests in the field, was selected in the base case. Fig. 6-4 (Design chart #2) compares the interactions between inlet fluid temperatures and average steady-state temperatures at the deck surface under various flow rates and indicated that the flow rate has a much slighter effect on the system's heating performance than ambient temperature or wind speed. When the supplied inlet fluid temperature is equal to 29.4 °C (85 °F), the average steady-state deck surface temperature difference between the flow rates of 7.6 L/min and 22.7 L/min is only 0.2 °C (0.3 °F). These simulated results are in

agreement with the research findings from Zhang et al. (2017). With a supplied inlet fluid temperature greater than 83 °F (28.3 °C), the average steady-state temperature at the deck surface can be reach above freezing, regardless of the value of the flow rate.

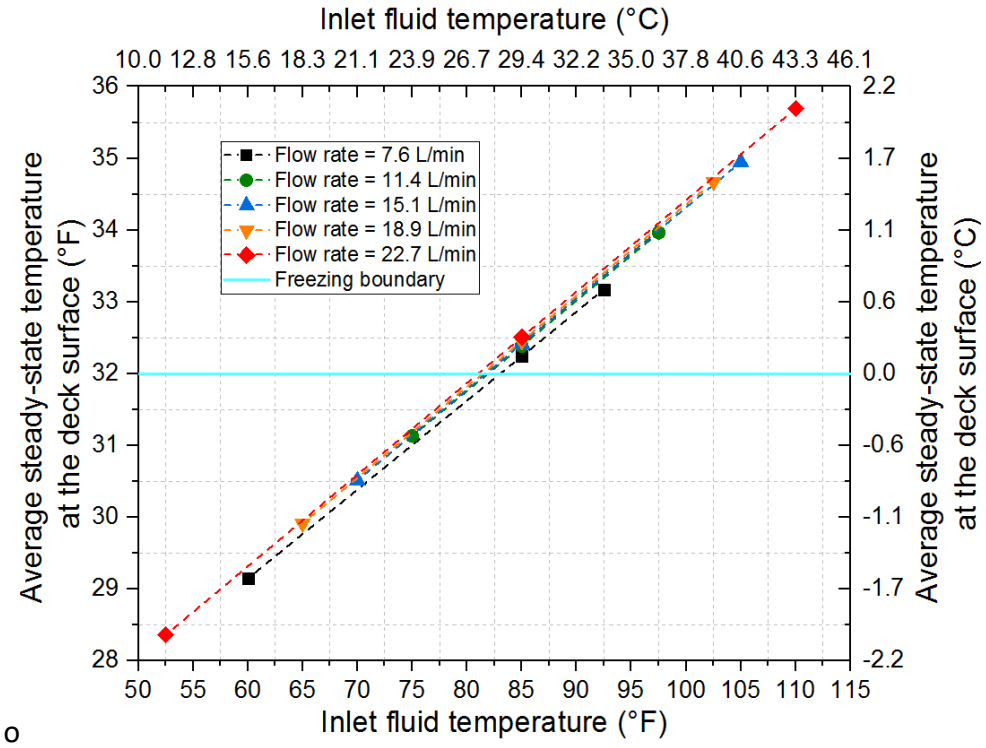

o

Figure 6-4. Design chart #4: Interactions between inlet fluid temperatures and average steady-state temperatures at the deck surface under various flow rates

Fig. 6-5 presents the heating time required to raise the average temperatures of the deck surface above freezing under different flow rates, which have a minor effect on the heating performance of this external design. When the bridge deck is supplied by the heat-carrying fluid of 43.3 °C (110 °F), the average surface temperature of the bridge deck can be heated above the freezing mark after 8 hours of heating, regardless of the flow rate of the circulating fluid.

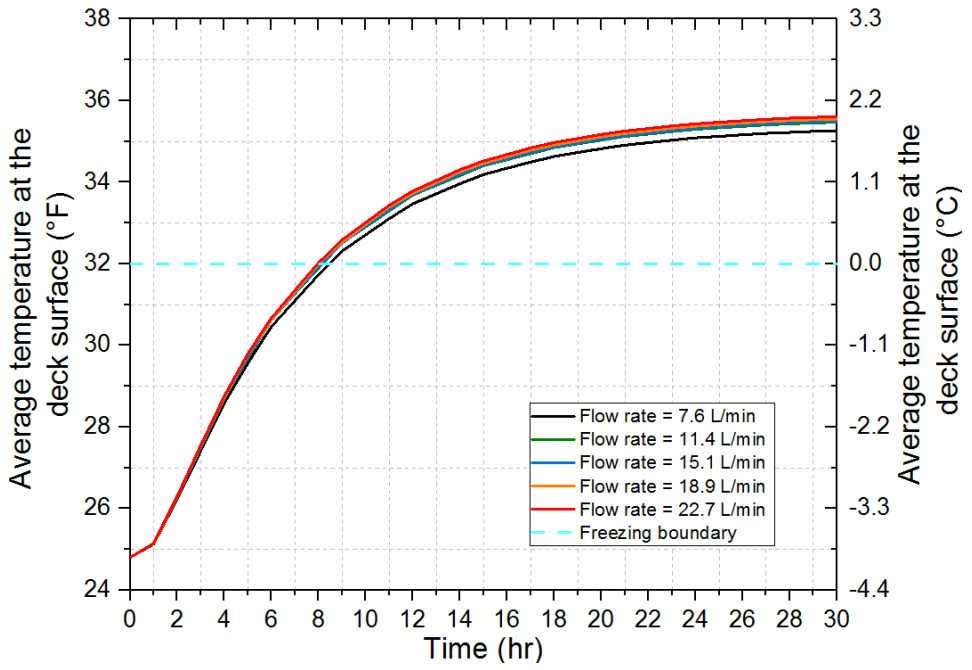

Figure 6-5. The heating hours required to raise the average temperatures at the deck surface above the freezing temperature under different flow rates

6.3.3 Effect of Deck Thickness

In this external design, the heat transfer distance from the heat source to the top surface of the bridge deck was the thickness of the bridge deck. Zhang et al. (2017) indicated that an internal heating system needs more time to heat the top surface of the bridge deck to the same average temperature if the concrete cover is larger. Therefore, the thickness of the bridge deck can directly affect the efficiency of heat transfer from the heat source to the bridge deck surface and needs to be taken into account as a primary factor in heating system design. The designed thickness of the mock-up bridge deck in the field was 8 inches. Based on the experimental study from Bowers (2016), the recommended thickness of the bridge deck is 10 inches. Therefore, deck thicknesses of 20.32 cm (8 inches), 22.86 cm (9 inches), and 25.4 cm (10 inches) were utilized for performing these parametric investigations to estimate the effect of deck thickness on the performance of the external heating system.

Figs. 6-6 (Design chart #3) and 6-17 show the descriptions of the heating performance of the external heating system under various concrete thicknesses by stationery and time-dependent methods, respectively. It was shown that the concrete thickness affects the heat transfer distance from the heat source (heat carrier fluid) to the surface of the bridge deck. The greater the concrete thickness is, the higher inlet fluid temperature and longer heating time are required. To obtain temperatures above freezing at the deck surface under different concrete thicknesses, the minimum supplied inlet fluid temperature and heating hours range from 27.8 °C (82 °F) to 35.6 °C (96 °F) and 8.3 to 22 hours, respectively.

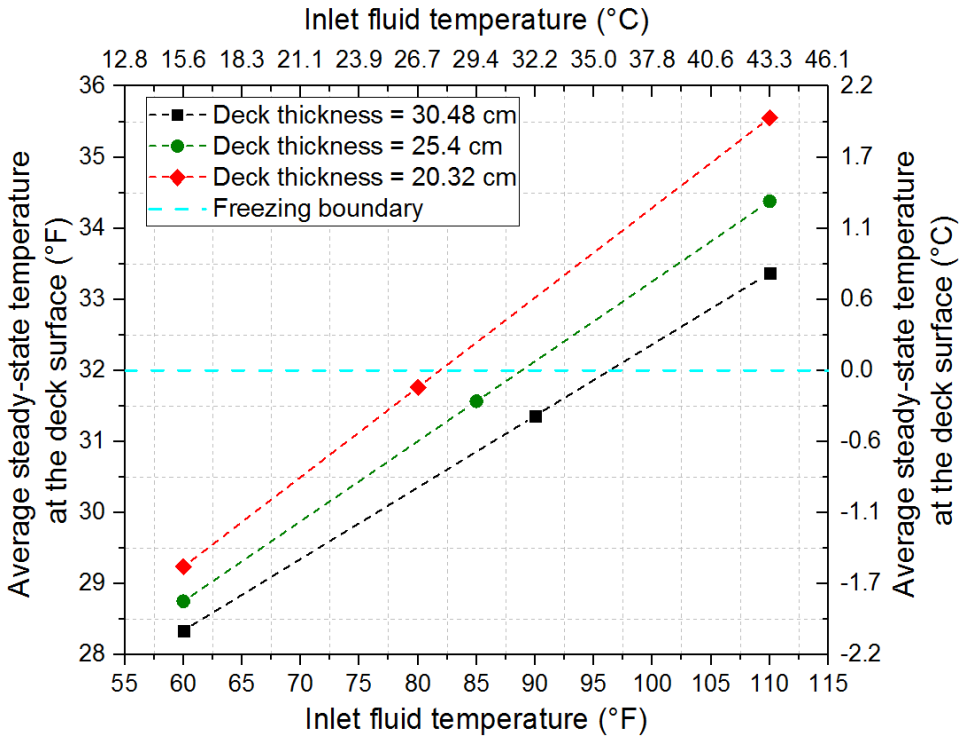

Figure 6-6. Design chart #5: Interactions between inlet fluid temperatures and average steady-state temperatures at the deck surface under various deck thicknesses

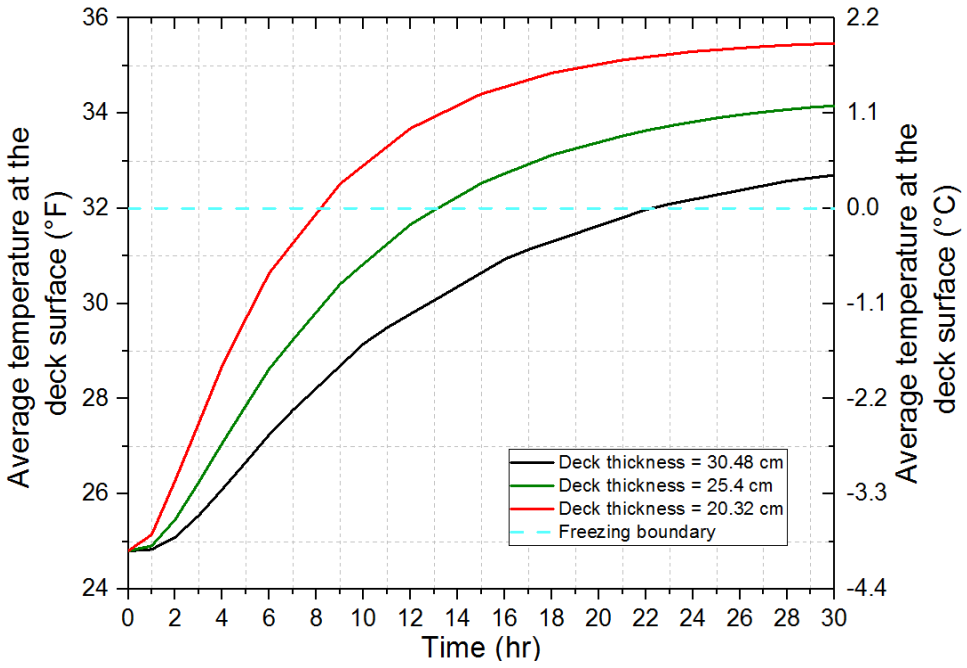

Figure 6-7. The number of heating hours required to raise the average temperatures at the deck surface above freezing under different deck thicknesses

6.3.4 Effect of Ambient Temperature

The ambient temperature of the environment has a remarkable effect on the performance of the system, as more heat energy has to be transferred to heat the deck surface under lower ambient temperatures. In this section, based on the recorded severe weather conditions in Dallas from 2011 to 2019, ambient temperatures ranging from -10 °C (14 °F) to -1 °C (30.2 °F) were set to equal the initial slab temperatures, in order to reach an equilibrium state between the environment and the bridge deck before the numerical tests were performed. The other parameters aforementioned were considered as the base case listed in Tables 6-1.

Fig. 6-8 (Design chart #4) shows the interactions between inlet fluid temperatures the average steady-state temperatures on the deck surface under different ambient temperatures. The slopes of the gridlines, developed from best-fit of the numerical analyses at ambient temperatures -1°C (30.2 °F), -2 °C (28.4 °F), -4 °C (24.8 °F), -6 °C (21.2 °F), and -10 °C (14 °F), are the same.

The lower the ambient temperature is, the greater the inlet fluid temperature is required to heat the average steady-state surface temperature above freezing. Under the severest weather condition (the ambient temperature at -10 °C (14 10 °F)), the inlet temperatures need to be greater than 26.7 °C (80 °F) to heat the average steady-state temperature on the deck surface above 0 °C (32 °F). The approximate minimum inlet fluid temperatures required to heat the average steady-state temperatures on the deck surface above the freezing temperature under ambient temperatures of 1°C (30.2 °F), -2 °C (28.4 °F), -4 °C (24.8 °F), -6 °C (21.2 °F), and -10 °C (14 °F) are 7.2 °C (45 °F), 15.6 °C (60 °F), 27.8 °C (82 °F), 42.2 °C (108 °F), 70 °C (158 °F), respectively, based on the computational results from Fig. 6-2.

Fig. 6-9 compares the heating times required to raise the average temperatures at the deck surface above freezing under different ambient temperatures. In this study, the inlet fluid temperature was 43.3 °C (110 °F), as listed in the base case in Table 6-1. It should be noted that the lower the ambient temperature is, the longer it will take to heat the average temperature at the deck surface above the freezing temperature. Under the ambient temperature at -10 °C (14 °F), this external heating system was not able to reach the desired heating and deicing performance with a thermal supply of 43.3 °C (110 °F), which matches the results from Fig. 6-8. The required heating time ranges from 2.5 hours to 21 hours when ambient temperatures vary from -1°C (30.2 °F) to -6 °C (21.2 °F).

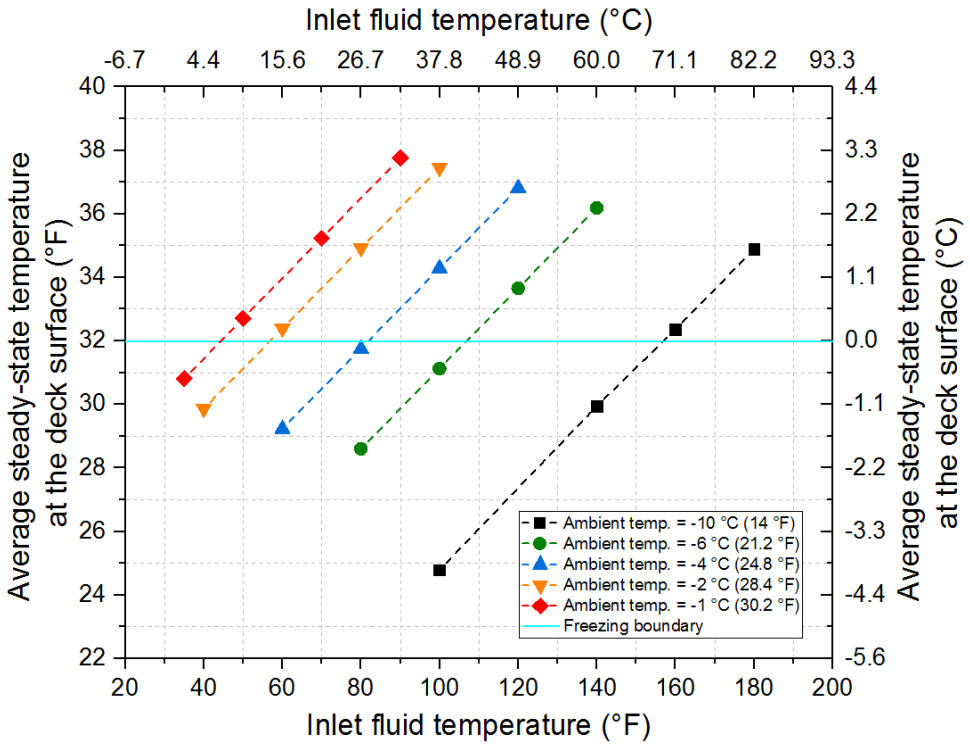

Figure 6-8. Design chart #4: Interactions between inlet fluid temperatures and average steady-state temperatures at the deck surface under various ambient temperatures

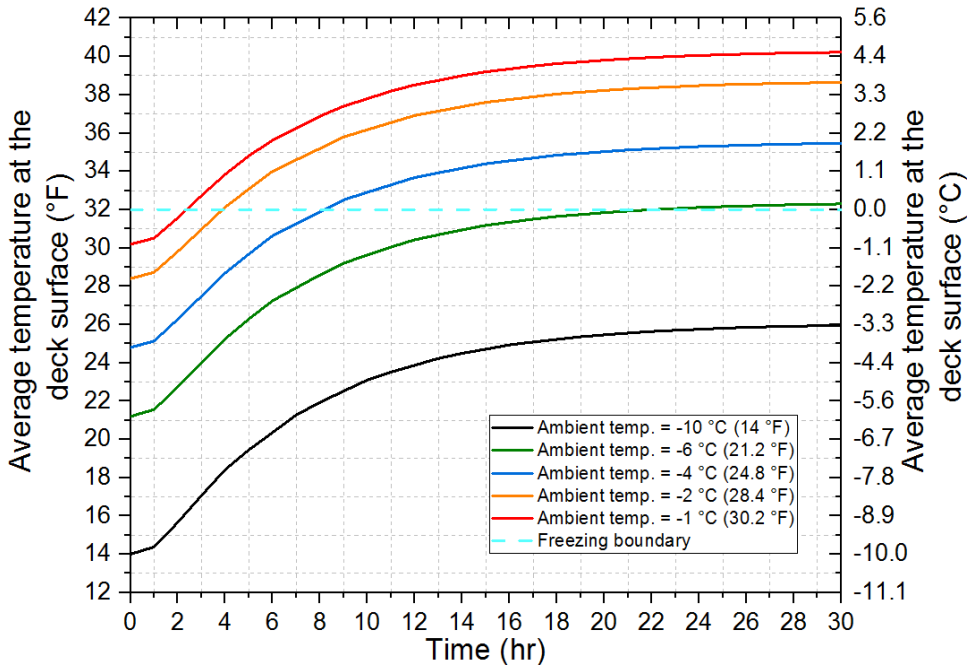

Figure 6-9. The number of heating hours required to raise the average temperatures at the deck surface above the freezing temperature under different ambient temperatures

6.3.2 Effect of Wind Speed

The effect of wind speed was also analyzed, as it is one of the most important environmental factors dominating the heat transfer that is attributable to convection. Although the value and direction of wind speed are rarely constant and vary instantaneously, it was held constant in this study to better understand the effects of wind speed on the heating performance of this external system. Wind speeds ranging from 1 m/s to 12 m/s were inputted into COMSOL to perform the parametric studies. The other related parameters were set based on Tables 6-2.

Fig. 6-10 (Design chart #5) compares the average steady-state temperature at the deck surface under various wind speeds. The greater the wind speed is, the smaller ratio between the average steady-state temperature at the deck surface and the inlet fluid temperature (the slope of gridline) is since more heat losses associated with convective heat transfer occur on the exposed surface of the bridge deck. When the supplied inlet fluid temperature is 26.7 °C (80 °F), the average

steady-state temperature at the deck surface under wind speed of 12 m/s decreases 13 °C (24 °F), compared to when the wind speed is equal to 1 m/s, which indicates the considerable effect of wind speed on the heat transfer behaviors within the externally heated bridge deck. When wind speed is greater than 8 m/s, the simulated average steady-state deck surface temperature under the same thermal supply (for example, the inlet temperature is equal to 26.7 °C (80 °F)) makes a minimal difference compared to wind speed of less than 5 m/s, which indicates that it is more difficult to increase the surface temperature by just supplying a lower inlet temperature (such as 26.7 °C (80 °F)) under severe wind conditions.

For the analyses of the heating times required to heat the deck surface temperature above the freezing temperature under different wind speeds, as illustrated in Fig. 6-11, it was found that the greater the wind speed is, the more time is required to heat the average temperature at the deck surface above the freezing temperature. When the wind speed reaches 12 m/s, the supplied inlet fluid temperature of 43.3 °C (110 °F) is not sufficient to heat the temperature at the top surface of the external bridge deck above the freezing temperature under the ambient temperature at -4 °C (24.8 °F). When wind speed is less than 8 m/s, 17 hours of heating time is capable of providing enough thermal energy for bridge deck deicing.

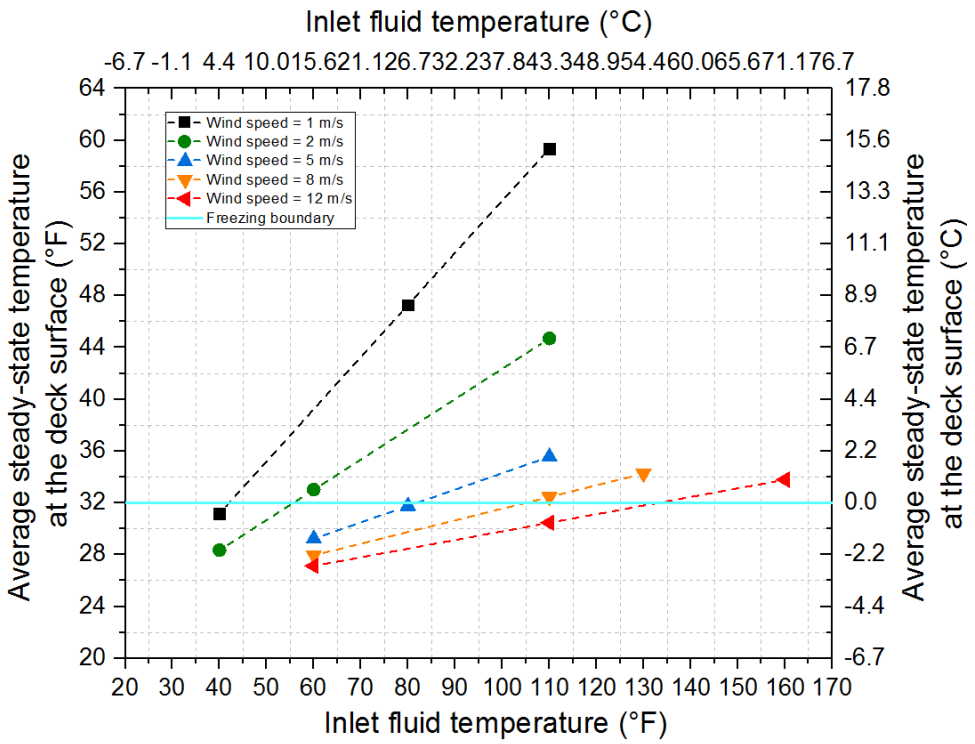

Figure 6-10. Design chart #5: Interactions between inlet fluid temperatures and average steady-state temperatures at the deck surface under various wind speeds

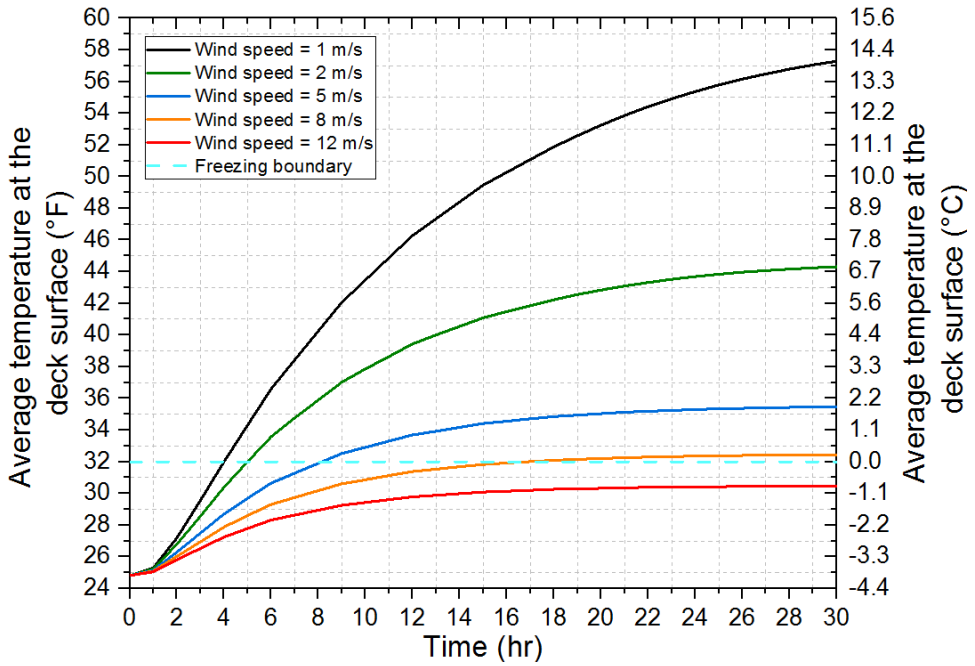

Figure 6-11. The number of heating hours required to raise the average temperatures at the deck surface above the freezing temperature under different wind speeds

6.4 Parametric Studies of System Performance with Consideration of Deicing Behaviors

In this section, three different rates of snowfall, including 2 cm/hr (base case), 5 cm/hr, and 10 cm/hr were considered in numerical simulations to evaluate the performance of the external heating system under deicing behaviors. To provide a comprehensive understanding of the deicing performance of externally heated bridge decks under various environmental circumstances, the ambient temperature and wind speed were considered as well. Based on the case study described in Chapter 5, the duration of snowfall for each simulation was assumed to be 6 hours. Snow melting fluxes of 94 W/m^2, 235 W/m^2, and 470 W/m^2 can be respectively calculated by Eq. (5-13) under rates of snowfall of 2 cm/hr, 5 cm/hr, and 10 cm/hr, which were set as boundary conditions applied on the deck surface. The base values of each parameter in this study are listed in Table 6-2. A series of parametric studies were performed under various ambient temperatures, wind speeds, and

rates of snowfall to evaluate the system's performance under different environmental circumstances. Flow rate, concrete thickness, and pipe spacing were not included.

6.4.1 Under Different Ambient Temperatures

Fig. 6-12 (Design chart #6) shows the interactions between the inlet fluid temperatures and the average steady-state temperatures on the deck surface under different ambient temperatures and rates of snowfall. The slopes of the gridlines plotted from the best-fit of the numerical analyses under different snowy scenarios, including rates of snowfall of 2 cm/hr, 5 cm/hr, 10 cm/hr, and no snow, were the same, regardless of the variations of the ambient temperature. The lower the ambient temperature and the greater the rate of snowfall are, the greater the inlet fluid temperature is required. In the case of the mild class of snowfall rate (2 cm/hr), the approximate minimum inlet fluid temperatures required to heat the average bridge surface temperatures above 0 °C (32 °F) under ambient temperatures of -4 °C (24.8 °F) and -6 °C (21.2 °F) are 42.2 °C (108 °F) and 57.2 °C (135 °F), respectively. For the moderate class (5 cm/hr), ice/snow on the deck surface can be melted if the bridge is heated by 65 °C (149 °F) and 79.4 °C (175 °F) heat carrier fluids under ambient temperatures of -4 °C (24.8 °F) and -6 °C (21.2 °F), respectively. Under the severest weather condition, where the ambient temperature and rate of snowfall are -10 °C (14 °F) and 10 cm/hr, respectively, it is not possible for this external hydronic system to heat the average surface temperature above 0 °C (32 °F), even by using a conventional heat pump. However, the external design still can be applied widely in the DFW area since severe snowy events are reported rarely there.

Fig. 6-13 compares the time-dependent relationships between the inlet fluid temperatures and the average steady-state temperatures on the deck surface under different ambient temperatures and rates of snowfall. The other related parameters, including wind speed, flow rate,

concrete thickness, and pipe spacing, were set to the values established in the base case, as shown in Table 6-2. It was observed that the decrease in surface temperature responses simulated under different rates of snowfall began at t = 7 hours due to the application of the snow-melting flux on the deck surface. The higher the rate of snowfall is, the greater the temperature drops, which is in agreement with the case study in Chapter 5. When the snowfall stopped at t = 14 hours, the temperature responses under different rates of snowfall began to increase, which is in good agreement with the temperature responses under the non-snowfall condition after t = 30 hours. Fig. 6-13 shows that except for the weather condition under the ambient temperature of -4 °C (24.8 °F) and rate of snowfall of 2 cm/hr, the externally heated bridge deck was not able to reach the desired snow-melting performance with a thermal supply of 48.9 °C (120 °F) under snowy events since the surface temperatures during snowfall were below the freezing temperature. A higher inlet fluid temperature is required for deicing.

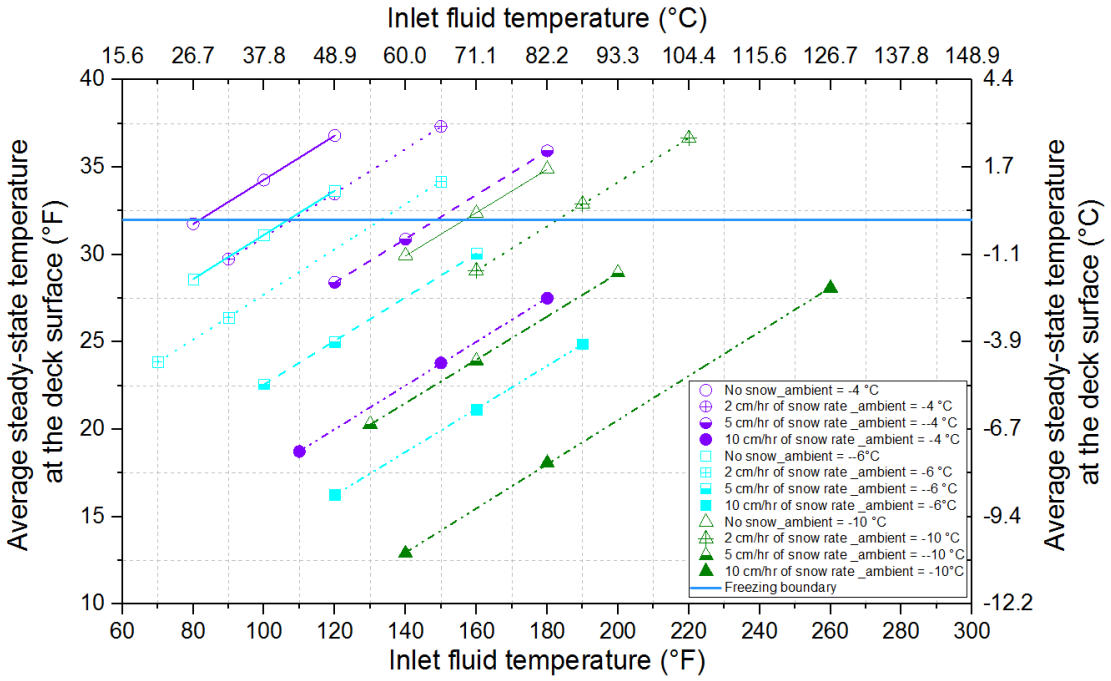

Figure 6-12. Design chart #6: Interactions between inlet fluid temperatures and average steady-state temperatures at the deck surface under various ambient temperatures and rates of snowfall

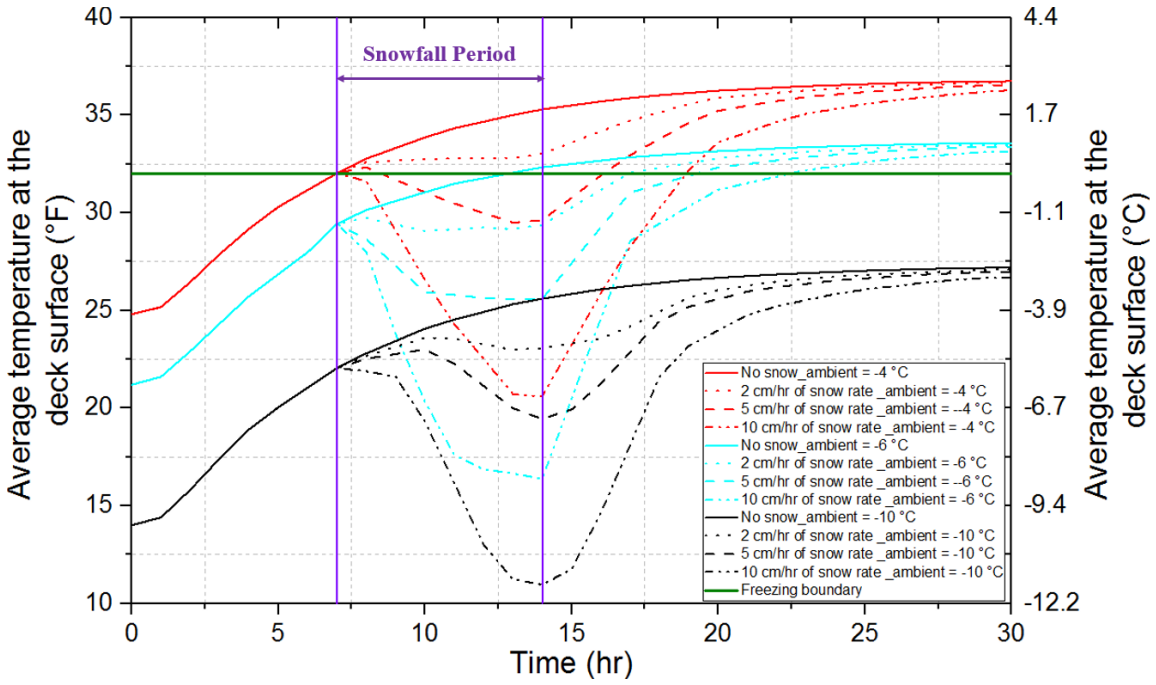

Figure 6-13. The number of heating hours required to raise the average temperatures at the deck surface above the freezing temperature under different ambient temperatures and rates of snowfall

6.4.2 Under Different Wind Speeds

Fig. 6-14 (Design chart #7) compares the average steady-state temperature at the deck surface under various wind speeds and snowy events. Similar to Section 6.3, the greater the wind speed is, the smaller the slope of the gridline is, which accounts for the relationship between the average steady-state surface temperatures and inlet fluid temperatures and shows that it is more difficult to increase the surface temperature under severe wind conditions. For the mild class of snowfall rate (2 cm/hr), the temperature of the supplied inlet fluid temperature has to reach 38.3 °C (101 °F), 42.2 °C (108 °F), and 55.6 °C (132 °F) for deicing when the wind speed flowing through the bridge deck is 4 m/s, 5m/s, and 8 m/s, respectively. The corresponding inlet temperature is required to be heated to 58.9 °C (138 °F), 65 °C (149 °F), and 77.8 °C (172 °F) if the rate of snowfall increases to 5 cm/hr. Similar to the example in Section 6.3.1, the external heating design

is not capable of providing sufficient heat energy for snow/ice melting under the most severe weather event (rate of snowfall and ambient temperature are equal to -10°C (14 °F) and 10 cm/hr, respectively) selected in this study.

Fig. 6-15 compares the transient correlations between the inlet fluid temperatures and the average steady-state temperatures on the deck surface under various wind speeds and rates of snowfall. The other related parameters, including ambient temperature, flow rate, concrete thickness, and pipe spacing were set to the specific values in the base case, as shown in Table 6-2. Similar to Fig. 6-13, the surface temperature responses under snowy conditions immediately dropped after t = 7 hours, due to the outward snow-melting flux applied on the deck surface. The higher the rate of snowfall is, the greater the temperature drops, which is in good agreement with the case study in Chapter 5. When the snowfall stopped, an increase of the temperature responses simulated under different snowy events was observed in Fig. 6-15. Good agreements can be obtained between the simulated temperatures under snowy scenarios and those under non-snowfall events after t = 30 hours. Similar to Fig. 6-13, this external heating system was not able to attain the desired snow-melting performance with a thermal supply of 48.9 °C (120 °F) under most snowy events selected in this study since the surface temperatures during the snowfall could not reach freezing. A higher inlet fluid temperature is required for deicing.

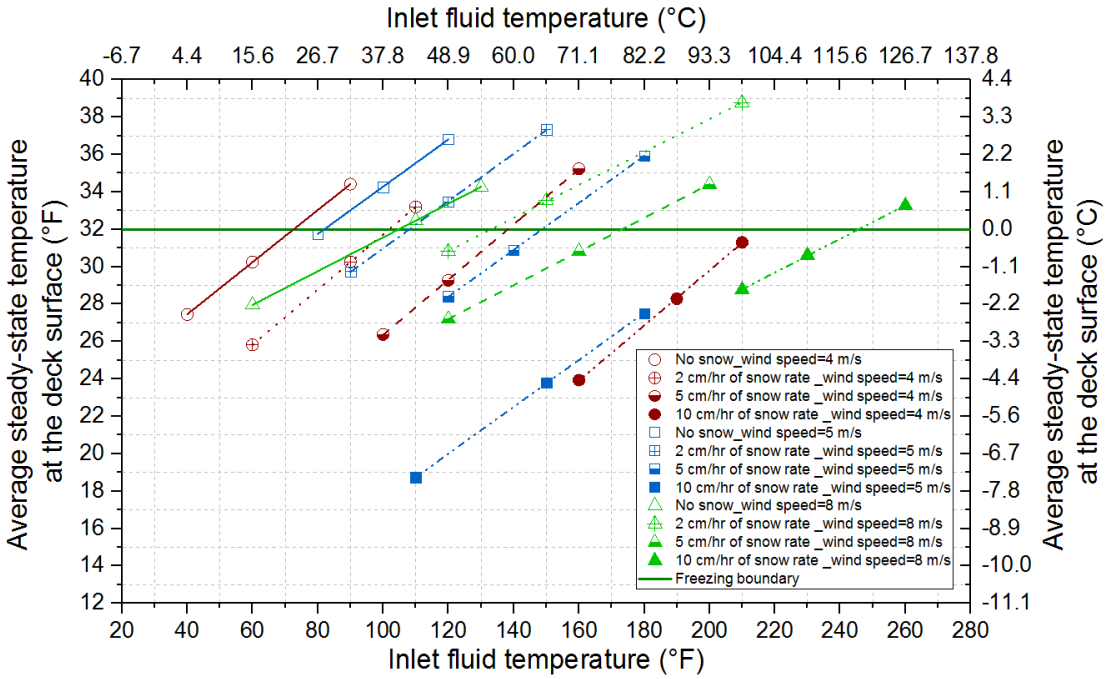

Figure 6-14. Design chart #7: Interactions between inlet fluid temperatures and average steady-state temperatures at the deck surface under various wind speeds and rates of snowfall

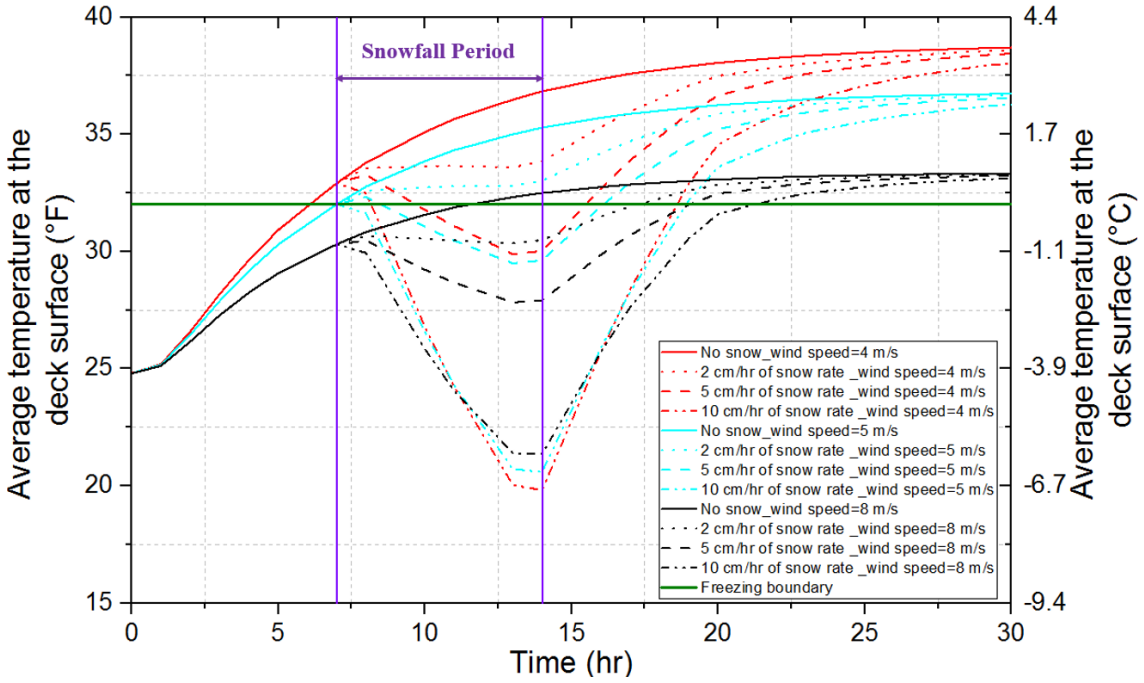

Figure 6-15. The number of heating hours required to raise the average temperatures at the deck surface above freezing under different ambient temperatures and rates of snowfall

6.5 Summary and Conclusions

This chapter described the design process for an externally heated bridge deck that used a series of design charts developed by the valuated FEM model depicted in Chapter 5 under various environmental and operational factors, including ambient temperature, wind speed, rate of snowfall, bridge deck thickness, pipe spacing, and flow rate. A simple example was presented in the appendix to provide a detailed process of how to use the design charts to design an external heating system under given conditions. This is the first time that this has been attempted, and it is expected to be viewed as a design guideline for externally heating bridge decks for deicing. In the future, more winter weather scenarios and parameters that may affect the performance of the heating system may be considered by researchers.

CHAPTER 7 CONCLUSIONS AND RECOMMENDATIONS

7.1 Introduction

The internal hydronic heating system is currently the most commonly utilized heating design for melting snow on bridge decks since it can serve as an alternative to chemical deicers, including calcium chlorides and sands, to prevent the corrosion of steel reinforcements and the degradation of pavements and bridges. Compared to the other environmentally friendly heating designs, such as heating pipes and electrical heating, the hydronic system can not only decrease the construction and installation cost, but also provide better heating performance and efficient heat transfers. Unfortunately, an internal hydronic design can be only applied to new bridge decks during the construction phase. To provide heating operations for existing bridge decks, external geothermally heated decks with insulated PEX pipe loops or hydronic loop systems encapsulated in a layer of geofoam for heat insulation have been developed recently. Many articles have been published on the investigations of internally heated bridge decks, and they can be important references for the study of external heating systems. However, this newly developed design still encounters a series of challenges due to a lot of gaps in the available research. There is little information on the efficiency of the heat transfer and the system's performance, and the lack of comprehensive design charts that focus on the heating performance of externally heated bridge decks under different weather and bridge construction conditions also limits the analysis of an external heating design. Therefore, the major objective of this dissertation research was to provide a comprehensive understanding of the system performance and heat transfer mechanisms of externally heated bridge decks under various thermal scenarios and environmental circumstances. Four major research tasks were performed in this dissertation work to achieve the objective.

In the first task, an external hydronically heated deck was fabricated and installed in an environmental chamber at the University of Texas at Arlington (UTA), and heating tests of the hydronic deck were performed under the conditions of controlled water and ambient temperatures. To model the newly tested hydronic deck and understand the heat transfer processes, a 3-dimensional Multiphysics model of the heated deck was developed in COMSOL. A transient analysis of the model was first performed and fully calibrated with the laboratory tests, and a thermal contact model was used to model a poor contact at the bottom of the bridge deck. The calibrated finite element model was further verified by the steady-state results of 15 environmental chamber tests. A heat flux and heat energy balance were performed on the heated deck to determine the heat energy flow and efficiency. It was found that the model is capable of accurately modeling the heat transfer processes in an externally heated deck and can be used for design.

The second task was to study two important interface heat transfer mechanisms, including convective heat loss to the environment and the thermal contact between the PEX pipes and the concrete. An internal heating system was installed in one concrete block, and an external heating system was attached to another concrete block. Both blocks were placed in a freezer box where environmental heating tests were conducted under controlled thermal supplies and ambient temperatures. Six heating response tests were performed to compare the heating performance and heat transfer efficiency of the two designs. Two 3-dimensional finite element models developed in COMSOL were utilized to replicate the heating tests to create time-dependent temperature response plots and gridlines under steady-state temperatures. Better agreement between the numerical outputs and experimental measurements were obtained for both the internally and externally heated blocks than were obtained in the first task, which signified that the improvements in the interface heat transfer modeling increased the accuracy of the FEM models. These improved

heated bridge deck models can be widely employed to analyze the practical feasibility of external heating systems in the field, as depicted in the third task.

The third task was to provide heating operations to existing bridges. The newly developed externally heated hydronic heating system presented in this study was installed on a mock-up bridge deck. A series of field tests, including non-heating, heating, and heating and deicing, were conducted under different scenarios. A 3-dimensional Multiphysics finite element model of the heated deck developed in COMSOL was fully calibrated with the field tests, under the transient approach. The heat transfer mechanisms of conduction, convection, radiation, and phase changes of ice/snow were also simulated in the finite element model to evaluate the system's performance and deicing behaviors within the deck. A numerical case study was performed by using the validated model to estimate the feasibility of melting snow with the novel external heating design under one of the most severe snowy events recorded in the DFW area. The results showed that the design of an externally heated bridge deck is feasible and promising for practical application.

In the fourth task, the fully validated FEM model of the mock-up bridge deck was employed to develop a series of design charts for an externally heated bridge deck design under parametric studies. Major parameters including ambient temperature, wind speed, rate of snowfall, bridge deck thickness, pipe spacing, and flow rate were considered in this research work. A comprehensive flow chart of the design process for externally heated bridge decks by application of design charts was presented as a design guideline. A simple example was also provided to show how to use the design charts to design an externally heated bridge deck.

A comprehensive numerical analysis of the heating and deicing performance of an externally heated bridge deck was developed through the contributions of the four research tasks

that created a series of design charts that can provide a detailed externally heated bridge deck design process. The major research findings are summarized in the next section.

7.2 Major Findings

The major findings that resulted from this research work are listed below.

1. A 3D FEM model of a concrete slab that is capable of modeling the laboratory heating tests under various thermal scenarios and environmental conditions was developed for an externally heated hydronic bridge deck. The maximum temperature deviation between the average simulated and recorded results at 2.5 cm (1 inch) below the deck surface was less than 0.5 ^{o}C (1 ^{o}F).
2. The 3D model was fully calibrated and validated with 16 test cases under time-dependent and stationary approaches. An R-square value of 0.999 was obtained for the best-fit line "y=x", which signified that the FEM outputs and experimental measurements were in reasonable agreement.
3. Comprehensive numerical modeling of heat transfer mechanisms, including conduction, convection, and radiation, from supplied circulating fluid to the deck surface for an externally heated bridge deck was developed in COMSOL and plays a crucial role in the accuracy of the FEM model.
4. An optimized combination of the h_c value of 80 W/(m^2·K) was employed to create a solid-to-solid thermal contact model to analyze the poor contact between the cement paste layer and the base of the concrete slab. This was the first attempt to model the heat transfer behaviors at the interface zone of an externally heated deck.
5. A satisfactory estimate of the convective coefficient of 38 W/(m^2·K) was found to model the convective heat transfer between the deck surface and the environment.

6. A proportional relationship between the average steady-state deck surface temperature and the supplied temperature of the external heating system can be expressed as a series of gridlines. The slope of each gridline remains constant and does not vary with ambient temperatures.
7. Two numerical predicted gridlines, respectively simulated under ambient temperatures of -6.7 ºC (20 ºF) and -1.1 ºC (30 ºF), indicated the same slope as those developed at above-freezing conditions, as described in the last finding.
8. The surface heat flux is approximately proportional to the thermal load (temperature difference between the inlet and the ambient temperature). The heat flux near the deck surface can be estimated using 1D heat conduction.
9. Compared to the heat efficiency of 60% evaluated by laboratory data, numerical energy balance analyses present that approximately 76% of total supplied heat can be transferred to the deck's top surface regardless of the ambient temperature. Measurement errors, material uncertainties, and heat losses from the interface zone may be associated with the difference in heat transfer efficiency.
10. The two FEM models of concrete blocks were utilized to simulate six laboratory heating tests under different ambient temperatures below freezing. The calculated R-square values of 0.999 (internal) and 0.997 (external) based on the best-fit line "y=x" indicated a reasonable match between the numerical and experimental measurements.
11. For internally and externally heated concrete blocks, the optimized combinations of h_c values were respectively 184 W/(m^2·K) and 122 W/(m^2·K), which were improved by installing more thermocouples at the interface zone between the installed PEX pipe and concrete.
12. Based on the finite difference method and an assumption of the one-dimensional heat transfer process, the average convective heat transfer coefficient, h, at the block's surface for each test

was 18.74 W/(m^2·K), 17.37 W/(m^2·K), 17.56 W/(m^2·K), 17.13 W/(m^2·K), 17.17 W/(m^2·K), and 16.47 W/(m^2·K), respectively.

13. With the improvements in the interface heat transfer analyses (convection at the block surface and thermal contact at interface zone), more accurate evaluations of vertical temperature profiles within the blocks can be developed and provide a comprehensive understanding of the vertical heat transfer behaviors within the blocks.
14. A new 3-dimensional finite element model of the externally heated hydronic mock-up bridge deck was created with a pipe flow module. The full cross-sectional 3D mesh of the pipe was not required to be generated in COMSOL, which can simplify the 3-D fluid flow equation for a 1-D approximation.
15. The newly developed model was fully calibrated by experimental data measured on-site under different operation scenarios including non-heating, heating, and heating and deicing tests.
16. The deicing behaviors were considered in terms of the amount of energy required to melt accumulated snow/ice on the deck surface, which can be performed by an outward boundary condition applied to the deck surface. This study is the first attempt to investigate the deicing behaviors of the surface of an externally heated bridge deck in the field.
17. A numerical case study was performed of one of the most severe snow events recorded in the DFW area by using the validated FEM model of the mock-up bridge deck. With the help of Eq. (5-3), an outward heat flux of 71 W/m^2 was applied to the deck surface for snow melting under a rate of snowfall of 1.5 cm/hr. The external heating system can heat the deck surface to 0.3 °C (32.6 °F) by supplying a minimum inlet temperature of 43.3 °C (110 °F). A minimum surface heat flux of 220 W/m^2 was required to maintain this surface temperature.

18. A series of design charts for an externally heated bridge deck design was developed by the fully validated FEM model of the mock-up bridge deck under a series of parametric studies, including ambient temperature, wind speed, rate of snowfall, pipe spacing, bridge deck thickness, and flow rate. This is the first design guideline for an externally heated bridge deck.
19. A comprehensive flow chart of the design process was developed to guide designers on how to use the design charts to design an externally heated bridge deck.

7.3 Recommendations for Future Research

The heating performance and comprehensive heat transfer behavior of an externally heated bridge deck were investigated in this research work. A detailed flow chart of the design process was developed by using a series of design charts created in COMSOL under parametric studies. The recommendations listed below may be considered to enhance the research on the design and application of an externally heated bridge deck.

1. A sufficiently accurate mesh analysis is crucial to simulating the heat transfer mechanisms in a heated deck. Therefore, a comprehensive mesh sensitivity analysis may be considered in future research, to obtain an optimized balance between the accuracy of FEM models and the computational expense.
2. A type T thermocouple from National Instruments with a measurement accuracy of +/-1°C (2°F) was utilized to measure the temperature responses within the deck slab. This thermocouple has a typical uncertainty that is adequate for many industrial applications, as well as activities in laboratories. Even if the difference between the inlet and outlet fluid temperature is small, however, the calculated thermal power may be too high, based on Eq. (3-11). To correctly estimate the thermal power exchanged by fluid with the ground, alternative

temperature sensors, such as PT100, that are much more accurate (less than 0.1 ^{o}C error, depending on the sensor model), could be considered in future research.

3. In this research, the deicing behaviors of the deck surfaces were evaluated in terms of energy balance to determine how much heat energy is required on the deck surface to melt the snow and/or ice. The complex snow/ice melting processes, including the change phase, were not modeled in COMSOL and would be an important topic for future research.
4. A series of design charts for externally heated bridge deck design were developed in this study. The heating performance and energy requirement for bridge deck deicing were evaluated under a series of environmental and operational parameters. The range of each parameter was selected, based on the recorded typical winter weather conditions in the DFW area, but it was not possible to cover all of the combinations of weather conditions. More design charts may be developed under more winter events in the future to extend the application of the external heating design. In addition, more parameters, such as relative humidity and solar radiative effects, may also be included in the development of the design charts.

APPENDIX

EXAMPLE FOR EXTERNALLY HEATED BRIDGE DECK DESIGN PROCESS

Step 1: Select typical weather and bridge deck conditions

Typical weather and bridge deck conditions: The selections are based on the typical conditions in the DFW area. The detailed information is presented in the following tables.

Table 1. Typical Weather Conditions Utilized in the Research

Ambient Temperature (°C)	Wind Speed (m/s)	Snowfall (cm/hr)
-10, -6, -4, -2, -1	1, 2, 4, 5, 8, 12	0, 2, 5, 10

Table 2. Typical Bridge Deck Conditions Utilized in the Research

Thickness of Bridge Deck (cm)	Pipe Spacing (cm)	Flow Rate (L/min)
20.32, 22.86, 25.4	20.32, 25.4, 30.48	7.6, 11.4, 15.1, 18.9, 22.7

Step 2: Calculate the heat flux required for heating and deicing at the surface.

The heat flux required for heating and snow/ice melting on the bridge deck surface was calculated by using Eq. (5-6) in Chapter 5, based on the selected weather data.

Step 3: Calculate the peak hourly bridge deck heating load by using the product of the heat flux calculated in the last step and the area of the bridge deck.

Step 4: Development of a series of design charts described in Sections 6.2 and 6.3

Step 5: Application of design charts

Step 5.1: Determine and design the weather and bridge conditions listed in the following table.

Ambient Temperature (°C)	Wind Speed (m/s)	Snowfall (cm/hr)	Thickness of Bridge Deck (cm)
-3	5	0	8

Step 5.2: Select 8 inches as the pipe spacing from design chart #3 in this example.

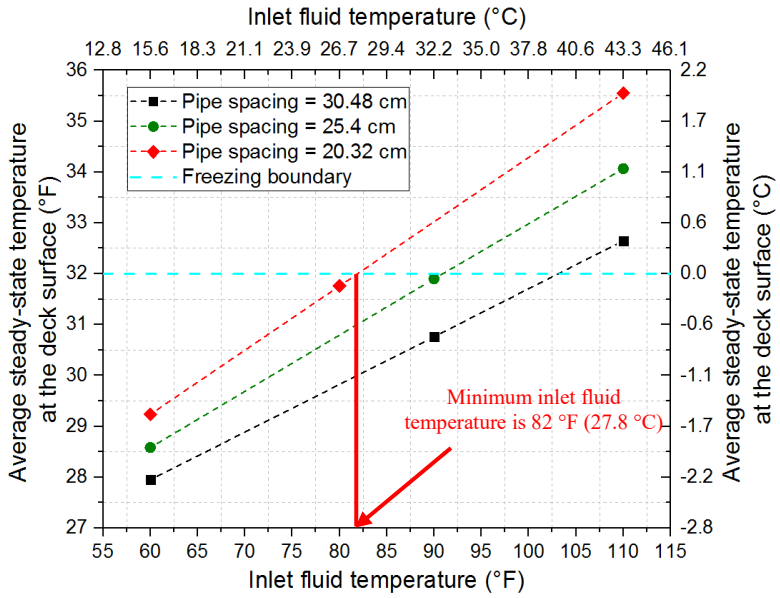

Design chart #1: Interactions between inlet fluid temperatures and average steady-state temperatures at the deck surface under different pipe spacing

From design chart #1, it was determined that the minimum inlet fluid temperature, under which the average steady-state surface temperature can be above the freezing under the selected pipe spacing (8 inches), is 82 °F (27.8°C).

Step 5.3: Select 11.4 L/min (4 gallons/min) as the flow rate from design chart #2 in this example. It was noted that the flow rate does not have a significant effect on the heating performance of the external design.

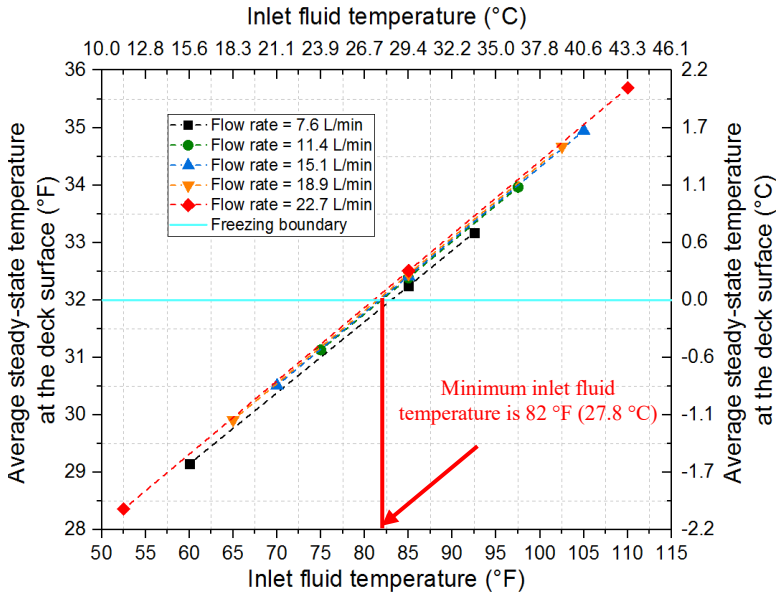

Design chart #2: Interactions between inlet fluid temperatures and average steady-state temperatures at the deck surface under various flow rates

From design chart #2, it was determined that the minimum inlet fluid temperature, under which the average steady-state surface temperature can be above the freezing under the selected flow rate, is 82 °F (27.8°C).

Step 5.4: Select 8 inches (20.32 cm) as the bridge deck thickness from design chart #3 in this example.

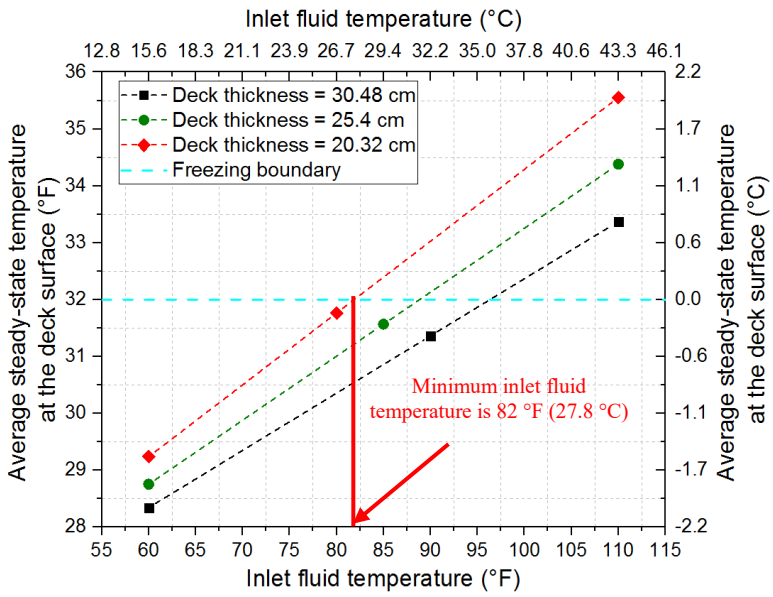

Design chart #3: Interactions between inlet fluid temperatures and average steady-state temperatures at the deck surface under various deck thicknesses

From design chart #3, it was determined that the minimum inlet fluid temperature, under which the average steady-state surface temperature can be above freezing under the selected deck thickness (8 inches), is 82 °F (27.8°C).

Step 5.5: Select 28.4 °F (-2 °C) as the ambient temperature from design chart #4 in this example.

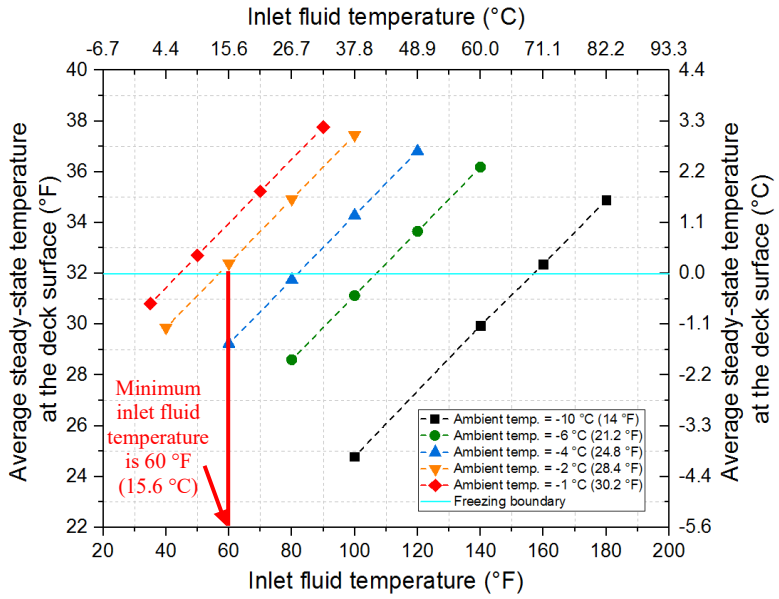

Design chart #4: Interactions between inlet fluid temperatures and average steady-state temperatures at the deck surface under various ambient temperatures

From design chart #4, it was determined that the minimum inlet fluid temperature, under which the average steady-state surface temperature can be above freezing under the selected ambient temperature of 28.4 °F (-2 °C) and wind speed of 5 m/s, is 60 °F (15.6 °C). However, the ambient temperature and wind speed are respectively 26.6 °F (-3 °C) and 5 m/s, which indicates that the actual minimum inlet fluid temperature under the design weather conditions should be greater than 60 °F (15.6 °C) to determine the required inlet fluid temperature.

Step 5.6: Select 5 m/s as the wind speed from design chart #5 in this example.

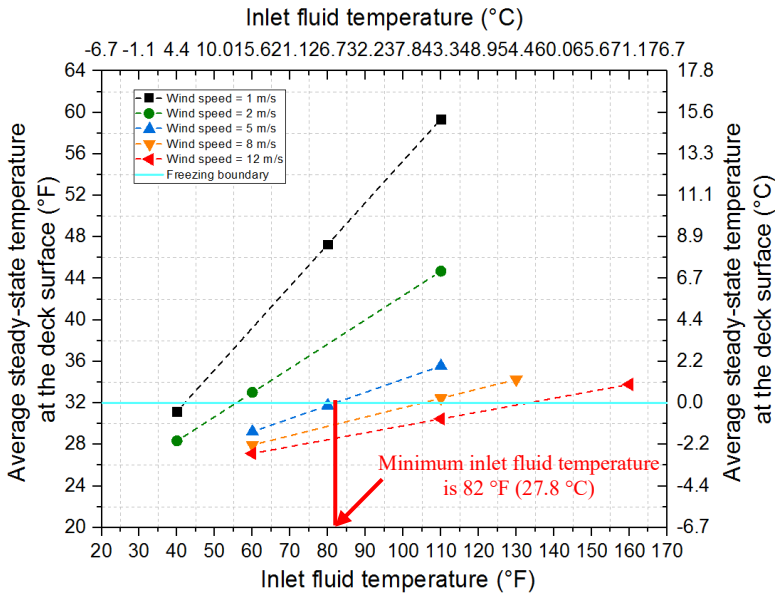

Design chart #5: Interactions between inlet fluid temperatures and average steady-state temperatures at the deck surface under various wind speeds

From Design chart #5, it was determined that the minimum inlet fluid temperature, under which the average steady-state surface temperature can be above the freezing under the selected 24.8 °F (-4 °C) of ambient temperature and 5 m/s of wind speed, is 82 °F (27.8 °C), which can be utilized as the upper limit of the required inlet fluid temperature.

Step 6. Determine the range of inlet fluid temperatures to reach deck surface temperature above freezing ≥ 32 °F (0 °C)

Through the mathematic knowledge of the set, the range of inlet fluid temperatures can be determined by the following figures.

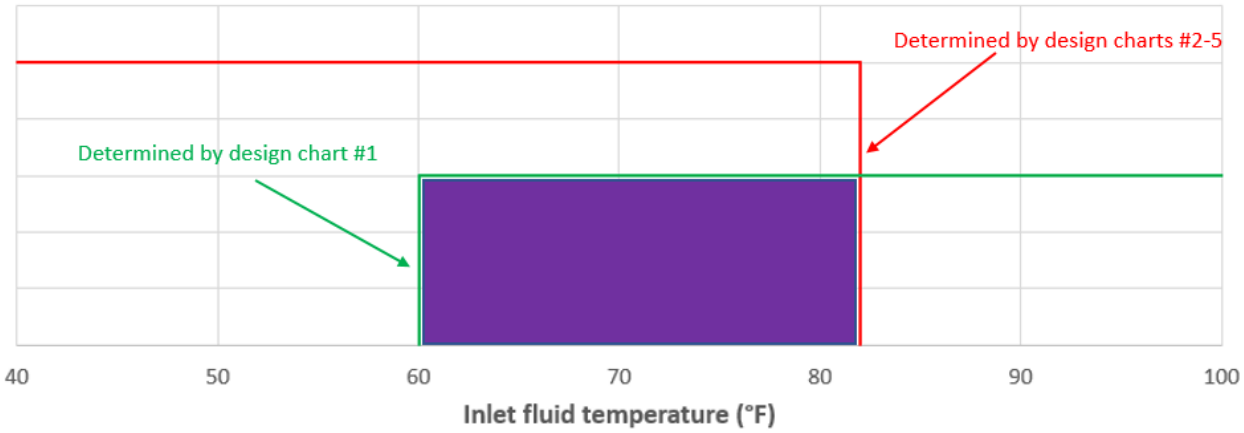

Therefore, the range of inlet fluid temperatures is from 60 °F to 82 °F, and an accurate value of the supplied inlet fluid temperature can be obtained by using the trial and error method.

Step 7: Select the number and arrangement of heat pump to supply the required inlet temperature.

Step 8: Design output requirements can be determined, as listed below:

- Ambient Temperature ≥ -3 °C
- Wind speed ≤ 5 m/s
- Pipe spacing ≤ 8 inches
- Flow rate ≥ 11.4 L /min
- Deck thickness ≤ 8 inches
- Rate of snowfall ≤ 2 cm/hr

If the environmental and operational factors meet the requirements listed above, the external heating system can melt snow and ice by supplying the selected inlet fluid temperature.

REFERENCES

Abdelaziz SL, Olgun CG, Martin IR (2011) Design and Operational Considerations of Geothermal Energy Piles. In: Han J, Alzamora DE (eds) Geo-Frontiers 2011 : advances in geotechnical engineering. American Society of Civil Engineers, Reston, Va., pp 450–459

Abdelaziz Sherif L., Olgun C. Guney, Martin II James R. (2015) Equivalent energy wave for long-term analysis of ground coupled heat exchangers. Geothermics 53:67–84. https://doi.org/10.1016/j.geothermics.2014.04.006

Acharya R, Bheemasetti TV, Ruttanaporamakul P, Chittoori B, Puppala AJ (2014) Numerical Modeling of a Highway Embankment Using Geofoam Material as Partial Fill Replacement 234:2986–2995. https://doi.org/10.1061/9780784413272.290

Adlam TN (1950) Snow melting: design, installation and control of systems for melting snow by hot water coils embedded beneath walks, roads, or other areas where snow is an obstruction or hazard. Industrial Press, New York

Alonso-Estébanez A, Pascual-Muñoz P, Sampedro-García JL, Castro-Fresno D (2017) 3D numerical modelling and experimental validation of an asphalt solar collector. Applied Thermal Engineering 126:678–688. https://doi.org/10.1016/j.applthermaleng.2017.07.127

Amayta BL, Soga K, Bounne-Webb PJ, Amis T, Laloui L (2012) Thermo-mechanical behaviour of energy piles. Géotechnique 62:503–519. https://doi.org/10.1680/geot.10.P.116

Asfour S, Bernardin F, Toussaint E, Piau J-M (2016) Hydrothermal modeling of porous pavement for its surface de-freezing. Applied Thermal Engineering 107:493–500. https://doi.org/10.1016/j.applthermaleng.2016.06.138

ASHRAE Handbook (2013) ASHRAE Handbook - Fundamentals (SI Edition), American Society of Heating, Refrigerating and Air-Conditioning Engineers, Inc.

At1m Balbay, M. Esen (2010) Experimental investigation of using ground source heat pump system for snow melting on pavements and bridge decks. Scientific Research and Essays 5:3955–3966

Barnard ALC, Hunt WA, Timlake WP, Varley E (1966) A Theory of Fluid Flow in Compliant Tubes. Biophysical Journal 6:717–724. https://doi.org/10.1016/S0006-3495(66)86690-0

Bienert WB, Pravda MF, Suelau HH, Wolf DA (1974) Snow and ice removal from pavements using stored earth energy. NASA STI/Recon Technical Report N 75

Bourne-Webb PJ, Amatya B, Soga K, Amis T, Davidson C, Payne P (2009) Energy pile test at Lambeth College, London: geotechnical and thermodynamic aspects of pile response to heat cycles. Géotechnique 59:237–248. https://doi.org/10.1680/geot.2009.59.3.237

Bowers JA (2016) Ground-Source Bridge Deck Deicing and Integrated Shallow Geothermal Energy Harvesting Systems. Doctoral Dissertation, Virginia Tech.

Bowers JGA, Olgun CG (2014) Ground-Source Bridge Deck Deicing Systems Using Energy Foundations 234:2705–2714. https://doi.org/10.1061/9780784413272.261

Brandl H (2006) Energy foundations and other thermo-active ground structures. Géotechnique 56:81–122. https://doi.org/10.1680/geot.2006.56.2.81

Carotenuto A, Marotta P, Massarotti N, Mauro A, Normino G (2017) Energy piles for ground source heat pump applications: Comparison of heat transfer performance for different design and operating parameters. Applied Thermal Engineering 124:1492–1504. https://doi.org/10.1016/j.applthermaleng.2017.06.038

Chapman WP (1952) Design of snow melting systems. Heating and Ventilating 49:96–102

Chapman WP (1956) Heat requirements of snow melting systems. Heating, Piping and Air Conditioning 28:149–153

Chávez-Galán J, Almanza R, Cuevas NR (2014) Convective heat transfer coefficients: experimental estimation and its impaction on thermal building design for walls made of different Mexican building materials. IMCYC 5:26–38

Chen J, Wang H, Xie P (2019) Pavement temperature prediction: Theoretical models and critical affecting factors. Applied Thermal Engineering 158:113755. https://doi.org/10.1016/j.applthermaleng.2019.113755

Chiasson A, Spitler JD (2001a) Modeling approach to design of a ground-source heat pump bridge deck heating system. In: ADVANCES AND ISSUES IN SNOW-REMOVAL AND ICE-CONTROL TECHNOLOGY: MAINTENANCE, pp 207–215

Chiasson A, Spitler JD (2001b) Modeling Approach to Design of a Ground-Source Heat Pump Bridge Deck Heating System. Transportation Research Record 1741:207–215. https://doi.org/10.3141/1741-29

Chiasson AD, Spitler JD, Rees SJ, Smith MD (2000) A Model for Simulating the Performance of a Pavement Heating System as a Supplemental Heat Rejecter With Closed-Loop Ground-Source Heat Pump Systems. Journal of Solar Energy Engineering 122:183–191. https://doi.org/10.1115/1.1330725

Colangelo F, Luca G de, Ferone C, Mauro A (2013) Experimental and Numerical Analysis of Thermal and Hygrometric Characteristics of Building Structures Employing Recycled Plastic Aggregates and Geopolymer Concrete. Energies 6:6077–6101. https://doi.org/10.3390/en6116077

COMSOL (2016) COMSOL Multiphysics version 5.2a: User's Guide and Reference Manual

Dorfman A, Renner Z (2009) Conjugate Problems in Convective Heat Transfer: Review. Mathematical Problems in Engineering 2009:1–27. https://doi.org/10.1155/2009/927350

Duffie JA, Beckman WA (2013) Solar engineering of thermal processes, Fourth edition. Wiley, Hoboken, New Jersey

Fadejev J, Simson R, Kurnitski J, Haghighat F (2017) A review on energy piles design, sizing and modelling. Energy 122:390–407. https://doi.org/10.1016/j.energy.2017.01.097

Fieberg C, Kneer R (2008) Determination of thermal contact resistance from transient temperature measurements. International Journal of Heat and Mass Transfer 51:1017–1023. https://doi.org/10.1016/j.ijheatmasstransfer.2007.05.004

GRIFFIN PA, SANVICENTE AZ (1982) Common Stock Returns and Rating Changes: A Methodological Comparison. The Journal of Finance 37:103–119. https://doi.org/10.1111/j.1540-6261.1982.tb01098.x

Habibzadeh-Bigdarvish O, Yu X, Lei G, Li T, Puppala AJ (2019) Life-Cycle cost-benefit analysis of Bridge deck de-icing using geothermal heat pump system: A case study of North Texas. Sustainable Cities and Society 47:101492. https://doi.org/10.1016/j.scs.2019.101492

Habibzadeh-Bigdarvish O, Yu X, Li T, Lei G, Banerjee A, Puppala AJ (2020) A Novel Full-Scale External Geothermal Heating System for Bridge Deck De-icing. Applied Thermal Engineering:116365. https://doi.org/10.1016/j.applthermaleng.2020.116365

Hockersmith SL (2002) Experimental and computational investigation of snow melting on heated horizontal surfaces. M.S. Thesis, Oklahoma State University, Stillwater, OK

Incropera FP, DeWitt DP, Bergman TL, Lavine AS (2007) Fundamentals of heat and mass transfer, 6th ed. / Frank P. Incropera … [et al.]. Wiley; Chichester; John Wiley [distributor], Hoboken, N.J.

J. A. Duffie, W. A. Beckman (eds) (2013) Solar Engineering of Thermal Processes, 4th ed. Inc., Hoboken, New Jersey

Johnston IW, Narsilio GA, Colls S (2011) Emerging geothermal energy technologies. KSCE J Civ Eng 15:643–653. https://doi.org/10.1007/s12205-011-0005-7

Kilkis IB (1992) Enhancement of heat pump performance using radiant floor heating systems. ASME AES 28:119–127

Kilkis IB (1994a) Design of embedded snow melting systems: Part 1, Heat requirements - An overall assessment and recommendations. Proc., Proceedings of the ASHRAE Winter Meeting 100:423–433

Kilkis IB (1994b) Design of embedded snow-melting systems: part 2, heat transfer in the slab - a simplified model. Proc., Proceedings of the ASHRAE Winter Meeting 100:434–441

Knellwolf C, Peron H, Laloui L (2011) Geotechnical Analysis of Heat Exchanger Piles. J. Geotech. Geoenviron. Eng. 137:890–902. https://doi.org/10.1061/(ASCE)GT.1943-5606.0000513

Koch GH, Brongers MPH, Thompson NG, Virmani YP, Payer JH (2002) Corrosion Cost and Preventive Strategies in the United States, Publication No. FHWA-RD-01-156. FHWA, U.S. Department of Transportation

Laloui L, Nuth M, Vulliet L (2006) Experimental and numerical investigations of the behaviour of a heat exchanger pile. Int. J. Numer. Anal. Meth. Geomech. 30:763–781. https://doi.org/10.1002/nag.499

Leal M, Miller PL (1972) An Analysis of the Transient Temperature Distribution in Pavement Heating Installations. ASHRAE Transactions 78:61–66

Lee S, Song S, Moran KP, Yovanovich MM (1993) Analytical modeling of thermal resistance in bolted joint. Enhanced Cooling Techniques for Electronics Applications ASME 263:115–122

Lei G, Yu X, Li T (2018) Design and Numerical Analysis of an Externally Heated Geothermal Bridge Deck. Civil Infrastructures Confronting Severe Weathers and Climate Changes Conference:150–159. https://doi.org/10.1007/978-3-319-95783-8_13

Lei G, Kaneza N, Yu X, Li T, Habibzadeh-Bigdarvish O (2019) Development of a one-dimensional heating soil test cell 310:682–690. https://doi.org/10.1061/9780784482124.069

Lei G, Yu X, Li T, Habibzadeh-Bigdarvish O, Wang X, Mrinal M, Luo C (2020) Feasibility study of a new attached multi-loop CO2 heat pipe for bridge deck de-icing using geothermal energy. Journal of Cleaner Production 275:123160. https://doi.org/10.1016/j.jclepro.2020.123160

Li T, Lei G, Yu X, Zhang N, Puppala AJ (2018) Numerical Feasibility Study of an Externally Heated Geothermal Bridge Deck. Proc., IFCEE 294:758–767. https://doi.org/10.1061/9780784481578.072

Li T, Yu X, Lei G, Habibzadeh-Bigdarvish O, Hurley M (2020) Numerical analyses of a laboratory test of a geothermal bridge deck externally heated under controlled temperature. Applied Thermal Engineering 174:115255. https://doi.org/10.1016/j.applthermaleng.2020.115255

Lienhard IV JH (2011) A heat transfer textbook, 4th ed. Dover Publications, Mineola N.Y.

Liu X (2005) Development and experimental validation of Development and experimental validation of simulation of hydronic snow melting system for bridges. Dissertation, Oklahoma State University

Liu X, Spitler JD (2004) Simulation based investigation on the design of hydronic snow melting system. Proc., Transportation Research Board 83rd Annual Meeting

Liu X, Rees SJ, Spitler JD (2003) Simulation of a Geothermal Bridge Deck Anti-Icing System and Experimental Validation. 82nd Annual Meeting of the Transportation Research Board

Liu X, Rees SJ, Spitler JD (2007a) Modeling snow melting on heated pavement surfaces. Part I: Model development. Applied Thermal Engineering 27:1115–1124. https://doi.org/10.1016/j.applthermaleng.2006.06.017

Liu X, Rees SJ, Spitler JD (2007b) Modeling snow melting on heated pavement surfaces. Part II: Experimental validation. Applied Thermal Engineering 27:1125–1131. https://doi.org/10.1016/j.applthermaleng.2006.07.029

Liu D, Luo Y, Shang X (2015) Experimental investigation of high temperature thermal contact resistance between high thermal conductivity C/C material and Inconel 600. International Journal of Heat and Mass Transfer 80:407–410. https://doi.org/10.1016/j.ijheatmasstransfer.2014.09.044

Liu K, Huang S, Jin C, Xie H, Wang F (2017) Prediction models of the thermal field on ice-snow melting pavement with electric heating pipes. Applied Thermal Engineering 120:269–276. https://doi.org/10.1016/j.applthermaleng.2017.04.008

Lund JW, Boyd TL (2016) Direct utilization of geothermal energy 2015 worldwide review. Geothermics 60:66–93. https://doi.org/10.1016/j.geothermics.2015.11.004

Madhusudana CV (1975) The effect of interface fluid on thermal contact conductance. International Journal of Heat and Mass Transfer 18:989–991. https://doi.org/10.1016/0017-9310(75)90193-3

Merrill BD (ed) (2002) Texas' use of precast concrete stay-in-place forms for bridge decks. National Concrete Bridge Council, Proc., Concrete Bridge Conference

Mirzanamadi R, Hagentoft C, Johansson P (2018) An analysis of hydronic heating pavement to optimize the required energy for anti-icing. Applied Thermal Engineering 144:278–290. https://doi.org/10.1016/j.applthermaleng.2018.08.053

Naito C, Sause R, Hodgson I, Pessiki S, Macioce T (2010) Forensic Examination of a Noncomposite Adjacent Precast Prestressed Concrete Box Beam Bridge. J. Bridge Eng. 15:408–418. https://doi.org/10.1061/(ASCE)BE.1943-5592.0000110

Nam Y, Chae H-B (2014) Numerical simulation for the optimum design of ground source heat pump system using building foundation as horizontal heat exchanger. Energy 73:933–942. https://doi.org/10.1016/j.energy.2014.06.108

Ozudogru TY, Olgun CG, Senol A (2014) 3D numerical modeling of vertical geothermal heat exchangers. Geothermics 51:312–324. https://doi.org/10.1016/j.geothermics.2014.02.005

Ramsey JW, Hewett MJ, Kuehn TH, Petersen SD (1999) Updated design guidelines for snow melting systems. ASHRAE Transactions 105:PART 1

Rees SJ, Spitler JD, Xiao X (2002) Transient analysis of snow-melting system performance. Proc., ASHRAE Transactions 108:406–423

Regis M, Leal LV, Miller PL (1973) Transient temperature field in a plane slab with embedded cylindrical sources. International Journal of Heat and Mass Transfer 16:1319–1322. https://doi.org/10.1016/0017-9310(73)90138-5

Ruttanaporamakul P, Puppala AJ, Pedarla A, Bheemasetti TV, Williammee RS (2016) Settlement mitigation of a distressed embankment in Texas by utilization of lightweight EPS geofoam material. Transportation Research Board 95th Annual Meeting:16–4179

Sartori E (2006) Convection coefficient equations for forced air flow over flat surfaces. Solar Energy 80:1063–1071. https://doi.org/10.1016/j.solener.2005.11.001

Schnurr NM, Rogers DB (1970) Heat Transfer Design Data for Optimization of Snow Melting Systems. ASHRAE Transactions 76:257–263

Schurr NM, Falk MW (1973) Transient analysis of snow-melting system performance. ASHRAE Transactions 79:159–166

Shang Y, Li S, Li H (2011) Analysis of geo-temperature recovery under intermittent operation of ground-source heat pump. Energy and Buildings 43:935–943. https://doi.org/10.1016/j.enbuild.2010.12.017

Sharples S, Charlesworth PS (1998) Full-scale measurements of wind-induced convective heat transfer from a roof-mounted flat plate solar collector. Solar Energy 62:69–77. https://doi.org/10.1016/S0038-092X(97)00119-9

Spitler JD (2000) A design tool for commercial building ground loop heat exchangers. Proc., 4th International Heat Pumps in Cold Climates Conference

Sterpi D, Angelotti A, Habibzadeh-Bigdarvish O, Jalili D (2018) Assessment of thermal behaviour of thermo-active diaphragm walls based on monitoring data. Journal of Rock Mechanics and Geotechnical Engineering 10:1145–1153. https://doi.org/10.1016/j.jrmge.2018.08.002

Vyas BG, Nirmal P (2016) Experimental analysis of thermal contact resistance across different composite material pair using different interface material in presence of pressure condition. International Journal of Current Research 8:39322–39328

Wang X, Zhu Y, Zhu M, Zhu Y, Fan H, Wang Y (2017) Thermal analysis and optimization of an ice and snow melting system using geothermy by super-long flexible heat pipes. Applied Thermal Engineering 112:1353–1363. https://doi.org/10.1016/j.applthermaleng.2016.11.007

Williams GP (1976) Design heat requirements for embedded snow-melting systems in cold climates. Transportation Research Record 576:20–32

Williamson PJ (1967) The estimation of heat outputs for road heating installations. Road Res. Lab. Report No. RRL-LR77:Crowthorne, UK.

Wu S, Chen M, Zhang J (2011) Laboratory investigation into thermal response of asphalt pavements as solar collector by application of small-scale slabs. Applied Thermal Engineering 31:1582–1587. https://doi.org/10.1016/j.applthermaleng.2011.01.028

Xiao S, Suleiman MT (2015) Investigation of Thermo-Mechanical Load Transfer (t-z Curves) Behavior of Soil-Energy Pile Interface Using Modified Borehole Shear Tests. Proc., IFCEE:1658–1667. https://doi.org/10.1061/9780784479087.150

Xiao S, Suleiman MT, Naito CJ, Neti S (2013) Use of Geothermal Deep Foundations for Bridge Deicing. Transportation Research Record 2363:56–65. https://doi.org/10.3141/2363-07

Yoshitake I, Yasumura N, Syobuzako M, Scanlon A (2011) Pipe Heating System with Underground Water Tank for Snow Thawing and Ice Prevention on Roads and Bridge Decks. J. Cold Reg. Eng. 25:71–86. https://doi.org/10.1061/(ASCE)CR.1943-5495.0000023

Yu X, Hurley MT, Li T, Lei G, Pedarla A, Puppala AJ (2020) Experimental feasibility study of a new attached hydronic loop design for geothermal heating of bridge decks. Applied Thermal Engineering 164:114507. https://doi.org/10.1016/j.applthermaleng.2019.114507

Yunovich M, Thompson NG, Virmani YP (2003) Life Cycle Cost Analysis for Reinforced Concrete Bridge Decks:Paper No. 03309

Zhang N, Yu X, Li T (2017) Numerical simulation of geothermal heated bridge deck. DEStech Transactions on Materials Science and Engineering